The structure, stellar population, and formation history of the Milky Way's nuclear star cluster

Universidad de Granada

Eulalia Gallego Cano

Radioastronomy and galactic structure department

Instituto de Astrofísica de Andalucía

Programa de Doctorado en Física y Ciencias del Espacio

A thesis submitted for the degree of

PhilosophiæDoctor (PhD)

May 2019

Examination date: May 10, 2019

Thesis supervisors:
Dr. Rainer Schödel

Cover design: Dra. María Passas Varo

Cover picture: The Center of the Milky Way. NASA / JPL-Caltech / S. Stolovy (Spitzer Science Center/Caltech)

Some of the figures included in this document have been previously published in *Astronomy & Astrophysics*

1. Reviewer:

2. Reviewer: Day of the defense: May 10, 2019

Signature from the head of the PhD committee:

o

Abstract

The center of the Milky Way is the only galactic nucleus and the most extreme astrophysical environment that we can examine on scales of milli- parsecs. It contains the nearest example of a nuclear star cluster (NSC). NSCs have been found at the photometric and dynamical centers of the majority of galaxies in the local Universe. With effective radii of a few parsecs and masses ranging between a few times 10^6–10^8 $M_\odot$, they are among the densest known stellar structures. NSCs possess complex stellar populations and show clear signs of recurrent star formation, with the most recent event having occurred less than 100Myr ago in many of them. Moreover, NSCs can coexist with massive black holes (MBHs) at their centers.

The Milky Way's nuclear star cluster (MWNSC) is located at a mere 8 kpc from Earth. While we can only study the integrated light in extragalactic NSCs, we can in the case of the Galactic center (GC) resolve physical scales on the order of a few milliparsecs (mpc) and thus study the properties, kinematics and even dynamics of individual stars. We possess unambiguous evidence for the existence of a 4×10^6 $M_\odot$ central black hole at the center of the MWNSC, thus making it an ideal target to study the interaction between a dense stellar cluster and a massive black hole. Due to the unique observational challenges – extreme crowding and extinction – the study of the NSC at the GC is confronted with unique difficulties. The high extinction

limits imaging studies of the stars to the near-infrared (NIR). While this allows us, on the one hand, to use techniques like adaptive optics (AO) to obtain high angular resolution images from the ground, it poses, on the other hand, serious problems for stellar classification because the intrinsic colours of stars are small in the NIR. Because of the observational difficulties, our knowledge about the NSC still contains significant gaps, despite of several decades of observations. Existing work is affected by either one or both of the following problems: (a) Low angular resolution, thus limiting it to the study of the brightest stars that represent less than one percent of the total population of the NSC; (b) limited spectral coverage, thus limiting their use for distinguishing between different types of stars. Spectroscopic studies with high angular resolution are necessarily limited to small numbers of stars or very small fields. They are therefore mostly limited to the central parsec.

This thesis aims at providing answers to unresolved questions in our understanding of the GC, as well as provide new constraints on the structure of the MWNSC by using high resolution images and by improving the analysis. I examine images in a broad span of distances from the center of the Galaxy: from very large distances ($\sim$ 860 pc x 280 pc) to the innermost arcseconds where the supermassive black hole inhabits.

Firstly, I aim to study the size and spatial structure of the MWNSC. I use data and methods that address potential shortcomings in previous work on the topic. I use $0.2''$ angular resolution K_s data to create a stellar density map in the central 86.4pc x 21 pc at the GC. I include data from selected AO assisted images obtained for the inner parsecs. In addition, I use IRAC/Spitzer MIR images. I model the Galactic bulge and the

nuclear stellar disk in order to subtract them from the MWNSC. Finally, I fit a Sérsic model to the MWNSC and investigate its symmetry. I find that the MWNSC is flattened with an axis ratio of $q = 0.71 \pm 0.06$, an effective radius of $R_e = (5.1 \pm 0.6)$ pc, and a Sérsic index of $n = 2.2 \pm 0.4$. Its major axis may be tilted out of the Galactic plane by up to -10 degree. The distribution of the giants brighter than the Red Clump (RC) is found to be significantly flatter than the distribution of the faint stars. The MWNSC shares its main properties with other extragalactic NSCs found in spiral galaxies. The differences in the structure between bright giants and RC stars might be related to the existence of not completely mixed populations of different ages. This may hint at recent growth of the MWNSC through star formation or cluster accretion.

I also revisit the problem of inferring the innermost structure of the MWNSC, to clarify whether it displays a core or a cusp around the central black hole. The existence of dynamically relaxed stellar density cusp in dense clusters around massive black holes is a long-standing prediction of stellar dynamics, but it has so far escaped unambiguous observational confirmation. In order to study the distribution of stars around Sgr A*, I use data obtained with the NACO instrument at the ESO/Very Large Telescope (VLT) and I focus on two different methods to analyze three different stellar brightness ranges. I find that a Nuker law provides an adequate description of the nuclear cluster's intrinsic shape (assuming spherical symmetry). I find that the stellar density decreases with a 3D power-law index inside the range $\gamma = 1.1 - 1.4$ for distances smaller than the influence radius of Sgr A* (~ 3 pc). We can rule out a flat core with high confidence. The cusp is shallower than the predicted one by the-

ory, but it can be explained if the star formation history of the NSC is taken into acount (*Baumgardt et al.*, 2018).

Finally, I peek at the very center of the Galaxy by improving the reduction and analysis of existing data. I use holographic technique and bootstrapping analysis. This has led to the detection of NIR emission of Sgr A* in epochs prior to 2003, when the first measurements were taken due to the development of AO. That allows *Chen et al.* (in preparation) to study the long-term NIR activity and explore the accretion flow onto the black hole in epochs where it had not been detected so far.

Resumen

El centro de la Vía Láctea es el único núcleo galáctico y el entorno astrofísico más extremo que podemos examinar en escalas de milli-parsecs. Contiene el ejemplo más cercano de un cúmulo estelar nuclear (o NSC, del inglés nuclear star cluster). Los NSCs han sido encontrados en los centros fotométricos y dinámicos de la mayoría de las galaxias en el Universo local. Con radios efectivos de unos pocos parsecs y masas que van entre unas pocas veces 10^6–10^8 $M_\odot$, se encuentran entre las estructuras estelares más densas conocidas. Además, los NSCs pueden coexistir con agujeros negros masivos (o MBHs, del inglés massive black holes) en sus centros. El cúmulo estelar nuclear de la Vía Láctea (o MWNSC, del inglés Milky Way's NSC) está situado a tan sólo 8 kpc de la Tierra. Mientras que podemos estudiar únicamente la luz integrada en NSCs extragalácticos, en el caso del centro galáctico (o GC, del inglés Galactic center) podemos resolver escalas físicas del orden de unos pocos milli-parsecs (mpc) y, por lo tanto, estudiar las propiedades, cinemática, e incluso la dinámica de estrellas individuales. Contamos con evidencia inequívoca de la existencia de un agujero negro de masa 4×10^6 $M_\odot$ en el centro del MWNSC, convirtiéndolo así en un objetivo ideal donde estudiar la interacción entre un cúmulo estelar nuclear y un agujero negro masivo. Debido a sus desafíos observacionales únicos - extremo hacinamiento y extinción - el estudio del NSC en el GC se enfrenta a dificultades únicas. La alta extinción limita los estudios de imágenes de las estrellas al infrarrojo (o NIR, del inglés

near-infrared). Mientras que esto nos permite el uso de técnicas como la óptica adaptativa (o AO, del inglés adaptive optics) para obtener imágenes con alta resolución angular desde la tierra por un lado, por otro lado tenemos serios problemas para la clasificación estelar debido a que el color intrínseco de las estrellas son pequeños en el NIR. A causa de las dificultades observacionales, nuestro conocimiento del NSC contiene todavía brechas significativas, a pesar de varias décadas de observaciones. El trabajo existente está afectado por uno o ambos de los siguientes problemas: (a) Baja resolución angular, limitándolo así al estudio de las estrellas más brillantes, que representan menos que el uno por ciento de la población total del NSC; (b) cobertura espectral limitada, lo que limita su uso para distinguir entre diferentes tipos de estrellas. Los estudios espectroscópicos con alta resolución angular están necesariamente restringidos a pequeños números de estrellas o campos muy pequeños. Por lo tanto, están en su mayoría limitados al parsec central.

Esta tesis tiene como objetivo proporcionar respuestas a preguntas sin resolver en nuestra comprensión del GC, así como proporcionar nuevas restricciones en la estructura del MWNSC mediante el uso de imágenes de alta resolución y la mejora del análisis. Examino las imágenes en un amplio rango de distancias desde el centro de la Galaxia: desde distancias muy grandes ($\sim$ 860 pc x 280 pc) hasta los arco-segundos más profundos donde habita el agujero negro supermasivo.

En primer lugar, mi objetivo es estudiar el tamaño y la estructura espacial del MWNSC. Utilizo datos y métodos que abordan posibles deficiencias en trabajos anteriores sobre el tema. Utilizo $0.2''$ resolución angular K_s datos para crear un mapa de

densidad estelar en el GC en los 86.4 pc x 21 pc centrales. Incluyo datos de imágenes asistidas por AO obtenidas para los parsecs internos. Además, utilizo imágenes del medio infrarrojo de IRAC/Spitzer. Modelo el bulbo galáctico y el disco estelar nuclear para subtraerlos del MWNSC. Finalmente, ajusto un modelo Sérsic a el MWNSC e investigo su simetría. Encuentro que el MWNSC está aplanado con una relación de eje de $q = 0.71 \pm 0.06$, un radio efectivo de $R_e = (5.1 \pm 0.6)$ pc, y un índice Sérsic de $n = 2.2 \pm 0.4$. Su eje mayor se puede inclinar desde el plano galáctico hasta -10 grados. La distribución de las estrellas gigantes más brillantes que el grupo rojo (o RC, del inglés red clump) es significativamente más plano que la distribución de las estrellas débiles. El MWNSC comparte sus principales propiedades con otros NSCs extragalácticos encontrados en galaxias espirales. Las diferencias en la estructura entre gigantes brillantes y las estrellas RC podrían estar relacionadas con la existencia de poblaciones de diferentes edades no completamente mezcladas. Esto puede indicar un crecimiento reciente del MWNSC a través de la formación de estrellas o la acreción de cúmulos.

También reviso el problema de inferir la estructura más interna del MWNSC, para aclarar si muestra un corazón o una cúspide alrededor del agujero negro central. La existencia de una cúspide de densidad estelar dinámicamente relajada en grupos densos alrededor de agujeros negros masivos es una antigua predicción de la dinámica estelar, pero hasta ahora ha escapado de la confirmación observacional sin ambigüedades. Para estudiar la distribución de estrellas alrededor de Sgr A*, uso los datos obtenidos con el instrumento NACO en el telescopio ESO/*Very Large Telescope* (VLT) y me centro en dos métodos diferentes

para analizar tres rangos de brillo estelar diferentes. Encuentro que una ley de Nuker proporciona una descripción adecuada de la forma intrínseca del cúmulo nuclear (asumiendo simetría esférica). Encuentro que la densidad estelar disminuye con un índice 3D de ley de potencia dentro del rango $\gamma = 1.1 - 1.4$ para distancias más pequeñas que el radio de influencia de Sgr A* ($\sim$ 3 pc). Podemos descartar un corazón plano con alta confianza. La cúspide es menos profunda que la pronosticada por la teoría, pero puede explicarse si se tiene en cuenta la historia de formación estelar del NSC (*Baumgardt et al.*, 2018).

Finalmente, me asomo al mismo centro de la Galaxia mejorando la reducción y al análisis de los datos existentes. Gracias a la técnica holográfica y el análisis bootstrapping, detectamos la emisión de NIR de Sgr A* en épocas anteriores a 2003, cuando se tomaron las primeras mediciones debido al desarrollo de AO. Esto permite a *Chen et al.* (in preparation) estudiar la actividad en el NIR a largo plazo y explorar el flujo de acreción en el agujero negro en épocas donde no se había detectado hasta el momento.

To Siro and Ana, my guide stars

Contents

Glossary

ADAF Advection-Dominated Accretion Flow

AGB Asymptotic-Giant-Branch

AGN Active Galactic Nucleus

AO Adaptive Optics

BH Black Hole

CGRO Compton Gamma-Ray Observatory

CMZ Central Molecular Zone

CND Circumnuclear Disk

COBE Cosmic Background Explorer

CXO Chandra X-ray Observatory

DIRBE Diffuse Infrared Background Experiment

ELT Extremely Large Telescope

EMRI Extreme Mass-Ratio Inspiral event

ESO European Southern Observatory

FOV Field of View

FWHM Full Width Half Maximum

GB Galactic Bulge

GC Galactic Center

GCOI Galactic Center Orbit Initiative

GD Galactic Disk

GMT Giant Magellan Telescope

GR General Relativity

GW Gravitational Waves

HAWK-I High Acuity Wide Field K-band Imager

HST Hubble Space Telescope

IB Intermediate-Band

IRAC Infrared Array Camera

$M_\odot$ Unit of mass equivalent to the mass of the Sun

mas milli-arcsecond

MBH Massive Black Hole

mpc milli-parsec

MS Main-Sequence

MWNSC Milky Way's Nuclear Star Cluster

NACO Nasmyth Adaptive Optics System/Coude Near Infrared Camera

NB Nuclear Bulge

NIR Near-InfraRed

NIRC Near-InfraRed camera

NSC Nuclear Star Cluster

NSD Nuclear Stellar Disk

pc parsec

PSF Point-Spread Function

QSO Quasi-Stellar Objects

RC Red Clump

RIAF Radiatively Inefficient Accretion Flow

S/N Signal to Noise ratio

SED Spectral Energy Distribution

SF StarFinder

Sgr A* Sagittarius A*

SMBH Super Massive Black Hole

SSA Shift-And-Add

submm submillimeter

TMT Thirty Meter Telescope

UT Unit Telescope

VLBI Very Large Baseline Interferometry

VLT Very Large Telescope

VLTI Very Large Telescope Interferometer

VVV VISTA Variables in the Via Lactea

WR Wolf-Rayet

Chapter 1

Introduction

"To date, the only secure detections of SBHs [supermassive black holes] (as opposed to dense clusters of stars or exotic particles) come from stellar proper motion in the Galactic center and the H_20 megamaser study of the nearby Seyfert 2 galaxy NGC 4258 [...]. The applicability of either method is, however, limited (to one galaxy, the Milky Way, in the case of proper motion studies)."
– Laura Ferrarese and Holland Ford, *Space Science Reviews, February, 2005*

1.1 Historical background

Practically all elliptical galaxies and spiral galaxies with a central bulge are thought to harbour supermassive black holes (SMBHs). The first evidence for unusual activity in the centers of the galaxies was reported by Lick Observatory astronomers at the beginning of the 20th century. They discovered the first active galactic nuclei (AGN) by measuring the emission lines in the spectra of NGC 1068 and M81f (*Fath*, 1909), although they could not find any hypothesis to explain it. After the rapid development of radio astronomy in the 1950s, astronomers detected the strongest radio sources in the Universe, the so-called radio galaxies, by measuring the extremely high non-thermal radio emission from energetic particles moving through

magnetic fields in these galaxies (*Bolton et al.*, 1949). However, the nature of the intrinsic physical process was not understood. In the early 1960s, the first quasars (quasi-stellar objects, QSO) were discovered (*Schmidt*, 1963): radio sources with visible counterparts detected very far away that emit more radiation than the entire host galaxy. Then, the theorists started to hypothesize that the energy emitted by the quasars and the AGN arises from the accretion processes of gas and stars onto a SMBH (*Wyller*, 1970; *Peebles*, 1972). Nevertheless, the first compelling evidence in the form of a mass density measurement for the existence of a SMBH came in 1995 with the detection of the nucleus of NGC 4258 with the very long baseline radio interferometer (VLBI). There exist no other astrophysical entities (e.g. a dense nuclear cluster of white dwarf, neutron stars or black holes) that can remain stable over astrophysical time scales and explain the high density of the dark mass [1] reported ($\sim 10^9 M_\odot/pc^3$) in the nucleus. Nowadays, there exist about 70 dynamical measurements of SMBH masses (*Ferrarese and Ford*, 2005; *Gültekin et al.*, 2009; *McConnell and Ma*, 2013). Their main characteristics match with the hypothesis that they are now-dead quasars, that were very bright and energetic AGNs in the past (*Yu and Tremaine*, 2002). Many of the detected SMBHs share their position with another compact object: NSCs. The NSCs are the densest and most massive star clusters in the Universe (see the Chapter 3). The position of these two central massive objects is unique in the Universe: they are located at the bottom of the potential well of the galaxies. Furthermore, their properties are related with the global properties of their host galaxies (*Ferrarese and Merritt*, 2000; *Gebhardt et al.*, 2000; *Häring and Rix*, 2004; *Ferrarese et al.*, 2006; *Neumayer and Walcher*, 2012; *Georgiev and Böker*, 2014; *Georgiev et al.*, 2016; *Neumayer*, 2017), suggesting a common history between them and the galaxies. What is the role of NSCs and SMBHs in the evolution of the galaxies?

[1] *Binney and Tremaine* (1987) defines "dark matter" as *any form of matter whose existence is inferred solely from its gravitational effects.*

1.2 The Galactic Center

The main limitation of studying extragalactic systems is their great distance. The center of the Milky Way is, however, the closest nucleus of a galaxy, located at only $\sim$ 8 kpc from Earth (*Ghez et al.*, 2008; *Gillessen et al.*, 2009; *Gravity Collaboration et al.*, 2018a). The MBH in Andromeda is $\sim$ 100 times further to us than the GC and the closest AGN is $\sim$ 2000 times further away. Harlow Shapley positioned the Galactic center (GC) for the first time in 1918, as a point in the constellation of Sagittarius (see Fig. 1.1) around which globular clusters of the Milky Way are spherically distributed.

The GC is embedded in the Galactic disk (GD) and the Galactic bulge (GB). With a radius of $\sim$ 2 kpc and a barred, box/peanut shape, the GB (the so-called pseudobulge in the case of the Milky Way) is composed of old and evolved stars (e.g. *Bland-Hawthorn and Gerhard*, 2016). The innermost central region of the Milky Way is the Nuclear Bulge (NB), a massive disk-like complex of stars and molecular clouds (*Launhardt et al.*, 2002), composed of the nuclear stellar disk (NSD), a flat disk-like structure with radius of 230 pc and height of $\sim$ 45 pc (*Launhardt et al.*, 2002), a NSC in the center, and a high concentration of gas ($\sim 4 \times 10^7 M_\odot$) in the inner 200 pc, the so-called central molecular zone (CMZ) (*Morris and Serabyn*, 1996).

There are two massive, young massive clusters within the NSD: the Arches and the Quintuplet. They contain a high number of the Wolf-Rayet (WR) stars known in the Galaxy (*van der Hucht*, 2006) and are located at a projected distance of 30 pc from the center (e.g., *Stolte et al.*, 2008; *Clarkson et al.*, 2012). They are less than 5 Myrs (*Figer et al.*, 2002; *Martins et al.*, 2008) and their masses are $\gtrsim 10^4 M_\odot$ (*Clarkson et al.*, 2012; *Figer et al.*, 1999, 2002).

Figure 1.2 shows the central region of the Galaxy ($\sim$ 40 pc$\times$30 pc) composed of the observations of three different telescopes in three different wavelengths. The infrared (red) radiation provided by Spitzer comes from the stars and the brightness of the hot dust clouds around them that

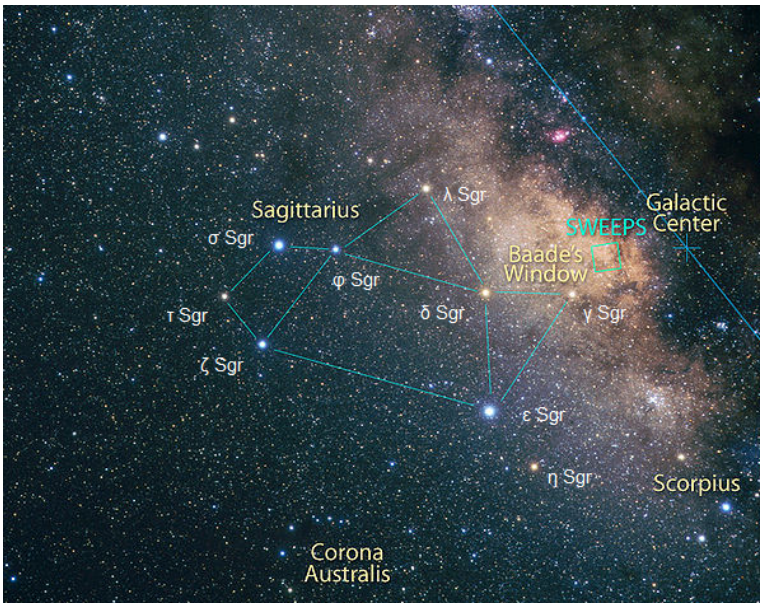

Figure 1.1: Location in the sky of the Galactic Center. Image credit: NASA, ESA, Z. Levay (STScI) and A. Fujii.

are heating up, cradle of the next generation of stars. Hubble provides the near-infrared observations (yelow) that show the bright arched filaments of gas heated by bright massive stars from Arches and Quintuplet (see to the left in Fig 1.2). The observations of the Chandra X-ray Observatory show the X-ray radiation (blue) that comes from the gas heated by outflows from the supermassive black hole, winds from giant stars, and stellar explosions.

The MWNSC (see Chapter 3) has a mass of $\sim 2.5 \times 10^7$ $M_\odot$ (*Schödel et al.*, 2014a,b; *Feldmeier et al.*, 2014; *Chatzopoulos et al.*, 2015a; *Feldmeier-Krause et al.*, 2017) and a half- light radius of $\sim 4.2 - 7$ pc (*Schödel et al.*, 2014a,b; *Fritz et al.*, 2016). At a projected distance of $\sim$ 2 pc from the center, there are three arms of ionised and atomic gas and several streamers of dust called mini-spiral (see Fig 1.3), that emits thermal emission (e.g. *Kunneriath et al.*, 2012). The MWNSC is composed of a mixture of an evolved stellar population and a young stellar population. The old ($<$ 1Gyr) stars are formed mainly by the red clump (RC), that are helium burning stars on

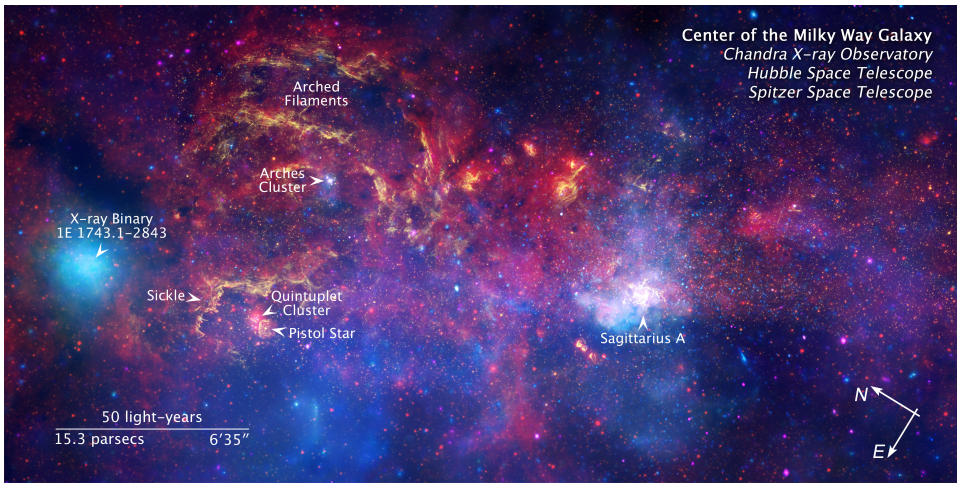

Figure 1.2: Composite image of the Galactic Center that combines observations using infrared light by Spitzer Space Telescope (red), X-ray light by the Chandra X-ray Observatory (blue and violet) and near-infrared by the Hubble Space Telescope (yellow). The scale of the image is 40 pc ×30 pc. Image credit: NASA, ESA, SSC, CXC, and STScI.

the horizontal branch, and the asymptotic giant branch (AGB), very bright and extremely cool stars that are thermally pulsating and losing mass.

The young stars (< 6 Myr) are OB main-sequence (MS) stars, WR stars, red supergiants (e.g. IRS 7), and OB supergiants (*Ghez et al.*, 2003; *Paumard et al.*, 2006; *Bartko et al.*, 2010; *Do et al.*, 2013; *Feldmeier-Krause et al.*, 2015) and they are concentrated within 0.5 pc of the center (*Feldmeier-Krause et al.*, 2015). Some of the young, massive stars lie close to the center (see Fig. 1.3) in the IRS 16, IRS 1, IRS 33, or IRS 13 complexes (e.g. *Genzel et al.*, 2003b; *Lu et al.*, 2005, 2009; *Paumard et al.*, 2006). The central arcsecond of the GC harbors the S-stars, that are young B-type MS stars (*Habibi et al.*, 2017). They are surrounding the SMBH Sagittarius A (Sgr A*). Their formation mechanism is still under debate since they are so close to the black hole that they could not form in situ due to the tidal force of the SMBH, what is known as the "paradox of youth" (*Ghez et al.*, 2003). They might have been deposited there by individual scatter or cap-

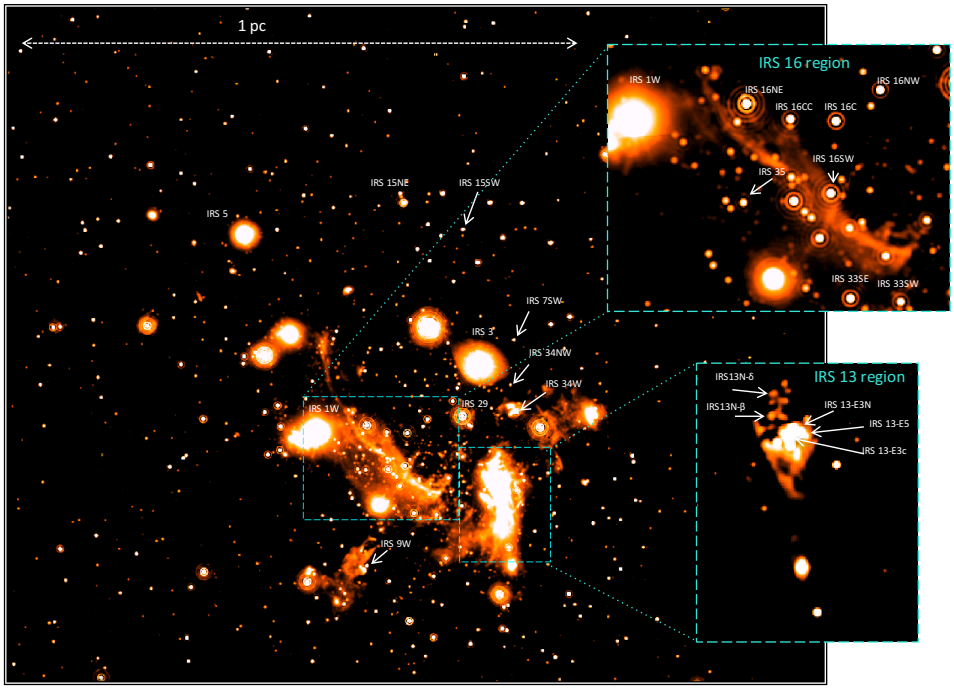

Figure 1.3: L'-band (3.8μm) image of the central $20'' \times 20''$ acquired with NACO instrument at the ESO-VLT telescopes. The stellar clusters IRS 16 and IRS 13 are shown in the close-up views. The image is similar to Fig. 3 in *Yusef-Zadeh et al.* (2015).

ture events (see, e.g., *Eisenhauer et al.*, 2005; *Genzel et al.*, 2010; *Alexander*, 2011).

The existence of the supermassive black hole Sgr A* at the center of the Galaxy was firstly suggested by D. Lynden-Bell and M. J. Rees in 1971 (*Lynden-Bell and Rees*, 1971). Although Karl G. Jansky detected radio emission coming from the GC in the early 1930s (*Jansky*, 1933), many years of instrumentation and theoretical development were necessary until the discovery of Sgr A* by *Balick and Brown* (1974). They determined that the bright non-termal radio source Sgr A* was an unresolved point source. However, the unambiguous evidence of the existence of the black hole came from the monitoring of stars in the S-cluster over more than a decade in the 1990s (see Fig. 1.4). These stars are moving with high velocity (a few

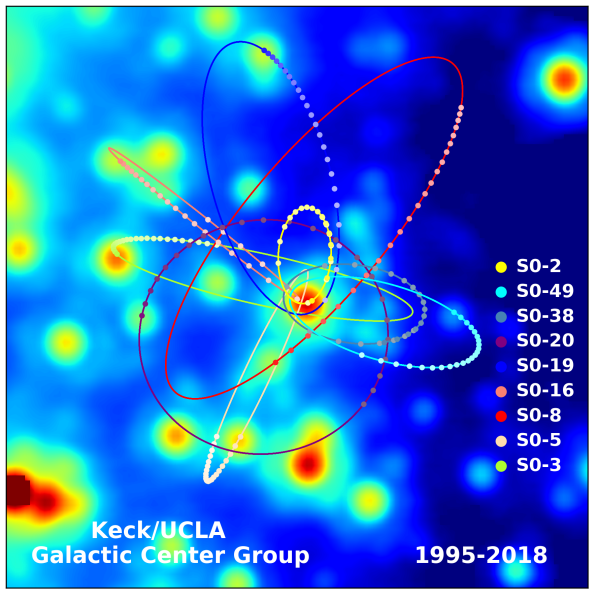

Figure 1.4: Stellar orbits of S-stars in the Central arcsec during the last ~ 20 yrs. The color points show the annual average position of the stars. The best fitting orbital solutions are shown. Image credit: Keck/UCLA Galactic Center Group.

thousand km/s) around Sgr A*, (*Genzel et al.*, 2000; *Eckart et al.*, 2002; *Ghez et al.*, 2003; *Eisenhauer et al.*, 2005). The mass of the SMBH is 4×10^6 $M_\odot$ (*Boehle et al.*, 2016; *Gillessen et al.*, 2017; *Gravity Collaboration et al.*, 2018a) which could be accurately measured by fitting Keplerian orbits to the S-stars orbits, which was firstly done for the S2/S0-2 [1] star (*Schödel et al.*, 2002, 2003; *Ghez et al.*, 2003, 2005; *Eisenhauer et al.*, 2005). S2/S0-2 (K$\sim$ 14 mag, mass$\sim$ 15$M_\odot$) is a short-period star very close to Sgr A* ($< 0.5''$) that spends 16 yrs in completing an orbit around the black hole.

The last observable closest approach of S2/S0-2 to the SMBH was in 2018. *Gravity Collaboration et al.* (2018a) and the Galactic Center Group at the University of California measured the relativistic redshift in S2/S0-2's radial velocity which was the first direct test of General Relativity (GR) in

[1] The star is named differently by the two groups: MPE (S2) and UCLA (S0-2).

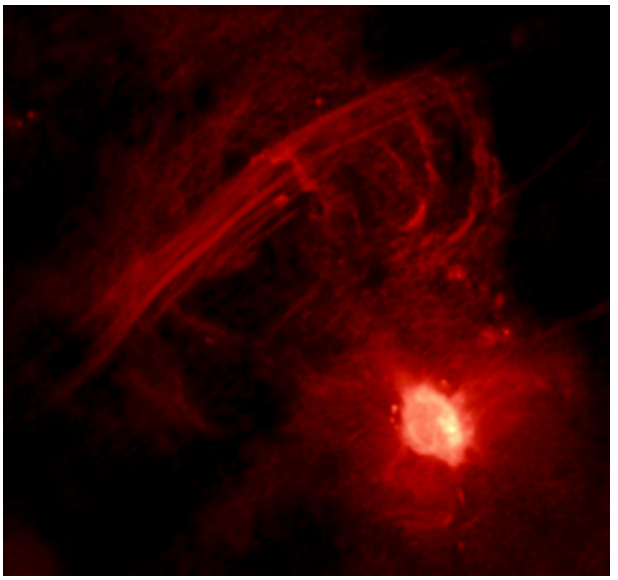

Figure 1.5: Radio image of Sgr A*. Credit: Farhad Zadeh, VLA, NRAO, APOD.

a strong gravitational field around an SMBH.

The GC is the only nucleus of a galaxy where we can actually resolve the stars observationally on scales of about 2 milli-parsecs inside the radius of influence of the black hole ($\sim$ 3 pc, *Alexander*, 2005). Therefore, it is a unique laboratory for making progress in many astrophysical phenomena, for instance by studying star formation under extreme conditions, the properties and evolution of dense stellar systems, and analysing accretion processes around the SMBH and the impact on its stellar and interstellar environment. Moreover, the GC is crucial for studying galactic nuclei and SMBHs in other galaxies and the relation between them and their host galaxies.

1.3 Observational constraints

Despite of the proximity of the GC, we have to overcome important observational obstacles. The Solar System is located in the plane of the Galaxy,

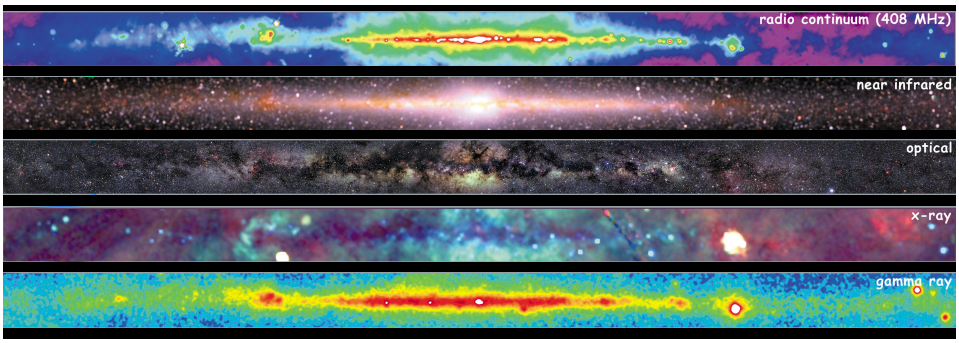

Figure 1.6: Views of the Milky Way along the Galactic plane over different wavelengths (indicated in the panels). The near-infrared image was taken by the Diffuse Infrared Background Experiment (DIRBE) instrument on the Cosmic Background Explorer (COBE). Image credit: NASA, http://adc.gsfc.nasa.gov/mw.

therefore the light that comes from the GC along the line of sight has to go through the dust clouds in the GD, suffering extreme interstellar extinction and reddening [1]. At optical wavelengths, this effect is extreme: more than 30 magnitudes of visual extinction (see middle panel in Fig. 1.6) that causes that only 1 photon between 10^{12} from the GC reaches the Earth. Therefore, the GC cannot be observed with optical telescopes. X-ray, infrared, and radio instruments are required to peer through the dust (see Fig. 1.6). In order to study the stars around the black hole (BH), the observations have to be carried out in the infrared. The extinction toward the GC in NIR ($A_k \gtrsim 2.5$, e.g. *Schödel et al.*, 2010), can be described by a power-law (*Fritz et al.*, 2011; *Nishiyama et al.*, 2008) of the form $A_\lambda \propto \lambda^{-\alpha}$, where A_λ is the extinction in magnitudes in a given wavelength and the power-law index α is ~ 2.30 according to *Nogueras-Lara et al.* (2018a). Figure 1.6 shows the effect of the extinction in the optical, where the GC is practically opaque (upper panels), while it shows very bright in infrared wavelengths (bottom panels).

An additional difficulty to observe the GC is the strong source crowding

[1] Attenuation of the light caused by the absorption and scattering by gas and dust.

near the SMBH that requires us to use the highest angular resolution possible in order to resolve individual stars. Along with the complexity of the star formation history of the NSC, studying the GC is very challenging.

Therefore, to study the GC, we need to use large ground-based telescopes or space telescopes, along with high angular resolution techniques. Two methods have been key to obtain diffraction-limited images in the GC: speckle imaging and AO. The speckle imaging technique consists in recording long series of short exposure images to freeze the turbulence caused by the Earth's atmosphere. A digital image reconstruction a posteriori is needed, like shift-and-add technique or speckle holography (see more details in Chapter 2). The AO technique corrects in real time the distorting effect of the atmospheric turbulence in the images through a deformable mirror. Both techniques have improved the angular resolution by more than one order of magnitude compared to previous work and increased the completeness limit by three to five magnitudes to $K_s \sim 16$ for spectroscopy and $K_s \sim 18$ for imaging observations (see review of *Genzel et al.*, 2010).

Because of these observational difficulties, our knowledge about the stellar population at the GC is highly incomplete. The spectroscopic identification of stars is limited to the brightest few percent of stars: a few million-year-old hot post MS giants and MS O/B stars (the latter being already at the faint limit of spectroscopic capabilities), on the one hand, and, on the other hand, giants with luminosities equal to or higher than RC stars. In fact, the typical spectroscopic completeness reaches only about $K_s = 15.5$ stars and thus only half of the RC (*Do et al.*, 2009; *Bartko et al.*, 2010; *Do et al.*, 2015; *Støstad et al.*, 2015; *Feldmeier-Krause et al.*, 2015).

1.4 Outline of the dissertation

This thesis aims at a significant progress in our understanding of the Milky Way's NSC. This will be achieved by analysing high-angular resolution data over a larger field, with more filters, and greater depth than in any previous

studies. High–precision point-spread function (PSF) fitting photometry and astrometry are used to extract stars and determine their fluxes, as well as artificial star experiments to determine the completeness due to crowding and the photometric uncertainty. An important part of the analysis is the improvement of the speckle holographic technique and the application of bootstrapping analysis to be able to push the completeness to the limits.

There are several hypotheses that will be examined within this thesis:

- Structure of the MWNSC and the surrounding components: Does the composition of stellar population change with distance from the centre of the MWNSC? Is the MWNSC aligned with respect to the GP like previous photometric work assumed? Does the MWNSC have similar properties to other extragalactic NSCs?

- Stellar cusp: Theoretical stellar dynamics predicts the existence of a stellar cusp around the central black hole. However, current observations indicate the absence of such a cusp. This contradiction may pose a severe problem to our understanding of stellar dynamics. This thesis aims at pushing the analysis of the structure of the NSC to fainter stars than what was examined before. Can we confirm the absence of a stellar cusp?

- Finally, this research work helps to build the longest time baseline of the variability of Sgr A* (*Chen et al.*, in preparation) by improving the reduction and analysis of existing data. We are able to detect NIR emission of Sgr A* in epochs prior to 2003, when the first measurements were taken due to the development of AO. That allows *Chen et al.* (in preparation) to study its long-term NIR activity and explore the accretion flow onto the black hole in epochs previous to the first NIR Sgr A* detections in 2003. Does the long-term variability of Sgr A* follow the short-term variability characteristics? Was the luminosity of Sgr A* affected by the increase in the accretion flow onto the black hole in the periapse passage of the dusty source G1?

Therefore, my objectives are examining the above-mentioned questions and provide new constraints on our hypotheses about the properties and formation of the Milky Way's NSC. In summary, my work covers the study of the GC from large distances ($\sim 6^\circ \times 2^\circ$) from Sgr A* to the innermost arcseconds around it: from the determination of the main structural components that forms the core of our Galaxy, going through the study of the stellar processes that take place in the central parsecs, until peeking into the accretion events that occur near the black hole and studying its emission.

The thesis is organized as follows: In Chapter 2, I present our observations and give detail about the data reduction. Some of the data reduction procedures have been published in *Gallego-Cano et al.* (2018) and *Schödel et al.* (2018). The Chapter 3 is devoted to deriving the global structure of the NSC and its surrounding components (NSD and GB). We show these results in *Gallego-Cano et al.* (Accepted). I zoom into the central parsecs in Chapter 4 to revisit the problem of inferring the distribution of stars around Sgr A* to clarify whether it displays a core or a cusp around the central black hole. We have also published these results in *Gallego-Cano et al.* (2018) and *Schödel et al.* (2018). I zoom again into the innermost arcseconds of the GC around the supermassive black hole in Chapter 5 and show the results of *Chen et al.* (in preparation) that study its long-term NIR variability and explore the accretion flow of Sgr A* and look for accretion events in the past.

To conclude, I would like to say that our quest to understand black holes is linked to the progress in technology. Since 1784, when John Michell suggested for the first time the existence of "dark stars" where *"all light emitted from such a body would be made to return towards it by its own proper gravity"*, until the detection of gravitational waves with LIGO in 2016 from the merger of two stellar-mass black holes (*Abbott et al.*, 2016), enormous theoretical and technological development was necessary. The great advance comes from the design of new experiments that verify the theory, on the one hand, and the establishment of new theoretical predictions that explain the

observations, on the other hand. Since Albert Einstein developed the theory of relativity in the last century, we are facing a new paradigm that involves a change in what we know about space and time. And all the information on astrophysics and physics is right here, at the center of our Galaxy.

Chapter 2

Observations and data reduction

"The problem of surveying our own galaxy may be likened to the problem of drawing a map of New York City on the basis of observations made from the intersection of 125th Street and Park Avenue. Although it would be clear to an observer at this spot that the city is a big one, any statement as to its extent and layout would clearly be impossible. London would offer an even better analogy, for the neighborhood is not only congested but foggy."

– C. H. Payne-Gaposchkin, *Nature, October 22, 1903*

2.1 ESO Very Large Telescope

The Very Large Telescope (VLT) is operated by European Southern Observatory (ESO) (see Fig. 2.1) and is located at Cerro Paranal, in the Atacama desert (Chile), one of the driest places in the world. The ESO VLT is formed by four 8.2-meter Unit Telescopes (UTs), that can work separately or together in an interferometric mode (VLTI). Due to the absorption of the IR emission by water vapor, a dry and high altitude region as Paranal is suitable to perform infrared observations. In addition, together with the

Figure 2.1: Center of the Milky Way over a sunset at the ESO VLT on Cerro Paranal. Image credit: ESO/B. Tafreshi [www.twanight.org].

fact that the GC passes through the zenith, they make the Atacama desert in Chile a unique place in the world to observe the center of our Galaxy. Two of the sets of data presented in this work were acquired with two instruments at the ESO VLT. According to the needs of the particular project that we wanted to address, we used one set or another. In order to infer the innermost structure of the central parsec around Sgr A* and revisit the problem of the cusp, we used judiciously selected adaptive optics assisted high angular resolution images obtained with the NACO instrument, which offers the highest angular resolution of the VLT instrument suite. To study the overall, large-scale structure of the MWNSC, we needed to focus on

larger distances. For this purpose, we used data obtained with the HAWK-I instrument, which offers high angular resolution in a very large FOV.

2.1.1 NAOS/CONICA

We used data obtained with the NAOS-CONICA instrument (hereafter NACO, *Lenzen et al.* (2003); *Rousset et al.* (2003)) at the UT 4, YEPUN. NAOS is the adaptive optic (AO) system designed to partially compensate the effects of atmospheric turbulence (seeings). CONICA is the infrared camera and spectrometer attached to NAOS. The AO was locked on the NIR bright supergiant CGIRS7 that is located about 5.5″ north of Sgr A*. As a result, NACO can achieve high Strehl ratios in K_s-band ($> 40\%$). The data that we used are summarised in Table 2.1. We used H and K_s-band data obtained with the S27 camera with a pixel scale of 0.027″. The data reduction was published in the journal *Astronomy & Astrophysics* in *Gallego-Cano et al.* (2018) and *Schödel et al.* (2018). The data were acquired with a similar 4 point dither pattern, roughly centered on Sgr A*, with the exception of the data from 11 May 2011, which covered a shallow, but wider mosaic with a 4×4 dither pattern, centered on Sgr A*. Preliminary data reduction was standard, with sky subtraction, bad pixel removal, and flat fielding. Subsequently, a simple shift-and-add (SSA) procedure was applied to obtain final images. The S27 pixel scale barely samples the angular resolution, which is roughly 0.06″ full width half maximum (FWHM) for all images. Therefore, in order to improve the photometry and reduce the residuals of PSF fitting, we used a quadratic interpolation with a rebinning factor of two. Along with the mean SSA images we also created noise maps that contain the error of the mean of each pixel in the SSA images.

In our analysis of the diffuse light in the central parsec, we also included intermediate-band (IB) imaging data at 2.27 μm as well as K_s-band NACO/VLT data taken by S13 camera that are presented in Table 2.1. The S13 images were stacked to provide a deep image, as done with the S27 images. In addition, we used the the HST/NICMOS 3 point-source subtracted

Table 2.1: Details of the NACO imaging observations used in this work.

Date[a]	Pixel Scale [″/pix]	$\lambda_{central}$ [μm]	$\Delta\lambda$ [μm]	N[b]	NDIT[c]	DIT[d] [s]
09 July 2004	0.027	2.27	0.06	8	4	36
05 August 2009	0.027	4.051	0.02	45	3	15
09 May 2010	0.027	1.66	0.33	4	64	2
04 May 2011	0.013	2.18	0.35	4	67	4
17 May 2011	0.027	2.18	0.35	4	9	2
12 June 2011	0.013	2.18	0.35	4	67	4
13 August 2011	0.013	2.18	0.35	2	67	4
04 May 2012	0.013	2.18	0.35	2	18	4
09 August 2012	0.027	2.18	0.35	8	60	1
09 August 2012	0.013	2.18	0.35	2	67	4
11 September 2012	0.027	2.18	0.35	8	60	1
12 September 2012	0.027	2.18	0.35	8	60	1
12 September 2012	0.013	2.18	0.35	2	67	4
29 March 2013	0.013	2.18	0.35	2	67	4
14 May 2013	0.013	2.18	0.35	2	18	4

Notes.

[a] UTC date of beginning of night.[b] Number of (dithered) exposures.[c] Number of integrations that were averaged on-line by the read-out electronics.[d] Detector integration time. The total integration time of each observation amounts to N×NDIT×DIT.

image of the emission from gas at 1.87μm, that was presented by *Dong et al.* (2011). We also make use of NACO/VLT S27 Brackett-γ (Brγ) narrow band (NB) observations included in Table 2.1. Data reduction was standard, as we described above for S27 camera data, including rebinning to a finer pixel scale by a factor of 2.

After that, we proceeded to remove the horizontal stripe patterns from the detector electronics contained in the images from individual epochs with DIT = 1. These horizontal stripes can be detrimental for source detection because they may either mask faint sources or be deblended into rows of

stars by the PSF fitting program. It is therefore important to remove them. We proceeded as follows: We used the *StarFinder* program to detect and subtract robustly detected point sources from each image (conservative settings of the *StarFinder* parameters: *min_correlation*= 0.85 and *deblend*= 0) and to fit the diffuse emission (from unresolved stars or dust and gas in the interstellar medium). The latter was fitted with an angular resolution of about 0.25″, a non-critical value that needs to be large enough to remove the variable background due to unresolved stellar emission and small enough to roughly correspond to the size of diffuse, unresolved structures in the mini-spiral (see Paper II). While fitting of the diffuse background is important in this procedure, the exact choice of its variability scale is not. It can easily be chosen to be a factor 2 larger or smaller.

The resulting residual images, i.e. the image where the diffuse emission and point sources have been removed, were then dominated by small-scale (on the order a few pixels width) random and systematic noise. We determined the pattern of horizontal stripes induced by the electronics through median smoothing each row of pixels with a median box width of about 2.7″, corresponding to 200 pixels (in the rebinned images). This pattern was then subtracted from the SSA images. We could thus remove most of the systematic noise without introducing any significant bias on the point sources or on the diffuse emission because most stars had already been subtracted and because the median smoothing box was a factor of a few to ten larger than the scales of the diffuse emission, of the size of PSF residuals, or of faint, unresolved sources. Finally, after having cleaned the images of each epoch, they were combined to a deep mean image (see next section). This last step further reduced any remaining systematics. To be conservative, we used the noise maps derived from the uncleaned images. Fig. 2.2 shows the details of K_s-images to illustrate the effect of the systematic readout noise and the improvement after removing it.

We treated each of the four pointings toward Sgr A* independently to avoid problems arising from camera distortions near the edges of the NACO

S27 camera's field (see *Trippe et al.*, 2008; *Schödel et al.*, 2009). The final images from all epochs were aligned with the one from 09 Aug 2012 via a polynomial fit of degree one (IDL POLYWARP and POLY_2D procedures). The parameters of the latter were determined via an iterative fit using lists of detected stars in the image. The images were combined in a simple mean and the corresponding noise maps were quadratically combined.

A possible concern in this stacking procedure is the use of different observing epochs because of the large proper motions of the stars in the GC. At the distance of the GC (here assumed as 8 kpc, see, e.g., *Genzel et al.*, 2010; *Meyer et al.*, 2012), a velocity of about 40 km s^{-1} on the plane of the sky corresponds to a proper motion of one milli-arcsecond per year. A displacement by one pixel of the NACO S27 camera per year therefore corresponds to a velocity > 1000 km s^{-1}. Since we are not interested in high precision astrometry or photometry, this effect is therefore negligible for our data, except possibly a small number of very fast moving stars within $\sim 0.1''$ of Sgr A*, which is not relevant to the problem and scales addressed in this work.

2.1.2 HAWK-I

We use K_s-band data obtained with the near-infrared camera High Acuity Wide field K-band Imager (HAWK-I) at the ESO Very Large Telescope (VLT) from the GALACTICNUCLEUS survey, a JHKs imaging survey of the center of the Milky Way (see *Nogueras-Lara et al.*, 2018a). The survey provides us accurate, high-angular resolution, multi-wavelength near-infrared photometry for an area of several 100 pc^2, a more than ten-fold increase compared to similar surveys (e.g. the VISTA Variables in the Via Lactea survey, VVV). The high angular resolution is $0.2''$, thanks to the application of the speckle holographic technique (*Schödel et al.*, 2013) that let us to reconstruct images of large, crowded fields from the ground by using a large series of short exposures, so-called speckle images (see a brief summary in Section 2.3). The pixel scale of HAWK-I is $0.106''$/pixel but

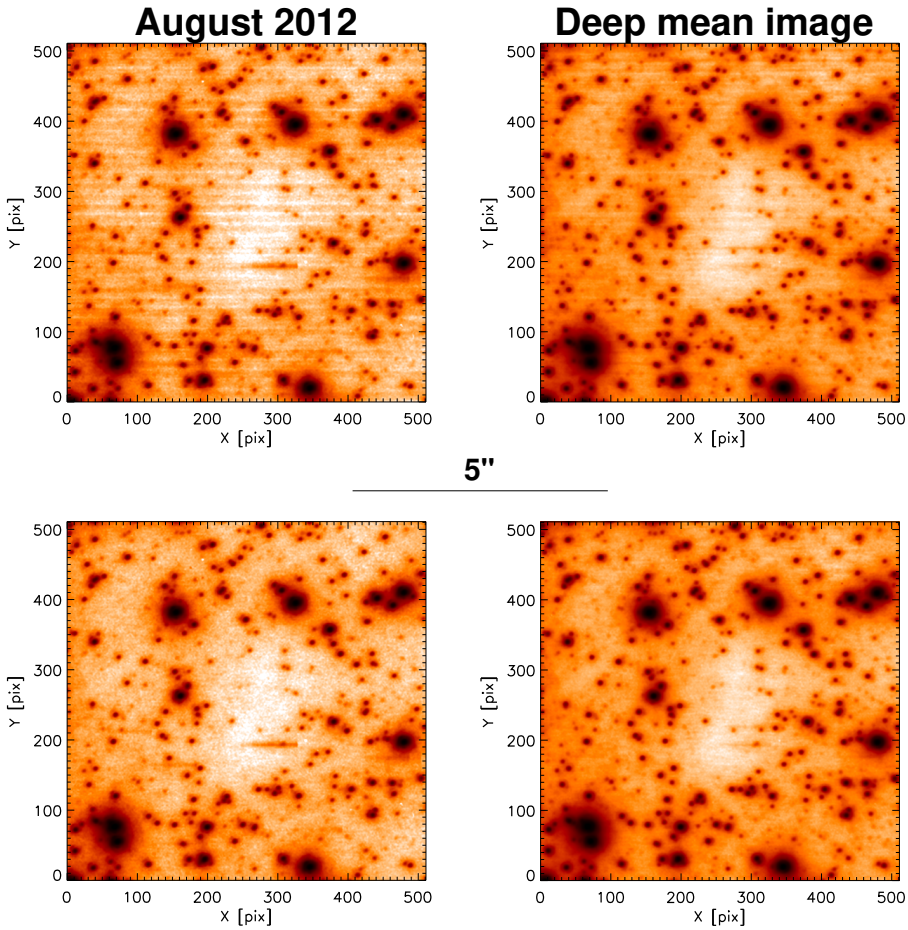

Figure 2.2: Cleaning of horizontal stripes (systematic readout noise). Upper left: Detail of August 2012 K_s-band NACO image. Lower left: As upper left, but cleaned. Upper right: Detail of deep, mean combined K_s-band image when the input images have not been cleaned. Lower right: Detail of deep, mean combined K_s-band image after cleaning of the input images. The displayed field is located about 12.0″ west and 1.7″ north of Sgr A*. The colour scale is logarithmic and identical for all images.

we obtained a final pixel scale of 0.053″/pixel by rebbining the images by a factor of 2 in order to obtain higher resolution and therefore accuracy. We use the central 14 fields of the survey described in detail in *Nogueras-Lara*

et al. (in preparation), that composed a region of about 84.4 pc x 21 pc around Sgr A*.

2.2 Spitzer Space Telescope

Figure 2.3: Artist view of the NASA's Spitzer Space Telescope and the infrared sky. The telescope scrutinizes the Rho Ophiuchi star-formation region above the incandescent emission of the Milky Way galaxy seen at 100 microns. Image credit: NASA/JPL-Caltech.

In order to avoid the distorting effect of the atmosphere in the astronomical images, Lyman Spitzer in 1946 analyzed for the first time the theoretical possibility of locating a telescope in outer space. The Spitzer Space Telescope, which was launched in 2004, was the last telescope to join the final mission in NASA's Great Observatory Program that, along with Hubble Space Telescope (HST), Compton Gamma-Ray Observatory (CGRO), and the Chandra X-ray Observatory (CXO) were planning to cover many different wavelengths (visible, gamma rays, X-rays, and infrared). We used Spitzer data obtained with the Infrared Array Camera (IRAC), that has four channels to obtain simultaneous broad-band images at 3.6, 4.5, 5.8, and 8.0 μm, respectively (see details in *Fazio et al.*, 2004). In particular, we used the 4.5μm image of the central 300 $\times$ 250 pc^2 of the Galaxy that was

corrected for extinction and Paschen α emission. The details of the data and its reduction are described in *Schödel et al.* (2014a).

2.3 W. M. Keck Telescope

Figure 2.4: Keck telescopes with stars on the summit of Mauna Kea. Image credit: W. M. Keck Observatory.

Near the summit of the volcano Mauna Kea in Hawaii Island, the twin Keck Observatory 10-meters telescopes are located at a height$>$ 4000 meters above sea level. The 36 hexagonal segments that compose their primary mirrors work together with optical and near-infrared instruments like a single unit. Their location, above the thermally calm sea, without surrounding mountains, has dry and clear skies, with one of the best observing conditions in the world.

We used K-band (2.2μm) speckle data from 1995 to 2005 obtained with the near-infrared camera (NIRC), that form part of the *Galactic Center Orbit Iniciative* (GCOI) (more details in *Chen et al.*, in preparation, and reference therein). During each epoch of observation, around 10, 000 frames were obtained using very short exposure times (0.1 s) to freeze the distorting effects of the Earth's atmosphere. We obtained diffraction-limited images but we need to apply a digital image reconstruction a posteriori. First, the

data were reduced by using the shift-and-add technique (SAA, *Ghez et al.*, 1998, 2000, 2005; *Lu et al.*, 2005; *Rafelski et al.*, 2007). They have been key to determine the orbits of stars around Sgr A*. The SSA algorithm shifts each frame to the brightest pixel of a reference star and averages the stack. The method is very fast and robust, although the Strehl ratios and sensitivity in the obtained images are low. The problem is that SSA does not use all the information and photons contained in the individual exposures: only the brightest speckle of each star contributes to the core of the point-spread function (PSF) in the final image (see Fig. 2.5 (a)). Later, a more sophisticated technique called speckle holography (see, e.g. *Primot et al.*, 1990; *Petr et al.*, 1998) was applied to the data, as implemented and optimized for crowded fields by *Schödel et al.* (2013). The algorithm allows us to obtain the object by the convolution in the Fourier space of the distorted images with the instantaneous PSF measured from a set of reference sources. In this approach, the information from all the speckles contributes to the final diffraction-limited core. The final images have reduced seeing halous around the point sources (see Fig. 2.5 (b)). and higher Strehl ratios than SSA images ($\sim$ 0.4 versus 0.06). The implementation of the holographic technique (version 2_1) to the speckle data is explained in detail in different papers (*Boehle et al.*, 2016; *Meyer et al.*, 2012; *Schödel et al.*, 2013) and its application allowed the study of short-period stars around the position of the supermassive black hole (S0-2, S0-102, S0-28).

We applied a new improved version of the holographic reconstruction technique (version 2_2) to obtain a higher-quality, deeper final image (see the details in *Chen et al.*, in preparation). We aimed at improving the previous version by optimising image quality, minimising edges effects and reducing systematic errors. The new technique is based on iteratively improved extraction of the instantaneous PSF from speckle frames, the simultaneous use of multiple reference stars, the improvement of the alignment of the speckle frames before the holographic procedure, the use of a quadratic interpolation with a rebinning factor of two, the estimation and subtraction

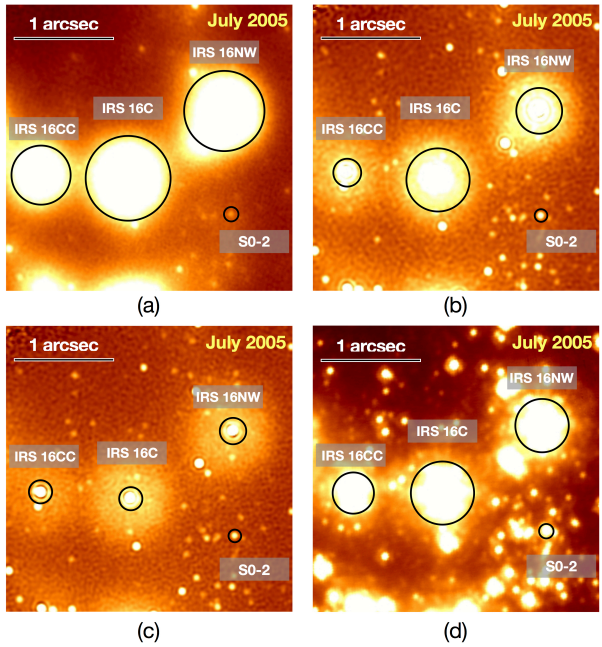

Figure 2.5: Comparison between the final images obtained by using different techniques: a) shift-and-add, b) speckle holography version 2_1, c) speckle holography version 2_2, d) adaptive optics (Figure 1 in *Chen et al.* in preparation).

of a variable sky from each frame and the improvement of the secondary star subtraction of a variable sky from each frame (see Fig. 2.5 (c)). We obtained higher-quality and deeper final images. The details of the 27 speckle observation epochs that we reduced are shown in Tab. 2.6. The field of view of the final images is $5'' \times 5''$ centered on the black hole (see right panel in Fig. E.1).

Date		Frames		FWHM	Strehl ratio [b]	N_{stars}	K_{lim} [c]	σ_{pos} [d]	Data Source [e]
(U.T.)	(Decimal) [a]	Obtained	Used	(mas)	post-process		(mag)	(mas)	
1995 Jun 9-12	1995.439	15114	5286	46	0.62	380	16.4	1.47	Ref. 1
1996 Jun 26-27	1996.485	9261	2336	47	0.57	246	15.7	3.11	Ref. 1
1997 May 14	1997.367	3811	3486	46	0.65	358	16.4	1.29	Ref. 1
1998 May 14-15	1998.366	16531	7685	47	0.49	251	15.9	0.92	Ref. 2
1998 Jul 3-5	1998.505	9751	2053	42	0.85	226	16.2	0.86	Ref. 2
1998 Aug 4-6	1998.590	20375	11047	46	0.65	293	16.4	0.75	Ref. 2
1998 Oct 9	1998.771	4776	2015	47	0.52	216	16.0	1.32	Ref. 2
1999 May 2-4	1999.333	19512	9427	45	0.78	344	16.7	0.69	Ref. 2
1999 Jul 24-2	1999.559	19307	5776	44	0.77	303	16.8	0.37	Ref. 2
2000 Apr 21	2000.305	805	662	48	0.46	141	15.4	2.48	Ref. 3
2000 May 19-20	2000.381	21492	15591	45	0.62	402	16.9	0.56	Ref. 3
2000 Jul 19-20	2000.548	15124	10678	46	0.61	410	16.7	1.10	Ref. 3
2000 Oct 18	2000.797	2587	2247	47	0.46	209	15.8	1.70	Ref. 3
2001 May 7-9	2001.351	11343	6678	45	0.58	344	16.3	0.95	Ref. 3
2001 Jul 28-29	2001.572	15920	6654	46	0.73	351	16.9	0.57	Ref. 3
2002 Apr 23-24	2002.309	16130	13469	46	0.65	452	16.9	0.90	Ref. 3
2002 May 23-24	2002.391	18338	11860	44	0.74	436	17.1	0.58	Ref. 3
2002 Jul 19-20	2002.547	8878	4192	48	0.52	300	16.5	1.23	Ref. 3
2003 Apr 21-22	2003.303	14475	3715	48	0.53	185	15.5	1.25	Ref. 3
2003 Jul 22-23	2003.554	6948	2914	46	0.65	276	16.2	1.16	Ref. 3
2003 Sep 7-8	2003.682	9799	6324	46	0.67	356	16.6	1.80	Ref. 3
2004 Apr 29-30	2004.327	20140	6212	47	0.66	275	16.1	0.51	Ref. 4
2004 Jul 25-26	2004.564	14440	13085	47	0.61	379	16.9	0.90	Ref. 4
2004 Aug 29	2004.660	3040	2299	49	0.79	289	16.3	0.83	Ref. 4
2005 Apr 24-25	2005.312	15770	9644	47	0.54	282	16.3	0.70	Ref. 5
2005 Jul 26-27	2005.566	14820	5642	50	0.64	332	16.6	1.79	Ref. 5

Figure 2.6: Table 1 in *Jia et al.* (2019) that shows the details of the Speckle Imaging Observations (see more details in their paper).

Notes.

[a] Julian Epoch year. [b] Strehl ratio from deconvolution method. [c] Magnitude where the cumulative distribution function of the observed K magnitude of all detected stars reaches 90% . [d] Positional error. [e] Papers where the data were reporter for the first time: 1) *Ghez et al.* (1998), 2) *Ghez et al.* (2000), 3) *Ghez et al.* (2004), 4) *Lu et al.* (2005), and 5) *Rafelski et al.* (2007).

Chapter 3

The nuclear stellar cluster of the Milky Way

"The centers of galaxies host two distinct, compact components: massive black holes and nuclear star clusters. Unlike black holes, nuclear star clusters provide a visible record of the accretion of stars and gas into the center of a galaxy. Studying their stellar populations, structure and kinematics allows us to disentangle their formation history and more generally that of galactic nuclei."

– Nadine Neumayer, *Nuclear Star Clusters, International Astronomical Union, 2007*

3.1 Introduction

Nuclear stellar cluster (NSCs) are the densest and most massive star clusters in the universe, with half-light radii $\sim 2-5$ pc and masses $\sim 10^6 - 10^7 M_\odot$ (*Böker et al.*, 2002, 2004; *Walcher et al.*, 2005; *Côté et al.*, 2006; *Georgiev and Böker*, 2014). They follow similar scaling relations with their host galaxies as super massive black holes (SMBHs), suggesting a common formation mechanism of NSCs and SMBHs, closely linked to galaxy evolution. The formation mechanisms of NSCs are still being discussed. There are two

formation scenarios: infall and subsequent merging of star clusters and in situ formation of stars at the center of a galaxy. To bring some clarity in this we need to study the structure, the stellar evolution and the kinematics of NSCs. The main limitation for detailed studies of NSCs is their compactness, which make it challenging to characterise their resolved structure for galaxies at large distances.

Close to us, the centre of the Milky Way harbors a $\sim 2.5 \times 10^7\,M_\odot$ nuclear star cluster (*Schödel et al.*, 2014a,b; *Feldmeier et al.*, 2014; *Chatzopoulos et al.*, 2015a; *Feldmeier-Krause et al.*, 2017) with a half-light radius or effective radius $\sim 4.2 - 7$ pc (*Schödel et al.*, 2014a,b; *Fritz et al.*, 2016). The MWNSC was discovered by *Becklin and Neugebauer* (1968) as a dense stellar structure with a diameter of a few arcminutes and a mass of a few $10^7\,M_\odot$. It lies embedded within the nuclear stellar disk (NSD), a flat disk-like structure with radius of 230 pc and scale height of ~ 45 pc (*Launhardt et al.*, 2002). The MWNSC is the only galactic nucleus where we can resolve the stars observationally on scales of about 2 milli-parsecs (mpc), assuming diffraction limited observations at about $2\,\mu$m at an 8-10m telescope. It is therefore a unique test system to study NSCs, and explore the transition regimen between SMBHs dominated or NSCs dominated galaxy cores (*Graham and Spitler*, 2009; *Neumayer and Walcher*, 2012).

Therefore, the MWNSC is a crucial laboratory for studying galactic nuclei in other galaxies, but its properties have not been determined unambiguously up to now. Due to the extreme extinction ($A_v \geq 30$, $A_k \sim 3$) toward the GC, the strong source crowding, and complex formation history (see *Pfuhl et al.*, 2011, and references therein), we have to overcome huge observational difficulties to study it. Moreover, the MWNSC is surrounded by miscellaneous components, the Galactic bulge (GB), the NSD and the Galactic disk (GD), so it is a challenge to isolated it.

The purpose of this work is to study systematically the size and spatial structure of the NSC of our Galaxy, building up on the works of *Schödel et al.* (2014a) and *Fritz et al.* (2014, 2016) but using new, different data, in

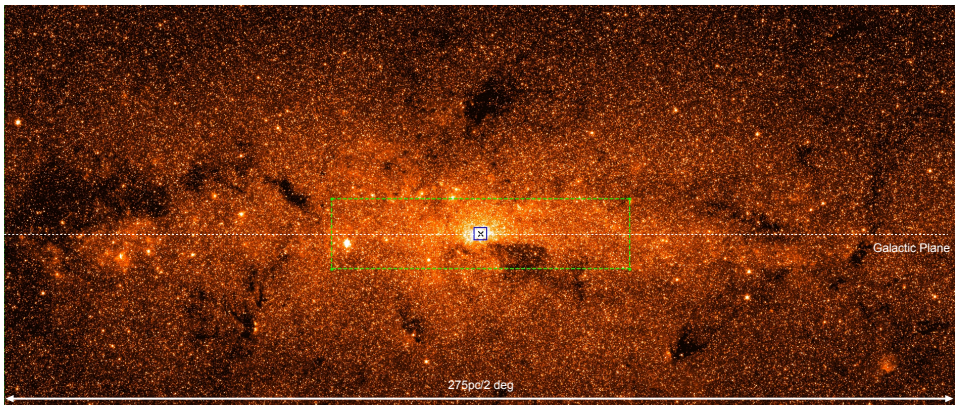

Figure 3.1: Extinction-corrected 4.5μm Spitzer/IRAC image of the GC from *Schödel et al.* (2014a). Galactic north is up and Galactic east is to the left. The blue square outlines the NACO FOV of $\sim 1.5' \times 1.5'$ ($\sim$3.6pc$\times$3.6pc) and the green rectangle the HAWK-I FOV of $\sim 35.8' \times 8.4'$ ($\sim$86pc$\times$20.2pc). Sgr A* is located at the position of the black cross.

particular high angular resolution near-infrared imaging on scales of several tens of parsecs. *Schödel et al.* (2014a) used data from Spitzer/IRAC data at 3.6μm and 4.5μm that are affected by strong diffuse emission from the mini-spiral and the presence of a few extremely bright sources (e.g. IRS1W or IRS7). The other comparable work is by *Fritz et al.* (2016). They used three different data sets: NACO/VLT data in the central 20$''$ (0.8 pc) with an angular resolution of $\sim 0.08''$; Hubble Space Telescope (HST) WFC3/IR data in the central 68$''$ (2.72 pc), with angular resolution of 0.15$''$; and VISTA Variables in the Via Lactea data in the central 2000$''$(80 pc), with an angular resolution of 1.0$''$.

This study uses data and methods that address potential shortcomings in previous work on the topic. We use 0.2$''$ angular resolution K_s data to create a stellar density map in the central 86.4pc x 21pc at the Galactic Centre. We include data from selected adaptive optics assisted images obtained for the inner parsecs. In addition, we use IRAC/ Spitzer MIR images. One novel aspect of this work is that we use a GB model to minimize the bias of the GB on the measured properties of the NSD and NSC. We also repeat

the work of *Schödel et al.* (2014a) to obtain independent constraints on the structure of the MWNSC and even improve it by using a larger FOV and including the GB model. Finally, we fit a Sérsic model to the MWNSC and investigate its symmetry.

We study the structure of the MWNSC in different stellar brightness ranges to test whether the composition of the stellar population changes with distance from the centre of the MWNSC and whether stars of different brightness outline the same structure. We explore in detail the systematic uncertainties that can affect the parameters, taking into account different potential sources of systematic errors. Another important aspect of our work is that we study the symmetry of the NSC assuming that it is aligned with respect the Galactic plane (GP), as previous work did, but we go one step further exploring it by leaving the tilt angle between the NSC and the GP free in the fits. We have submitted the results in the journal *Astronomy & Astrophysics* in *Gallego-Cano et al.* (Accepted).

3.2 Stellar number density maps

In order to study the overall, large-scale structure of the MWNSC we create stellar density maps by using two data sets, depending on the distance to Sgr A*. We use Ks-band data of HAWK-I in the central 84.4 pc x 21 pc of the Galaxy that are described in Sec. 2.1.2 (see the green rectangle in Fig. 3.1). Nevertheless, HAWK-I images are not complete due to the crowding in the magnitude ranges that we wanted to study in the central $\sim$ 1.5 pc of the Galaxy. For this reason, we need higher angular resolution data in this region. We use Ks-band data from 11 May 2011 of NACO presented in Sec. 2.1.2 in the central 2pc$\times$2pc around the SMBH (see the blue square in Fig. 3.1).

The steps to create the stellar density maps are the following:

1. Alignment of NACO and HAWK-I images data via a polynomial fit of degree two (IDL POLYWARP and POLY_2D procedures). We per-

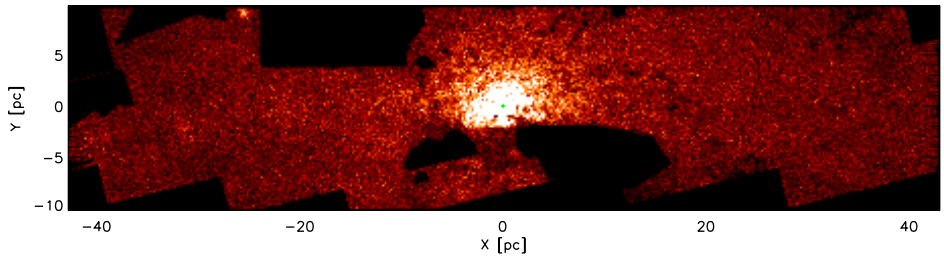

Figure 3.2: Extinction-corrected stellar number density map of the central 86 pc x 20.2 pc of the Galaxy for stars with $11.0 \leq K_s \leq 16.0$ ($9.0 \leq K_{s,extc} \leq 14.0$). The magnitudes of individual stars are corrected for extinction by using the extinction map of *Dong et al.* (2011). The green asterisk marks the location of Sgr A*. Galactic north is up and Galactic east is to the left. The Galactic plane runs horizontally.

form iterative fit using lists of detected stars in the images to compute the parameters.

2. Applying a inner mask to HAWK-I data with the shape of the NACO data FOV in the central $\sim$ 1.5 pc.

3. Joining NACO and HAWK-I data, by registering the astrometry of the detected sources in the overlapping region and using NACO in the inner region.

4. Exclusion of all spectroscopically identified early-type stars, i.e. massive and young ones, from our sample (using the data of *Do et al.*, 2013).

5. Applying extinction correction to compute the intrinsic magnitudes for the stars (see Sec. 3.2.2).

6. Selection of the range of K_s-magnitude of the stars (see Sec. 3.2.3).

7. Creation of the maps by using two dimension density functions (IDL HIST_2D procedure). We consider a size bin of $5'' \times 5''$. (See Appendix A.4 where we study the selection of the bin size).

8. Computation of the mean density in the overlap region between HAWK-I and NACO data.

The image in Fig.3.2 shows the extinction-corrected density map for stars in the range $9.0 \leq K_{s,extc} \leq 14.0$, where $K_{s,extc}$ is the extinction-corrected magnitude.

3.2.1 Crowding and completeness

For HAWK-I data, we study 14 fields that have different quality mostly because of the different atmospheric seeing conditions during the observations. Firstly, we create masks to take into account the inhomogeneity of the field, as well as the different crowding in the regions. In Fig3.2, we can see regions with different stellar number density. We create two masks: a global mask, where regions with extremely low (large IR-dark clouds to the SW) and high density (H2 regions to the NE and quintuplet cluster) are masked; a local mask to take into account the different completeness of the fields. For the global mask, we test two different density thresholds to mask regions with low density. For the local one, we mask positions in the density maps where the values are too low or high by comparing with their neighbors. For each position in the density map, the mean density is computed by considering the values of the density in the closest positions inside a ring with radius of $15''$ (0.6 pc), rejecting the points whose values are larger than 3σ from the mean. The final masks are obtained by multiplying both local and global masks (see more details in AppendixA.2).

In order to determine the faintest magnitude down to which the counts can be considered complete for all fields, we study the KLFs of the individual fields. Figure 3.3 shows a comparison between the K_s-luminosity functions (KLFs) determined from our mosaic (the black line), from the worst field (the red line), from the best field (the blue line) and from NACO data (the dashed line). The regions where the KLFs are computed are circular with radius = 1.5 pc, centered at a distance of $\sim$ 6 pc from Sgr A* to the west

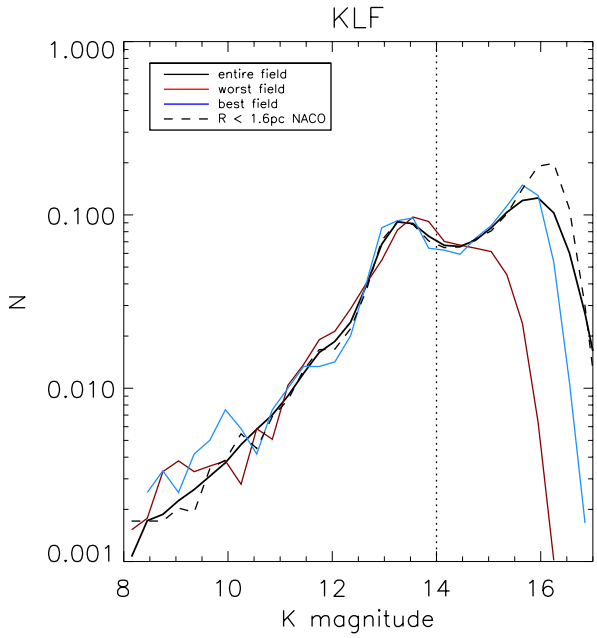

Figure 3.3: Comparison between the KLFs determined from the entire field (black line), from the worst field (red line), from the best field (blue line) and from NACO data (dashed line). The KLFs are computed after correcting the magnitude of each star using the extinction map of *Dong et al.* (2011) and applying the mask. The dotted straight line indicates the faintest magnitude down to which the counts can be considered complete for all fields.

(the worst field), and a distance of $\sim$ 29 pc to the NE (the best field), respectively. The KLF from NACO data was computed in the central $\sim$ 1.5 pc around Sgr A*. The faintest magnitude down to which the counts can be considered complete is $K_{s,extc} = 14.0$ ($K_s \sim 16.0$), for all fields (the dotted straight line in Fig. 3.3).

We do not apply completeness correction for NACO data because the high angular resolution data used here are complete in the range of magnitudes that we study ($K_s \leq 16.0$, see *Gallego-Cano et al.*, 2018). We do not apply completeness correction for HAWK-I data either but we apply masking generously to those regions with very low density, as we described above.

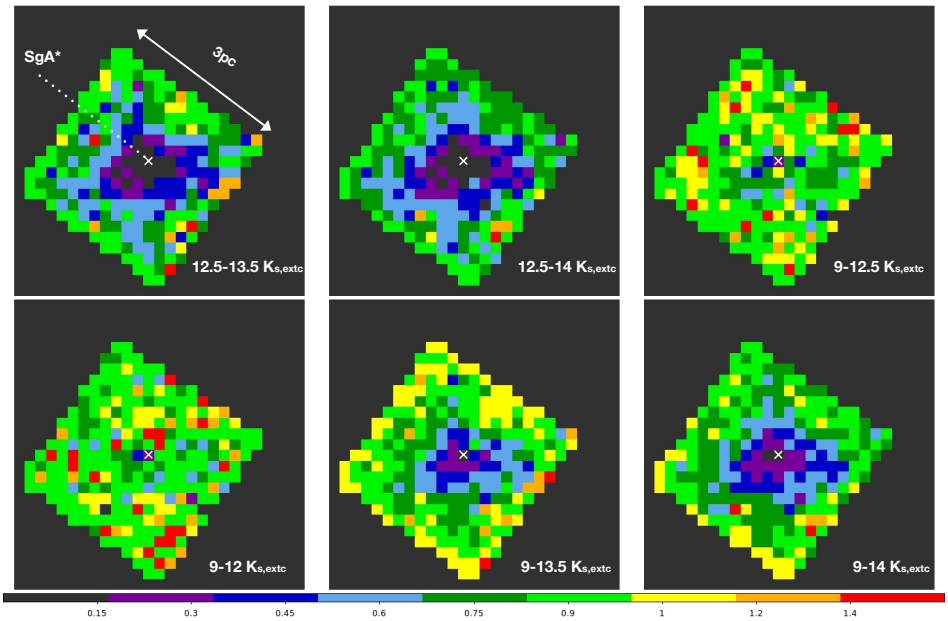

Figure 3.4: Completeness maps for HAWK-I in the central ~ 1.5 pc of the Galaxy by comparing with NACO data. The maps represent the number of stars from HAWK-I data divided by the number of stars from NACO data. We can see that the completeness is greater than 88% in the edges in all the cases, therefore we do not apply any scaling factor when we join the data. We take the mean between both data in the overlapping region.

We analyze the completeness of HAWK-I within a projected radius of $R \sim 1.5$ pc around Sgr A* by comparing with NACO data. We define the completeness of HAWK-I in the central region as the number of stars from HAWK-I data divided by the number of stars from NACO data. Figure 4.2 shows the completeness maps computed for different magnitude ranges. We can see that in the overlapping region the completeness is greater than 88% for stars brighter than $K_{s,extc} = 14.0$. Therefore, we consider that it is not necessary to apply any scaling factor to the HAWK-I data in the overlap region with NACO, but simply take the mean of the two data sets.

3.2.2 Extinction

We do not correct the effect of extinction on the density of the detected sources, because we exclude highly extincted regions. Furthermore, in fields with moderate extinction, differential extinction is $\leq$ 1 mag. Since our detection limit is about $K_s \sim 18 - 19$ in all fields, but our completeness cut off (due to data quality and crowding) is $K_s = 16$, these variations in extinction are not considered to have any significant impact on our results. We corrected the magnitudes of the individual stars by using the extinction map of *Dong et al.* (2011). They created the extinction map by using $F187N$ and $F190N$ filters[1] from the Hubble Space Telescope/Near-Infrared Camera and Multi-Object Spectrometer (HST/NICMOS). In order to convert into K_s magnitude, we consider that the extinction curve in the NIR can be described by a power law (e.g. *Nishiyama et al.*, 2008; *Fritz et al.*, 2011) and we use the extinction index obtained by *Nogueras-Lara et al.* (2018a) $\alpha = 2.30 \pm 0.08$. Figure 3.5 shows the extinction map of *Dong et al.* (2011) converted into K_s magnitude. We compute the intrinsic $K_{s,extc}$ magnitude for individual stars by using the obtained extinction map. Figure 3.2 shows the extinction-corrected density map for stars with $9.0 \leq K_{s,extc} \leq 14.0$. The shape of the FOV of the map is due to the FOV of the extinction map. By cause of dark foreground clouds, the source density in the map of *Dong et al.* (2011) is very low and the extinction was averaged over large regions. The latter can be easily identified as large patches in the extinction map that do hardly show any variation. We mask those regions by hand because they will be heavily contaminated by foreground stars (see green polygons in Fig. 3.5). The same stars are not necessarily used in the non-corrected density map (without applying extinction correction) and in the extinction-corrected density map because the extinction correction may move stars in and out of the faintest considered bin. In Appendix A.1, we provide

[1] We consider the following values of the effective wavelengths: $\lambda_{F187N} = 1.8745$ and $\lambda_{F190N} = 1.9003$.

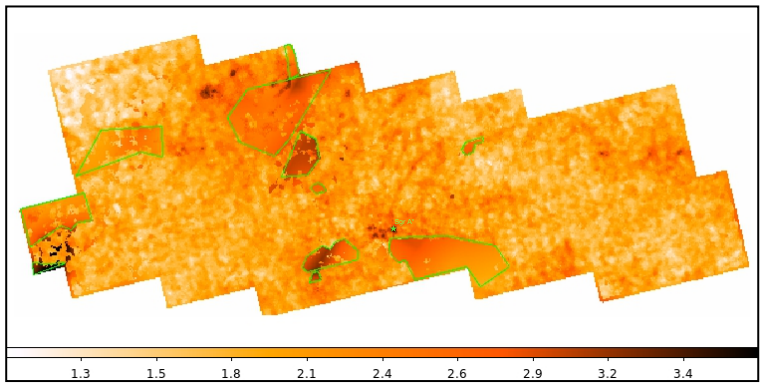

Figure 3.5: Extinction map A_{K_s} from the central 416 arcmin^2 ($\sim$1kpc^2) used for the extinction correction. The extinction map is computed by converting the extinction map of *Dong et al.* (2011) into K_s magnitude. We apply masks to some regions (green polygons). The median value of A_{K_s} is 1.9. The spatial resolution is $\sim$ 9.2 arcsec. The green star shows the position of Sgr A*.

further tests to study the systematic uncertainty derived by the extinction-correction, such as considering a value less steep of the extinction index α.

3.2.3 Selection of the magnitude ranges for the analysed stars

In order to test whether the composition of the stellar population in the MWNSC changes with distance from Sgr A*, we study the density maps in the following brightness ranges (in parentheses for extinction-corrected magnitudes):

(a) RC stars and bright giants in the range: $11.0 \leq K_s \leq 16.0$ ($9.0 \leq K_{s,extc} \leq 14.0$);

(b) only bright giants in the range: $11.0 \leq K_s \leq 14.0$ ($9.0 \leq K_{s,extc} \leq 12.0$);

(c) RC stars in the range: $14.5 \leq K_s \leq 16.0$ ($12.5 \leq K_{s,extc} \leq 14.0$).

We select the magnitude ranges of RC and bright stars with the purpose of avoiding to mix different kinds of stars. The magnitude ranges in the non-corrected density maps are selected in order to consider roughly the same number of stars than in the extinction-corrected density maps. We study the brightness ranges (a) in order to compare with previous studies. Although we do not need any precision photometry, we select the brightest magnitude in the range of the stars in order to avoid saturation effects in our sample. Furthermore, in Appendix A.8 we explore the results by considering another brightest magnitude limit.

3.3 Surrounding component models

Our main goal is studying the structure of the MWNSC. Since the MWNSC is not isolated, when we compute the star density toward the GC we have to take into account several superposed components: NSD, GB, and GD (in decreasing order of star density). The GD contributes a negligible contamination within the central $\sim$ 10 pc (see the possible contamination by foreground stars in Appendix A.6). The primary source of systematic uncertainty is due to the NSD, and the secondary one is due to the GB. We apply the term "background" to both foreground and background contributions that contaminate our sample. We use the stellar density map of the central $6^\circ \times 2^\circ$ of our Galaxy from *Nishiyama et al.* (2013) (see left panel in Fig. 3.7) to model the GB and NSD in order to subtract them from the NSC. Furthermore, we use IRAC/Spitzer 4.5μm images described in Chapter 2 Sec. 2.2 to constrain the NSD, following up the work of *Schödel et al.* (2014a).

3.3.1 Galactic Bulge

We model the GB as a triaxial ellipsoidal bar with a centrally peaked volume emissivity ρ (*Dwek et al.*, 1995; *Stanek et al.*, 1997; *Freudenreich*, 1998). We consider the best GB parameters computed by *Launhardt et al.* (2002)

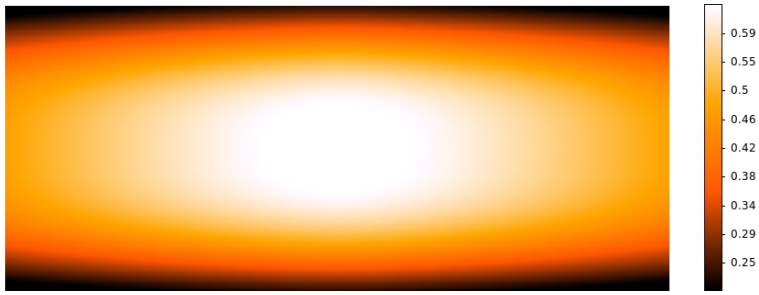

Figure 3.6: Triaxial ellipsoidal bar model with a centrally peaked volume emissivity ρ for the GB of the central $6° \times 2°$ of our Galaxy. Galactic north is up and Galactic east is to the left. The GP runs horizontally through the center.

(See Table 4 in their paper). They found that the best fit for the surface brightness profile of the GB is the one that represents the volume emissivity by an exponential model:

$$\rho(r) \propto exp(-R_s) \tag{3.1}$$

They selected the shape of the bar as a "generalized ellipsoid" (*Athanassoula et al.*, 1990; *Freudenreich*, 1998), where R_s is the effective radius (see equations 5 and 6 in *Launhardt et al.*, 2002).

The intensity of light from the bulge region in the $\{l, b\}$ direction is given by an integral of the volume emissivity ρ along the line of sight s (for more details see equation 1 of *Dwek et al.*, 1995):

$$I(l, b) = 2 \cdot N_0 \cdot \int_0^\infty exp(-R_s) \cdot ds \tag{3.2}$$

We apply the previous equation to compute the projected stellar number density of the GB. The parameter N_0 is a normalization constant given in units of stellar number density and is determined from fitting the model $I(l, b)$ to the stellar number density map from *Nishiyama et al.* (2013). We mask a region of $\sim$ 500x72 pc^2 centered on Sgr A* occupied by the NSD (*Launhardt et al.*, 2002) and some dark clouds to fit the GB. We consider

that its central stellar density can be derived from its outer parts. Figure 3.7 shows the GB model that fits for the stellar density map. Table 3.1 summarize the parameters that we consider in the model and the best-fit parameters that we obtain.

3.3.2 Nuclear stellar disc

In this section, we analyze the NSD, the component with the overall highest star density and smallest angular scale. As we described above, we model the NSD by using two different datasets: the stellar density map of *Nishiyama et al.* (2013) (NSD Model 1), and MIR Spitzer images (NSD Model 2).

In order to compute the NSD Model 1, we mask regions of the density map with low density (see dark clouds in the right image in Fig. 3.7) and a region of approximately 10 pc×10 pc centered on Sgr A* occupied by the NSC. The NSD can be modelled by an elliptical model. We use a Sérsic model (*Graham*, 2001) given by

$$I(x,y) = I_e exp\Big\{ - b_n \Big[\Big(\frac{p}{R_e} \Big)^{1/n} - 1 \Big] \Big\}, \tag{3.3}$$

where I_e is the intensity at the effective radius R_e, which encloses 50% of the light. The factor b_n is a function of the Sérsic index n. We use the approximation $b_n = 1.9992n - 0.32$ given by *Capaccioli* (1987) for $1 < n < 10$. We use the modified projected radius p for elliptical models

$$p = \sqrt{x^2 + (y/q)^2}, \tag{3.4}$$

where x and y are the 2D coordinates and q is the ratio between minor and major axis. We are interested in studying the star count contribution of the NSD, therefore we convert the $I(x,y)$ into stellar number density in the $\{x,y\}$ position. Finally, we fit the Sérsic model for the NSD plus the GB model computed in the previous section to the stellar number density map.

Table 3.1: Galactic bulge and nuclear stellar disc Model 1 parameters by using the stellar density map of the central $6^\circ \times 2^\circ$ of our Galaxy of *Nishiyama et al.* (2013).

Parameter	Value
Sun dist. from GC $R_0^{\rm a}$	8.5 kpc
Bar X scale lenght $a_x^{\rm a}$	1.1 kpc
Bar Y scale lenght $a_y^{\rm a}$	0.36 kpc
Bar Z scale lenght $a_z^{\rm a}$	0.22 kpc
Bar face-on parameter $C_\perp^{\rm a}$	1.6
Bar edge-on parameter $C_\parallel^{\rm a}$	3.2
Stellar number density at R_e	(19.84 ± 0.16) stars/arcmin^2
Flattening q	(0.338 ± 0.002)
Sérsic index n	(0.782 ± 0.008)
Effective radius R_e	(116.2 ± 0.6)pc

[a] Fixed input parameter from *Launhardt et al.* (2002).

The best- fit parameters were obtained by using a gradient-expansion algorithm to compute a non-linear least squares fit to the model (IDL CURVEFIT procedure). The value of $\chi^2_{reduced}$ is 1.082. They best-fit parameters are summarized in Table 3.1.

Although we assume a larger value of the distance of the GC to compute the GB, if we consider a more updated value of 8 kpc (see, e.g. *Genzel et al.*, 2010; *Meyer et al.*, 2012; *Gravity Collaboration et al.*, 2018a) the differences between the parameters obtained using both values are negligible ($< 0.001\%$).

Finally, we compute the NSD Model 2 by using the same data and technique as outlined in *Schödel et al.* (2014a). However, while the latter used images no larger than 200 pc x 200 pc in order to avoid the difficulties of the spatial change in the background contributed by the GB and due to large dark clouds, we here fit the NSD to the full images as delivered by the survey of *Stolovy et al.* (2006) and include our GB model to take the

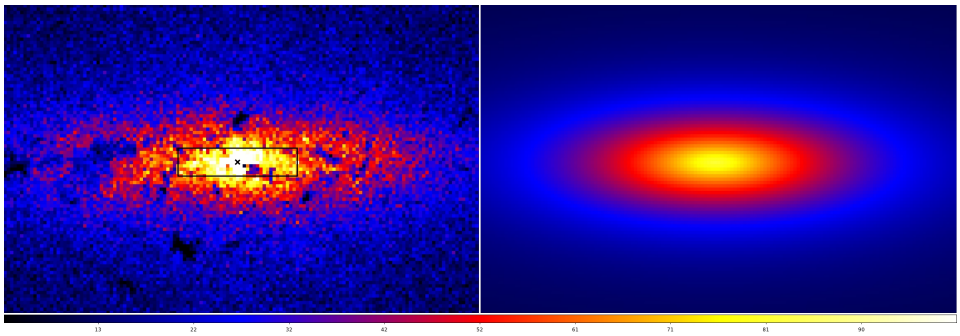

Figure 3.7: Map of the stellar density in the central 341 pc x 219 pc of our Galaxy. Both panels use the same color linear scales. Left: stellar number density map from *Nishiyama et al.* (2013). The black rectangle indicates the FOV of our data (∼86 pc×20.2 pc). Sgr A* is located in the position of the black cross. Right: Sérsic plus triaxial ellipsoidal fit to the data after masking the central 10 pc occupied by the NSC and regions with low density.

Table 3.2: Nuclear stellar disc Model 2 by using MIR imaging. I_e is the flux density at R_e.

Nuclear stellar disk	
Parameter	Value
I_e	(0.279 ± 0.003) mJy arcsec^{-2}
q	(0.372 ± 0.005)
n	(1.09 ± 0.03)
R_e	(86.9 ± 0.6)pc

influence of the latter into account. All large dark clouds were masked. By using the full extent of the images from the Spitzer survey we expect to have better constraints on the NSD with its large scale length. Table 3.2 shows the final results obtain for the NSD Model 2.

To conclude, we provide two new sets of analysis of the NSD, by using completely different data and methods. The main advantage of using NSD Model 1 is that we apply a similar procedure to fit the Sérsic model to the extinction-corrected stellar number density maps built from NIR images, using star counts analysis. Furthermore, the images are larger which allows

us to constrain better the GB model. The main advantage of NSD Model 2 is that the images have better resolution than the images from NSD Model 1. Also, the MIR images are less affected by extinction and were corrected for it. Taking into account the effect of extinction is of great importance in the highly extincted GC region. In particular, dust in the central molecular zone appears in projection concentrated toward a strip between ±30 pc around the GP (e.g., Fig. 6 in *Schödel et al.* 2014a; see also *Molinari et al.* 2011). Although the brightness of the individual stars in the data set that underlies Model 1 have been corrected for extinction, the overall systematic effect of the non-random distribution of highly extinguished regions on this model has not been taken into account. Such a bias would result in a systematically thicker NSD model. Similarly, a gradient of extinction along Galactic longitude can bias the model toward a larger effective radius. We, therefore, believe that Model 2 is the more accurate one.

3.4 Structure of the nuclear stellar cluster

The Sérsic model gives a good description of the large-scale structure of the NSC (*Schödel et al.*, 2014a). Firstly, we apply it to the extinction-corrected density maps computed for the different magnitude ranges of the stars (see Sec. 3.2.3) by using NACO plus HAWK-I data. We use the following steps to fit the models:

1. We apply a mask to take into account the variable completeness across the FOV due to the different observing conditions, extinction, and crowding, as we described in Sec. 3.2.1. We study the systematic errors caused by the selection of the masks in Appendix A.2.

2. To avoid biased results in the Sérsic model that has a central peak, we mask the inner 0.6pc. This is due to the fact that in our study, the number counts are dominated by bright stars ($K_s < 16.0$) that show a flat profile, different to the cusp profile that is shown by faint

stars ($K_s > 16.0$) (see *Buchholz et al.*, 2009; *Bartko et al.*, 2010; *Yusef-Zadeh et al.*, 2012; *Do et al.*, 2013; *Gallego-Cano et al.*, 2018; *Schödel et al.*, 2018).

3. We consider the triaxial ellipsoidal bar model for the GB computed in Sec. 3.3.1 and we subtract it from the NSC.

4. We consider the Sérsic model for the NSD obtained in Sec. 3.3.2 and we subtract it from the NSC.

5. We fix the tilt angle between the NSC with respect to the GP to 0 degree. In the next section, we leave this angle free.

6. We fit the Sérsic model to the stellar density maps for the different magnitude ranges.

We found the best-fit solution by using a gradient-expansion algorithm to compute a non-linear least squares fit to the model with 12 parameters (IDL MPCURVEFIT procedure). We explored the systematic effects of the different choices of masks and other parameters by changing their values and fitting the data repeatedly. The resulting best-fit values are listed in Table A.1. Figure 3.8 shows the comparison between the density map for stars with $9.0 \leq K_{s,extc} \leq 14.0$ (upper panel) and the Sérsic model plus the background model (middle panel) that we obtain in the fit (ID 10 in Table A.1).

As a second approach to the problem, we assume symmetry of the cluster with respect to the GP and with respect to the Galactic north-south axis through Sgr A*. We obtain the symmetrized image by replacing each pixel in each quadrant with the median of the corresponding pixels in the four image quadrants and ignoring the masked areas. The pixels along the vertical and horizontal symmetry axes are not averaged. The uncertainty for each pixel is computed by taking the standard error of the mean. Figure 3.9 shows the comparison between the stellar density map and the symmetrized image for

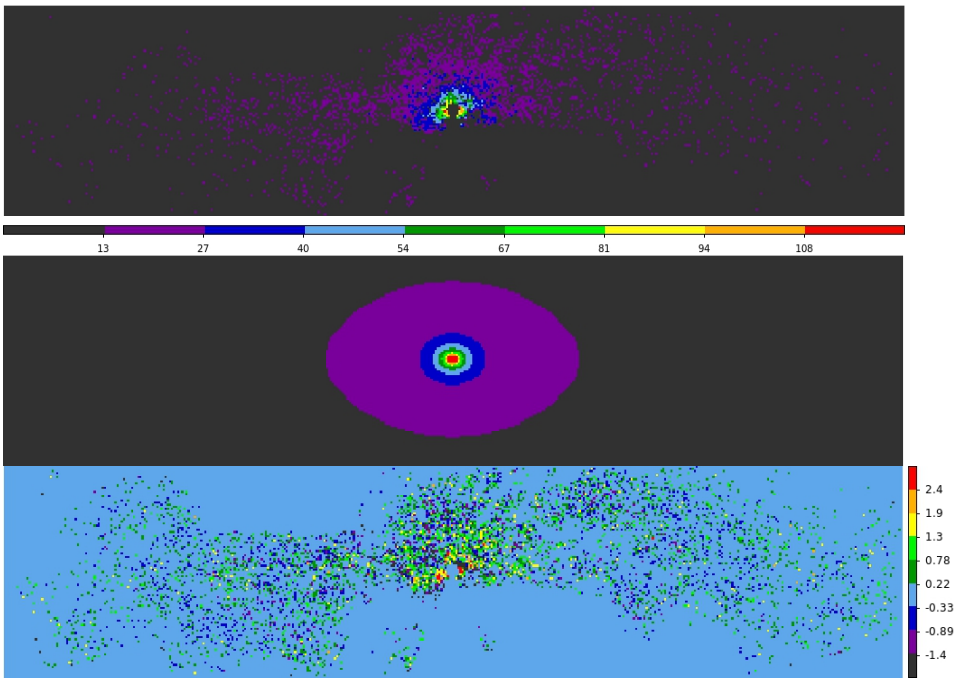

Figure 3.8: Comparison between the stellar density map of the central 86 pc x 20.2 pc of the Galaxy and the model. Upper: Extinction-corrected stellar density map for stars with $9.0 \leq K_{s,extc} \leq 14.0$. The dark regions are masked in the fit. *Middle*: Sérsic model for the NSC plus the background model (ID 10 in Table A.1). Lower: Residual image given by the difference between the upper and middle panels divided by the uncertainty map of the density map. The color bar shown for the lower panel is in unit of the standard deviation. The other two panels use the same linear color scale, shown between upper and middle panels. Galactic north is up and Galactic east is to the left.

stars with $9.0 \leq K_{s,extc} \leq 12.0$ (ID 7 for Table A.1). We fit the Sérsic model to the symmetrized images corresponding to the different magnitude ranges.

The resulting best-fit values are listed in Table A.1. Table 3.3 shows the final parameters that we obtain taking the mean value of the best-fit parameters from Table A.1. The uncertainties are the standard deviations of all the best-fit parameters. We add the statistical errors quadratically to the final uncertainties.

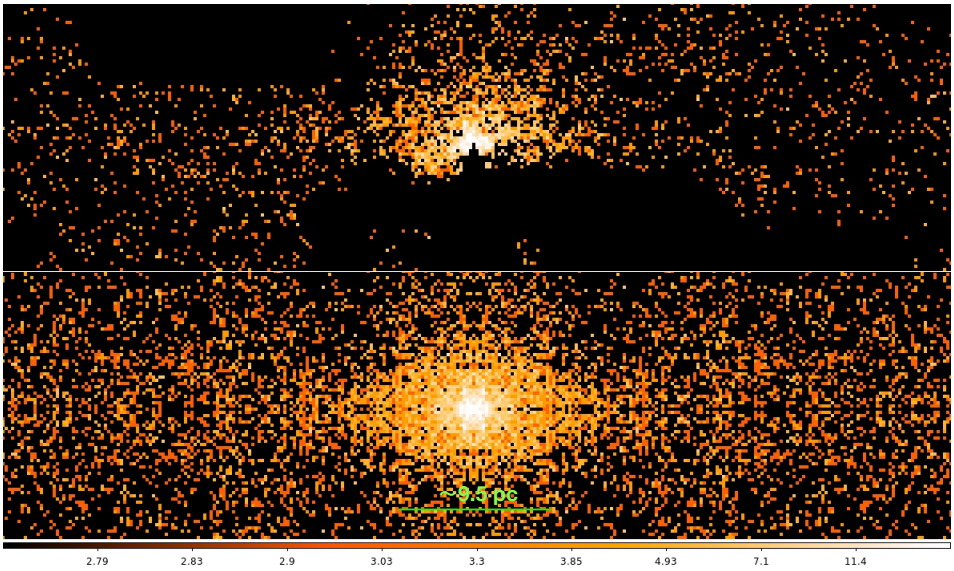

Figure 3.9: Comparison between the stellar density map of the central 58 pc x 16 pc of the Galaxy and the symmetrized image. Upper: Extinction-corrected density map for stars with $9.0 \leq K_{s,extc} \leq 12$. The mask applied is shown (dark regions). Lower: Symmetrized image is obtained from taking the median of the pixels from the four quadrants by assuming symmetry of the cluster with respect the GP and with respect to the Galactic north-south axis through Sgr A*. Both panels use the same color scale. Galactic north is up and Galactic east is to the left.

Table 3.3: Best-fit model parameters for Sérsic fits to the stellar number density maps. The MWNSC is aligned with respect to GP.

ID	Mag. range ($K_{s,extc}$)	$N^b_{e,nsd}$ (stars/bin^{2,a})	$N^c_{e,nsc}$ (stars/bin^{2,a})	q^d	n^e	R^f_e (pc)
1	$12.5-14$	2.45 ± 0.10	3.94 ± 0.39	0.85 ± 0.05	2.59 ± 0.19	5.66 ± 0.22
2	$9-12$	0.55 ± 0.09	1.16 ± 0.21	0.60 ± 0.03	2.28 ± 0.42	4.57 ± 0.78
3	$9-14$	3.22 ± 0.19	6.55 ± 0.99	0.78 ± 0.02	2.02 ± 0.46	5.38 ± 0.19

Notes.

[a] The bin size in the density maps is $5'' \times 5''$.[b] Stellar number density for the NSD at its effective radius (see value in Table 3.1).[c] Stellar number density for the NSC at the effective radius R_e.[d] The flattening q is equal to the minor axis divided by the major axis.[e] n is the Sérsic index.[f] R_e is the effective radius for the NSC.

Table 3.4: Best-fit model parameters for Sérsic fits to the stellar number density maps. θ is the tilt angle between the NSC and the GP, that is a free parameter in the fits. Positive angle is clockwise with respect to GP.

ID	Mag. range ($K_{s,extc}$)	θ (degree)	N_{nsd} (stars/bin^2)	N_{nsc} (stars/bin^2)	q	n	R_e (pc)
1	$12.5-14$	$-8.51\pm2.81_{sys}\pm0.66_{stat}$	2.43 ± 0.10	3.38 ± 0.43	0.83 ± 0.04	3.01 ± 0.37	6.19 ± 0.67
2	$9-12$	$-5.60\pm1.22_{sys}\pm0.57_{stat}$	0.55 ± 0.08	1.24 ± 0.19	0.64 ± 0.10	1.93 ± 0.46	4.31 ± 0.52
3	$9-14$	$-6.98\pm1.19_{sys}\pm0.40_{stat}$	3.21 ± 0.20	6.63 ± 1.19	0.75 ± 0.01	2.26 ± 0.21	5.36 ± 0.35

We explore also to leave the tilt angle between the NSC and the GP free in the fits without assuming any symmetry of the cluster a priori. First of all, we create different symmetrized maps varying the tilt angle θ from $\theta = 0°$ (NSC aligned to the GP) to $\theta = 15°$ (NSC is symmetric with respect to an axis rotated θ respect to the GP and with respect an axis perpendicular to it through Sg A*). We compute the residual images given by the difference between the stellar density map and the symmetrized image. Figure 3.10 shows the average of the residual maps given by the root mean square of all values for the different magnitude ranges. We can see that there is an improvement in the residual for a tilted, symmetrized cluster, compared to a non-tilted one. For bright stars, we find a minimum value around $\theta = 6°$ (middle panel in Fig. 3.10). For RC stars, we find a minimum around $\theta = 5°$ (left panel in the figure). We obtain similar result for stars with $9.0 \leq K_{s,ext} \leq 14.0$ (right panel in the figure). For all the cases, the average of the residuals are very similar from $\theta = 0°$ to $\theta = 10°$. We also performed a fit of NSC + NSD on the un-tilted and un-symmetrized map, but introducing the tilt angle as an additional free parameter. As we can see in Fig. 3.10, there are local minima for the value of θ, what make us explore the fits by considering different initial values for the angle (see Appendix A.10).

The resulting best-fit values are listed in Table A.2. Figure 3.11 shows the symmetrized image corresponding to ID 7 in Table A.2. Table 3.4 shows the final results that we obtain taking the mean value of the best-fit parameters from Table A.2 and the uncertainties are the standard deviations of the systematic errors. The statistical errors for the parameters are negligible. In the case of θ, we have to include also the systematic errors associate to the selection of different initial θ (see Appendix A.10). In this case, we also consider the statistical errors. The value of θ obtained for bright stars is very consistent with the value that minimizes the residuals. For the other stars, the values are inside the range of the angles that minimize the residuals.

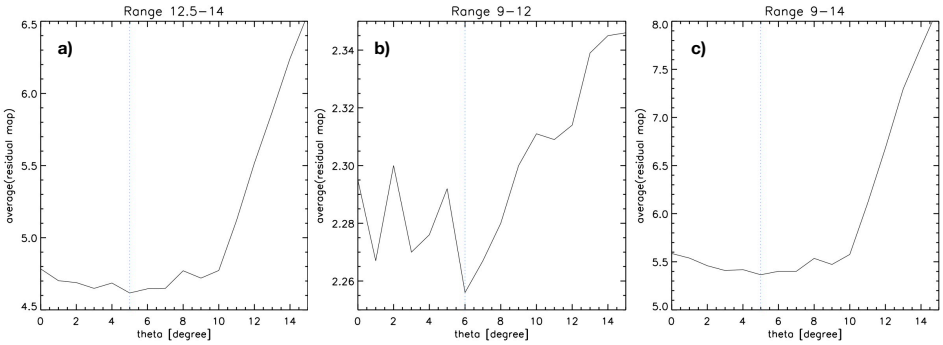

Figure 3.10: Average of the residuals in the difference image between the original and the symmetrized image of the NSC versus the absolute value of the tilt angle θ used to symmetrize the image. **a)** Average of the residuals for stars with $12.5 < K_{s,ext} < 14.0$. We find a not very significant minimum at $\theta = 5°$. **b)** Average of the residuals for stars with $9.0 < K_{s,ext} < 12.0$. We find a minimum for $\theta = 6°$. **c)** Average of the residuals for stars with $9.0 < K_{s,ext} < 14.0$. In this case, we obtain similar results for stars with $12.5 < K_{s,ext} < 14.0$. For the three cases, the residuals are similar from $\theta = 0°$ to $\theta = 10°$. The dotted blue lines indicate the value of θ that minimizes the residuals.

Finally, in order to obtain an independent constraint on the projected structure of NSC, we compute the double Sérsic NSC plus NSD fit to the NIR images as we described above, including also our GB emission model based on *Launhardt et al.* (2002) and leaving the tilt angle free. Table 3.5 shows the final results obtain for the best NSC parameters. Our results are very similar to what was obtained by *Schödel et al.* (2014a), but should be better constrained because of the larger field-of-view and the use of a more accurate GB model. Due to the low resolution of the data, we can compare approximately the results with the values obtained for stars with $9.0 \leq K_{s,extc} \leq 12.0$ (ID 2 in Table 3.4). All the parameters that we obtain in the fits are consistent with the final results at the 1σ level.

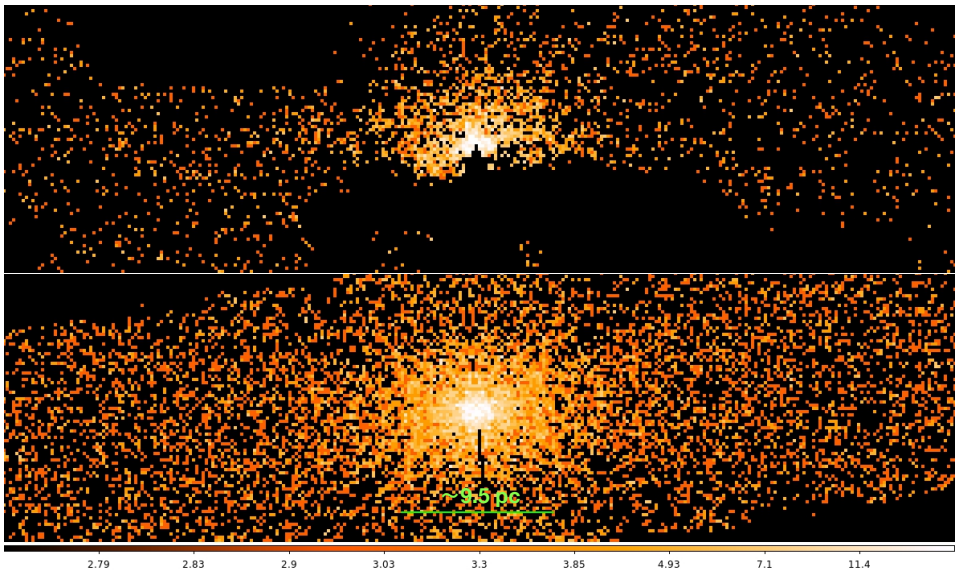

Figure 3.11: Comparison between the stellar density map of the central 73pc x 20pc of the Galaxy and the rotated symmetrized image. Upper: Extinction-corrected density map for faint stars with $9.0 \leq K_{s,extc} \leq 12$. The mask applied is shown (dark regions). Lower: Symmetrized image obtained by assuming symmetry of the cluster with respect to tilted axes through Sgr A* with an angle of ~ -5.6. Both panels use the same color scale. Galactic north is up and Galactic east is to the left.

3.4.1 Overall properties of the MWNSC

Our work aims to build a bridge between the last two comparable works of *Schödel et al.* (2014a) and *Fritz et al.* (2016) and improve the lacks of them described in the following.

Table 3.6 shows a comparison between the results obtained here and in previous studies. The values inferred in this work and in previous work agree within their $1-2\sigma$ uncertainties, indicating that none of them suffers any major bias. Due to the higher angular resolution of our work, we are able to constrain the range of the stars to study the distribution of giants in the RC and at brighter magnitudes, separately. Due to its generally very well defined brightness and mass, the RC is a very-well suited tracer to study

Table 3.5: Nuclear stellar cluster model parameters by using MIR imaging. I_e is the flux density at R_e and θ is the tilt angle defined positive in the direction east of Galactic north.

Nuclear stellar cluster	
Parameter	Value
θ	(-6.9 ± 1.7) degree
I_e	(2.64 ± 0.43) mJy arcsec^{-2}
q	(0.66 ± 0.03)
n	(1.8 ± 0.1)
R_e	(4.9 ± 0.5)pc

stellar structures older than $\sim$ 2 Gyr. RC stars are the most abundant stars at $K_s \leq 17$ in the GC and thus an important tracer population, but it was not reached in previous studies because of their low angular resolution, which made brighter stars dominate the measurements.

We use the same NIR wavelength and method of star counts like *Fritz et al.* (2016) but with a more than twice higher angular resolution, which allows us to use the RC as a tracer of structure, limit the influence of crowding, and improve the number statistics. Also, we explicitly model and take into account stellar structures that overlap with the NSC along the line of sight, in particular the Galactic bulge and the nuclear bulge. Finally, *Fritz et al.* (2016) could not clean their sample of foreground stars across their entire field because they did not have two filter measurements for all regions. Here, we can reliably exclude foreground stars.

Schödel et al. (2014a) uses MIR images and study also the contribution of the GB and NSD. The disadvantages are that the resolution is lower than in our study and they only used the central most parts of the images available to them, which may have biased their work. We repeat their study and improve it by analyzing the entire images and including the GB model.

In order to give the final values of the MWNSC parameters, ID 1 and ID 2 in Table 3.4 can be taken like independent measurements because the

samples that we study in each case are different, composed by stars in two different ranges of magnitudes. If we add also the results from MIR imaging (Table 3.5), we can consider that the final values obtained from our work are the mean of the three parameters and the uncertainties are the error of the mean. We obtain for the effective radius: $R_e = (5.1 \pm 0.6)$ pc; for the axis ratio: $q = 0.71 \pm 0.06$; for the tilt angle: $\theta = (-7.0 \pm 0.8)$ degree ;and for the Sérsic index: $n = 2.2 \pm 0.4$. The ellipticity is $\epsilon = 1 - q = 0.29 \pm 0.06$. The effective radius and the ellipticity of the MWNSC are very well constrained (see Fig. 3.12). *Fritz et al.* (2016) study the flattening in different ranges of distances from the SMBH. They report $q = 0.80$ at distances smaller than 2.3 pc, but for larger distances, they obtain larger values of the flattening, very similar to our results. These somewhat different results have probably their cause in them not taking into account the MWNSC as a separate entity form the GB and NB. The value of the Sérsic index depends highly on the distribution in the central parsec. *Fritz et al.* (2016) consider the central parsec in the fits, in the same way that we do in the present work, but we mask the central 0.6 pc to avoid contamination of young stars and biases results of the fits because of the flat profile showed by bright stars. *Schödel et al.* (2014a) reported a smaller value for the Sérsic index the than ours. The difference comes from the NIR images, because they are forced to mask the central parsec, due to the low resolution of the data and to the existence of a few extremely bright sources and a strong diffuse emission from the mini-spiral. It appears that the Sérsic index can easily suffer bias and caution is required in its application. Its precise value also depends strongly on the assumptions on and fit of any structures overlapping with the NSC.

Both previous work quote that they may underestimate the systematic errors in component fitting. We give very robust and reliable uncertainties of the best-fit NSC parameters, not only by taking into account different potential sources of systematic errors but analyzing the MWNSC structure by two completely different approaches: MIR and NIR imaging. We explore

in detail the systematic uncertainties that can affect the parameters, taking into account different potential sources of systematic errors. We choose to let these uncertainties be reflected in the error bars of the best-fit parameters in order to give robust and reliable values.

Finally, in addition to assuming that the MWNSC is aligned with respect to the GP like previous work (upper panels in Fig. 3.13), we leave the tilt angle between the NSC and the GP to be free in the Sérsic models (lower panels in Fig. 3.13). We obtain for the first time in a photometric study that the MWNSC is consistent with a tilt of the major axis out of the Galactic plane by up to -10 degrees. This result corroborates the misalignment of the kinematic position angle of ~ -9 degrees found by *Feldmeier et al.* (2014), somewhat smaller but within the uncertainties. *Fritz et al.* (2016) determine also the orientation of the major axis in proper motion data. They find that it agrees within 1.2 degrees with the GP in contrast to line of sight and star distribution data. That hints that a simple rotation of the cluster is not sufficient to explain all data. Figure 3.13 shows a comparison between the symmetrized images of the inner $\sim$ 42 pc x 16 pc of the Galaxy for stars with $12.5 \leq K_{s,extc} \leq 14.0$ (left panels) and the Sérsic models (right panels). For upper panels we assume that the MWNSC is aligned with respect to the GP in the fits (ID 3 in Table A.1). For lower panels, we leave the tilt angle free in the fits (ID 3 in Table A.2).

Table 3.6: Comparison with previous studies.

Study	Wavelength (μm)	Angular resolution (arcsec)	Scales (pc^2)	q	n	R_e (pc)
Schödel et al. (2014)	4.5	2	200×200	0.71 ± 0.02	2 ± 0.2	4.2 ± 0.4
Fritz et al. (2016)	2.2	1	80×80	0.80 ± 0.04	1.5 ± 0.1	7 ± 2
Present work NIR	2.2	0.2	86×20.2	0.75 ± 0.01	2.26 ± 0.21	5.36 ± 0.35
Present work MIR	4.5	2	300×250	0.66 ± 0.03	1.8 ± 0.1	4.9 ± 0.5

Notes:

Fritz et al. (2016) use data with different resolution. We show the resolution for larger distances (R> 2.72pc) where they used VISTA data. For distances R≤ 0.8 pc, they use NACO data with an angular resolution of 0.08". For distances 0.8 pc≤R≤ 2.72 pc they use (HST) WFC3/ IR data with an angular resolution is 0.15". Present work presents our results for stars with magnitude in the range $11.0 \leq K_s \leq 16.0$ (ID 3 in Table 3.4). We show the resolution for larger distances where we use the GALACTICNUCLEUS survey. For distances R≤ 2 pc, we use NACO data with an angular resolution of 0.05". We also present the results by using MIR.

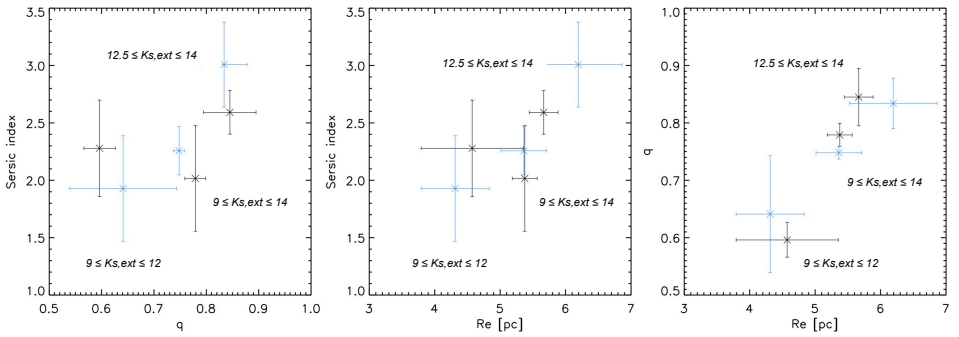

Figure 3.12: Comparison between the best-fit NSC parameters for a MWNSC that is assumed to be aligned with the GP (black points) or for the case when a small tip-angle is included in the fits (blue points). The magnitude of the stars are indicated in the panels.

Figure 3.12 shows a comparison between the best-fit parameters for the case when the MWNSC is aligned with the GP and for the case when the tilt angle is left free. The values are consistent with each other, inside the uncertainties. Considering also Fig. 3.10, that shows the average of the residuals obtained by the subtraction of the symmetrized image of the MWNSC from the original image, we can see that it is very difficult to constrain the tilt angle of the system, but out-of-plane tilt up to $-10°$ cannot be excluded.

3.4.2 Distribution of the stars at the GC

The stars in our sample are predominantly giants, mostly in the RC and Asymptotic Giant Branch (AGB) with more than 5 Gyr (*Blum et al.*, 1996; *Pfuhl et al.*, 2011). An overabundance of bright stars has been found in the Nuclear Bulge (NSD + MWNSC) compared with the stellar population of the GB/Bar (*Blum et al.*, 1996; *Philipp et al.*, 1999). This result is a consequence of different star formation histories of both entities since the GB does not have experienced any significant amounts of recent star formation, contrary to the NB. Due to the low angular resolution of previous work, any potential differences between the distribution of RC stars and brighter

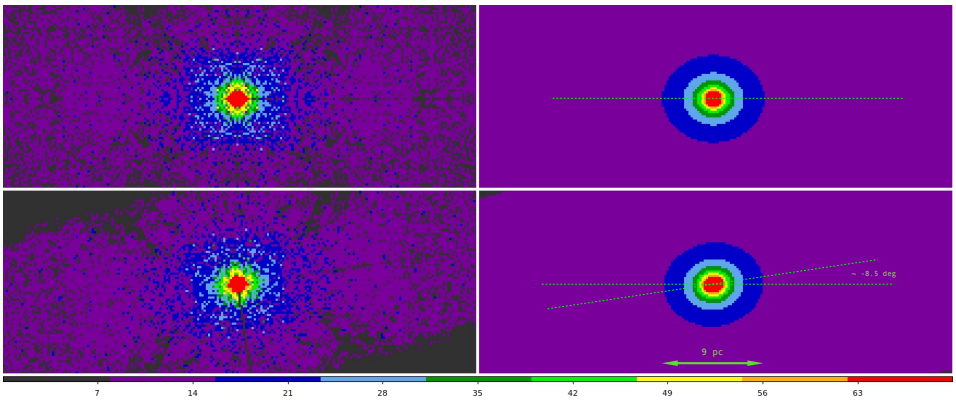

Figure 3.13: Zoom-in to compare the symmetrized images of the inner $\sim$ 42 pc x 16 pc of the Galaxy for stars with $12.5 \leq K_{s,extc} \leq 14.0$ obtained by keeping the angle between the NSC and GP equal to 0 (upper panels, ID 3 in Table A.1) and leaving the tilt angle free in the fits (lower panels, ID 3 in Table A.2). Right panels show the Sérsic model that we obtain from the fits for each case. The color scale is linear and all the images have been scaled in an identical way. Galactic north is up and Galactic east is to the left.

stars could not be studied before. If the ratio between stellar populations of different ages changes, the ratio between the number of bright giants and giants in the RC will change. For example, adding populations of ages $\lesssim 1.5$ Gyr can enhance the number of bright giants in the luminosity function.

In this work we find slightly different best-fit parameters for the MWNSC, depending whether we fit our models to the star counts of RC stars or those of brighter giants. The R_e for RC stars appears somewhat larger than for bright stars, and the distribution of the latter is more flattened. Furthermore, we study the projected radius profiles for both distributions (see Fig. 3.14). Although the differences between both distributions are not very significant, it may be a clue that the distributions of the stellar populations within the MWNSC are not homogeneous, as a result of distinct star formation histories at different distances from the SMBH. The flat distribution of the bright stars can indicate that some of the stars belong to a star formation event or a dissolved star cluster of a few hundred Myr age.

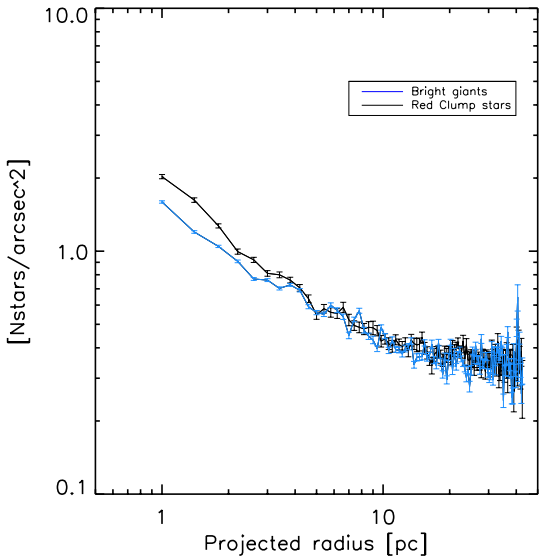

Figure 3.14: Comparison between the projected radius profiles computed for different ranges of magnitudes along the GP. We consider only the data closer than 50" (2pc) to the GP. The black line shows the density profile for RC stars ($12.5 \leq K_{s,extc} \leq 14$) and the blue line indicates the density profile for bright stars ($9.0 \leq K_{s,extc} \leq 12$). In order to facilitate the comparison between both profiles, the data for the bright stars are scaled by using the median ratio of both number counts at distances larger than 10pc. We mask the inner 0.6 pc around Sgr A*.

However, we cannot have a concrete conclusion because the innermost fields of HAWK-I data that correspond to the MWNSC have less signal to noise and resolution that further out and we need better resolution across the FOV for not being dominated by systematics.

When we fit the Sérsic model to the MWNSC, we subtract the NSD model from it. If the stellar populations are different in both components, that would lead to different results for the stars corresponding to different magnitude ranges. Currently, the dissimilarity in the stellar populations has not yet been investigated, but there are indications for differences (*Nogueras-Lara et al.*, in preparation).

To conclude, the previous hypothesis have to be studied in further work, by using higher angular resolution imaging and spectroscopy.

3.5 Comparison with extragalactic NSCs

This work is complementary to previous work on the structure of the MWNSC. After having addressed potential shortcomings of previous work, through the use of sensitive, high angular resolution star counts over a large field and careful modelling of the surrounding structures, we have now firmly established that the MWNSC has an effective radius of $R_e = 5.1 \pm 0.6$ pc and that it is flattened, with its major axis almost parallel to the Galactic plane. Two new findings contributed by our work are: (1) The major axis of the MWNSC may be tilted out of the Galactic plane by as much as -10 degrees. (2) We find that the giants brighter than the RC show a different distribution than the faint stars, in particular, a significantly stronger flattening.

The size and mass of the MWNSC lie well within the distribution of these quantities for other NSCs in spiral galaxies (e.g. *Georgiev and Böker*, 2014; *Schödel et al.*, 2014b). Also, the complex star formation history of the MWNSC is consistent with those of other NSCs. A range of structural variability has also been found in NSCs in other spiral galaxies (*Georgiev and Böker*, 2014). Flattening along the galactic plane and potential, small tilt angles between the NSC major axes and the host galaxy planes have been observed in detail in high angular resolution observations of a small number of nearby spirals (*Seth et al.*, 2006; *Carson et al.*, 2015). Figure 3.15 represents the axis ratio versus tilt angle between the NSC major axis and the galaxy plane for different NSCs in edge-on spiral galaxies (data of Tab.2 in *Seth et al.*, 2006). We average the results from the two different filters for every NSC. Three of the clusters in their sample (IRAS 09312-3248, NGC 3501, NGC 4183) are very compact and surrounded by complex emission. We exclude them from the Fig. 3.15 because their values do not come from

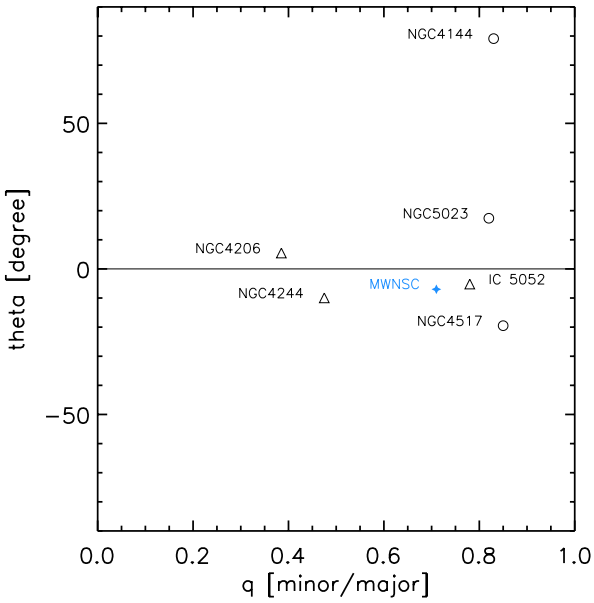

Figure 3.15: Axis ratio "q" versus "theta", the tilt angle between the NSC major axis and the host galaxy plane for different NSCs found in edge-on spiral galaxies (data of Tab.2 in *Seth et al.*, 2006). The data have been averaged for the two different filters for every NSC. The name of the galaxy is indicated in the panel. The three "multicomponent" nuclear clusters are all aligned within -10 degree of the galactic plane of the galaxy (triangles), similar to the value of the MWNSC found in the present work (the blue star). All the NSCs are flattened along with the plane of the galaxy, similar to the MWNSC.

good fits (*Seth et al.*, 2006). The three "multicomponent" nuclear clusters, that have elongated disk or ring component and a spheroidal component, are all aligned within -10 degree of the galactic plane of the galaxy (see triangles in Fig. 3.15). We can see that the values of the axis ratio and the angle for the MWNSC (the blue star in the figure) lie inside of the values for NSCs, especially very close to the values for multicomponent NSCs. *Carson et al.* (2015) also find that the effective radius of NSCs may change, depending on the observation wavelength used. This indicates that populations of different ages may not be fully mixed. This is consistent with our finding of a different structure of the brightest giants. From stellar evolution models,

we can expect that, on average, the bright giants are younger than the ones in the Red Clump. Interestingly, *Carson et al.* (2015) also find that NSCs appear rounder at redder wavelengths. Since young stellar populations tend to have bluer colors than older ones and, as we just mentioned, bright giants may, on average, be younger than RC stars, this also agrees with our finding of a rounder MWNSC when we measure the distribution of the RC stars, and a flatter one when we measure the brighter giants.

3.6 Clues to the Milky Way nuclear star cluster formation

NSCs may grow by in situ star formation or by the accretion of stellar clusters formed sufficiently close to them so that they can be accreted within a Hubble time. Since the relaxation time in NSCs can be as long as a Hubble time (for example in the case of the MW, according to *Alexander*, 2017), this implies that accretion or star formation events may be observable in the form of structural or dynamical peculiarities. Such peculiarities have been observed: a starburst happened a few million years ago within 0.5 pc of the central black hole of the Milky Way (see *Genzel et al.*, 2010, and references therein) and also some extragalactic NSCs show centrally concentrated young populations (*Georgiev and Böker*, 2014; *Carson et al.*, 2015). But younger populations can also be find at greater radii in NSCs (*Carson et al.*, 2015). Our observation of the flattened bright giants distribution and the observation of a potential rotating substructure perpendicular to the Galactic plane at a projected radius of about 0.8 pc from the center by *Feldmeier et al.* (2014) indicates that dynamically unrelaxed populations may also be present at larger radii in the MWNSC. While we cannot really constrain the formation of the MWNSC from the existing incomplete observational data, those substructure at least provide an indication that it can grow through in situ formation and accretion of nearby clusters. To look into what mechanism plays a more important role in the formation of the

MWNSC, we need higher angular NIR imaging and spectroscopy to try to disentangle the different stellar populations inside the NSC.

3.7 Conclusions

In order to constrain the overall properties of the Milky Way's nuclear star cluster and overcome some potential shortcomings of previous work, we have analyzed two different datasets and methods. On the one hand, by star counts analysis of high angular resolution images from NACO and HAWK-I, we created extinction-corrected stellar density maps for old stars. On the other hand, we improved the analysis of IRAC/Spitzer MIR images that are less affected by extinction that the former. We model the Galactic bulge and the nuclear stellar disc that are surrounding the MWNSC. We subtracted both fore/background contributions from the MWNSC and fit Sérsic models to the images. We obtained a value of the effective radius $R_e = 5.1 \pm 0.6$. We found that the MWNSC is flattened, with its major axis almost parallel to the Galactic plane. The axis ratio is $q = 0.71 \pm 0.06$, the ellipticity is $\epsilon = 1 - q = 0.29 \pm 0.06$, and the Sérsic index is $n = 2.2 \pm 0.4$. The structure of the MWNSC is similar to other extragalactic NSCs found in spiral galaxies.

We analyzed the symmetry of the MWNSC, firstly assuming that it is aligned with respect the Galactic plane as previous work did, and secondly leaving the angle between the major axis of the MWNSC and the GP free in the fits. We found that its major axis may be tilted out of the GP by as much as -10 degree, consistent for the first time with the value of the angle in the kinematic position obtained by *Feldmeier et al.* (2014) and with the observations of NSCs from nearby galaxies.

Due to our high angular resolution images, we were able to study the structure of the MWNSC in different ranges of magnitudes. We found some differences between the distributions of brighter giants and RC stars, the former was significantly more flattened. Bright giants are younger, on

average, than RC stars, according to stellar evolutionary models, and are expected to have bluer colors than the older ones. Furthermore, NSCs appear rounder at redder wavelengths, as the distribution of the RC stars from our work. Therefore, our findings agree with the differences between the effective radius of NSCs depending on the wavelength used that have been observed in nearby galaxies, that may mean that the populations of different ages are not completely mixed. The observation of the flattened bright giants distribution may support the in situ star formation scenario for the MWNSC.

Chapter 4

The stellar cusp at the Galactic Center

"The question of the stellar density and the dynamical state around Sgr A is important because the rate of strong interactions with the massive black hole scales with the stellar density close to it. In particular, the Milky Way serves, by a coincidence of technology,*[1] *as the archetypal nucleus for cosmic sources of low-frequency GWs from stellar BHs inspiraling into an MBH (extreme mass-ratio inspiral events, EMRIs), which are targets for planned spaceborne GW detectors. [The central role of the Milky Way in the planning of such experiments is reflected by the fact that the target galactic nuclei are sometimes denoted Milky Way equivalent galaxies (MWEGs).] The numbers and dynamics of stars and compact objects in the inner few*$\times 0.01$ *pc of Sgr A* therefore have, by extrapolation, direct bearings on the predicted cosmic low-frequency GW event rates"*

– Tal Alexander, *Stellar Dynamics and Stellar Phenomena Near a Massive Black Hole, Annual Review of A&A, 2017*

[1] The longest laser interferometric baseline that can be reliably maintained in space at present is $\mathcal{O}(10^6 km)$, which has maximal sensitivity to GW (gravitational waves) in the 1–10 mHz range. This corresponds to GWs emitted from near the horizon of an $\mathcal{O}(10^6 M_\odot)$ MBH (*Amaro-Seoane et al.*, 2007).

4.1 Introduction

Studying the distribution of stars around a massive black hole in a dense star cluster allows us to explore the theory of stellar dynamics in a real system and compare the theoretical predictions with the observations, e.g. in globular clusters or galactic nuclei.

Inside the cluster, the movements of the stars are undergoing gravitational encounters that perturb their initial orbits. After many encounters, all the stars eventually lose the memory of their original trajectories. The characteristic time in which the system becomes independent of the initial conditions is called *relaxation time*, and it is defined (*Binney and Tremaine*, 1987):

$$t_{relax} = \frac{0.1N}{lnN} \cdot t_{cross} \tag{4.1}$$

where t_{cross} is the time that a star takes to get through the system and N is the number of stars in the system. If $t_H > t_{relax}$, where t_H is the age of the system, the evolution of system is dominated by two-body scattering and it loses the memory of the initial conditions. Moreover, the most massive stars transfer their kinetic energy to lighter ones due to the equipartition of energy, therefore the former become slower and the latter faster. Over the relaxation time, this leads to mass segregation: the heaviest stars sink to the center of the cluster and the less massive ones move away. The stars of the system are more bound with each other over time and they are distributed more and more compactly, forming a power-law density cusp inside the *radius of influence* of the black hole r_h, the region where the dynamics is dominated by the MBH (e.g., *Lightman and Shapiro*, 1977; *Bahcall and Wolf*, 1976; *Freitag et al.*, 2006; *Hopman and Alexander*, 2006). All theoretical stellar dynamic studies reach the same conclusion, by using analytical, Monte Carlo, and N-body simulations: the stellar number density is described by a power law of the form $\rho \sim r^{-\gamma}$, where ρ is the stellar density and r is the distance from the black hole.

For a star cluster composed of a single-mass stellar population, the cusp develops with $\gamma = 1.75$ inside the radius of influence of the central BH. In general, if the star cluster consists of a range of stellar masses, we would expect a value of gamma between $1.5 - 2$, greater values for larger stellar masses.

Nevertheless, there are no observational confirmations supporting unambiguously the existence of stellar cusps up to now. Due to the large distance of the extragalactic systems, we only can study the averaged light density of hundreds to thousands (even millions) of stars, that are dominated by the brightest and youngest stars and therefore, not dynamically relaxed.

The Galactic centre (GC) is an ideal case for testing the existence of a stellar cusp. It is the closest nucleus of a galaxy, located at only ~ 8.12 kpc from Earth (*Gravity Collaboration et al.*, 2018a) and it has a $4 \times 10^6\,\mathrm{M}_\odot$ (*Boehle et al.*, 2016; *Gillessen et al.*, 2017; *Gravity Collaboration et al.*, 2018a) massive BH, Sagittarius A* (Sgr A*), surrounded by a $\sim 2.5 \times 10^7\,\mathrm{M}_\odot$ NSC (*Schödel et al.*, 2014a,b; *Feldmeier et al.*, 2014; *Chatzopoulos et al.*, 2015a; *Feldmeier-Krause et al.*, 2017). We can actually resolve the stars observationally on scales of about 2 milli-parsecs inside the radius of influence of the BH ($\sim 3\,\mathrm{pc}$, *Alexander*, 2005). Based on observations, the MWNSC share with other relaxed galactic nuclei the fundamental relation between SMBHs and their host galaxies, $M_\bullet/\sigma$ (*Ferrarese and Merritt*, 2000), in the form of $M_\bullet \propto \sigma^\beta$, with $4 \leq \beta \leq 5$ (*Alexander*, 2005), where σ is the stellar velocity dispersion of the spheroid of the host galaxy, the bulge in the case of the GC. The cusp is the signature of a relaxed system, therefore the most important question to be addressed is whether the NSC is (or not) dynamically relaxed. Is $t_{relax} < t_H$ at the GC? The relaxation time t_{relax} at the GC is the order of a few Gyr (*Alexander*, 2005), shorter than its age t_H ($\sim$ Hubble time). Therefore, the NSC is expected to be relaxed.

However, we cannot find strong evidence for the existence (or not) of a stellar cusp at the GC so far. Many previous works have studied the surface density of old stars. The first studies found a cusp-like structure (*Genzel*

et al., 2003b; *Schödel et al.*, 2007), but the successive ones, after removing properly young stars from the sample, determined that the distribution of stars around Sgr A* shows a core-like profile, resulting in the so-called *missing cusp* problem (*Bartko et al.*, 2010; *Buchholz et al.*, 2009; *Do et al.*, 2009; *Schödel et al.*, 2007). Many theoretical papers have tried to explain this lack of cusp, mainly in two different research lines. On one hand, some of them claim that the distribution that we observe is representative for the entire old population and there is no cusp, perhaps because the relaxation time is very long (> 10 Gyr) (*Merritt*, 2010) or because the cusp has been already destroyed (*Merritt and Szell*, 2006). On the other hand, other studies suggest that the distribution we observe is only representative for bright stars, and there is a hidden cusp. They explain the deficit of giants around Sgr A* by the destruction of their envelopes rendering them to invisible for observations, due to stellar collisions but this cannot fully explain the observed distribution (*Dale et al.*, 2009). Another possibility, that has been recently put forward, is that they interacted in the past with (a) fragmenting gaseous disc(s), which is an efficient way to get rid of their envelopes (*Amaro-Seoane and Chen*, 2014).

The most important difficulty that we have to overcome to study this fundamental problem of theoretical stellar dynamics is the stellar classification. We have to select suitable tracer populations, old enough to be dynamically relaxed. Due to the extreme interstellar extinction toward the GC and source crowding, observational studies are challenging. The spectroscopic identification of stars is limited to brightest giants and massive, young stars ($K \leq 16$). Moreover, the SF history of the NSC is complex: we find stellar population made up of multiple generations of stars: old (> 1 Gyr) population of stars, but also a young generation of stars (< 100 Myr). In order to study the cusp, we have to focus on stars with ages greater than the relaxation time at the GC, a few Gyr as we mentioned above. Only red clump (RC) stars fulfil this condition up to now and dominate the measurements. Moreover, the NSC is not isolated, so that when we

measure the stellar number density and diffuse flux toward the GC, we find several superposed components: Galactic disc (GD), Galactic bulge (GB), nuclear stellar disc (NSD), and NSC. Therefore, our knowledge about the stellar population is limited to the brightest few percents of stars, either few million-years old hot post main sequence (MS) giants and MS O/B stars, or giants on the RC. In fact, the only study that analyzed fainter stars found a cusp within $5''/0.2$pc of Sgr,A* (*Yusef-Zadeh et al.*, 2012).

In summary, studying the *missing cusp* problem is fundamental for the following questions:

1. Do we have the theory on stellar dynamics right?

2. Due to the density of stars and stellar remnants near Sagittarius A*: What exotic phenomena can we expect? Is there a invisible cusp?

3. What is the formation history of the MWNSC?

4. Is the MWNSC a relaxed system? The existence of the stellar cusp at the GC implies that the properties of the MWNSC can be extrapolated to other extragalactic relaxed nuclei.

5. What implications do the existence of stellar cusps in other galactic nuclei have for the detection of extreme-mass ratio inspirals (EMRIs) with gravitational wave detectors? The frequency of EMRIs (see *Amaro-Seoane et al.* 2007 and the review *Amaro-Seoane* 2018 and references therein), and thus the detection rate of sources of gravitational radiation (*Hopman and Alexander*, 2005) depends on the existence of stellar cusps. Moreover, for a coincidence of the technology, the GC is a typical nucleus (see quote of *Alexander*, 2017, at the beginning of the chapter) for cosmic sources of EMRIs that will be targets for space-borne gravitational wave detectors (LISA or Taiji). Therefore, if stellar cusps exist EMRIs might be observed with significant frequency.

Therefore, the importance of studying the cusp at the center of the Milky Way goes beyond the GC. In the next sections, we revisit the problem of inferring the innermost structure of the Milky Way's nuclear star cluster to clarify whether it displays a core or a cusp around the central black hole. We focus on two different methods and stellar populations. Finally, we compare our findings with new N-body simulations. We have published the analysis and results in the journal *Astronomy & Astrophysics* in *Gallego-Cano et al.* (2018) and *Schödel et al.* (2018).

4.2 Analysis

The observations and data reduction that we used for the analysis are presented in Section 2.1.1. In order to compute the surface density profiles in the deep mosaic after the basic reduction explained in Section 2.1.1, we followed the procedure outlined in Fig. 4.1. The four pointings are analysed independently to avoid distortion problems. In step (1), the images from the different epochs for each of the four pointings are combined. In step (2), we analysed the photometry for the four pointings with four different values of the *Starfinder* parameters, determined the source detection completeness, computed the extinction map[1]. Finally, we computed the extinction- and completeness-corrected surface density profiles. In the step (3), we computed the surface density profile for all *Starfinder* parameter sets by combining the results from the four pointings. In step (4), the surface density profiles obtained for each *Starfinder* set are mean-combined.

4.2.1 Source detection

Point source extraction was carried out with the PSF fitting program *Starfinder* (*Diolaiti et al.*, 2000). Since the images cover areas similar to or larger

[1]Tables with the photometric and astrometric parameters for the point source detections, for each pointing and *StarFinder* parameter set are available at the CDS via anonymous ftp to cdsarc.u-strasbg.fr (130.79.128.5) or via http://cdsarc.u-strasbg.fr/viz-bin/qcat?J/A+A/609/A26.

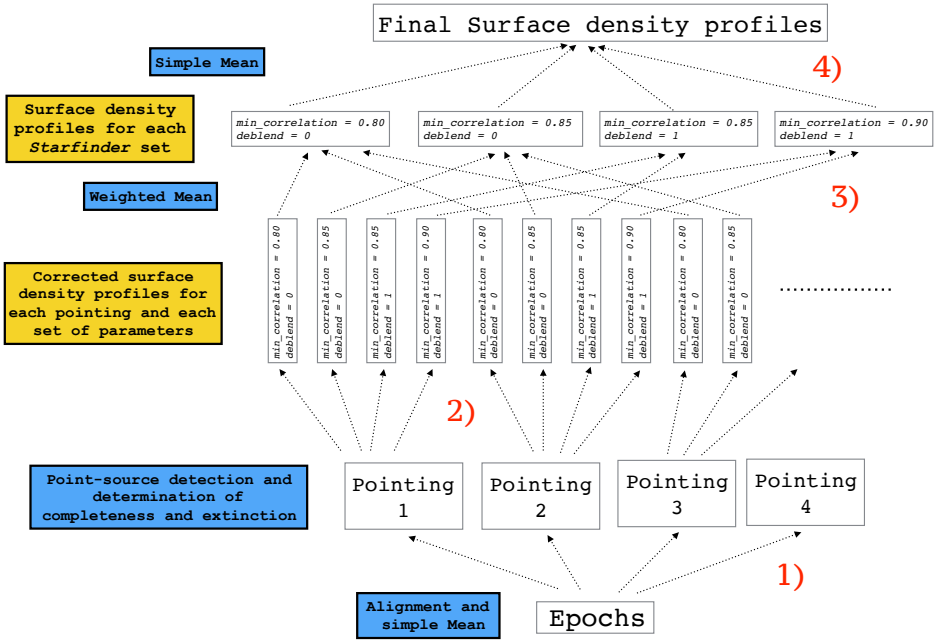

Figure 4.1: Scheme of the procedure to compute the surface density profiles in the deep mosaic.

than the isoplanatic angle at K_s-band, care was taken to deal with the spatial variability of the PSF. We parted the images into sub-fields of approximately $10.5'' \times 10.5''$ size. Subsequently, ten of the brightest, most isolated stars in each sub-field were used for an iterative extraction of a local PSF (similar to what was done in *Schödel et al.*, 2010). Because of variable extinction and source density, not all sub-fields contained PSF reference stars of similar brightness, which would lead to a systematic change of the zero point across the field. Also, not taking into account the extended seeing halo from the light that could not be corrected by the AO, can lead to an enhanced detection of spurious faint stars near bright stars. As remarked by *Schödel* (2010), the seeing halo is affected in a rather minor way by anisoplanatic effects. We therefore used the brightest star in the field, GCIRS 7, to estimate the seeing halo. The local PSFs were masked beyond radii of about $0.3''$, up to which they could be reliably determined. Then

they were matched to the seeing halo (using a least-squares fit to determine flux offsets and normalisation factors). Thus, we could create local PSFs that avoided large systematic photometric effects across the field. Some tests (similar to what was done in *Schödel*, 2010) showed that we could constrain the systematic photometric effects from the variability of the PSF to a few percent across the field.

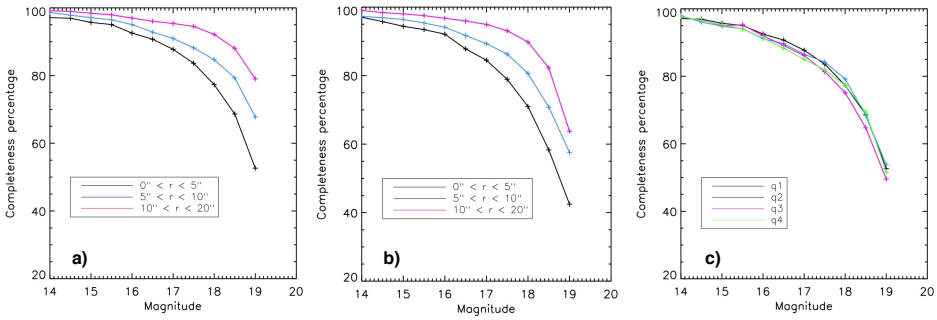

Figure 4.2: Completeness of the star counts in the deep NACO K_s images. a) Completeness in pointing 1 for different projected distance ranges from Sgr A*, for *min_correlation*= 0.80 and *deblend*= 0. b) As in a), but for *min_correlation*= 0.90 and *deblend*= 1. c) Completeness for all four pointings and within 5″ of Sgr A*, for *min_correlation*= 0.80 and *deblend*= 0. The corresponding plots for other used combinations of *min_correlation and deblend* look very similar.

In PSF fitting we have to walk a thin line between achieving an almost complete detection of sources while, at the same time, avoiding to pick up spurious ones, which can arise, in particular, close to bright stars or due to systematic effects from the detector electronics. We visually verified that taking the PSF seeing halos into account, along with the use of our SSA noise maps, effectively suppressed the detection of spurious sources near bright stars (see also *Schödel et al.*, 2013). The PSF halos include effects such as diffraction spikes and static speckles. Our empirical noise maps seemed to deal well with suppressing the detection of spurious sources near bright stars.

Finally, since there can be no absolute certainty in the reliability of source detection, we also repeatedly analysed the images with different values of the *StarFinder* parameters that dominate the probability of source detection (for a fixed detection threshold, which was chosen as 3σ in all cases). These parameters are *min_correlation* and *deblend*. For the minimum correlation value we chose $0.8-0.9$, always more conservative than the standard value of 0.7, the default value of *StarFinder*. The key word *deblend* can be set to deblend close sources. While deblending can be very useful, it can lead also to the detection of a significant number of spurious sources in a crowded field. We included measurements with and without setting this keyword. We used the following four combinations of *min_correlation* and *deblend*: $[0.80, 0]$, $[0.85, 0]$, $[0.85, 1]$, and $[0.90, 1]$ (step 2 in Fig. 4.1).

4.2.2 Photometric calibration and source selection

Finally, the photometry was calibrated with the stars IRS 16C, IRS 16NW, and IRS 33N (apparent magnitudes $K_s = 9.93, 10.14, 11.20$ and $H = 11.90$, $12.03, 13.24$, see *Schödel et al.*, 2010). The uncertainty of the zero points was a few percent. We note that for the purposes in this study we do not require any high accuracy/high precision photometry and astrometry.

Almost all stars in the field have intrinsic colours $-0.1 \leq H - K \leq 0.3$ (see, e.g., *Do et al.*, 2009; *Schödel et al.*, 2010). The mean colour due to reddening is $H - K \approx 2.1$. We excluded all stars with $H - K < 1.5$ as foreground stars. We also excluded spectroscopically identified young stars from our final star list (*Do et al.*, 2009; *Bartko et al.*, 2010). Subsequently, we created an extinction map, by using the 20 stars nearest to each point. The resulting map is similar, to within the uncertainties, to the one presented in *Schödel et al.* (2010).

4.2.3 Crowding and completeness

We determined the source detection completeness in the K_s-images through the technique of inserting and recovering artificial stars for each of the four pointings (the second step in Fig. 4.1) . We used a magnitude step of 0.5 mag and inserted the stars on a $0.5'' \times 0.5''$ grid. With this relatively wide spacing we avoided artificially increasing the crowding. The grid was shifted several times to finally probe completeness on a dense $0.1'' \times 0.1''$ grid (as done by *Schödel et al.*, 2007). We used the respective local PSFs (see above). Subsequently, PSF fitting was carried out with *StarFinder* and a source was considered as detected if it was found within a magnitude range of 0.5 mag of the input magnitude and within a distance of $0.054''$ of the input position (corresponding to 2 pixels of the S27 camera or roughly the angular resolution of the data). If a real star of a similar magnitude was already present within this distance to the grid point of an artificial star, then the artificial star was considered as detected. This latter point is critical to avoid bias because the relatively high density of artificially introduced stars would otherwise lead to non-detection of real sources and thus an over-estimation of incompleteness.

As mentioned above, to estimate the systematic errors induced by either the non-detection of real sources or the detection of spurious sources, we repeated the source detection and completeness determination for the following combinations of the *StarFinder* parameters: *min_correlation*= $0.80, 0.85, 0.85, 0.90$ and *deblend*= $0, 0, 1, 1$ (each value in the first list corresponds to the value with the same index in the second list). In Fig. 4.2, we show the values of completeness for two of these cases and for different projected distance ranges from Sgr A*. The differences between the different choices of parameters are generally small, on the order of a few percentage points, except for the faintest magnitudes, where the differences are somewhat more pronounced. Also, we can observe the expected general trend of less completeness for fainter magnitudes and in the more crowded

areas near Sgr A*. Finally, Fig. 4.2 also shows that the differences of completeness between the four pointings are small. For all cases, we found that source detection was, at all projected distances, at least 50% complete for magnitudes $K_s \leq 18.5$ (Step 2 in Fig. 4.1).

4.2.4 Extinction

We used the $H - K_s$ photometry and the intrinsic small colours of stars at these bands to create an extinction map for each of the four pointings (the second step in Fig. 4.1), with the same method as applied in *Schödel et al.* (2010). We do not consider stars with $H - K_s < 1.5$ because we consider them as foreground stars. Neither do we consider stars with $H - K_s > 3.0$ because they may either be background stars or intrinsically reddened objects (in any case, their number is very small, see Fig 4 in *Schödel et al.*, 2010). Median stellar colours were obtained from the individual colours of the 20 nearest stars at each position and the extinction was then calculated as in *Schödel et al.* (2010), assuming $A_{K_s} \propto \lambda^{-2.2}$.

On the one hand, the extinction map was used to correct the individual stellar magnitudes for differential extinction. On the other hand, we applied the methodology of *Chatzopoulos et al.* (2015b) to compute the stellar detection completeness variation caused by variable extinction: We modeled the luminosity function (LF) by taking the product of a power-law stellar LF and an error function that represents the completeness function, as in expression (2) in *Chatzopoulos et al.* (2015b). The approximation of the LF with a power-law – which ignores the presence of the RC bump – does not introduce any significant error because our data are sensitive enough to reach well below the RC bump over the entire field and because including the RC bump would only have a minor effect as shown by *Chatzopoulos et al.* (2015b). First, we measured the observed KLF for each pointing and each *StarFinder* parameter set (excluding a radius of about 5″ around Sgr A*, where the KLF is more incomplete because of crowding). We computed the power law for each case. Finally, we used these power-laws, combined it

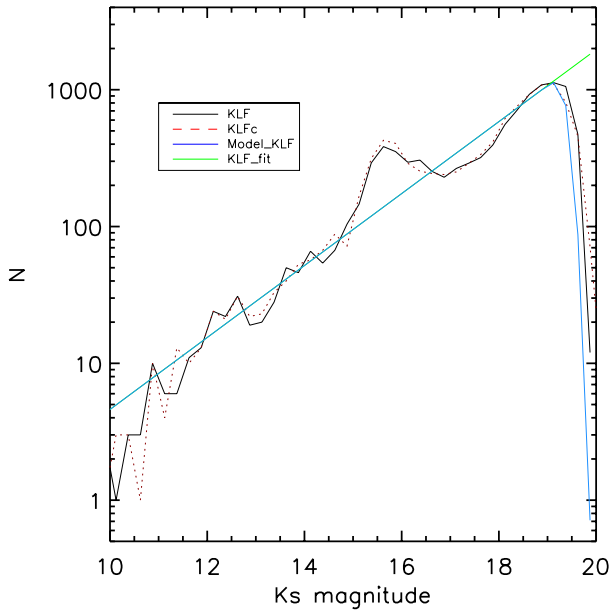

Figure 4.3: The Ks LF in pointing 1 for *min_correlation*= 0.8 and *deblend*= 0 if shown as a black line. The dotted red line is the K_s LF after correcting the magnitude of each star for differential extinction. The green lines shows a power law fit to the bright stars $11 < K_s < 14.5$ with power law index of 0.26 ± 0.02. The blue line shows the effect of the completeness function according to equation (2) in *Chatzopoulos et al.* (2015b).

with the measured local extinction and computed the corresponding local correction factors according to equation (5) in *Chatzopoulos et al.* (2015b), but using the approximation of a single extinction screen, i.e. no variability of A_{K_s} along the line-of-sight. Since we approximate the LF with a power law, the equation takes on the form $p = L(-\Delta A_k) = 10^{-\gamma * \Delta A_k}$ (see *Chatzopoulos et al.*, 2015b), where p is the reduction factor for the number of locally detected stars, ΔA_k is the difference between the local extinction and the mean extinction over the field, and γ is the power law index of the luminosity function. If the local extinction is lower than the mean extinction, then $p > 1$, and if the local extinction is higher than the mean extinction, then $p < 1$.

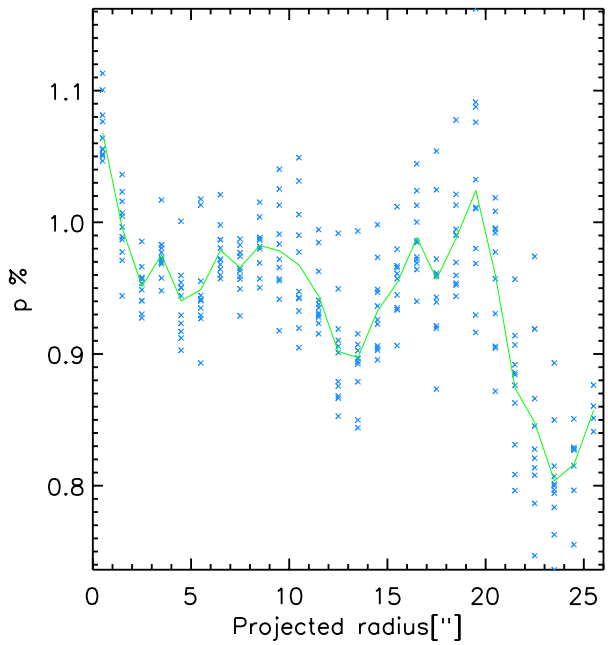

Figure 4.4: Relative detection frequency due to extinction versus projected distance to Sgr A*, in pointing 1 for *min_correlation*= 0.8 and *deblend*= 0. The blue crosses give the values of p for each magnitude bin. The green line represents the mean of the $p(\%)$ considering detected stars at the same distance from Sgr A*. We can observe that for close distances to Sgr A*$p(\%)$ is higher than for large distances, as we expected, because the extinction near Sg A* is lower.

We apply the correction factor $1/p$ to each detected star. In Fig. 4.3 we show the K_s LF for pointing 1 , for *min_correlation*= 0.8 and *deblend*= 0, along with the LF corrected for differential extinction, a power law fit to the stars $11 < K_s < 14.5$ ($\gamma = 0.26 \pm 0.02$, similar to the value obtained in *Schödel et al.* (2010)), and the completeness function (blue line), as defined by *Chatzopoulos et al.* (2015b). For the latter, we use $m_0 = 19.4$ and $\sigma = 0.2$ because these values approximate our K_s LF well. These values are different from those used in *Chatzopoulos et al.* (2015b) because our data are significantly deeper than theirs. In Fig. 4.4 the percentage reduction in observed stars versus projected radius is represented for the detected

stars in pointing 1,for *min_correlation*= 0.8 and *deblend*= 0. One can see that extinction is, on average, higher at larger distances from Sgr A*, but that the effect of differential extinction on completeness is relatively minor, typically $< 10\%$ and at most 20%.

4.2.5 Wide field

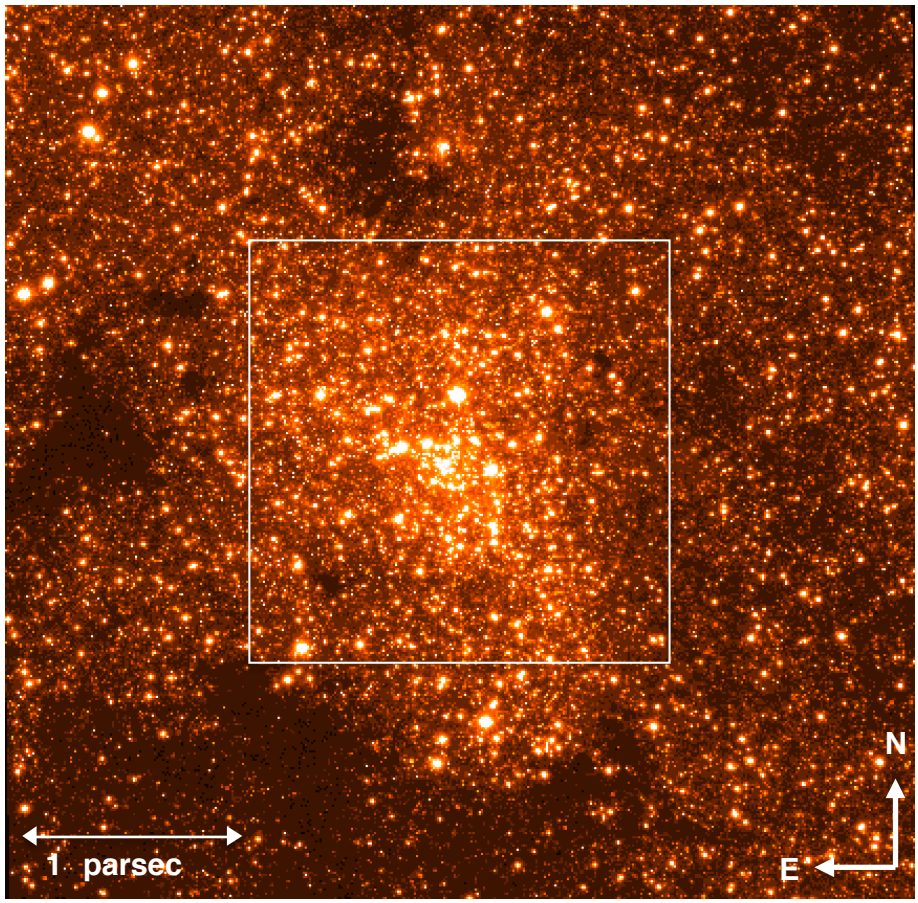

Figure 4.5: Wide-field mosaic the observations from 11th May 2011. The field-of-view is $1.5' \times 1.5'$. The field of about $40'' \times 40''$ that corresponds to the deep imaging data is marked by a white square.

The 2011 data are of excellent quality, but relatively shallow. On the

other hand, there are 16 pointings that cover a field of about $1.5' \times 1.5'$, compared to the smaller fields of about $40'' \times 40''$ covered by the other NACO observations. The 2011 observations are therefore ideally suited to extend the sensitive central observations with high angular resolution, albeit somewhat shallower, data out to larger distances. Fig. 4.5. Although the wide field data are shallow, in the sense of small total exposure time, they are used here at large projected radii, R. Since crowding, not integration time, is the main factor that limits source detection at the GC, the 50% completeness limit of the wide field data is still as low as $K_s \approx 18.5$ at $R > 0.5$ pc. They are therefore ideal to be combined with our deep data at smaller R.

In order to deal with the distortions of the NACO S27 camera (see, e.g., *Trippe et al.*, 2008; *Schödel et al.*, 2009) we aligned each pointing of the NACO mosaic with a reference frame created from positions measured in HST WFC3 observations of the same field (Dong et al., in prep.). We apply variable PSF fitting as we explain in section 2.4. In this case, *min_correlation*= 0.8 and *deblend*= 0 were selected for the *StarFinder* parameters.

4.2.6 Source subtraction

Subtraction of detected stars is a critical step when estimating the diffuse light. A particular challenge in AO observations is the presence of the large seeing halo (FWHM on the order $1''$) around the near-diffraction limited core of the PSFs. The dynamic range of the detected stars comprises >10 magnitudes, from the brightest star, GCIRS 7 with $K_S \approx 7$ to the faintest detectable stars with $Ks \approx 19$ (see last section). Many of the brightest stars ($K_S = 9 - 11$) are young, massive stars concentrated in the IRS 16, IRS 1, IRS 33, or IRS 13 complexes in the central 0.5 pc (e.g. *Genzel et al.*, 2003b; *Lu et al.*, 2005, 2009; *Paumard et al.*, 2006). They must be carefully subtracted to avoid a bias in the surface light density. In addition, the PSF changes across the field due to anisoplanatic effects, and the variable source

density and extinction mean that the faint wings of the PSFs cannot be estimated with similar signal-to-noise in all parts of the field because there is not a homogeneous density of bright, isolated stars.

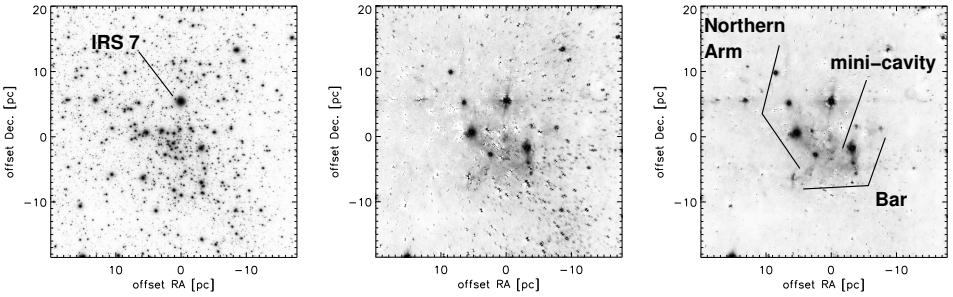

Figure 4.6: Source subtraction. Left: Deep K_S-band mosaic. Middle: Deep K_S-band mosaic with all detected stars subtracted, using a single, constant PSF, for the entire field. Right: Deep K_S-band mosaic with all detected stars subtracted, using a locally extracted PSF kernel merged with a constant halo, that is estimated from IRS 7. Typical features of the mini-spiral of gas are indicated. Logarithmic colour scale in all images, with the same scale used in the middle and right panels. North is up and east is to the left.

After the detection of the point sources (see Sec. 4.2.1), we proceeded to subtract them. Since the detection of occasional spurious sources is no source of concern for the analysis of diffuse light, we chose a more aggressive approach than for the star counts analysis, setting the *StarFinder* parameters $min\_correlation = 0.70$ and $deblend = 1$ for all images (except if stated explicitly otherwise). We note that even with these settings the detection completeness falls below 50% for sources fainter than about $K_S = 18.5$ in the centralmost arcseconds. We note that we only perform point-source fitting and subtraction, but do not model the diffuse background with *StarFinder*, that is, the keywords $BACK\_BOX$ and $ESTIMATE\_BG$ are set to zero.

In order to have an extinction map that covers even the large area of the wide field observations from May 2011, we created an extinction map from HAWK-I H and K_S speckle holography-reduced FASTPHOT observations of the central square arcminutes (*Nogueras-Lara et al.*, 2018a).

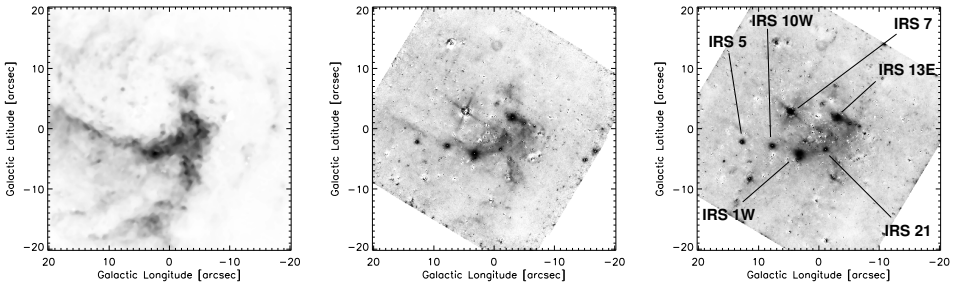

Figure 4.7: Left: HST NIC3 point-source-subtracted Pa α image of the GC. Middle: VLT NACO point-source-subtracted Br-γ image. Right: VLT NACO point-source-subtracted K_S image. Some prominent point-like emission sources (see text) are labelled.

We used the extinction law of *Schödel et al.* (2010) ($A_\lambda \propto \lambda^{-2.2}$), assumed a constant intrinsic colour of $(H - K_S)_0 = 0.1$ for all the stars, and used the mean of the 20 nearest stars for each pixel. This results in an extinction map with a variable angular resolution of roughly $2''$. The results presented in this work are not sensitive in any significant way on the variation in these assumptions within their uncertainties. In particular, changing the exponent of the extinction law to other plausible values (e.g. 2.0, see *Nishiyama et al.*, 2009) will have an impact on any of the parameters of interest that is a factor of a few smaller than other sources of uncertainties that will be discussed here.

We demonstrate the result of this strategy in Fig. 4.6. There, we show the mosaic of the deep K_S image, and the same field after subtraction with a single, constant PSF, and after subtraction with a variable PSF, composed of a local core plus a global halo. As can be seen, using a single, constant PSF leads to variable artefacts associated with the stellar sources across the field (see also *Schödel*, 2010). Also, when the wings of the PSF are not determined with high signal-to-noise, then the diffuse emission is dominated by flux from the seeing halos around bright stars.

With the variable core plus halo PSF (determined from the brightest star IRS 7, right panel), the residuals around bright stars are strongly suppressed

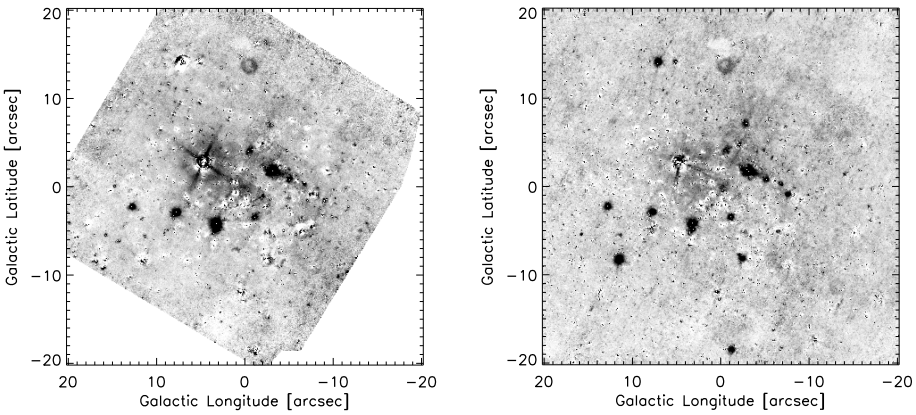

Figure 4.8: Left: Point-source-subtracted Br-γ image minus scaled Pa α image. Right: Point-source-subtracted K_S wide field image minus scaled Pa α image.

and any remaining residuals are largely constant across the field, as can be seen in the right panel of Fig. 4.6. These remaining residuals are typical for PSF subtraction with an empirical PSF when the PSF is not fully constant across the field: Since several stars have to be used to derive a median PSF, their slightly different PSFs will result in a slightly too broad median PSF. This leads to the typical and inevitable artefacts in the form of core-excesses with surrounding negativities that can be seen around bright stars. Nevertheless, as can be seen, the residuals around the bright stars have been strongly suppressed with our method. The only exception is GCIRS 7, which is extremely bright (a few magnitudes brighter than any other source in the field). The filamentary structure of the so-called mini-spiral (see *Genzel et al.*, 2010, and references therein) becomes apparent, with features such as the northern arm, the bar, or the mini-cavity clearly visible. We provide further detailed tests of our methodology in Appendix D.

4.2.7 Subtraction of mini-spiral emission

As we can see in the right panels of Figs. 4.6 and 4.7, diffuse emission from the so-called mini-spiral (see., e.g. *Genzel et al.*, 2010) contributes significantly to the diffuse emission within about 0.5 pc ($\sim$12″ for a GC distance of 8 kpc) of Sgr A*, even in broad band images. We therefore have to correct for it before we will be able to estimate the diffuse emission arising from unresolved *stellar* sources. At the wavelengths considered, the emission can arise from hydrogen and helium lines (e.g. HI at 2.17, 1.64 or 1.74 μm, HeI at 1.70, 2.06, or 2.11 μm), but some contribution from hot and warm dust is also plausible. In Fig. 4.7 we show the mini-spiral as seen in the Paschen α line with NIC3/HST and in the Brackettγ line as well as in K_S with NACO/VLT, respectively. The Pa α image is from the survey by *Wang et al.* (2010) and *Dong et al.* (2011).

Since we will use the HST image as a reference for gas emission, we aligned all our images via a first order polynomial transform with the HST image. The positions of detected stars were used to calculate the transformation parameters with IDL POLYWARP and the images were then aligned using IDL POLY_2D. The pixel scale of the resulting images is set to the one of the HST image (0.101″ per pixel).

As can be seen in Fig 4.7, the Pa α image traces the gas emission very clearly (with the exception of a few Pa α excess sources, see *Dong et al.*, 2012) and the K_S and Br γ images of the diffuse emission trace the same structures of the mini-spiral. Some differences are given by residuals around bright stars, by some residual emission associated with the brightest star, GCIRS 7, by hot dust emission around the probable bow-shock sources IRS 21, IRS 10W, IRS 5, and IRS 1W, and by enhanced emission in and around the IRS 13E complex, probably from a higher gas temperature. We mark some of these sources and areas in Fig. 4.7 and will mask them when deriving scaling factors for gas subtraction and when computing the brightness of diffuse stellar light in the following sections.

Figure 4.8 shows the point source-subtracted Br γ and K_S images after subtraction of the scaled Pa α image. The scale factor was assumed constant and estimated by eye. All images were corrected for differential extinction. We also determined the scaling factor in a numerical way fitting the azimuthally averaged surface brightness distribution with a least χ^2 fit with a linear combination of the scaled azimuthally averaged surface brightness distribution of the Pa α emission plus a simple power-law diffuse light density distribution centred on Sgr A*.

$$\Sigma(R) = \Sigma_0 * (R/R_0)^{-\Gamma} + \beta Pa\,\alpha, \tag{4.2}$$

where Σ_0 is the surface flux density at a the projected distance $R_0 = 0.5$ pc, Γ is the power-law index, Pa α is the Paschen α SB, and β the scaling factor for the latter. There are three free parameters, Σ_0, Γ, and β . We limited the estimation of β to the region $R \leq 0.5$ pc, where the gas emission is strongest. Varying this value up to $R = 1.5$ pc does not have any significant effects on the SB profiles, but some negativities can then appear after minispiral subtraction in the images because the fit is dominated by regions at large R with low gas SB, where the excitation conditions of the gas may also be different (greater distance from the hot stars near Sgr A*). The resulting best-fit factor was close to our by-eye estimate.

We considered fitting the azimuthally averaged surface brightnesses as marginally more reliable than directly fitting the images because the azimuthal average will suppress noise from the data acquisition and reduction process, from the point-source subtraction, and from potential variations of the gas temperature. Nevertheless, we also tested direct fitting of the models to the images and obtained the same results within the formal uncertainties of the fits. As can be seen in Fig. 4.8, most of the emission from the gas and dust in the mini-spiral can be effectively removed by this simple procedure. From our by-eye fit we estimated an uncertainty of 10% for the best scale factor, while its uncertainty from the least χ^2 fits is $< 5\%$. This uncertainty has a negligible effect on the parameters we are interested in,

in particular the slope of the power-law surface density. For all images and wavelengths used in the following we applied the numerical procedure to estimate the scaling factor for the subtraction of the diffuse gas emission.

An alternative way of subtracting the mini-spiral emission may be by using the intrinsic line ratio of $Br\,\gamma/Pa\,\alpha$. However, this is not practical in our case because most of our data are broad-band observations and include additional lines, for example from the 2.058 μm He I line in the K_S-band. Also, in the case of the $Br\,\gamma$ image, no accurate calibration was possible because no zero point observations were taken at the time of the observation and the sky conditions were not photometric.

Finally, NIR emission from the mini-spiral may also arise, at least partially, from hot dust, in particular near young, massive stars, such as the IRS 13 region or the putative bow-shock sources IRS 21, IRS 1W, etc. (see, e.g. *Eckart et al.*, 2004; *Fritz et al.*, 2010; *Sanchez-Bermudez et al.*, 2014). This is plausible because the morphology of the emission from warm/hot dust in the mini-spiral region resembles closely the one observed in line emission (compare, e.g. the images of the mini-spiral seen through different filters in *Mužić et al.*, 2007; *Wang et al.*, 2010; *Genzel et al.*, 2010; *Lau et al.*, 2013). We did some experiments in this respect, with point-source subtracted 8.6 μm and 3.8 μm imaging data (*Schödel et al.*, 2011) and found dust temperatures on the order of 250-350 K. This is hotter than in the SOFIA observations analysed by *Lau et al.* (2013) and is probably related to us using data of considerably higher angular resolution and considerably shorter wavelengths or to the fact that the 8.6 μm image may be dominated by emission from PAHs.

When we correct the measured diffuse SB profile in K_s with our dust emission map, we get roughly similar results than with the HST Pa α image. However, the quality of the correction is considerably worse because (a) the HST data provide much cleaner measurements of the diffuse gas emission, (b) the FOV of our 8.6 μm and 3.8 μm imaging data is smaller than the one of the HST images, (c) point sources must first be subtracted from the

NIR/MIR images, which introduces additional systematic errors, and (d) further systematics are introduced by the very challenging determination of the variable sky background in the MIR observations (it is impossible to chop into an emission-free region inside the GC). The fundamental assumption in our work is that the non-stellar diffuse emission can be obtained from the HST Paschen α image through applying a constant scaling factor. As long as this assumption is approximately valid, it does not really matter whether we are dealing with line emission and/or dust emission. A study of variable line-emission and variable gas or dust temperature in the mini-spiral is beyond the scope of this work. As we show below, our method to remove the non-stellar diffuse emission appears to work very well and provides consistent results across many filters. We therefore believe our method to be solid.

4.3 K_s-luminosity function

The goal of this study is to investigate the existence of a stellar cusp at the GC. This requires us to select stars old enough to have undergone dynamical relaxation. The relaxation time at the GC is roughly a few Gyr (e.g., *Alexander*, 2005, 2011). We specifically exclude all spectroscopically identified early-type, i.e. young and massive, stars from our sample (using the data of *Do et al.*, 2013). Unfortunately, spectroscopic stellar classification is limited to stars of about $K_s \leq 15.5$ at the GC. For fainter stars, we can only use their luminosity as a proxy for their type. Figure 16 of *Schödel et al.* (2007) illustrates the LF, mean masses, and old star fractions for stars of different magnitudes at the GC, assuming continuous star formation at a constant rate over the last 10 Gyr. It shows that we can probe old ($\gtrsim 1$ Gyr), low-mass stars in the range $15 \lesssim K_s \leq 16$. This is the RC, which dominates all previous star density measurements. The fraction of old stars rises again above ∼50% for stars $K_s > 17.5$, reaching practically 100% at $K_s \approx 18$.

Therefore, in this study, we focus on the magnitude ranges $15 \leq K_s \leq 16$, the RC, and $17.5 \leq K_s \leq 18.5$, i.e. the faintest stars accessible by our data.

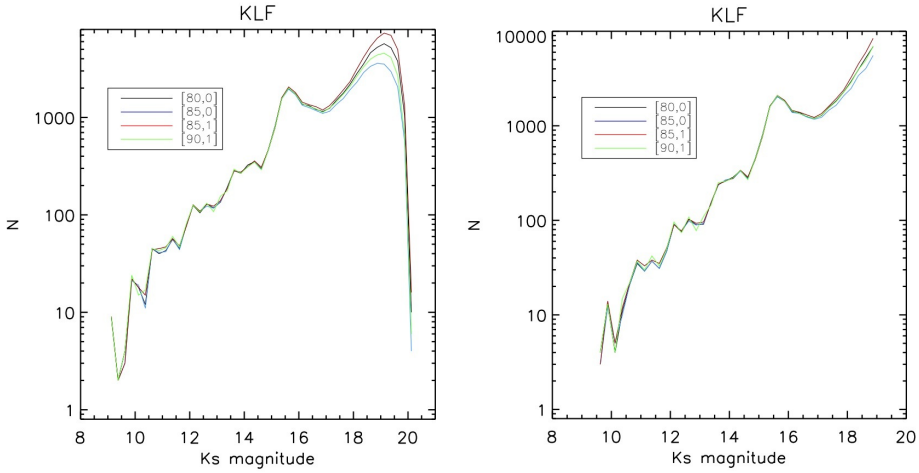

Figure 4.9: KLF for the deep K_s mosaic. The different colours correspond to the different combinations of the values of *min_correlation* and *deblend*, as listed in the legend (see also section 4.2.1). Left: Raw KLF. Right: Completeness- and extinction-corrected KLF.

We show the K_s luminosity function (KLF) determined from our deep mosaic in Fig. 4.9. The KLFs corresponding to the four different *StarFinder* parameter settings are shown. The KLF derived in this work is about one magnitude deeper compared to previous work (Fig. 10 in *Schödel et al.*, 2007). This is a decisive advantage. When we want to probe the existence of a dynamically relaxed stellar cusp around Sgr A*, we need to focus on stars that are at least several Gyr old. As shown in the illustrative Figure 16 in *Schödel et al.* (2007), the only magnitude range where this was previously possible was around the RC ($15.25 \leq K_s \leq 16.25$). Now, with the deeper data from our new analysis, we can probe another, fainter magnitude range with a high fraction of old stars ($17.5 \leq K_s \leq 18.5$). Also, the stars in these two brightness ranges have similar masses, which lets us expect a similar surface density distribution. We discuss in sections 5.2 and 5.3 the different populations that we can expect in the faintest range of stars, based on

the latest determined star formation history for the GC, and the possible contamination of our star counts by stars too young to be dynamically relaxed.

4.4 The distribution of stars around the Milky Way's central black hole

In order to analyse the surface density of stars at the Galactic Center, we assume that the underlying spatial distribution of the stars in the central parsec is spherically symmetric. Although the nuclear cluster is flattened, a spherical approximation should be acceptable at projected radii $R \lesssim 2\,\mathrm{pc}$ because the difference between the density profiles along the orthogonal directions of maximum difference is only on the order of $10\% - 20\%$ in this region (see *Schödel et al.*, 2014a; *Fritz et al.*, 2016). Therefore, we computed the azimuthally averaged stellar surface densities in annuli around Sgr A*.

4.4.1 The 2D density of old stars in the GC

Firstly, we analyse the central parsec (deep field). In order to choose a number of bins sufficiently large to capture the major features in the data while ignoring fine details due to random fluctuations, we followed the studies of *Knuth* (2006) and *Witzel et al.* (2012). We first determine the best bin size. The dependence of the Relative Logarithmic Posterior Probability (RLP) on the bin number for pointing 1 is shown in Fig. A.2. The maximum for the RLP for the star number is reached for 21 bins, and the best bin size is $1''$. We applied this methodology for all pointings, with similar results.

We computed extinction and completeness-corrected stellar surface densities for the stars detected in the different *StarFinder* runs and for the different pointings (the second step in Fig. 4.1). At this point we included the uncertainties of the different correction factors into the uncertainties of the stellar surface densities. For faint stellar magnitudes, we masked the regions with completeness below 30%. We tested the effect of different masks,

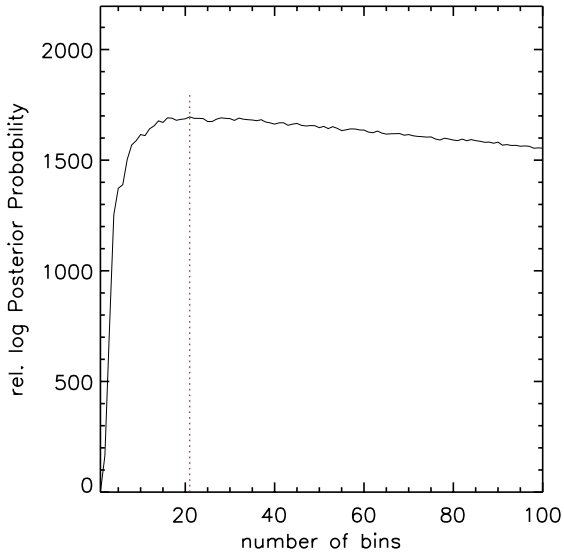

Figure 4.10: Optimal binning. We show the RLP as a function of the number of bins. The maximum for the RLP is reached for 21 bins (red dotted line).

with *completeness*$< 30\%, 40\%, 50\%$ respectively, and found that the results did not vary significantly. Finally, we obtained the surface density profiles for each set of *Starfinder* parameters by combining the measurements on the four pointings in a weighted mean (the third step in Fig. 4.1). Finally, we combined the surface density profiles obtained with the four settings of the *StarFinder* parameters. Mean densities and standard deviations were computed and all uncertainties were quadratically combined (the last step in Fig. 4.1).

Secondly, in order to study the stellar number density in a broader range of distances from Sgr A*, we analysed the large mosaic image from the 2011 data. We did not apply any extinction and completeness corrections because the effect of the extinction correction is small and crowding does not pose any serious problem at $R > 20''$ and with the high angular resolution data used here. We did, however mask all the regions occupied by the dark clouds that can be seen show in Fig. 4.5. Finally, we combined the data from the

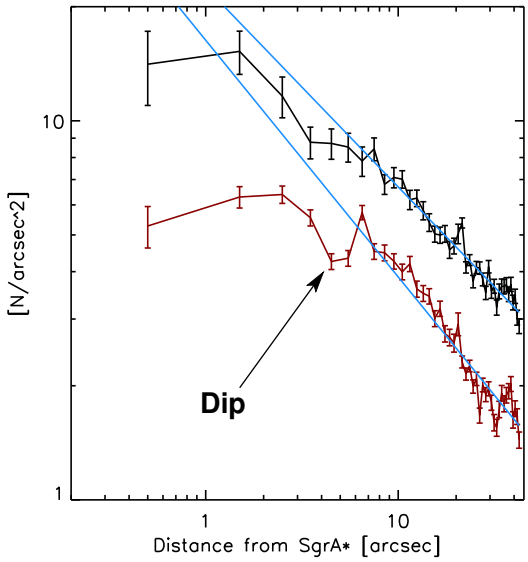

Figure 4.11: Combined deep field plus wide field surface density plots for stars in the magnitude intervals $12.5 \leq K_s \leq 16$ and $17.5 \leq K_s \leq 18.5$. The blue lines are simple power-law fits to the data at $0.2\,\mathrm{pc} \leq R \leq 1.0\,\mathrm{pc}$.

deep field and the wide field. The surface densities from the wide field data were scaled to the completeness and extinction corrected ones from the deep images in the overlap region from $R = 10'' - 20''$.

Figure 4.11 shows the combined number density plots for stars in the magnitude range $12.5 \leq K_s \leq 16.0$ and $17.5 \leq K_s \leq 18.5$ stars (right), along with simple power-law fits[1]. The brighter magnitude interval was chosen to trace bright, old giant stars, based on current estimates of the star formation history in the central parsec (see section 4.5). The faint magnitude interval corresponds to the faintest stars that we detect with completeness higher than 50% across the field (see sec. 4.2.3).

The projected surface density of the old stars can be described by simple power laws of the form $\Sigma(R) \propto R^{-\Gamma}$ were fit to the surface number densities, where Σ is the surface number density, R the projected radius, and Γ the

[1]Tables with the stellar surface density data have been made available at the CDS.

Table 4.1: Values of the power-law index, Γ, for the extinction and completeness-corrected surface density profiles.

ID	Fit range (pc)	Magnitudes range (K_s)	Γ	$\chi^2_{reduced}$
1	0.04-0.5	17.5-18.5	0.36± 0.04	0.8
2	0.04-0.5	12.5-16.0	0.24± 0.02	4.9
3	0.2-1.0	17.5-18.5	0.53± 0.03	2.6
4	0.2-1.0	12.5-16.0	0.62± 0.02	5.1
5	0.04-1.0	17.5-18.5	0.47± 0.02	2.8
6	0.04-1.0	12.5-16.0	0.45± 0.01	9.2
7	0.5-1.5	17.5-18.5	0.50± 0.03	3.2
8	0.5-1.5	12.5-16.0	0.73± 0.03	4.1
9	0.5-2.0	17.5-18.5	0.50± 0.03	3.1
10	0.5-2.0	12.5-16.0	0.66± 0.03	4.6

power-law index. We fitted the power laws to the data in different distance ranges. The corresponding power law indices and the χ^2 values of the fits are listed in Tab. 4.1 and the data and one of the fits are shown in Fig. 4.11. All formal uncertainties from the fits were rescaled to a reduced $\chi^2 = 1$ here and in the rest of the chapter. We observe that: (1) a simple power-law provides a better fit to the faint stars ($K_s \approx 18$) than to the bright giants. (2) The value of Γ depends on the range in R used for the fitting, with a tendency for a steeper power-law at greater distances. (3) The data point at $R < 1''$ lies below the fit in all cases. This region is the most crowded region with a possibly altered stellar population (the S-stars) and we omitted it therefore from our fits. (4) The giant stars show a flat, or even decreasing surface density at $R \lesssim 8''$, in agreement with what has been found before (*Buchholz et al.*, 2009; *Do et al.*, 2009; *Bartko et al.*, 2010). They also display a significant dip around $R = 0.2\,\mathrm{pc}$ ($5''$) in the density profile and, possibly, an excess at $R \approx 7''$, that are also visible in the works of *Schödel et al.* (2007) and *Buchholz et al.* (2009).

The projected surface number density of the stars in the interval $17.5 \leq$

$K_s \leq 18.5$ can be described well by a single power-law. Its mean value and standard deviation, taking into account the different fitting radii in Tab. 4.1 is $\Gamma_{faint} = 0.47 \pm 0.07$ The giants present a somewhat different picture: A single power-law provides only a good fit to the data at $R \gtrsim 8''/0.24\,\mathrm{pc}$. To take this into account, we exclude fit ID 2 from Tab. 4.1 and obtain a mean value of $\Gamma = 0.62 \pm 0.12$.

Finally, we studied the influence of the correction factors to compensate the effects of variable stellar crowding and interstellar extinction in our results. Fig. 4.12 shows the measured surface density profile for stars of magnitude $17.5 \leq K_s \leq 18.5$ detected in the deep mosaic without any correction, after applying the completeness correction for crowding, and after applying the completeness corrections for crowding and extinction. As we can see, the completeness correction steepens the profile somewhat. The extinction correction only introduces minor changes because the azimuthal averaging compensates most of the effects of differential extinction across the field. Fitting a simple power-law to the uncorrected data in the range $0.04\,\mathrm{pc} \leq R \leq 1\,\mathrm{pc}$, we obtain $\Gamma = 0.33 \pm 0.03$ (for the fully corrected data we obtain $\Gamma = 0.47 \pm 0.02$, see Table 4.1). The effect of crowding correction is almost negligible for the giants brighter than $K_s \approx 16$. We note that the uncertainties of the crowding and extinction corrections are included in all error bars and will therefore be reflected in the formal uncertainties of the best-fit parameters.

For the wide field data we did not apply any extinction and completeness corrections because we lacked the necessary complementary wide-field $H-$band imaging data. In any case, the effect of the extinction correction on the number density is small and crowding does not pose any serious problem beyond $20''$. Hence, the wide field data are scaled to the deep data in the overlap region. We mask the regions occupied by the dark clouds in the wide field image (see Fig. 4.5) to compute the surface density profile. In summary, the applied correction factors, albeit necessary, do not significantly alter our results. This shows that our data are robust. We

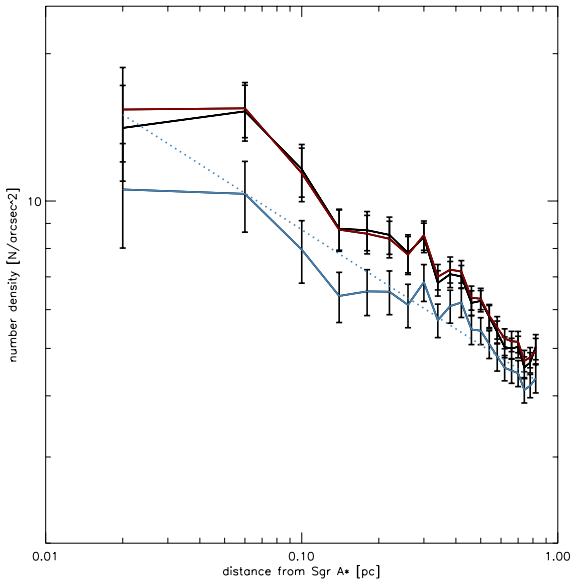

Figure 4.12: Mean surface density profile for stars with ($17.5 \leq K_s \leq 18.5$), after averaging over the four runs with different *Starfinder* parameters. Blue: Uncorrected data. Red: Data corrected for crowding. Black: Data corrected for crowding and extinction.

note, however, that the wide field image in Fig. 4.5 appears to show that extinction is higher at larger R, in particular to the west of Sgr A*. Since we do not correct the magnitudes of the stars detected in the wide image for extinction, this may result in giants dropping out of the brightness bin considered here. This may explain why the projected surface density of the giants appears to show a slightly steeper decrease at large R than the surface density of faint stars (Fig. 4.11).

4.4.2 The surface density of faint stars in the GC

In this section we explore the surface brightness (SB) profile of the diffuse stellar light in observations taken with different cameras and filters, as well as at different epochs. We will also perform various checks on potential sources of systematic bias.

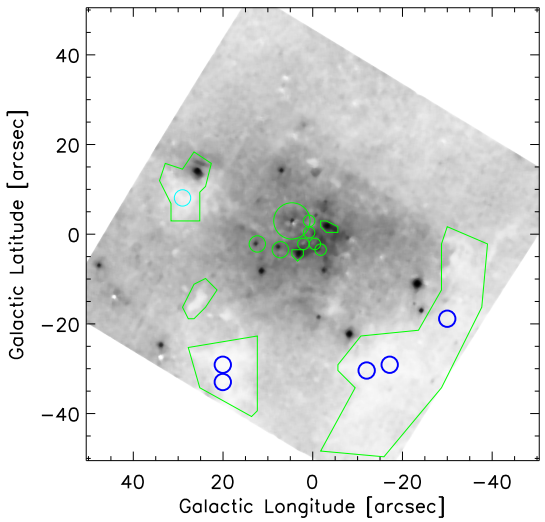

Figure 4.13: Point-source-subtracted K_S wide field image. Contaminated regions (residuals from bright stars, hot dust, and IRS 13) and dark clouds, that are excluded from measuring the surface light density, are indicated by green polygons. The blue circles indicate regions that were used to estimate the offset of the diffuse flux density.

First, we examine a wide-field mosaic that was obtained with NACO/VLT S27 in May 2011. In total, 4×4 pointings were observed in K_S, centred approximately on Sgr A*. The simages are relatively shallow, with a total on-target exposure time of only 72 s per pointing (4 exposures with $DIT = 2s$, $NDIT = 9$), but of excellent and homogeneous quality.

Figure 4.13 shows the point-source subtracted wide-field image. As mentioned above, we assumed that the diffuse light from the stars follows a power law and that a constant scaling factor is adequate to remove the emission from the mini-spiral. That is, our model is described by Equation 4.2. We measured the mean diffuse emission in one pixel wide annuli around Sgr A*, using the IDL ASTROLIB routine ROBUST_MEAN, rejecting $> 5\,\sigma$ outliers. The corresponding uncertainties were taken as the

uncertainties of the means. The same was done for the Paschen α image. Subsequently, we used a least χ^2 fit to determine the best parameters to scale the gas emission and determine the power law emission for the stars.

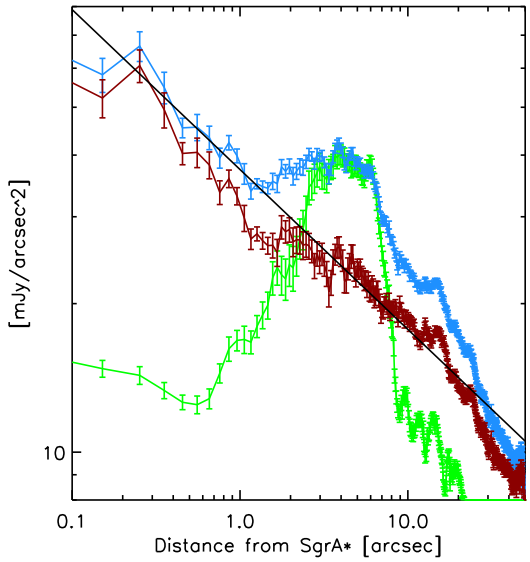

Figure 4.14: Left: Mean diffuse SB profiles in the K_S wide-field image before (blue) and after (red) subtraction of the appropriately scaled Pa α emission (green; multiplied by arbitrary factor to optimise the plot). The straight black line is the best power-law fit to the red data within $R \leq 25''$ pc (corresponding to $R \lesssim 1$ pc for a GC distance of 8 kpc).

Figure 4.14 shows the measured surface brightness (SB) profile for the wide-field Ks-image, for the Paschen α emission, and the wide-field SB profile after a scaled subtraction of the latter. The continuous black line is the best-fit power law to the data at $R \leq 1.0$ pc. It has a reduced $\chi^2 = 14.3$, $\Sigma_0 = 16.4 \pm 0.1$ mJy arcsec^{-2}, and $\Gamma = 0.32 \pm 0.01$. The relatively high χ^2 is mainly due to systematic deviations of the profile from a power-law at certain restricted ranges of R. We found that these deviations are mainly related to the difficulties of precise subtraction of bright stars at small R. These systematics are slightly different for each data set that we present in

this work (see, e.g. Fig 4.15), but do not significantly affect the overall result. The formal uncertainties resulting from the fit code have been rescaled to a reduced $\chi^2 = 1$ here and for all other fits reported in this work. In appendix D.1 we study several potential sources of systematic errors, such as sky offset, binning, fitting range, or application of the extinction correction. The sky offset, a probable systematic effect from inaccurate sky background subtraction and diffuse foreground (i.e. nor originating within the GC), was estimated on small regions of dark clouds (see Fig. 4.13) and subtracted prior to measuring the SB on the wide field image.

Secondly, we analysed the surface brightness in the Br γ narrow band filter image that is an interesting test case because here the emission from the ionised gas will provide a relatively large fraction of the overall diffuse emission. The resulting raw and ionised-gas-corrected SB profiles are shown in panel (a) of Fig. 4.15. A simple power-law provides a very good fit, with the best-fit power-law exponent of $\Gamma_{in} = 0.23 \pm 0.01$.

We analysed the deep K_S broad band image that we use for measuring the stellar number surface density. The SB profiles are shown in panel (b) of Fig. 4.15. A simple power-law provides a very good fit, with the best-fit power-law exponent of $\Gamma_{in} = 0.25 \pm 0.01$.

In order to test the diffuse flux in a regime where differential extinction is stronger, where the sky background behaves in a different way, and where the ratio of line emission relative to Pa α is different, we analysed H band image. Moreover, due to increased anisoplanatic effects, point-source-subtraction removal is more difficult in H than in K_s. Hence, the H-band can be very helpful in constraining systematic effects. We had to correct the H-band image for a systematic negative offset of the sky background, which could be measured on some small dark clouds in the field. The SB profiles are shown in panel (c) of Fig. 4.15. A simple power-law provides a good fit, with the best-fit power-law exponent of $\Gamma_{in} = 0.29 \pm 0.01$.

We also examine the diffuse light density in a deep, multi-epoch K_S-band image obtained with data from the S13 camera of NACO/VLT. A

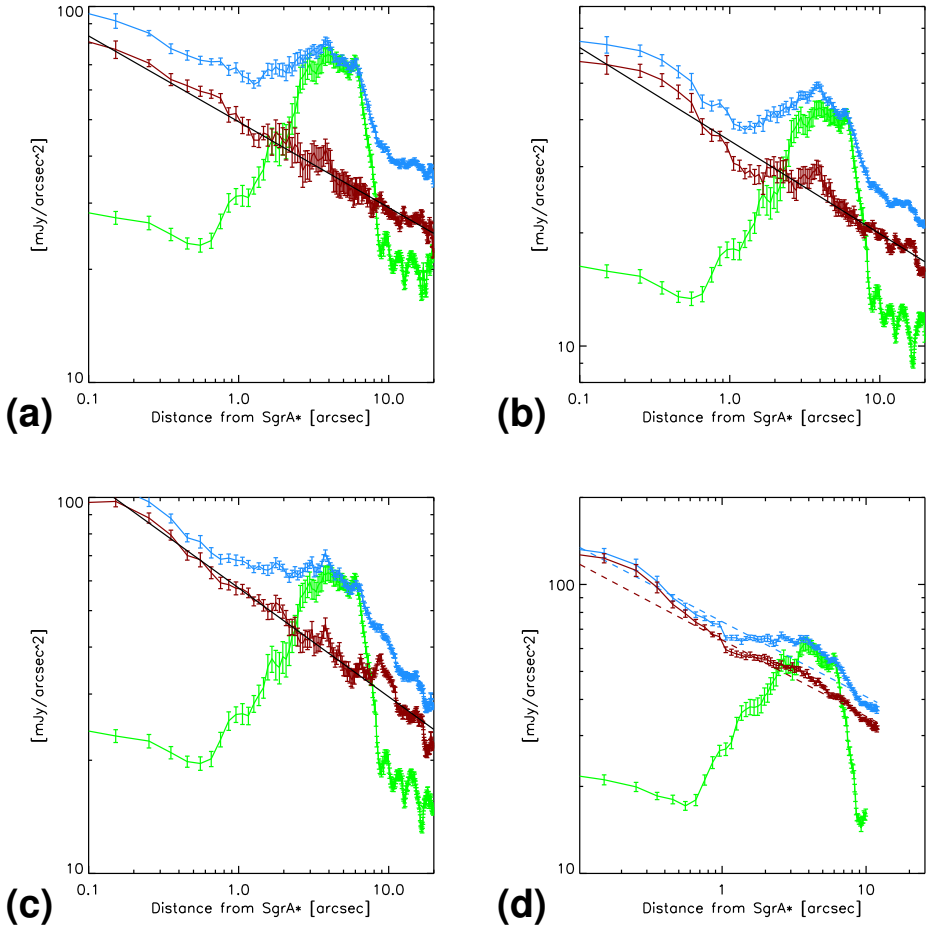

Figure 4.15: **(a)** Plot of the $Br\gamma$ diffuse SB profile before (blue) and after (red) subtraction of the appropriately scaled Pa α emission (green; multiplied by arbitrary factor to optimise the plot). The black line is for the best-fit power-law in the range $R \leq 25''$ pc (corresponding to $R \lesssim 1$ pc for a GC distance of 8 kpc). **(b)** As (a), but for the deep K_s image. **(c)** As (a), but for the H image. **(d)** As (a), but for the K_s S13 image.

simple power-law provides a good fit, with the best-fit power-law exponent of $\Gamma_{in} = 0.26 \pm 0.01$. We tested again the systematics of subtracting the stars down to different limiting magnitudes ($K_{s,lim} = 16, 18, 20$). The power-law index changes between 0.25 ± 0.01 and 0.29 ± 0.01 and the plot looks similar

Table 4.2: Best-fit power law indices for the diffuse stellar light inside of $R < 0.5\,\mathrm{pc}$. All *formal* uncertainties are ≤ 0.01 after having been rescaled to a reduced $\chi^2 = 1$, i.e. we are dominated by systematics.

Data	Γ_{in}
K_S, wide field	0.32
Br γ	0.23
K_S deep field	0.25
H	0.29
K_S S13	0.26
IB227	0.19

in all cases (not shown). Compared to the NACO S27 K_s data there appears to be an offset of the SB towards brighter values. We could not identify the source of this offset, but we note that it does not affect our main conclusions, in particular the existence of a power-law cusp and its index.

Finally, we used the IB227 image from *Buchholz et al.* (2009). A simple power-law provides a good fit, with the best-fit power-law exponent of $\Gamma_{in} = 0.19 \pm 0.01$. We do not show the corresponding fit in Fig. 4.15 to not overcrowd the plot. It is very similar to all the other plots.

As we see in the last section, we fitted a simple model of a single power-law at $R \lesssim 1\,\mathrm{pc}$ to the projected stellar surface for all our different measurements. In order to look into potential systematics errors that affect to the computation of the diffuse stellar light, we used several completely independent data sets obtained at different times and with significantly different setups (deep and shallow images, broad and narrow band observations, shorter and longer wavelength filters). The subtraction of the flux of both the bright stars and the gas and dust is prone to systematic errors, but they will change with the observing conditions, for example seeing and adaptive optics correction, camera used, or observing wavelength. Table 4.2 lists the resulting best-fit power-law indices for the projected diffuse light in the inner 1.0 pc. The corresponding power-law indices are consistent with

each other. From these measurements to independent data sets we obtain a mean estimate of $\Gamma = 0.26 \pm 0.02_{stat} \pm 0.05_{sys}$. This value is smaller than, but agrees within its uncertainties, with what we observe for the number density of the stars in the range $17.5 \lesssim K_S \lesssim 18.5$. We conclude that the projected surface density distribution of stars around Sgr A* can be described well by a single power law with the same exponent for different stellar populations. Also, we do not find it necessary to use any broken power-law for the SB profile at projected radii $R \leq 1\,\mathrm{pc}$, as it was used by previous authors (e.g. *Genzel et al.*, 2003b; *Schödel et al.*, 2007; *Do et al.*, 2009). As studied and explained in detail in appendix D.1, the systematic error is dominated by effects of potential additive sky offsets and fitting range. The atmospheric contribution of the former is, however, variable in nature between sets of different observations and is therefore absorbed into the statistical error from the mean of the different values for Γ observed. The latter is mainly caused by a systematic steepening of the slope with increasing R and contributes an estimated 0.05 to the uncertainty budget of Γ. As concerns the contribution of a potential source of diffuse emission from a stellar foreground population, for example in the nuclear disc, we do not take it into account here. We note, however, that its contribution would always be an additive offset. If taken into account, this would systematically steepen the observed Γ.

4.5 Age of tracer populations

In order to study the existence of a relaxed cusp, we need to focus on stars that are at least several Gyr old, similar to the relaxation time of the NSC at the GC (*Alexander*, 2005). To obtain a better understanding of which kind of stars contribute dominantly to our different samples, we study the KLF. First, we use the star formation history for the central parsec derived by *Pfuhl et al.* (2011) to construct a theoretical KLF. We used their Eq. (3) to compute the masses of nine single age stellar populations. The ages were

taken to be the middle of the intervals $10-13\,\mathrm{Gyr}$, $8-10\,\mathrm{Gyr}$, $3-8\,\mathrm{Gyr}$, $1-3\,\mathrm{Gyr}$, $0.5-1\,\mathrm{Gyr}$, $200-500\,\mathrm{Myr}$, $50-200\,\mathrm{Myr}$, $10-50\,\mathrm{Myr}$, and $0-5\,\mathrm{Myr}$. We emphasise the illustrative nature of our model, which is not constructed to provide a precise fit to our data.

The model KLFs were calculated assuming Solar metallicities and Chabrier lognormal initial mass functions. [1]

The resulting total KLF and the individual contributions of the populations of different ages (where we summed over four broad age ranges) can be seen in the upper panels of Fig. 4.16. The lower left panel compares the smoothed (to take into account differential extinction and measurement uncertainties) model KLF to the completeness corrected KLF (see Sec. 4.3). The agreement is satisfactory. The peaks around $K_S \approx 15.5$ arise from Red Clump (RC) stars. We point out that we have not made any specific effort to match the model KLF to the measured one, except for applying a scaling factor. Studies of star formation history or metallicity are beyond the scope of this work.

4.5.1 Stars with $K_s = 18$

The faintest stars in our sample are consistent with being (sub-)giants on the ascending branch or MS stars of $\sim 2.5\,\mathrm{M}_\odot$. They could also be pre-MS stars of a few solar masses or less (*Lu et al.*, 2013). From what is known about the star formation history of the NSC we may expect that the majority of stars is old ($\sim$80% of the NSC's mass were formed $> 5\,\mathrm{Gyr}$ ago, according to *Blum et al.*, 2003; *Pfuhl et al.*, 2011) and that most of the faint stars in our sample are thus old, (sub-)giants.

However, there are two important caveats:

1. We know that a star formation event created on the order $10^4\,\mathrm{M}_\odot$ of young stars in the region about $0.5\,\mathrm{pc}$ around Sgr A* (*Bartko et al.*,

[1] See *http://stev.oapd.inaf.it/cgi-bin/cmd_2.8* and *Chabrier* (2001); *Bressan et al.* (2012); *Chen et al.* (2014, 2015); *Tang et al.* (2014).

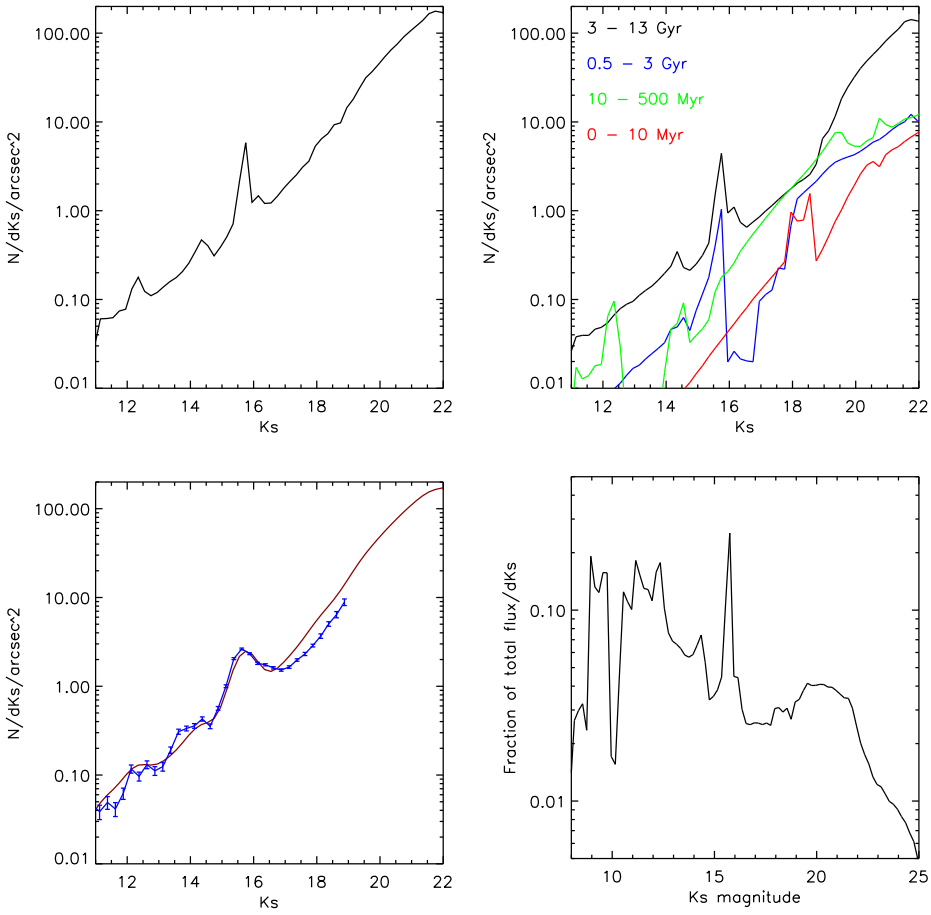

Figure 4.16: Estimates of the KLF within $R \leq 1\,\mathrm{pc}$ of Sgr A*. Upper left: Model K_S luminosity function (KLF) based on the star formation history derived by *Pfuhl et al.* (2011). Upper right: KLFs for stellar populations in certain time windows, using the star formation model by *Pfuhl et al.* (2011). Lower left: The red line is the model KLF smoothed with a Gaussian kernel to roughly take differential extinction into account. Lower right: Fraction of total flux contributed by stars of different magnitudes, i.e. the KLF multiplied by the flux density of stars in a given bin and divided by the total flux. Please note the different range of the x-axis in this plot, which is chosen to show the decrease of the flux contribution at $K_s > 22$.

2010; *Lu et al.*, 2013; *Feldmeier-Krause et al.*, 2015). Therefore contamination by pre-MS stars is possible.

2. There is evidence that the star formation rate in the central parsec was high about 100 Myr ago (e.g., *Blum et al.*, 2003; *Nishiyama et al.*, 2016; *Pfuhl et al.*, 2011).

As we can see in Fig. 4.16, contrary to what we assumed in section 4.3 based on a model of constant star formation rate in the GC (*Schödel et al.*, 2007), the magnitude interval around $K_s = 18$ may be dominated by relatively young, dynamically unrelaxed stars.

Table 4.3: Parameters used in the estimation of the surface density profile of pre-MS stars and resulting corrected Γ for the density profile of stars with magnitudes $17.5 \leq K_s \leq 18.5$, fitted at $0.04\,\mathrm{pc} \leq R \leq 0.5\,\mathrm{pc}$. We test two values of the η-parameter: $\eta = 1.40$ from (*Bartko et al.*, 2010) and $\eta = 0.93$ from (*Do et al.*, 2013), and assume the IMF of *Lu et al.* (2013).

ID	η^{a}	$\Sigma(2'')^{b}$	Γ^{c}	$\chi^2_{reduced}$
1	0.93	4.0	0.22± 0.06	0.7
2	0.93	6.0	0.13± 0.07	0.7
3	1.40	4.0	0.21± 0.05	0.7
4	1.40	6.0	0.12± 0.06	0.9

Notes.

[a] Power-law index of the surface-density profile for young stars.[b] Estimated surface density of $K_s = 18$ pre-MS stars at $R = 2''$. [c] Power-law index of the surface-density profile of $K_s = 18$ stars after correction for pre-MS stars.

As we see in Sec. 4.3, we excluded from the analysis all spectroscopically identified early-type stars from our sample. The problem is that the limit of spectroscopic identification of early-type stars with current instruments is $K_S \approx 16$ in the GC (with the exception of a few, very deep exposures of small fields that reached $K_s \approx 17.5$, see *Pfuhl et al.*, 2011). Therefore, we have to consider explicitly the possibility that our stellar surface number densities are contaminated by pre-MS stars

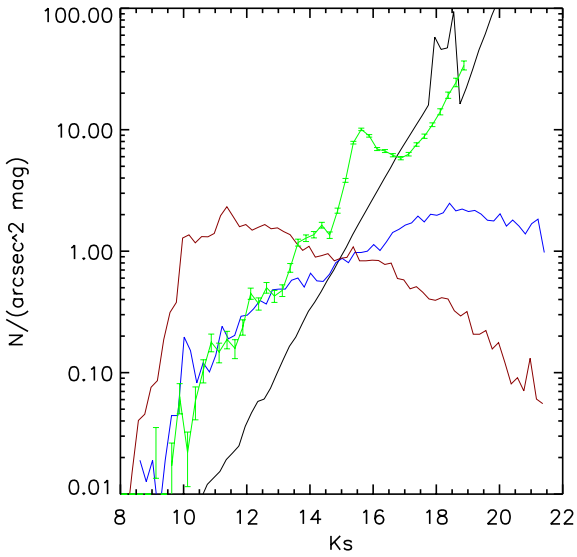

Figure 4.17: Model KLFs for the youngest, ∼5 Myr old stellar population at $R = 2''$. Black line: Kroupa IMF; blue line: IMF from *Lu et al.* (2013); red line: IMF from *Bartko et al.* (2010). The latter two KLFs were created with a tool that does not include pre-MS evolution and therefore lack the bump at $K \approx 18$. The surface density is normalised to $R = 2''$ (0.08 pc), assuming that it rises as R^{-1} toward Sgr A*. The surface density was normalised with the densities measured by *Lu et al.* (2013). The green line is the KLF measured from our data and normalised to the star counts at $K_s = 18$. Note that all known massive, young stars at $K_s \lesssim 16$ are excluded from this KLF.

To estimate the surface density of young stars from the most recent star formation event in the GC, we assumed a 5 Myr old cluster of mass $2.5 \times 10^4\,M_\odot$ of solar metallicity. From some experiments with different values we concluded that assuming somewhat different ages, masses, or metallicities will not change our conclusions significantly. We created different present-day model KLFs for this star formation event. On the one hand, we used the CMD 3.0 tool [1] with a Kroupa IMF and the photometric system based on

[1] See *http://stev.oapd.inaf.it/cgi-bin/cmd_2.8* and *Bressan et al.* (2012); *Chen et al.* (2014, 2015); *Tang et al.* (2014)

the works of *Maíz Apellániz* (2006) and *Bessell* (1990). On the other hand, we used the IAC-STAR tool (*Aparicio and Gallart*, 2004) to create KLFs with similar parameters, but with a different IMF, using, on the one hand, the extremely flat IMF $dN/dm \propto m^{-0.45}$ of *Bartko et al.* (2010) and, on the other hand, the steeper, but still top-heavy IMF $dN/dm \propto m^{-1.7}$ of *Lu et al.* (2013). We normalised with the value of 0.3 stars per square arcsec at $K \approx 15$ (*Do et al.*, 2013; *Lu et al.*, 2013) and computed the surface density at $R = 2''$ assuming that the surface density of the young stars follows a power law of the form $\Sigma(R) \propto R^{-\eta}$ ($\eta = 0.93 - 1.1$ *Bartko et al.*, 2010; *Lu et al.*, 2013). The resulting KLFs for the young stars at $R = 2''$ is shown in Fig. 4.17, where we also over-plot the KLF from our full data set, scaling with the surface number density of $K_s = 18$ stars at $R = 2''$.

As was pointed out in previous work (e.g., *Paumard et al.*, 2006; *Bartko et al.*, 2010; *Lu et al.*, 2013), the IMF of the most recent star formation event near Sgr A* appears to have been top-heavy. This is supported by our analysis of the KLF here: As can be seen in Fig. 4.17 the surface number density of young stars at $R = 2''$ would strongly exceed the measured surface number density of *all* stars in case of a standard Kroupa/Chabrier IMF (*Chabrier*, 2001; *Kroupa*, 2001; *Kroupa and Weidner*, 2003). This problem does not appear in case of a top-heavy IMF. The IAC-STAR tool used to infer the top-heavy KLFs does not take pre-MS evolutionary tracks into account and therefore misses the bump of stars on the pre-MS at around $K_s = 18$. The actual surface number densities can therefore be expected to be a factor of two to three higher at this magnitude (where we roughly estimated the excess from the pre-MS onset bump in the KLF that includes pre-MS tracks). If the IMF of the 5 Myr-old stellar population is indeed as top-heavy as suggested by *Bartko et al.* (2010), then its contamination of our number counts can be neglected. For a less extreme IMF, as suggested by *Lu et al.* (2013), the contamination may reach a value up to about 40% at $R = 2''$, but will rapidly diminish due to the steep decrease of the surface density of the young stars with R.

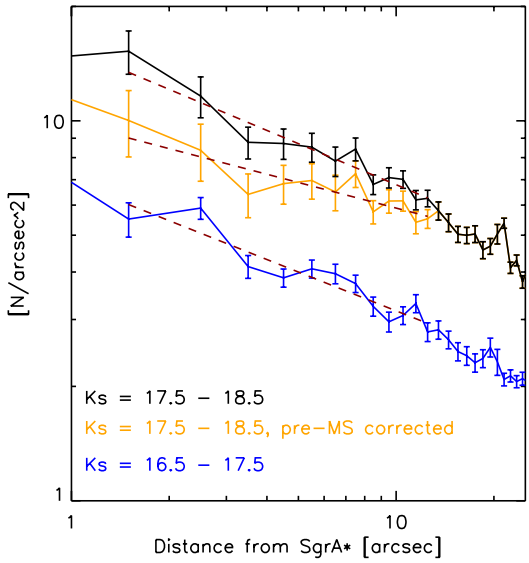

Figure 4.18: Extinction and crowding-corrected surface number density profiles for $16.5 \leq K_s \leq 17.5$ (blue line), $17.5 \leq K_s \leq 18.5$ (black line), and for $17.5 \leq K_s \leq 18.5$ after correction for potentially present pre-MS stars from the most recent star formation event (using parameters from ID 1 in Tab. 4.3). The dashed red lines are simple power-law fits in the range $0.04\,(pc) \leq R \leq 0.5\,\mathrm{pc}$.

We have created model surface density distributions for the potential pre-MS stars, assuming two different parameters for their power-law index and for their surface density at $R = 2''$. Subsequently, those models were subtracted from the star counts at $17.5 \leq K_s \leq 18.5$ and a simple power-law was fitted to the data at $0.04\,(pc) \leq R \leq 0.5\,\mathrm{pc}$. The resulting values of the projected power-law index, Γ are listed in Tab. 4.3. They lie in the range $\Gamma = 0.12 - 0.22$, flatter than for the uncorrected surface density ($\Gamma = 0.36 \pm 0.04$, ID 1 in Tab. 4.1). We note that this is a conservative scenario, with a high correction factor based upon the relatively steep IMF of *Lu et al.* (2013). When we apply the extremely top-heavy IMF of *Bartko et al.* (2010), we can neglect this correction for pre-MS stars. This is supported by an additional test, where we also measured the power-law index of the

stars in the brightness range $16.5 \leq K_s \leq 17.5$ at $0.04\,(pc) \leq R \leq 0.5\,\mathrm{pc}$. It is $\Gamma = 0.34 \pm 0.03$, consistent with the value for the fainter stars without correction for pre-MS stars (for the fitting range $0.04\,(pc) \leq R \leq 1.0\,\mathrm{pc}$ it is $\Gamma = 0.41 \pm 0.02$).

The value of $\Gamma = 0.36 \pm 0.04$ that we derive for the power-law index of stars at $K_s \approx 18$, using only data at a projected distance of $R \leq 0.5\,\mathrm{pc}$ from Sgr A*, lies $9\,\sigma$ away from a flat core. Even if we take into account the possible contamination by pre-MS stars, then we can still exclude a flat core, as discussed in the preceding paragraph. We therefore conclude that the contamination of the measured surface densities by pre-MS stars from the most recent star formation event is probably not significant. However, we note that the contamination by slightly older stars, from star formation about 100 Myr ago, is probably a more important source of systematic error than the pre-MS stars. Unfortunately, currently there do not exist any adequate data on the age composition of the $K_s = 18$ stars and on the surface density of the potential different populations, which would allow us to consider an explicit correction for young stars. Depending on the exact properties and spatial distribution of these stars, the cusp signature could be enhanced or diminished. This is a source of systematics of unknown impact and needs to be investigated by future research. We note that the spectroscopic classification of $K_s = 18$ stars at the GC is beyond the reach of current instrumentation and may require telescopes of the 30m class.

4.5.2 Stars that contribute to the diffuse light

The stars that contribute dominantly to the diffuse light in our point-source subtracted images must be fainter than $K_S = 18$. The bottom right panel in Fig. 4.16 shows the fraction of the total flux contributed by the stars in the different bins of the model KLF. As can be seen, stars in the regime $K_S = 19 - 22$ do not differ significantly in their overall weight. We expect these stars, to dominate our measurements of the diffuse light density. As can be seen in the upper right panel, these stars belong predominantly to

the oldest stellar population. They will be of type G to F, have masses $\lesssim 1.5\,M_\odot$ and will live for several Gyrs (see also Fig. 16 in *Schödel et al.*, 2007). They can thus be old enough to be dynamically relaxed and serve as tracers for the existence of a stellar cusp. We want to explore whether the contamination by young stars from the most recent $\sim$5 Myr-old star formation event in the central $R < 0.5$ could, in principle, also be present in the diffuse light. While we cannot completely rule out this possibility, the top right panel of Fig. 4.16 shows that stars older than a 3 Gyr will be a factor of a few more frequent than younger stars at $K_s > 20$.

As discussed in the last section, the youngest stellar population is concentrated within $0.8 \leq R \leq 12''$, or $0.03 \leq R \leq 0.5$ pc, of Sgr A*. We cannot directly measure the contamination of our SB profiles by pre-main sequence stars, but we can estimate it. Since the surface density of young stars is strongly peaked towards Sgr A*, this contamination is more severe at small R. As Figure 4.17 shows, the number density of pre-MS stars at $K_s \approx 20$ is roughly two orders of magnitude below the one from the other stars at $R = 2''$. We therefore conclude that contamination by pre-MS stars is not an issue for the SB profiles presented here.

As can be seen in the upper right panel of Fig. 4.9, the population younger than 500 Myr could also contaminate significantly star counts at magnitudes $17 \lesssim K_s \lesssim 19$. The importance of this effect can currently not be well constrained because it depends on the unknown distribution of stars in this age range. On the other hand, the surface brightness measurements are dominated by older stars. The fact that we observe similar surface densities and brightnesses for all the samples is reassuring and suggests that contamination effects are not severe.

4.6 The 3D structure of the cluster

Our observations provide us with the projected surface density and surface brightness, respectively, but we would like to know the *intrinsic* structure

of the NSC. There are two important caveats to consider:

1. The morphology of the cluster at large radii will impact the measured projected quantities. As we could see in section 4.4.1, the value of the projected power-law index depends on the radial fitting range, with a tendency to steepen at large R. For example, for smaller clusters the inner projected density slope will appear flatter.

2. The 3D structure of the cluster cannot be described by a simple power-law. The NSC is a finite system, with a half-light radius on the order of 5 pc (*Feldmeier et al.*, 2014; *Schödel et al.*, 2014a; *Fritz et al.*, 2016). Moreover, from previous studies of the stellar density in the GC indicates, we know that the nuclear cluster follows a density of approximately $n(r) \propto r^{-2}$ outside of the central parsec, with a steepening slope at larger distances (see, e.g. references and discussions in *Launhardt et al.*, 2002; *Schödel et al.*, 2007, 2014a; *Fritz et al.*, 2016). A steepening density profile is also required to avoid that the cluster mass diverges.

So, to better constrain the shape of the NSC, we consider it therefore necessary to use a 3D model for a fit to the observed projected surface densities and constrain it on scales larger than what we could measure with NACO.

For this purpose we use the data from *Fritz et al.* (2016), which they acquired from observations with NACO/VLT, WFC3/HST, and VIRCAM/VISTA. For the study of the diffuse light, we included also data on the flux density of the NSC from *Schödel et al.* (2014a), that used extinction-corrected Spitzer 4.5 μm surface brightness maps. Moreover, we repeated the analysis for faint stars by using higher resolution data from HAWK-I described in Chapter 2 to have two independent data sets. A caveat is that the data sets that we used are focussed on significantly brighter stars than what we are examining in the present work. The Spitzer data of

Schödel et al. (2014a) are of low-angular resolution and long wavelength and completely dominated by a few bright stars and by emission from the mini-spiral in the inner parsec. The data from *Fritz et al.* (2016) are, in principle, more suitable, but are dominated by RC stars and brighter giants, similar to HAWK-I data. Therefore, the data sets are not adequate to sample the light density profile inside $R \approx 1\,\mathrm{pc}$. Nevertheless, for simplicity – and because we assume that it is a good approximation on large scales – we will assume that the distribution of all populations is described well by these data. A study of the density of different stellar populations throughout the nuclear cluster out to distances beyond a few parsecs is beyond the scope of this work and will be addressed in a later work. Again, we note that we find similar profiles for stellar components in significantly different brightness ranges, which supports our assumption that the individually detectable stars can be used as a good proxy for the cluster shape on large scales.

To isolate the nuclear cluster from the emission of the nuclear disc and Galactic Bulge, we used the Sérsic models for the non-NSC emission listed in Table 2 of *Schödel et al.* (2014a). They were scaled to the data at $R \geq 18\,\mathrm{pc}$ and subtracted from the data sets described above. We then applied a 3D *Nuker* model and projected it onto the sky to fit the measured surface brightness. We use the *Nuker* model (*Lauer et al.*, 1995) in the form of Equ. 1 of *Fritz et al.* (2016):

$$\rho(r) = \rho(r_b) 2^{(\beta-\gamma)/\alpha} \left(\frac{r}{r_b}\right)^{-\gamma} \left[1 + \left(\frac{r}{r_b}\right)^{\alpha}\right]^{(\gamma-\beta)/\alpha}. \tag{4.3}$$

Here, r is the 3D distance from Sgr A*, r_b is the break radius, ρ is the 3D density, γ is the exponent of the inner and β the one of the outer power-law, and α defines the sharpness of the transition. We explicitly point out that the *Nuker* model was previously always used for 2D data, while we use it as a convenient mathematical model to describe the 3D shape of the cluster. The density was then projected along the line of sight via an integral:

$$\Sigma(R) = 2 \int_r^{\infty} \frac{r\rho(r)dr}{\sqrt{r^2 - R^2}}. \tag{4.4}$$

For numerical reasons, to avoid a singularity, we could not integrate down to $r = R$ and therefore set the minimum $r = R + 0.001\,\mathrm{pc}$. The best-fit was found with the IDL MPFIT package (*Markwardt*, 2009). Uncertainties were re-scaled to a reduced $\chi^2 = 1$. We fixed the parameter $\alpha = 10$ and used only data at $R \leq 20\,\mathrm{pc}$. The 3D *Nuker* model was fitted to the three different distribution that we studied. We show the results in the next sections.

4.6.1 Distribution of faint stars

As we explaned above, we used the data from *Fritz et al.* (2016). To combine these data with ours, we have to assume that, on large scales, the NSC stellar population is well mixed and that its average properties (mass function) do not change. We scaled their data to ours in the range $0.5\,\mathrm{pc} \leq R \leq 1.0\,\mathrm{pc}$.

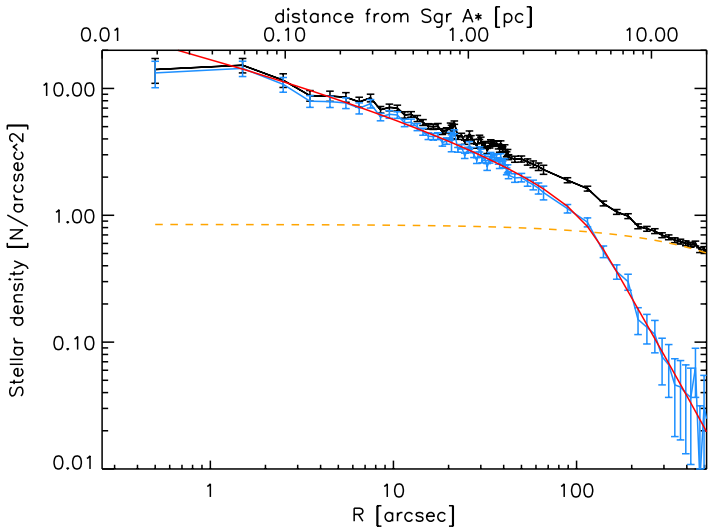

Figure 4.19: Black: Combined, corrected surface density data for stars in the magnitude interval $17.5 \leq K_s \leq 18.5$ from our deep plus wide field image, complemented at large radii by scaled data from *Fritz et al.* (2016). The dashed orange line is a model for the emission from the nuclear disk (model 5 in Tab. 2 of *Schödel et al.*, 2014a) that is subtracted from the black data points, resulting in the blue data points. The red line is a Nuker model fit (ID 5 in Tab. 4.4).

Table 4.4: Best-fit model parameters for Nuker fits to faint stars.

ID	r_b (pc)	γ	β	$\rho(r_b)$ (pc^{-3})	$\chi^2_{reduced}$
1^a	5.2 ± 0.6	1.45 ± 0.03	4.6 ± 0.7	40 ± 7	1.7
2^b	5.0 ± 0.5	1.44 ± 0.03	4.1 ± 0.5	46 ± 7	1.7
3^c	5.0 ± 0.5	1.44 ± 0.03	4.1 ± 0.5	46 ± 7	1.7
4^d	4.8 ± 0.5	1.43 ± 0.03	3.5 ± 0.3	53 ± 7	1.7
5^e	4.9 ± 0.5	1.42 ± 0.03	3.5 ± 0.3	53 ± 7	1.7
6^f	5.0 ± 0.7	1.43 ± 0.03	3.6 ± 0.6	46 ± 14	2.0
7^g	5.0 ± 0.5	1.46 ± 0.03	3.6 ± 0.3	46 ± 7	1.7
8^h	5.3 ± 0.7	1.41 ± 0.03	3.7 ± 0.4	39 ± 14	1.7
9^i	4.8 ± 0.4	1.43 ± 0.03	3.5 ± 0.3	53 ± 7	1.7
10^j	4.3 ± 0.5	1.29 ± 0.05	3.4 ± 0.3	72 ± 14	2.0
11^k	4.4 ± 0.4	1.29 ± 0.05	3.4 ± 0.2	72 ± 14	1.9

Notes.
[a] Fit range: $0.04 \leq R \leq 20pc$. Fore-/background emission model 1 of Table 2 in *Schödel et al.* (2014a). [b] Fit range: $0.04 \leq R \leq 20pc$. Fore-/background emission model 2 of Table 2 in *Schödel et al.* (2014a). [c] Fit range: $0.04 \leq R \leq 20pc$. Fore-/background emission model 3 of Table 2 in *Schödel et al.* (2014a). [d] Fit range: $0.04 \leq R \leq 20pc$. Fore-/background emission model 4 of Table 2 in *Schödel et al.* (2014a). [e] Fit range: $0.04 \leq R \leq 20pc$. Fore-/background emission model 5 of Table 2 in *Schödel et al.* (2014a). [f] Fit range: $0.04 \leq R \leq 10pc$. Fore-/background emission model 5 of Table 2 in *Schödel et al.* (2014a). [g] Fit range: $0.04 \leq R \leq 20pc$. Fore-/background emission model 5 of Table 2 in *Schödel et al.* (2014a). Lower integration boundary at $r = R + 0.01\,\mathrm{pc}$. [i] Fit range: $0.04 \leq R \leq 20pc$. Fore-/background emission model 5 of Table 2 in *Schödel et al.* (2014a). $\alpha = 5$. [j] Fit range: $0.04 \leq R \leq 20pc$. Fore-/background emission model 5 of Table 2 in *Schödel et al.* (2014a). Subtracted potential contamination by pre-MS stars as in model 4 of Tab. 4.3. [k] Fit range: $0.04 \leq R \leq 20pc$. Fore-/background emission model 5 of Table 2 in *Schödel et al.* (2014a). Subtracted potential contamination by pre-MS stars as in model 1 of Tab. 4.3.

The results of our fits are listed in Table 4.4. We also performed a fit with the correction for the potential pre-MS stars (ID 11 in Table 4.4). In Appendix B we explain the computation of the systematic uncertainties for the different parameters that may result from the deprojection (denoted by the subscript *sys* in the following). We use the mean of the parameters and their standard deviation to obtain orientative values for the average best *Nuker* model: $r_b = 4.9 \pm 0.3 \pm 0.2_{sys}$ pc, $\gamma = 1.41 \pm 0.06 \pm 0.1_{sys}$, $\beta = 3.7 \pm 0.4 \pm 0.1_{sys}$, and a density at the break radius of $\rho(r_b) = 52 \pm 12\,\mathrm{pc}^{-3}$. We note that $\rho(r_b)$ is strongly correlated with the values of the other parameters.

Its mean value is orientative and we do not cite a systematic error for this parameter. The best fit according to model ID 5 in Table 4.4 is shown in Fig. 4.19.

When we take into account the possible contamination by pre-MS stars, then there is a systematic shift toward lower values in the best-fit values for r_b, γ, and β , as illustrated, e.g., by fit ID 11 in Tab. 4.4: $r_b = 4.3 \pm 0.5$ pc, $\gamma = 1.29 \pm 0.05$, $\beta = 3.4 \pm 0.3$.

The *Nuker* fit shows that the faint stars show a cusp-like distribution around Sgr A*. A flat core can be excluded with high significance. We explicitly note that in the fits presented in this work we omit the region $R \leq 1''$ (0.04 pc). In this region, the star counts appear to drop slightly below the expected levels. However, this region is also the most crowded region, which may lead to strong systematics in the star counts. Additionally, the stellar population in the extremely close environment of Sgr A* may have been altered, as is indicated by the presence of the so called "S-stars", apparently B-type MS stars that appear concentrated within $R < 1''$ of Sgr A* and may have been deposited there by individual scatter or capture events (see, e.g., *Eisenhauer et al.*, 2005; *Genzel et al.*, 2010; *Alexander*, 2011).

Finally, we computed the *Nuker* fit by using data from GALACTICNUCLEUS survey for distances larger than 1.5 pc. Moreover, we use the model for the non-NSC emission computed in Chapter 3 Sec. 3.3 to subtract the GB and NSD contributions from our sample. We use the NSD Model 2 from Tab. 3.2. The resulting best-fit parameters are given in Tab. C.2, where we explore different source of systematics errors (see Appendix C.4).

Figure 4.20 shows the *Nuker* fit ID 10 in Tab. C.2. The black point represent the corrected surface density data for stars in the magnitude interval $17.5 \leq K_s \leq 18.5$ from *Gallego-Cano et al.* (2018), complemented at large radii by scaled data from GALACTICNUCLEUS data. In order to obtain the value for the inner power-law γ that describes the cusp, we use the mean and standard deviation of the best-fit values of the Table C.2

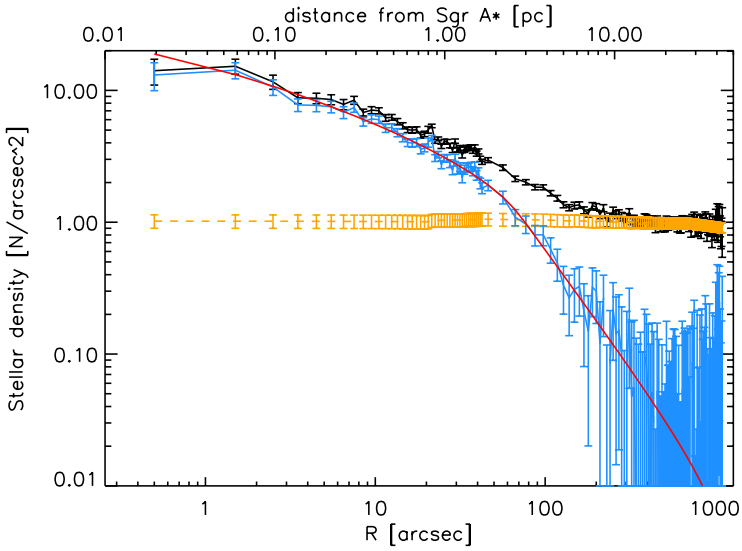

Figure 4.20: Black: Combined, corrected surface density data for stars in the magnitude interval $17.5 \leq K_s \leq 18.5$ from *Gallego-Cano et al.* (2018), plus scaled data from GALACTICNUCLEUS survey at large radii. The blue data points are the data after the subtraction of the Model 2 in Tab. 3.2 for the emission from the nuclear stellar disk and the Galactic bulge (the dashed orange line). The red line is a *Nuker* model fit (ID 10 in Tab. C.2).

and we add quadratically the statistical systematics. We obtain a value of $\gamma = 1.38 \pm 0.06_{sys} \pm 0.01_{stat}$. As we can see, the mean parameters agree within the uncertainties with the value of $\gamma = 1.43 \pm 0.02 \pm 0.1_{sys}$ determined in *Gallego-Cano et al.* (2018).

4.6.2 Distribution of giants stars near Sgr A*

In agreement with previous work, we have found an unexpectedly flat surface density for RC stars and brighter giants within about 0.3 pc of Sgr A*. This indicates a deficit of giants in this region. Here we produce a 3D *Nuker* model fit for the giant stars and try to constrain the number of potentially missing giants. We proceeded as we explained above. At large radii, we used the data from *Fritz et al.* (2016) as described in the preceding section. The resulting best-fit parameters are given in Table 4.5.

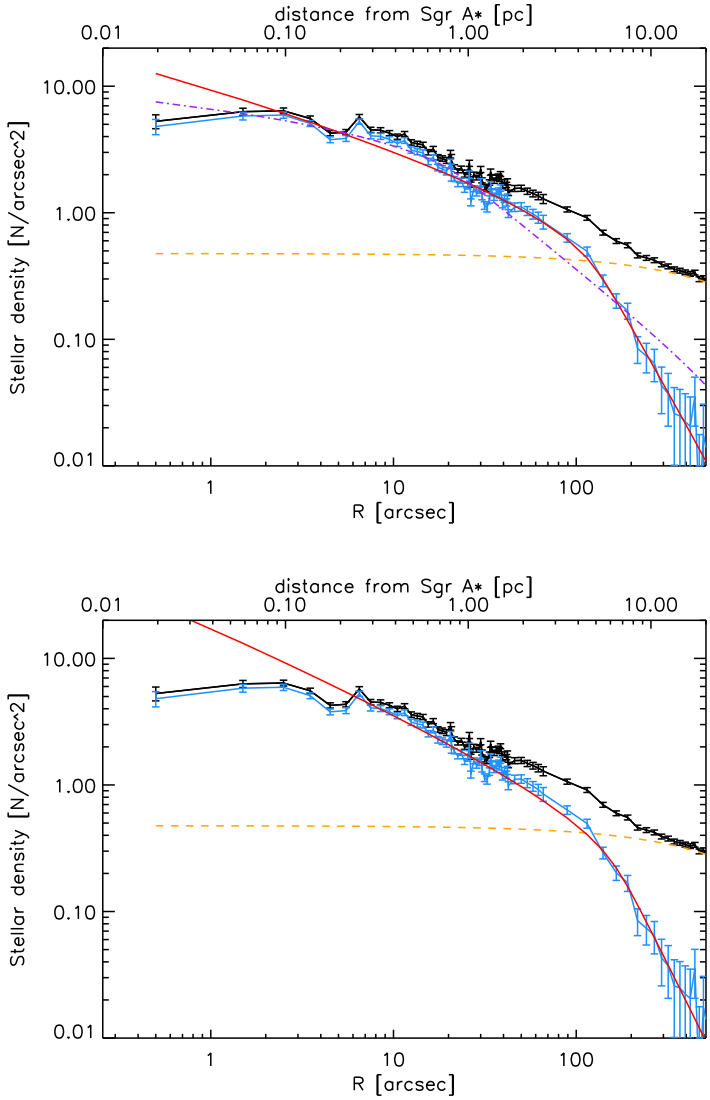

Figure 4.21: Upper panel: Black: Combined, corrected surface density data for stars in the magnitude interval $12.5 \leq K_s \leq 16$ from our deep plus wide field image, complemented at large radii by scaled data from *Fritz et al.* (2016). The orange line is a model for the emission from the nuclear disk (model 5 in Tab. 2 of *Schödel et al.*, 2014a) that is subtracted from the black data points, resulting in the blue data points. The red line is a *Nuker* model fit (ID 1 in Tab. 4.5). The dash-dotted purple line is a *Nuker* model fit with $\gamma = 1.0$ fixed (ID 7 in Tab. 4.5). Lower panel: Like upper panel, but *Nuker* fit from ID 4 in Tab. 4.5.

Table 4.5: Best-fit model parameters for *Nuker* fits of old giants.

ID	r_b (pc)	γ	β	$\rho(r_b)$ (pc^{-3})	$\chi^2_{reduced}$
1^a	5.2 ± 0.9	1.45 ± 0.04	3.6 ± 0.5	23 ± 8	5.1
2^b	5.6 ± 1.0	1.52 ± 0.04	3.7 ± 0.6	19 ± 7	4.7
3^c	6.3 ± 1.2	1.63 ± 0.04	3.8 ± 0.7	14 ± 5	3.8
4^d	6.8 ± 1.3	1.70 ± 0.05	3.9 ± 0.7	11 ± 5	3.3
5^e	5.8 ± 1.0	1.50 ± 0.00	3.7 ± 0.6	18 ± 6	5.2
6^f	4.5 ± 0.9	1.37 ± 0.04	3.4 ± 0.5	32 ± 11	6.4
7^g	0.9 ± 0.1	1.00 ± 0.00	2.2 ± 0.1	572 ± 89	7.2

Notes.
[a] Fit range: $0.04 \leq R \leq 20pc$. Fore-/background emission model 5 of Table 2 in *Schödel et al.* (2014a). [b] Fit range: $0.1 \leq R \leq 20pc$. Fore-/background emission model 5 of Table 2 in *Schödel et al.* (2014a). [c] Fit range: $0.2 \leq R \leq 20pc$. Fore-/background emission model 5 of Table 2 in *Schödel et al.* (2014a). [d] Fit range: $0.3 \leq R \leq 20pc$. Fore-/background emission model 5 of Table 2 in *Schödel et al.* (2014a). [e] Fit range: $0.04 < R < 20pc$. $\gamma = 1.5$ fixed. Fore-/background emission model 5 of Table 2 in *Schödel et al.* (2014a). [f] Fit range: $0 \leq R \leq 20pc$. Fore-/background emission model 5 of Table 2 in *Schödel et al.* (2014a). [g] Fit range: $0.0 \leq R \leq 20pc$. $\gamma = 1.0$ fixed. Fore-/background emission model 5 of Table 2 in *Schödel et al.* (2014a).

As can be seen from the reduced χ^2 values, the quality of the fit is significantly worse than for the faint stars, but improves as we omit the centralmost data points. We use the mean and error of the mean of the best-fit parameters in Tab. 4.5 to obtain orientative values for the average best *Nuker* model for giants: $r_b = 5.7 \pm 0.8 \pm 0.2_{sys}$ pc, $\gamma = 1.53 \pm 0.13 \pm 0.1_{sys}$, and $\beta = 3.7 \pm 0.2 \pm 0.1_{sys}$. As we can see, the mean parameters agree within $1 - 2\sigma$ with the ones determined from the *Nuker* fits to the faint stars, omitting fit 7, which we believe to be not adequate (see below). The differences between the best-fit values for giants and faint stars may indicate either systematics that we have not accounted for or that the two brightness ranges do not trace populations of similar mean age and therefore dynamical state. As can be seen in Fig. 4.21, a projected *Nuker* law can provide a reasonable fit to the projected surface densities of giants down to projected distances $R \approx 0.1$ pc. Also, if we consider the *Nuker* fits to be reasonable 0th order approximations, then they are consistent with a cusp-like 3D density

distribution of the giants, in spite of the flat projected density at small R. Forcing a flattish inner cusp, e.g. by fixing $\gamma = 1.0$ as in fit ID 7 in Tab. 4.5 will lead to a bad fit at large distances, as shown by the dash-dotted purple line in the upper panel of Fig. 4.21, with parameters that deviate strongly from the best fit-parameters for all other cases (both star counts in this work and diffuse light). We therefore argue that, in spite of the observed core *projection* at small R, the observed surface density of giants in the GC is inconsistent with such a structure.

We point out that this does not contradict previous work. Some differences can be explained by the use of different data or references to constrain the structure of the cluster on scales out to 20 pc. Also, contrary to other studies, in this work we have subtracted the projected density of stars that we do not consider to form part of the NSC proper, but to belong to the fore-and background population. We do this in order to facilitate comparison with theory, which always considers isolated systems. While our methodology may make a comparison with other publications therefore difficult, we point out that, given the statistical and systematic uncertainties, our γ for the old stars still overlaps within about $2\,\sigma$ with the values given by other work (e.g., *Do et al.*, 2009; *Fritz et al.*, 2016). Hence, while we find consistently an observed *projected* flat surface density of giants in the innermost few arcseconds, we find that this does not require a flat core in 3D.

The observed flat projected profile within $\sim$0.3 pc and the fact that the quality of the fit improves when we omit the innermost data points may indicate that something has altered the apparent distribution of giants in this region. To estimate the number of potentially "missing" giants, we focus on the region $R \leq 0.3$ pc. Since it is impossible to know what would be the "correct" number density model for giants stars, we use the following simple approach. We fit different *Nuker* laws to the data, where we omit the data inside $R = 0.0, 0.1, 0.2, 0.3$ pc. The fit for $R = 0.0$ can serve as a benchmark for the actually measured distribution, while the fits that omit

data approximate the cluster structure without potentially missing stars at small R. The benchmark fit is shown in the upper panel of Fig. 4.21, and the fit omitting data at $R \leq 0.3\,\mathrm{pc}$ is shown in the lower panel of the same figure.

Subsequently, we compute the amount of stars at $r < 0.2\,\mathrm{pc}$ for each model and compare it to the benchmark solution. The difference in number provides the estimate of possibly missing stars at $r < 0.2\,\mathrm{pc}$. For the three fits that omit data at small R, this numbers varies between 40 to 200. While the uncertainty of this crude estimate is high, it provides us with an idea of the order of magnitude of the problem. The lesson to take away here is, in our opinion, that any mechanisms that intends to explain the deficit of giant stars near Sgr A* should be able to be efficient enough to account for roughly 100 missing giants.

4.6.3 Distribution of unresolved stellar population

We proceeded as we explained above, but in this case we used the data sets from *Schödel et al.* (2014a) and *Fritz et al.* (2016), respectively. We then scaled the latter data to our data in the ranges $1.5\,\mathrm{pc} \leq R \leq 2.0\,\mathrm{pc}$. At $R < 1.5\,\mathrm{pc}$, we used exclusively our data.

Table 4.6 contains the best-fit parameters that we obtained for the model-fits to different data and under different assumptions and constraints. Two of the fits, using the azimuthally averaged data of *Schödel et al.* (2014a) and *Fritz et al.* (2016) are shown in Fig. 4.22 (We note that the plots corresponding to all fits performed by us have a very similar appearance). The χ^2 values and the uncertainties of the different models and parameters are similar to each other. We can obtain an approximate, mean model for the nuclear cluster by taking the mean of each mean; we do not include fixed parameters in these means): $r_b = 3.1 \pm 0.3\,\mathrm{pc}$, $\gamma = 1.13 \pm 0.03$, $\beta = 3.5 \pm 0.3$, and $\rho(r_b) = 0.028 \pm 0.005\,\mathrm{mJy\,arcsec^{-3}}$. It is important to note that there are covariances between these parameters. For example, the value of $\rho(r_b)$ depends clearly on the value of β, with larger β related to smaller $\rho(r_b)$.

Table 4.6: Best-fit model parameters for the *Nuker* fits to the SB profiles.

ID	r_b (pc)	γ	β	$\rho(r_b)$ (mJy arcsec^{-3})
1^a	3.1 ± 0.1	1.11 ± 0.01	3.8 ± 0.1	0.029 ± 0.002
2^b	2.9 ± 0.2	1.16 ± 0.01	2.9 ± 0.1	0.029 ± 0.003
3^c	3.4 ± 0.2	1.17 ± 0.02	3.5 ± 0.2	0.023 ± 0.002
4^d	3.0 ± 0.1	1.12 ± 0.01	3.6 ± 0.1	0.029 ± 0.001
5^e	3.0 ± 0.1	1.12 ± 0.01	3.6 ± 0.1	0.029 ± 0.001
6^f	3.1 ± 0.1	1.12 ± 0.01	3.7 ± 0.1	0.029 ± 0.002
7^g	3.2 ± 0.2	1.15 ± 0.02	3.3 ± 0.1	0.027 ± 0.003
8^h	3.2 ± 0.2	1.15 ± 0.02	3.5 ± 0.2	0.026 ± 0.003
9^i	3.2 ± 0.2	1.15 ± 0.02	3.3 ± 0.1	0.027 ± 0.003
10^j	3.2 ± 0.1	1.14 ± 0.01	3.9 ± 0.1	0.028 ± 0.002
11^k	3.4 ± 0.2	1.20 ± 0.02	3.4 ± 0.2	0.027 ± 0.02
12^l	3.1 ± 0.1	1.12 ± 0.01	3.7 ± 0.1	0.029 ± 0.002
13^m	3.0 ± 0.1	1.13 ± 0.01	3.6 ± 0.1	0.033 ± 0.001
14^n	3.3 ± 0.1	1.09 ± 0.01	3.8 ± 0.1	0.023 ± 0.001
16^o	2.3 ± 0.1	1.05 ± 0.02	3.0 ± 0.0	0.046 ± 0.002
17^p	3.4 ± 0.1	1.14 ± 0.01	4.0 ± 0.0	0.024 ± 0.001
19^q	3.6 ± 0.2	1.15 ± 0.02	3.6 ± 0.2	0.019 ± 0.002
20^r	3.0 ± 0.2	1.15 ± 0.02	3.1 ± 0.2	0.028 ± 0.003

Notes.
[a] Data from *Schödel et al.* (2014a), azimuthally averaged. Fore-/background emission model 2 of Table 2 in *Schödel et al.* (2014a). [b] Data from *Schödel et al.* (2014a) perpendicular to Galactic Plane. Fore-/background emission model 2 of Table 2 in *Schödel et al.* (2014a). [c] Data from *Schödel et al.* (2014a) along Galactic Plane. Fore-/background emission model 2 of Table 2 in *Schödel et al.* (2014a). [d] Like (a), but fore-/background emission model 5 of Table 2 in *Schödel et al.* (2014a). [e] Like (a), but fore-/background emission model 4 of Table 2 in *Schödel et al.* (2014a). [f] Like (d), but using only data at $R \leq 10\,\mathrm{pc}$. [g] Data from *Fritz et al.* (2016). Fore-/background emission model 5 of Table 2 in *Schödel et al.* (2014a). [h] Like (g), but fore-/background emission model 2 of Table 2 in *Schödel et al.* (2014a). [i] Like (g), but fore-/background emission model 4 of Table 2 in *Schödel et al.* (2014a). [j] Like (d), with lower integration boundary at $r = R + 0.01\,\mathrm{pc}$. [k] Like ($g$), with lower integration boundary at $r = R + 0.01\,\mathrm{pc}$. [l] Like ($d$), fitting only data at $R \leq 10\,\mathrm{pc}$. [m] Like (d), with $\alpha = 30$. [n] Like (d), with $\alpha = 5$. [o] Like (d),with $\beta = 3.0$ fixed.

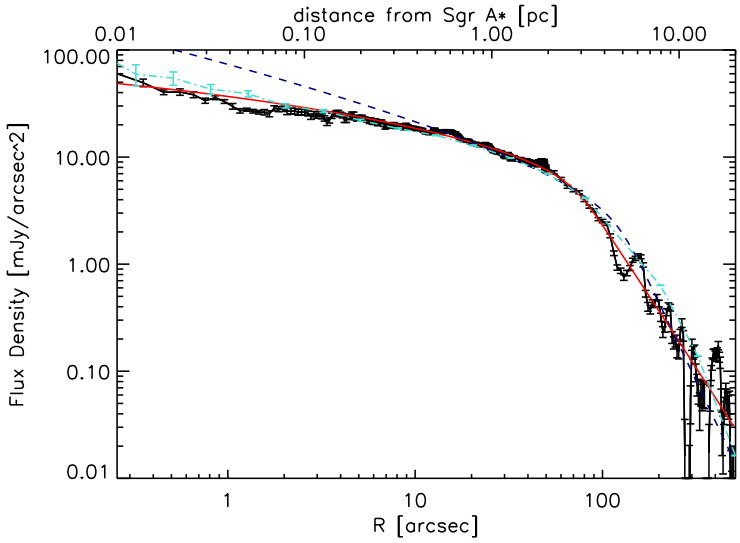

Figure 4.22: *Nuker* model fit (red solid line) to the diffuse SB in the GC. The data at $R \geq 1.5\,\mathrm{pc}$ are the azimuthally averaged, extinction corrected Spitzer $4.5\,\mu\mathrm{m}$ data from *Schödel et al.* (2014a) minus model to remove the contribution from components not part of the NSC. The dashed blue line is a fit with a forced inner slope of $\gamma = 1.5$, corresponding to the lighter stars in a two-component Bahcall-Wolf cusp (*Bahcall and Wolf*, 1977). The dash-dotted turquoise line indicates the SB profile of the faint stars in the simulated cluster of see Section 4.7

Co-variance is also present between r_b and β. On the other hand, the mean values sare fairly well constrained and provide us with a good approximation of the overall 3D shape of the NSC. Finally, and most importantly with respect to the aim of this study, the value of γ is relatively tightly constrained and does not vary much between the different fits.

4.7 Comparison with the simulations

In this section, we compare our results with new N-body simulations, that were undertaken in parallel to this observational work (see *Baumgardt et al.*, 2018, for more details). They studied the evolution of a star cluster sur-

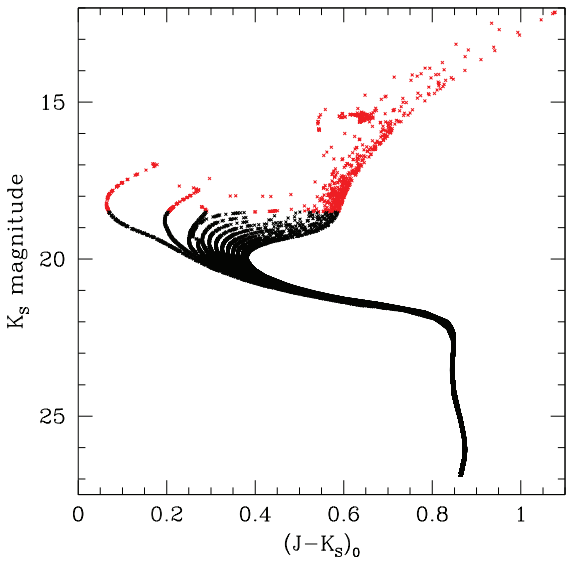

Figure 4.23: $J - K_s$ Colour-magnitude diagram of the stars obtained by *Baumgardt et al.* (2018) in their simulations after 13 Gyr of evolution (Figure 1 in their paper). The different paths reflect the different stellar generations that were added to the simulations following the decreasing star formation rate from *Pfuhl et al.* (2011).

rounding a central massive black hole over a Hubble time under the combined influence of two-body relaxation, continuous star formation, and stellar evolution. The main differences with previous theoretical approaches are:

1. A mass distribution of stars given by a *Kroupa* (2001) mass function from $0.1\,M_\odot$ to $100\,M_\odot$ is included in the simulations. Therefore, the new simulations have taken into account the effects of the mass segregation in the expected density profiles.

2. The star formation history of the NSC from *Pfuhl et al.* (2011) is considered in the simulations. New generations of stars were added every 1 Gyr following the formation rate given by $SFR(t) \propto e^{-t/5.5Gyr}$.

Figure 4.23 shows the colour-magnitude diagram (CMD) of the stars ob-

tained by *Baumgardt et al.* (2018) in their simulations after 13 Gyr (Figure 1 in their paper). We can see the different stellar generations that they have included in the simulations. They compared their results for stars with $K_s \leq 18.5$ (red points in the figure) with the density of resolved stars (see Sec. 4.4.1). The rest of fainter stars are compared with our results of the diffuse light distribution (see Sec. 4.4.2). The masses of resolved stars are in the range $0.86 < m < 2.31 M_{\odot}$. The 90% of the diffuse light is composed by stars with masses $0.78 < m < 1.76 M_{\odot}$.

Left panel in Fig. 4.24 represents the 3D stellar densities obtained from the simulations in *Baumgardt et al.* (2018) (Figure 2 in their paper). Due to the mass segregation, they obtained different values of the 3D power-law index for the different stellar populations. The steepest slope is obtained for black holes and neutron stars (green) with a value of $\gamma = 1.55$. The index for giant stars (red) with $K_s < 18.5$ is $\gamma = 1.20$, for upper main-sequence (MS) stars with masses between 0.6 and 0.8 $M_{\odot}$ (blue) is $\gamma = 1.13$, and for lower MS stars with masses between 0.1 and 0.3 $M_{\odot}$ (purple) is $\gamma = 1.04$. The dashed lines are the power-law fits to the distributions inside the radius of influence of Sgr A*. The right panel in Fig. 4.24 shows a comparison between the surface density of old stars in three different brightness ranges observed at the GC (circles) and the results from the simulations for giant stars (black dashed lines) (Figure 3 in *Baumgardt et al.*, 2018). The value of the index for simulated stars with $K_s < 18.5$ is $\Gamma \sim 0.46$ at 0.04 pc$< R <$ 1.0 pc, very similar to our values ($\Gamma \sim 0.45$ for RC and bright giants, and $\Gamma \sim 0.47$ for faint stars). Finally, Figure 4.25 compares the observed diffuse SB in this work with the one obtained of the simulated star cluster. The value of the index for simulated stars with $K_s > 18.5$ is $\Gamma \sim 0.37$, very similar to the index for the observed diffuse light ($\Gamma \sim 0.26$). Furthermore, they obtained a value of the influence radius of $r_{BH} = 2.8$ pc, similar to the values that we obtained in the last sections for the break radius for the different distributions (see Tab. 4.4, 4.5, and 4.6).

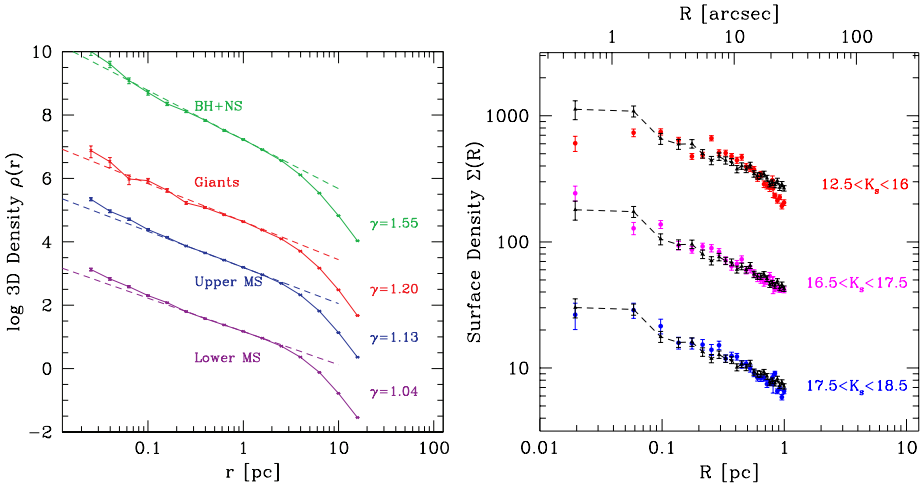

Figure 4.24: Left: 3D stellar densities obtained for different stellar populations at the end of the simulations in *Baumgardt et al.* (2018) (Figure 2 in their paper). Due to the mass segregation, they obtained different values of the 3D power- law index for the different stellar populations. The distributions follow power-law cusp with different values of the index due to the mass segregation. The dashed lines are the power-law fits to the distributions inside the radius of influence of Sgr A*. Right: Comparison between the surface density of old stars in three different brightness ranges observed at the GC (colored circles) and the results from the simulations for giant stars (black dashed lines) (Figure 3 in *Baumgardt et al.*, 2018). For better visualization, the distributions are shifted.

To conclude, we can see that simulations and observations agree very well with each other for the first time (differences between both profiles are smaller than 10%). The distributions obtained from the simulations are flatter than what previous theoretical studies obtained due to the consideration of continuous stars formation, that also decreases the mass segregation. The NSC could not be completely relaxed yet.

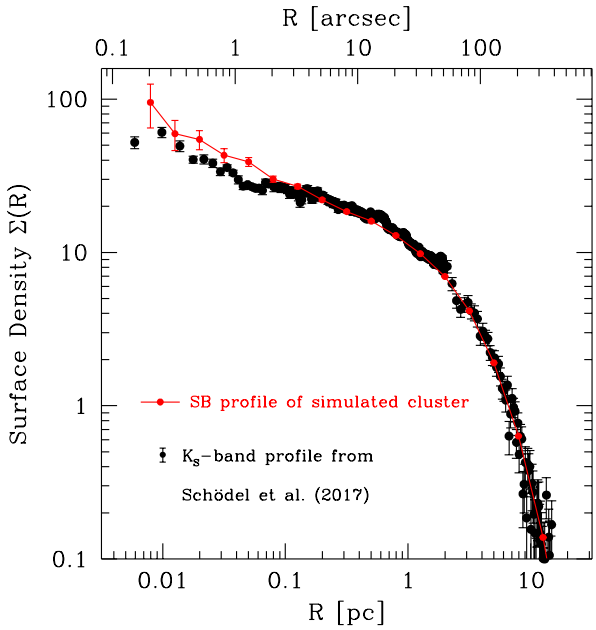

Figure 4.25: Comparison between the observed diffuse SB in this work (black) and the one obtained of the simulated star cluster (red) (Figure 4 in *Baumgardt et al.*, 2018).

4.8 Conclusions

The existence of a cusp in a relaxed stellar cluster around a massive black hole is a firm prediction of theoretical stellar dynamics, that has not yet been confirmed observationally so far. The NSC in the GC is a ideal target to study it. In this work, we have addressed the distribution of stars around the massive black hole in the Galactic Center to clarify the existence of the stellar cusp. We aimed to overcome some limitations that could exist in previous works, both observational and theoretical. On the observational side, we used the same data obtained with NACO instrument at the ESO VLT, but we focused on different methods and stellar populations with improved methodologies. On the one hand, we analysed star counts and through image stacking and improved PSF fitting we pushed the completeness limit about one magnitude deeper than in previous works. We also focused on

stars in well-defined magnitudes ranges to be able to constrain their masses and ages. On the other hand, we analysed the surface brightness profile of the diffuse light in high angular resolution, point source-subtracted images of the GC, taking into account the contamination by line emission from gas and dust in the mini-spiral, which traces even fainter stars, probably sub-giants and main sequence stars of less than 1.5 solar masses. On the theoretical side, new N-body simulations, that were undertaken in parallel to this observational work (*Baumgardt et al.*, 2018), take the complex star formation history of the NSC into account.

The main results of our study can be summarized in the following points:

- The projected surface density profile of the $K_s \approx 18$ and $K_s \approx 17$ stars can be described very well by a single power- law. We estimate a power-law index of $\Gamma = 0.47 \pm 0.07$. For the unresolved stars, the index of the power-law is $\Gamma = 0.26 \pm 0.02_{stat} \pm 0.05_{sys}$ at $R < 0.5$. Both values are consistent with each other on the $< 2\sigma$ level.

- An important caveat is that we cannot directly determine which kind of stars we are observing and the contamination of the star counts by young, dynamically unrelaxed stars may be high. We studied the possible contamination by pre-MS stars from the most recent star formation event in $K_s \approx 18$ stars. We obtained a ~ 0.3 lower value for the power-law index if we considered that the contamination is very high. Given the probably highly top-heavy IMF of this most recent star formation event, for which we present some additional evidence in this work (Fig. 4.17), a strong contamination seems unlikely, however. In contrast, the contamination for slightly older stars, from star formation about 100 Myr ago, is probably a more important source of systematic error. The fact that we obtained similar results for resolved and unresolved stars by using different methodologies gives us confidence in our results.

- We studied the 3D global structure of the NSC by using previous studies of the cluster morphology on large scales and new high resolution data as constraints, along with a spherical approximation. We found that the cluster can be described well by a three-dimensional Nuker law. The break radius of the Nuker model that contains about a stellar mass of twice the mass of Sgr A* lies about 5 pc for resolved stars, and about 3pc for unresolved. This radius coincides with the radius of influence of the black hole (e.g. *Alexander*, 2005), although somewhat larger. The three- dimensional density inside of the break radius follows a power law with an exponent $\gamma = 1.41 \pm 0.06 \pm 0.1_{sys}$ for the $K_s \approx 18$ stars, and $\gamma_{in} = 1.13 \pm 0.03_{model} \pm 0.05_{sys}$ for the diffuse light. Therefore, we can exclude a core-like stellar density distribution with high confidence.

- The cusp is shallower than what is predicted by theory, but the analysed systems were too simple so far. If repeated star formation events and/or cluster infall, and the mass segregation between stars of different masses are included in the simulations, the cusp obtained is flatter than the expected value of $\gamma_{theor} = 1.5$ for the low-mass stellar component in a multi-mass cluster (see *Alexander*, 2005, and references therein) and similar to the values obtained from the observations. Therefore, we finally find agreement between theoretical predictions and observations.

- The bright giants and the Red Clump stars do indeed display a deficiency in numbers within a projected radius of a few 0.1 pc around Sgr A* like previous work obtain. We estimate that on the order of 100 giants may be "missing". This region overlaps with the region where we find young massive stars that may have formed in a dense gas disc a few Myr ago. Repeated collisions with proto-stellar clumps in this disc may have stripped the giants of their envelopes, rendering

them thus unobservable (*Amaro-Seoane and Chen*, 2014; *Kieffer and Bogdanović*, 2016).

- The existence of a cusp in our Galaxy supports the existence of stellar cusps in other, similar systems that are composed of a nuclear cluster and a massive black hole.

- The existence of stellar cusps is an important prerequisite for the observation of EMRIs that will be targets for space-borne gravitational wave detectors (LISA or Taiji). The large number of stellar-black holes that are expected to inhabit the cusp would imply the detection of gravitational waves from the inspiral events in other galaxies very likely (on the order a few to a few tens per year), with important transcendence for fundamental physics and astrophysics (*Amaro-Seoane et al.*, 2007; *Amaro-Seoane*, 2012, 2018).

Chapter 5

Long-term activity of the supermassive black hole at the Galactic Center

"ESO's GRAVITY instrument on the Very Large Telescope (VLT) Interferometer has been used by scientists [...] to observe flares of infrared radiation coming from the accretion disc around Sagittarius A, the massive object at the heart of the Milky Way. The observed flares provide long-awaited confirmation that the object in the centre of our galaxy is, as has long been assumed, a supermassive black hole. The flares originate from material orbiting very close to the black hole's event horizon. [...] This emission, from highly energetic electrons very close to the black hole, was visible as three prominent bright flares, and exactly matches theoretical predictions for hot spots orbiting close to a black hole of four million solar masses. The flares are thought to originate from magnetic interactions in the very hot gas orbiting very close to Sagittarius A*."*

– ESO, October 31, 2018, *https://phys.org*

5.1 Introduction

The spectral energy distribution (SED) of the emission from Sgr A*, the electromagnetic counterpart of the supermassive black hole at the center of our Galaxy, allows us to explore the different accretion and emission processes that are taking place in the vicinity of the black hole. Sgr A* has been known to be a variable source at radio wavelengths during more than 30 years. The left panel in Fig. 5.1 shows the SED of Sgr A* in its quiescent state, where the radio flux dominates the emission of the black hole (Figure 30 in *Genzel et al.*, 2010). The submillimeter (submm) bump is the peak where the luminosity of Sgr A* reaches the maximum ($\sim 10^{35}$ erg/s according to *Serabyn et al.*, 1997). The SED allows us to investigate the accretion flows around the SMBH. The radio spectrum can be well explained by synchrotron emission from thermal electrons moving at high velocity through the SMBH magnetic field (dashed-dotted line in the left panel in Fig. 5.1). Sgr A* is underluminous at all wavelengths by many orders of magnitude, radiating at $\sim 10^{-8.5}$ of its Eddington luminosity at NIR wavelengths despite of the observed gas and stars that are surrounding Sgr A*. The low accretion onto the black hole ($\sim 10^{-5} M_{\odot}$/year according to *Baganoff et al.* 2003) can be described with different theoretical models, such as the radiatively inefficient accretion flow (RIAF *Yuan et al.*, 2003) or the advection-dominated accretion flow (ADAF, *Narayan et al.*, 1995). The accretion rate in the center of our Galaxy is lower than that of active galactic nuclei (AGNs) with similar masses.

The high confusion around the black hole in NIR and X-ray bands due to the extreme crowding and large amounts of gas, made it mandatory to develop high angular resolution technologies. The first observations of X-ray and NIR flares around 18 years ago reported short ($\sim$ 100 min long) increases of the emission from Sgr A* by factors of $\sim$ 100 in X-ray and $\sim$ 10 in NIR above its steady state. The IR emission appears to come from synchrotron radiation from non-thermal electrons (*Witzel et al.*, 2018, and

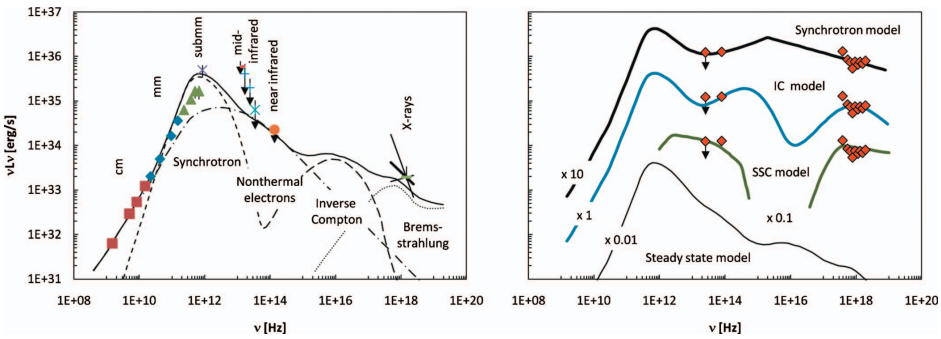

Figure 5.1: Spectral energy distribution of the emission from Sgr A* (Figure 30 from *Genzel et al.* 2010). Left: Quiescent state. Right: SED of the black hole during a simultaneous X-ray and infrared flare. Different models to describe the emission are indicated in the panels (see more details in *Genzel et al.* 2010).

reference therein). The mechanisms that describe the X-ray emission are not very well known yet, including inverse Compton, synchrotron self-Compton or Bremsstrahlung models in addition to synchrotron model (see the right panel in Fig. 5.1). Different scenarios have been proposed to explain the flare emission, among others, e.g.: the ejection of material in a jet, some hot spots orbiting the black hole, and statistical fluctuations in the accretion flow.

Next, we summarise the main properties of the NIR flares of Sgr A*:

- NIR variability is well described as a red-noise process and its characteristic timescale is $\tau_b \sim 245$ (*Witzel et al.*, 2018).
- The NIR radiation is polarised (polarization degrees $\sim 20\%$ and polarization angle $\sim 13°$ according to *Shahzamanian et al.* 2015)

The variability of Sgr A* on short timescales from few to ~ 300 minutes has been studied deeply, observing the black hole emission simultaneous in X-ray, IR band and radio (*Witzel et al.*, 2018, and references therein). The observations have gone even further, peering into the event horizon of Sgr A* and observing bright flares with GRAVITY instrument at ESO

due to orbital motions near the last stable circular orbit of the black hole (*Gravity Collaboration et al.*, 2018b).

Despite of more than a decade of intense studies of the short-term variability of Sgr A* at IR wavelengths, we did not have information about its NIR long-term variability as well as its NIR emission prior 2003, when the first measurements were taken due to the development of AO instrumentations (*Genzel et al.*, 2003a; *Ghez et al.*, 2003). *Chen et al.* (in preparation) aimed at exploring the properties of the NIR Sgr A* emission in previous epochs over longer timescales and looking for flares in the past. We improved the sensitivity of the old speckle data from 1995 to 2005 by applying a new version of speckle holographic, which let us detect Sgr A* in NIR imaging data prior to the use of AO, for the first time. Next, we present some of the results obtained in *Chen et al.* (in preparation).

5.2 Analysis

The observations and data reduction that we used for the analysis are presented in Section 2.3. In order to obtain robust and reliable uncertainties without loss of sensitivity, we applied the bootstrapping method described in Appendix E (Method 3). In previous work, the photometric and astrometric uncertainties were obtained by dividing the dataset for each epoch into 3 subsets with 1/3 of frames each, creating 3 final images and analysing them with SF (see Method 2 in Appendix E). We can see in the appendix, that although both methods give reliable uncertainties, we can go almost one magnitude deeper by using bootstrapping analysis. The new speckle holography reduction along with the new error estimation by bootstrapping, allows us to detect more sources in 2/3 of the epochs. Furthermore, the completeness of the detections in the range $15 < K < 17$ (where Sgr A* is expected to be) is significantly increased (see more details in *Chen et al.*, in preparation).

In order to extract and characterize Sgr A* from the final images, we carried out the point source extraction with the PSF fitting program *Starfinder* (*Diolaiti et al.*, 2000). We selected *min_correlation*= 0.80 as the threshold value to accept a object as a star. The detection threshold was chosen 3σ above the background.

We aimed at studying the variability of Sgr A*, therefore we needed precise relative photometric calibration. We selected non-variables stars as the photometric calibrators identified by *Gautam et al.* (2019). The details of the photometric calibration are presented in Appendix B from *Chen et al.* (in preparation).

Besides the improvements in the reduction, error computation, and photometric calibration, two factors have been the key to help us to identify unambiguously Sgr A* in the speckle holographic images (see more details in *Chen et al.* in preparation):

1. Sgr A*'s position can now be located within 1 milliarcsec. In this work, along with the speckle data, we used AO data in order to register the accurate position of IRS16C and SO-2 in each image and computed their offsets with respect to Sgr A* (see more details in *Jia et al.*, 2019, and references therein). Therefore, we estimated Sgr A* positions with improved accuracy by a factor of 40 compared to original search in speckle images (*Hornstein et al.*, 2002).

2. Better knowledge of stellar orbits, that allowed us to perform tests of source confusion and artifact source analysis, and to confirm if the detected candidates were real detections of Sgr A*.

5.2.1 Sgr A* detections

From the 27 epochs that we analyzed from 1995 to 2005, only 19 epochs have detections of Sgr A* without strong confusion with another bright source.

Furthermore, some of the remaining Sgr A* candidates could still be confused with other nearby dimmer sources (S0-102, S0-42, S0-2, S0-38, S0-103, and S0-104). We used their predicted orbits from *Dehghanfar et al.* (in preparation) and excluded the Sgr A* candidates whose positions coincided with the projections of predicted positions of those stars. Moreover, we took into account that the holographic technique could introduce some residuals due to the deconvolution of the images, including some spurious sources in the detections. By using our knowledge about proper potions and orbits fit from AO imaging data, that are around 3 magnitudes deeper than the speckle data, we can control if a detected source is real or not with high certainty (see more details in *Chen et al.*, in preparation). That analysis allows us to determine that if we select the bootstrap detection frequency [1] greater than 20%, the probability of detecting an artifact instead of real Sgr A* is $<<$ 1%. We excluded 5 Sgr A* candidates from the sample. Therefore, we detected Sgr A* in 13 epochs from 1998 to 2005 (Figure 5.2).

5.3 Light curve

Figure 5.3 shows the light curve of Sgr A* from 1998 to 2005. The average magnitude of Sgr A* is K= 16.0 ± 0.4, the average flux density is 0.27 ± 0.10 mJy, and the average dereddened flux density is 2.60 ± 0.97 mJy (see more details in *Chen et al.* in preparation). The values agree very well with the average magnitude of Sgr A* obtained from AO images from 2005 to 2017 (K= 16.1 ± 0.3 from *Gautam et al.* 2019).

Finally, we analyzed if the the long-term variability of Sgr A* follows the short-term variability characteristics. As we described above, the short-term variability is well characterized by a red-noise process. *Witzel et al.* (2018) analyzed the most exhaustive NIR variability dataset so far. They used a power-law in order to model the NIR power-spectral density (PSD) and

[1] Detection frequency parameter is the percentage of bootstrap images where each star is detected (see more details in Appendix E)

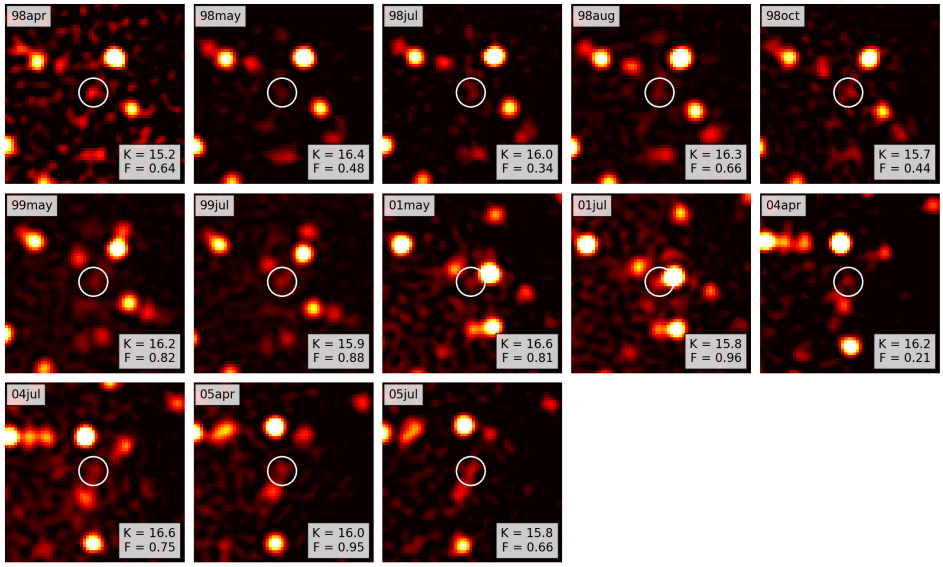

Figure 5.2: Confirmed detections of Sgr A* (white circles) in the speckle holographic images in the different epochs (Figure 5 from *Chen et al.* in preparation). K is the magnitude of the detection and F is the bootstrap fraction of the detection.

reported a break timescale of $\sim$ 245 minutes. We compared the structure function of the black hole computed from observations with the simulated structure function from model assuming the short-term features from *Witzel et al.* (2018). The structure function measures the flux density variance at a given time lag (see more detail in *Chen et al.* in preparation). The $\sim$ 245 minutes is the only NIR PSD break in longer timescale, too.

5.4 The dusty source G1

The spatially resolved, hot dusty source G1 is a good case to explore accretion events in epochs prior to 2003 by using our long-term variability NIR data of Sgr A*. G1 was tidally interacting with the black hole during its closest approach in 2001 (*Witzel et al.*, 2017, and references therein). G1 is similar observationally to G2, the first object observed interacting with

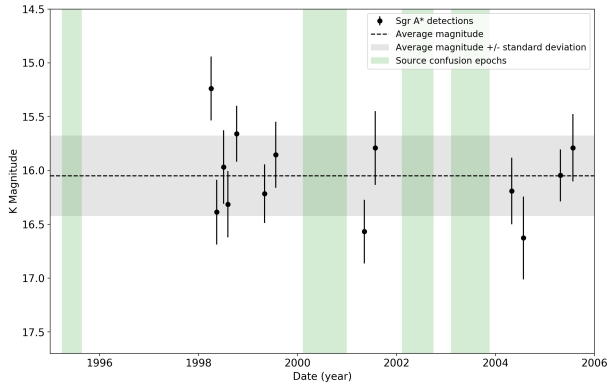

Figure 5.3: Light curve of Sgr A* from 1998 to 2005 from our speckle holographic method version 2_2 (Figure 6 from *Chen et al.* in preparation).

Sgr A* when went through periapse in 2014 (*Witzel et al.*, 2014; *Pfuhl et al.*, 2015; *Shahzamanian et al.*, 2015; *Witzel et al.*, 2018). We expected an enhancement of the luminosity of Sgr A* due to the increase in the accretion flow onto the black hole in the periapse passage of G1 and several years later.

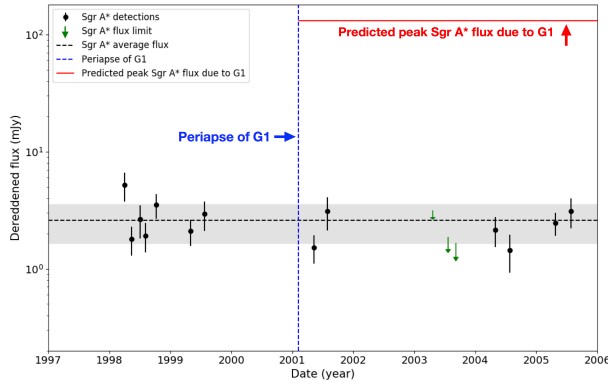

Figure 5.4: Light curve where we can test the impact on the accretion flow of Sgr A* G1 went to the closest position to the black hole (periapse) in 2001. We cannot see any apparent impacts of G1 on the Sgr A* NIR emission from 2001 to 2005.

Figure 5.4 shows the light curve of Sgr A*. The time of the periapse of G1 is indicated in the panel. We cannot observe any increase in the flux

of the black hole. This result ruled out the gas cloud nature of G1 and it is consistent with G1 being a self-gravitating object as suggested by *Witzel et al.* (2017).

5.5 Conclusions

The main results of our study can be summarized in the following points:

- We reported for the first time NIR detections of Sgr A* in epochs prior to AO measurements in 2003 by analysing speckle data from 1995-2005. We reached enough sensitivity to detect the black hole through to the application of an improved speckle holographic technique and a new bootstrapping analysis. Furthermore, the better knowledge of the Sgr A* position and the stellar orbits to avoid source confusion gave us the certainty of our detections.

- We studied the NIR long-term variability of Sgr A* from 1998 to 2005. The photometric analysis of Sgr A* gives the average magnitude of K= 16.0 ± 0.4, that agrees very well with the average value obtained from AO images (K$\sim$ 16.1 according to *Gautam et al.* 2019). The average flux density is 0.27 ± 0.10 mJy. The average dereddened flux density is 2.60 ± 0.97 mJy.

- Sgr A* is quite stable over the 7 years of timescale without any significant change. The long-term variability follows the short term variability characteristics. The $\sim$ 245 minutes is the only NIR PSD break in longer timescale, too.

- We could search for enhanced luminosity due to accretion prior 2003, when the dusty source G1 was approaching with the black hole. We did not observe any enhancement of the luminosity of Sgr A* during the closest approach of G1 in 2001 and a few years later. This result

rules out the gas cloud nature of G1 and it is consistent with G1 being a self-gravitating object (*Witzel et al.*, 2017).

Chapter 6

Future Work

"Our current understanding of the relationship between central massive black holes and their host galaxies have reached a point where we are limited by the range of systems that are available for observations with the telescopes available today. The next leap in our understanding of the formation of central black holes and galaxy evolution will only be possible with the next generation of very large telescopes such as TMT [Thirty Meter Telescope] in combination with the integral-field spectroscopic capabilities of an instrument like IRIS."

– *Do et al.* (2014), *The Astronomical Journal*

6.1 Future Work

Our knowledge of the supermassive black hole at the center of the Galaxy has made great progress. The distance and mass of Sgr A* have now been measured with high accuracy (uncertainty of its mass is $< 0.9\%$ and its distance $< 0.4\%$ according to *Gravity Collaboration et al.*, 2018a).

Despite of several decades of observations, there are still many gaps in our understanding of the distribution of stars around Sgr A* due to the observational difficulties we are facing (extreme extinction and crowding, see

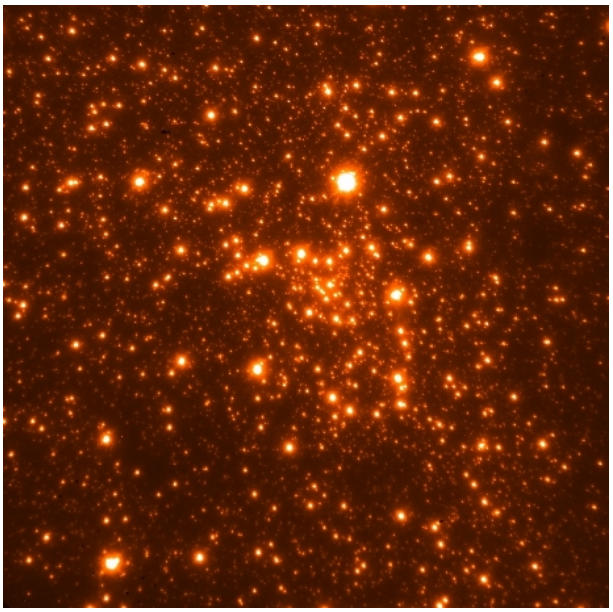

Figure 6.1: Final image for IB filter with K= 2.30μm.

Chapter 1). Future investigations need to be done to refine our understanding of the MWNSC and its star formation history. On the observational side, we need to infer robust data on the large-scale two-dimensional distribution of stars out to about 10 pc from Sgr A* with high sensitivity and angular resolution. We will then be able to reconstruct the intrinsic three-dimensional profile of the cluster. The next step will then be an accurate determination of the different types of faint stars near Sgr A* (e.g.: Which ones are pre-MS stars?) in order to understand the age structure of the nuclear star cluster. While the future generation of 30-40 m extremely-large ground-based telescopes [1] will allow us to study photometrically solar-mass stars at the GC ($\sim$ 21 magnitudes in the K-band), their spectroscopic identification will be out of reach.

My next goal is developing a new method of stellar classification based on

[1] Thirty Meter Telescope (TMT) International Observatory on Maunakea in Hawaii, the Giant Magellan Telescope (GMT) in Las Campanas Observatory in Chile, and Extremely Large Telescope (ELT) in the Atacama Desert in Chile.

the intermediate-band (IB) photometry and H-band, to be able to identify faint early-type and late-type candidate stars in the extended vicinity of the central massive black hole. Then I will use the new information of the stellar population to study the structure and formation history of the MWNSC. I use high resolution images obtained by NACO instrument at the ESO VLT. I use NIR H-band and 7 IB filters covering the NIR, the same data as the previous work (*Buchholz et al.*, 2009; *Plewa*, 2018) but we go deeper and detect more stars by improving the reduction and analysis (rebbining, optimising the PSF fitting, improving the alignment and the repair saturated stars), and by applying bootstrapping to determine robust uncertainties.

I have finished the reduction and bootstrapping analysis of all the epochs. The next steps are the following:

1. Calibration of the measured spectral energy distribution (SED):
   - Absolute calibration: The measured counts for each source in each band is converted into magnitude.
   - Relative calibration: the bands have to be calibrated relative to each other to ensure smooth spectral smooth spectral energy distributions (SEDs).
2. Compare the resulting SEDs with a blackbody of variable extinction then allows us to determine the presence and strength of a CO absorption feature to distinguish between early and late type stars.
3. Classification and comparison to sources of known classification.

Beside the images of the inner parsec around Sgr A*, we have other sets of data never studied so far of regions further out, with a radial distance of ~ 3 pc from the black hole.

My next work goes beyond using observations from current telescopes. I aim also at determining the optimal K intermediate bands to separate

different types of stars, up to MS stars, for the next generation of telescopes (TMT, ELT...) in the vicinity of the central massive black hole.

Appendix A

Systematic errors of the 2D fit of the stellar density maps

In this appendix we examine some of the potential sources of systematic errors in the computation of the main NSC parameters in Chapter 3.

A.1 Extinction and completeness

As we saw in the section 3.2.1, we do not apply any completeness correction to the data but we mask out the pixels where the density is too low (or high) by comparing with their neighbors. Moreover, we limit us to study only the fields where the completeness is greater than 50% in the range of magnitudes considered.

In order to study the systematic uncertainty derived by the extinction-correction we analyze the density map without any corrections. All the parameters that we obtain in the fits are consistent with the final results in Table 3.3 at the 3σ level. We also repeat all the procedure to create the stellar density maps by considering a less steep value for the extinction index. We use $\alpha = 2.11 \pm 0.06$ from *Fritz et al.* (2011). The best-fit parameters are

consistent with the final values in Table 3.3 at the $1-2\sigma$ level. Therefore, no significant impact on the results is found due to this effect. Although the value of $\alpha \sim 2.30$ from *Nogueras-Lara et al.* (2018a) that we use has been obtained for the central field ($\sim 7.95' \times 3.43'$), *Nogueras-Lara et al.* (2018b) have studied other regions further out and have obtained a value of α very similar within the uncertainties. Therefore, we can expect that the value of the extinction index is approximately constant for the entire FOV of our data. We conclude that extinction and completeness are not a significant source of systematic errors.

A.2 Mask

In this section, we test the effect of different masks in the fits. As we explain in section 3.2.1, we create masks to take into account the inhomogeneity of the field of HAWK-I data. Figure A.1 shows two of the masks that we applied. Masks range from less restrictive (Mask 1) to more restrictive (Mask 4). The differences between the masks are due to the selection of different values for the density thresholds to mask out regions with low density.

Table A.1 shows all the results for masks 1, 2, 3 and 4. The uncertainties are the standard deviations of the best-fit parameters. The selection of the mask is an important source of systematic error that we have already considered in Table 3.3.

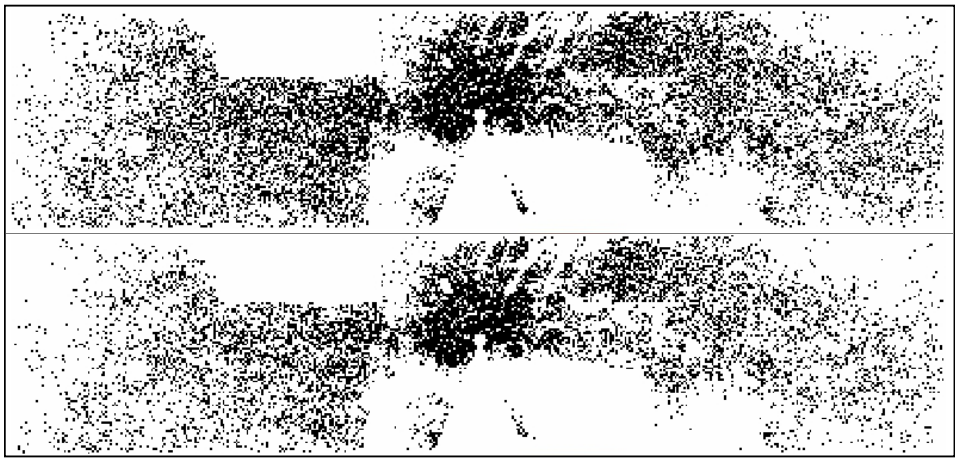

Figure A.1: Masks 2 and 3 applied to the extinction-corrected stellar number density maps of the central 86pc x 20.2pc of the Galaxy. The masked regions are in white color. The differences between both masks are due to the selection of two different values for the density thresholds to mask out regions with low density. Galactic north is up and Galactic east is to the left. The Galactic plane runs horizontally.

Table A.1: Test of potential sources of systematic errors in the NSC parameters obtained in the Sérsic fits due to the selection of the masks. The MWNSC is aligned with respect to GP.

ID	Mag. range ($K_{s,extc}$)	Mask	$N^b_{e,nsd}$ (stars/bin^2)	$N^c_{e,nsc}$ (stars/bin^2)	q^d	n^e	R^f_e (pc)
1	$12.5-14$	3	2.39 ± 0.01	3.49 ± 0.27	0.83 ± 0.01	2.73 ± 0.11	5.83 ± 0.28
2	$12.5-14$	4	2.57 ± 0.01	3.86 ± 0.28	0.79 ± 0.01	2.73 ± 0.10	5.42 ± 0.24
3	$12.5-14^a_{sym}$	1	2.36 ± 0.01	4.32 ± 0.19	0.89 ± 0.01	2.38 ± 0.07	5.68 ± 0.15
4	$12.5-14^a_{sym}$	2	2.49 ± 0.01	4.09 ± 0.20	0.87 ± 0.01	2.52 ± 0.07	5.73 ± 0.17
5	$9-12$	3	0.47 ± 0.00	1.25 ± 0.13	0.59 ± 0.01	2.22 ± 0.17	3.92 ± 0.23
6	$9-12$	4	0.49 ± 0.00	1.21 ± 0.13	0.56 ± 0.01	2.25 ± 0.17	4.09 ± 0.25
7	$9-12^a_{sym}$	1	0.61 ± 0.01	1.26 ± 0.09	0.62 ± 0.01	2.04 ± 0.11	4.68 ± 0.19
8	$9-12^a_{sym}$	2	0.64 ± 0.01	0.91 ± 0.09	0.61 ± 0.01	2.61 ± 0.16	5.61 ± 0.35
9	$9-14$	3	3.23 ± 0.01	5.52 ± 0.28	0.78 ± 0.01	2.43 ± 0.07	5.54 ± 0.17
10	$9-14$	4	3.46 ± 0.01	5.99 ± 0.28	0.75 ± 0.01	2.40 ± 0.06	5.20 ± 0.15
11	$9-14^a_{sym}$	1	2.99 ± 0.01	7.52 ± 0.16	0.80 ± 0.01	1.60 ± 0.03	5.40 ± 0.07
12	$9-14^a_{sym}$	2	3.19 ± 0.01	7.17 ± 0.16	0.79 ± 0.01	1.63 ± 0.03	5.37 ± 0.07

Notes.

[a] Fits to the symmetrized images that we create by assuming symmetry of the NSC with respect to the GP and with respect to the Galactic north-south axis through Sgr A*.[b] Stellar number density for the NSD at its effective radius. [c] Stellar number density for the NSC at the effective radius R_e. [d] The flattening q is equal to the minor axis divided by the major axis. [e] n is the Sérsic index.[f] R_e is the effective radius for the NSC.

We test the systematic errors associated with the selection of the masks for the fits where we leave the tilt angle between the NSC and the GP free. Table A.2 shows all the obtained results. It is an important source of systematic error that we have already considered in Table 3.4. The parameters do not show a systematic behavior if we apply a more restrictive.

Table A.2: Test of potential sources of systematic errors in the NSC parameters obtained in the Sérsic fits due to the selection of the masks. The tilt angle θ between the NSC and the GP is a free parameter in the fits.

ID	Mag. range ($K_{s,extc}$)	Mask	θ^b (degree)	$N_{e,NSD}$ (stars/bin^2)	$N_{e,NSC}$ (stars/bin^2)	q	n	R_e (pc)
1	$12.5-14$	3	-8.50 ± 1.03	2.39 ± 0.01	3.53 ± 0.26	0.82 ± 0.01	2.70 ± 0.10	5.83 ± 0.26
2	$12.5-14$	4	-8.52 ± 0.83	2.56 ± 0.01	3.87 ± 0.28	0.77 ± 0.01	2.71 ± 0.10	5.45 ± 0.24
3	$12.5-14^a_{sym}$	1	-8.51 ± 0.00	2.32 ± 0.01	3.18 ± 0.24	0.87 ± 0.01	3.20 ± 0.14	6.69 ± 0.30
4	$12.5-14^a_{sym}$	2	-8.51 ± 0.00	2.45 ± 0.01	2.92 ± 0.25	0.87 ± 0.01	3.43 ± 0.16	6.80 ± 0.35
5	$9-12$	3	-5.65 ± 0.87	0.47 ± 0.01	1.33 ± 0.12	0.57 ± 0.01	2.06 ± 0.15	3.85 ± 0.20
6	$9-12$	4	-5.56 ± 0.74	0.49 ± 0.01	1.28 ± 0.12	0.54 ± 0.01	2.12 ± 0.15	4.04 ± 0.23
7	$9-12^a_{sym}$	1	-5.60 ± 0.00	0.60 ± 0.01	1.26 ± 0.07	0.75 ± 0.01	1.67 ± 0.08	4.42 ± 0.15
8	$9-12^a_{sym}$	2	-5.60 ± 0.00	0.63 ± 0.01	1.08 ± 0.08	0.71 ± 0.01	1.87 ± 0.10	4.94 ± 0.22
9	$9-14$	3	-7.47 ± 0.60	3.23 ± 0.01	5.60 ± 0.27	0.76 ± 0.01	2.39 ± 0.07	5.53 ± 0.16
10	$9-14$	4	-6.49 ± 0.54	3.45 ± 0.01	5.92 ± 0.27	0.74 ± 0.01	2.40 ± 0.06	5.27 ± 0.15
11	$9-14^a_{sym}$	1	-6.98 ± 0.01	2.96 ± 0.00	6.88 ± 0.25	0.75 ± 0.01	2.23 ± 0.07	5.69 ± 0.12
12	$9-14^a_{sym}$	2	-6.98 ± 0.01	3.18 ± 0.00	8.14 ± 0.23	0.74 ± 0.01	2.00 ± 0.05	4.97 ± 0.08

Notes.

[a] Fits to the symmetrized images that we create by assuming symmetry of the NSC with respect to a rotated axis with the GP. The value of the tilt angles are the mean of the values obtained in the fits for the images applying two different masks. [b] The tilt angle between the NSC and the GP in degrees. Positive angles are clockwise with respect to the GP.

A.3 Inner mask

In this section, we examine several potential sources of systematic errors in the NSC parameters due to mask different central regions around Sgr A*. In order to explore the systematic errors, we test masking the central 0.4pc, 0.6pc, 0.8pc, respectively. Table A.3 shows the results. The final uncertainties are included in Table 3.3 and Table 3.4 by adding quadratically to the uncertainties due to the selection of the mask computed in the previous section.

Table A.3: Test of potential sources of systematic errors in the NSC parameters obtained in the Sérsic fits due to mask the inner 0.4pc, 0.6pc and 0.8pc, respectively, around Sgr A*. We only show the parameters of the magnitude ranges affected significantly by this effect. The first three rows corresponding to the fits considering $\theta = 0$ (the MWNSC aligned with respect to GP). The last three rows corresponding to the fits where we leave θ free.

ID	Mag. range ($K_{s,extc}$)	θ^b (degree)	$\sigma(\theta)$ (degree)	N_{nsc} (stars/bin^2)	$\sigma(N_{nsc})$ (stars/bin^2)	n	$\sigma(n)$	R_e (pc)	$\sigma(R_e)$ (pc)
1	$12.5-14$	0	-	$3.84, 3.86, 3.66$	0.11	$2.75, 2.73, 2.86$	0.07	$5.44, 5.42, 5.57$	0.08
2	$9-12$	0	-	$1.11, 1.21, 1.35$	0.12	$2.53, 2.25, 1.85$	0.34	$4.22, 4.09, 3.92$	0.15
3	$9-14$	0	-	$5.78, 5.99, 6.24$	0.23	$2.47, 2.40, 2.33$	0.07	$5.30, 5.20, 5.06$	0.12
4	$12.5-14$	$-5.5, -8.5, -10.8$	2.6	$3.84, 3.87, 3.96$	0.06	$2.73, 2.71, 2.69$	0.02	$5.47, 5.45, 5.38$	0.05
5	$9-12$	$-3.8, -5.6, -6.2$	1.2	$1.18, 1.28, 1.48$	0.15	$2.42, 2.12, 1.61$	0.41	$4.14, 4.04, 3.82$	0.16
6	$9-14$	$-5.6, -6.5, -7.3$	0.9	$5.75, 5.92, 6.33$	0.30	$2.47, 2.40, 2.28$	0.09	$5.34, 5.27, 5.06$	0.14

A.4 Binning

We analyzed the results considering different ways of binning the data. Firstly, we study the optimal bin size for our density maps following the studies of *Knuth* (2006) and *Witzel et al.* (2012). We limit our sample to the stars brighter than $K_s = 16.0$. The dependence of the Relative Logarithmic Posterior Probability (RLP) on the bin number is shown in Fig. A.2. The maximum for the RLP for the star number is reached for 147 bins, and the best bin size is $7''$. Secondly, we test different values of binning ($2''$, $5''$, $7''$) and we obtain all the values for the NSC parameters consistent with the final results in Table 3.3 at the 2σ level. We select a bin size of 5" × 5" because it is more suited for our data and let us to study the major features in the large scale of the NSC with enough detail without taking into account the random fluctuations. We conclude that binning is not any significant source of systematic errors in our analysis.

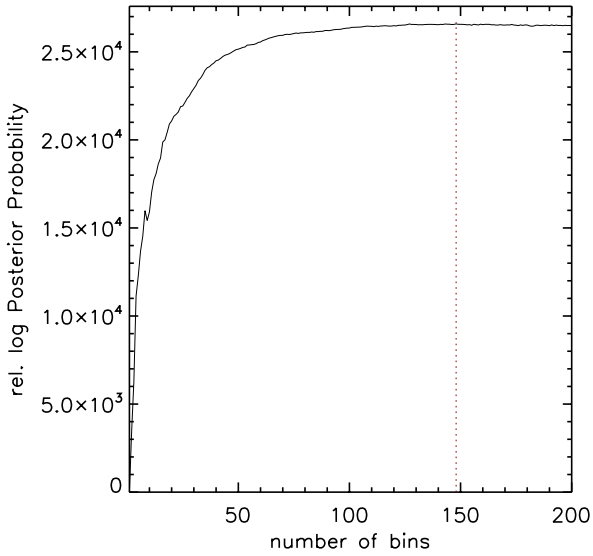

Figure A.2: Optimal binning. We show the RLP as a function of the number of bins. The maximum for the RLP is reached for 147 bins (red dotted line). We study all stars brighter than $K_s = 16.0$

A.5 Edges between NACO and HAWK-I

As we saw in section 3.2, we compute the mean density in the edges between HAWK-I and NACO data. We explore the source of systematics associated with the size of the edges that we choose. The differences between the obtained NSC parameters and the values in Table 3.3 are negligible.

A.6 Contamination by foreground stars

We have removed in the fits for the NSC the contribution of NSD and GB. We explore also to exclude foreground stars from the GD based on their color H - K_s. If we do not consider stars with $H - K_s < 1.2$, the best-fit parameters are consistent with the final values in Table 3.3 at the 1σ level. Therefore, no significant impact on the results is found due to this effect.

A.7 Magnitude cut

We analyze the fits if we create the density maps by considering a magnitude cut $K_s = 15.5$ before the extinction correction. All the values for the NSC parameters are consistent with the final results in Table 3.3 at the 2σ level.

A.8 Saturation of stars

We select the brightest magnitude in the range of the stars to be not significantly affected by saturation. For HAWK-I data, stars with $K_s \sim 11.0$ ($K_{s,extc} \sim 9.0$) are saturated. We have selected the bright limit of $K_s = 11.0$ ($K_{s,extc} = 9.0$) in our analysis, but we explore another bright limit, $K_s = 10.0$ ($K_{s,extc} = 8.0$). The differences in the NSC parameters that we obtain are very small (for $\Delta Re < 3.1\%$, $\Delta n < 2.5\%$ and $\Delta q < 0.7\%$).

A.9 Possible contamination for young stars

We aim to study the structure of the relaxed stars in the NSC. We know that a star formation event created on the order $10^4\,M_\odot$ of young stars in the region about 0.5 pc around Sgr A* (*Bartko et al.*, 2010; *Lu et al.*, 2013; *Feldmeier-Krause et al.*, 2015). As we saw in section 3.2, we exclude all spectroscopically identified early-type stars from our sample (using the data of *Do et al.*, 2013). In addition, the 90% of the young stars found in *Feldmeier-Krause et al.* (2015) are identified within 0.5 pc, therefore, further out we do not expect important contamination by young stars in our sample. We apply an inner mask in the region 0.6 pc around Sgr A*. We conclude that the contamination of young stars in our data is not significant.

A.10 Initial tilt angle

In this section, we focus on the sources of systematic errors that affect the possible tilt angle (θ) between the NSC and the GP obtained in the fits. We have already studied the effect of the mask in the last section. In this section, we explore the systematic errors associated with the selection of different initial θ to perform the fit. As we see in previous sections, in order to find the best-fit parameters, we use the IDL MPCURVEFIT procedure that performs a Levenberg-Marquardt least-squares fit. The algorithm finds the local minimum that minimizes the chi-square, which is not the global minimum in most cases. We compare the average of the residuals obtained by subtracting the symmetrized maps from the images (see Fig 3.10) and we find multiple minima for different tilt angles. For this reason is very important to provide an initial guess for θ close to the final solution in order to obtain the global minimum. Figure A.3 shows the best-fit tilt angles versus different initial values of the angle for the different magnitude ranges. The median values are indicated in the plots. The errors are the average deviation from the median. We reject data more than 3σ from the median.

We conclude that the initial θ is a significant source of systematic errors in our analysis and we include them in our final budget in Table 3.4.

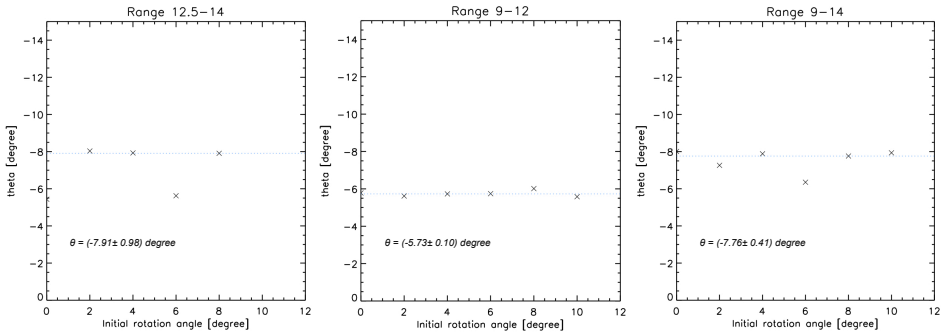

Figure A.3: Mean values of the best-fit tilt angles (θ) for the different magnitude ranges obtained from the fits by considering different initial values. The dotted blue line indicates the median θ and their values are shown in the different panels.

Appendix B

Systematic errors of the 2D fit of the surface density profile

In this appendix we examine some of the potential sources of systematic errors in the computation of the power law indices for the surface density fits in Chapter 4. The analysis was published in the journal *Astronomy & Astrophysics* in *Gallego-Cano et al.* (2018).

B.1 *Starfinder* parameters, extinction, and completeness

There can be no absolute certainty in the reliability of source detection. For that reason, we analysed the images with different values of the *StarFinder* parameters, as described in section 4.2.1. All error bars used in this work include the uncertainties due to different choices of *StarFinder* parameters, as well as the uncertainties of extinction and completeness corrections.

B.2 Binning

We analyse the results considering different ways of binning the data. As we see in Section 4.1, we study the maximum for the RLP for the star number and we obtain the best bin size for our sample. We also test other values of binning($0.5''$, $1''$, $1.5''$) and we obtain a value of the systematic error in the index of the power law less than 0.01 for RC stars and less than 0.001 for fainter stars($17.5 \leq K_s \leq 18.5$). We conclude that binning is not any significant source of systematic errors in our analysis.

B.3 Fitting range

As we can see in Table 4.1, the assumed fitting range can lead to significant variations in the best value of the projected power-law index Γ. It is on the order $\Delta\Gamma = 0.1$.

B.4 Correction for young stars

When we study the distribution of fainter stars we have to consider the possibility that our stellar surface number density is contaminated by pre-MS stars from the latest star formation event, as discussed in section 4.5.1. As we see, we model the surface density profile of the young stars by a simple power-law and compute the number of young stars considering different scenarios. The uncertainty of this correction depends primarily on the assumed surface density distribution and mass of the young stars and is on the order of 0.05. While the precise age of the cluster does not matter, the assumed IMF is paramount. Here, we assumed the IMF of *Lu et al.* (2013) as a conservative case. If the IMF is chosen as top-heavy as in *Bartko et al.* (2010), then the contamination by pre-MS stars can be considered insignificant

Appendix C

Systematic errors of the 3D fit of the Surface Density Profile

In this section we examine several potential sources of systematic errors in the computation of the power law indices for the fits of the 3D density (see Section 5.4) for the two analysed ranges of old stars: RC and fainter stars. The analysis was published in the journal *Astronomy & Astrophysics* in *Gallego-Cano et al.* (2018).

C.1 Subtracted contribution from the nuclear disk

When fitting the Nuker profiles we assume different models for the contribution of stars that do not belong to the nuclear cluster. Table 4.4 lists the best-fitting parameters under those different assumptions, which are included in our final error estimation.

C.2 Correction for young stars

When we compare models 5 and 11 in Table 4.4 we can see that the contamination by pre-MS stars can change the best-fit value of γ by about 0.1

dex.

C.3 Uncertainties from deprojection

As we see in Section 5.4, we are interested in studying the 3D structure of the old cluster. We need to convert the measured 2D profile into a 3D density, so we need to consider the source of uncertainty from deprojection. For this purpose, a 3D cluster was simulated in order to project it and apply our procedure for density estimation. We proceed as follows:

1. Different 3D clusters are simulated, where 1.000.000 stars are distributed following a 3D Nuker model (equation 1). In order to explore which parameters in the Nuker fit are more sensitive to the variations of the model, we test different cluster: clusters with a systematic variation in the break radius($r_b = 1.6, 5.8, 6.4$), clusters with a systematic variation in the exponent of the inner power-law ($\gamma = 0.68, 1.74, 2.32$) and clusters with a systematic variation in the exponent of the outer power-law($\beta = 4.8, 6.4$).

2. Extraction of 100 randomised samples from each model with the same star number of our sample.

3. Computation of projected density.

4. Apply the fit to the samples.

5. Comparison the input parameters in the simulation and computed parameters in the samples for each of the different models.

Table C.1: 3D cluster simulations to analyse the effect of the deprojection from 3D cluster into a 2D one. The three first columns show the values of the Nuker parameters adopted for the simulations. The last six columns show the standard deviation and the median of the parameters obtained with our fit for each of the samples of each of the different model clusters.

ID	r_b	γ	β	$\sigma(r_b - r_{b0})$	$median(r_b - r_{b0})$	$\sigma(\gamma - \gamma_0)$	$median(\gamma - \gamma_0)$	$\sigma(\beta - \beta_0)$	$median(\beta - \beta_0)$
1	3.20	1.16	3.20	0.15	-0.01	0.09	-0.05	0.07	0.01
2	1.60	1.16	3.20	0.06	0.02	0.08	-0.01	0.03	0.05
3	4.80	1.16	3.20	0.32	0.04	0.09	-0.05	0.14	-0.05
4	6.40	1.16	3.20	0.67	-0.23	0.12	-0.11	0.36	-0.18
5	3.20	0.58	3.20	0.18	-0.04	0.19	-0.21	0.07	0.02
6	3.20	1.74	3.20	0.19	0.12	0.04	0.09	0.08	0.03
7	3.20	2.32	3.20	0.37	0.81	0.02	0.18	0.10	0.09
8	3.20	1.16	4.80	0.06	0.13	0.04	0.03	0.07	0.25
9	3.20	1.16	6.40	0.04	0.11	0.03	0.01	0.11	0.34

Table C.1 shows the results. We can see that γ is the least sensitive parameter to the break radius variations or to beta exponent variations of the model ($\sigma(\gamma) < 0.1$) . Only in the case of $\gamma = 0.58$ we can see a large difference between the gamma input parameter and the recovered ones. In general, the break radius parameter is the most sensitive to variations of the model. As we can see, if we ignore the model with $\gamma = 0.58$ as an outlier (it is basically excluded by our data), safe assumptions for the systematic uncertainties due to deprojection are $\Delta\gamma \approx 0.1$; for $\Delta\beta \approx 0.1$, and $\Delta r_b \approx 0.2$.

C.4 Systematic errors of the inner power-law index by using HAWK-I data

In this section, we examine several potential sources of systematic errors in the computation of the power-law indices for the fits of the 3D density. We only focus on the possible systematics due to the computation of the star density at large distances, by using data from the present work. The Table shows the best-fit parameters for the break radius r_b, for the exponents of the inner, γ, and the outer, β power-law. Table C.2 shows the results of our fits, where we consider two ways of binning the data (5 arcsec and 10 arcsec, respectively), use two different masks, and consider two different ranges of magnitudes for the stars that we select (bright and faint stars). Finally, we compute the density along the GP in a strip $\pm 50''$ and azimuthally averaged in annuli around Sgr A*.

Table C.2: Best-fit model parameters for *Nuker* fits.

ID	Mag. range ($K_{s,extc}$)	Mask	Bin size (arcsec)	r_b (pc)	γ	β	$\chi^2_{reduced}$
1^a	$12.5-14$	3	10	1.99 ± 0.19	1.34 ± 0.05	2.64 ± 0.10	1.39
2^a	$12.5-14$	4	10	1.97 ± 0.20	1.34 ± 0.05	2.70 ± 0.12	1.16
3^a	$12.5-14$	3	5	1.86 ± 0.12	1.30 ± 0.05	2.75 ± 0.08	1.30
4^a	$9-12$	3	10	2.23 ± 0.47	1.45 ± 0.05	2.38 ± 0.16	0.64
5^a	$9-12$	4	10	2.04 ± 0.45	1.44 ± 0.05	2.33 ± 0.15	0.51
6^a	$9-12$	3	5	2.11 ± 0.32	1.44 ± 0.04	2.51 ± 0.14	0.70
7^b	$12.5-14$	3	10	2.04 ± 0.15	1.33 ± 0.05	2.81 ± 0.08	1.82
8^b	$12.5-14$	4	10	2.00 ± 0.15	1.32 ± 0.05	2.86 ± 0.10	1.60
9^b	$12.5-14$	3	5	1.95 ± 0.11	1.30 ± 0.05	2.93 ± 0.07	1.67
10^b	$9-12$	3	10	2.67 ± 0.37	1.44 ± 0.04	2.80 ± 0.19	1.00
11^b	$9-12$	4	10	2.63 ± 0.39	1.44 ± 0.04	2.87 ± 0.23	0.85
12^b	$9-12$	3	5	2.54 ± 0.25	1.42 ± 0.04	3.01 ± 0.18	0.96

Notes.
[(a)] Fit range: $0.04 \leq R \leq 20$ pc. Stellar number density for large radii computed along the GP in a strip ± 50 arcsec. [(b)] Fit range: $0.04 \leq R \leq 20$ pc. Stellar number density for large radii has been computed azimuthally averaged in annuli around Sgr A*.

C. SYSTEMATIC ERRORS OF THE 3D FIT OF THE SURFACE DENSITY PROFILE

Appendix D

Photometric accuracy and recovery of diffuse light with StarFinder

In this section we explore two issues via simulations of the Galactic Centre: (1) Photometric accuracy and point-source residuals when the PSF varies across the field due to anisoplanatic effects. (2) The capability of recovering the diffuse light with Starfinder in a GC-like environment and with a spatially variable PSF. The analysis was published in the journal *Astronomy & Astrophysics* in *Schödel et al.* (2018). As a test case we use observations of NACO through the Brγ filter, where the diffuse background is particularly high and variable due to the strong line emission from the minispiral.

The simulated images are based on the Brγ observations described in section 2. We used stellar sources detected down to $K_s = 18$, where the star counts are reasonably complete across the field and source detection is highly reliable. The guide star PSF was extracted from IRS 7 in the original Brγ data, after having repaired the saturated core of IRS 7. To simulate the variation of the PSF across the field, we modelled the loss of Strehl and elongation of the PSFs via convolution with Gaussian kernels. The latter are chosen as being elongated along the line connecting any given star to the

guide star, a typical manifestation of anisoplanatic effects. The FWHM of the Gaussians along these lines grows by 0.027″ for every 10″ distance from IRS 7 and by 0.008″ in the perpendicular direction. In this way we obtain a simulated image that appears similar to the original image, albeit with a somewhat stronger anisoplanatic effect, which is good because it means that we are carrying out our simulations for a conservative test case. We use a FWHM of the PSF of about 0.08″ for the guide star. At a distance of 20″ from the guide star, the PSF has a FWHM of about 0.1″ along the line connecting it with the guide star.

Finally, we added readout and photon noise (both from sources and from the sky). We then carried out runs of *StarFinder* both with a constant and with a variable PSF, the latter as described in section 2.

We simulated images with a flat, zero background, with a complex background by including the minispiral, and with a complex background that includes the minispiral and an additional diffuse power-law component. As described in section 2, we do not fit the background with *StarFinder*, that is, the keywords $BACK\_BOX$ and $ESTIMATE\_BG$ are set to zero. Instead, we determined the diffuse light directly from the point-source-subtracted images. As a side note, we point out that throughout this paper we use the terms background and diffuse emission in an equivalent way.

In all simulated images, we first repaired the core of the PSF of the brightest star, IRS 7. Although it was not saturated in the simulated images, of course, it is saturated in the real data and this step is necessary because if forms an integral part of the data reduction. It will lead to a slight broadening of the guide star's PSF because its core is replaced by the median of the cores of nearby stars, that have a somewhat lower Strehl. We note that we wrote our own code for repairing the core of IRS 7 because the native *StarFinder* code for this purpose, REPAIR_SATURATED.PRO will only work accurately if the complete PSF is known a priori. However, this is not the case here, where we actually use the brightest, saturated star to estimate the broad, extended wings of the PSF. We mention this problem

here because it may arise in most similar situations where a user wants to repair the cores of saturated stars with *StarFinder*. The key is that, while *StarFinder* only applies a multiplicative scaling factor, one must also use an additive offset when fitting the core to the saturated star.

When we apply PSF fitting with a variable PSF, we sub-divide the simulated image into overlapping square fields of $10.8''$ size on a side, that we call 'sub-images'. A local PSF is estimated from the brightest, isolated stars in each field. Subsequently, the wings from the bright guide star are fitted to this local PSF and PSF fitting is performed on each sub-image. The sub-images overlap by half of their size. When recomposing the point-source-subtracted images, the borders of the sub-images (about $2''$ width) are removed and the remaining overlapping areas are averaged. In this way we can create a homogeneous residual image.

D.0.1 Variable PSF and constant zero background

Our first test is performed with a constant background of value zero. Several images and plots that evaluate this test quantitatively are shown in Fig. D.1.

We can see that the residuals are significant and systematic in case of using only a single, constant PSF. They are significantly smaller and more constant across the field when we use a variable PSF. Quantitatively, this effect can be seen nicely in the plot of the differences between measured and input magnitudes for the stars. They show a systematic trend with distance from the guide star in case of use of a single PSF. With a variable PSF, some local systematics appear (as expected because we do not model the PSF for each position), but they are far smaller. In general, systematic photometric uncertainties due to PSF variability are on the order of just a few 0.01 mag when we use a variable PSF. As concerns the measured background, after point-source subtraction, it is close to zero, but has a small, positive bias that increases with distance from the guide star. This trend can possibly be partially explained by the fact that measurements become

less accurate towards the image edges because we cannot minimise uncertainties by multiple measurements in overlapping fields near the edges and because the potential PSF reference sources are fewer and fainter towards the image edges. Variable PSF fitting performs better in background recovery than constant PSF fitting. We also note that there is a small dip of the recovered background close to the position of Sgr A*. We believe that this is due to the strong concentration of bright stars there. It appears that the broadening of the PSF caused by the necessary superposition of several reference stars leads to negative residuals close to bright stars. In any case, the positive residual is very small. It is, in the worst case, not more than a few percent of the surface brightness of the mini-spiral or diffuse stellar emission that we analyse in this work. We thus conclude that it is safe to ignore it. We also conclude that using a variable PSF is superior to using a constant PSF and that a constant flat background $\gtrsim 1.0\,\mathrm{mJy\,arcsec^{-2}}$ can be accurately recovered by our method.

D.0.2 Variable PSF plus complex diffuse emission from gas

To model highly complex diffuse emission we used the HST Paschen α image of the minispiral, transformed it to the frame of the NACO Brackett-γ image, and scaled its flux accordingly. Some smoothing was applied to mitigate the effects of interpolation. Then we proceeded as described above. In Fig. D.2 we show the simulated image after fitting and subtracting the point-sources and the residual after, additionally, subtracting the input gas emission. Finally, we show the plot of residual light density as a function of distance from Sgr A*. It is close to zero at all distances, very similar as in the case of a flat, zero background. We conclude that our variable PSF fitting with *StarFinder* can reproduce very well the details of complex diffuse emission and that the residual light can be reproduced accurately after the complex diffuse emission is removed. Here, we remind the reader again that we do not fit the diffuse emission with *StarFinder*. We just fit and subtract the point-sources.

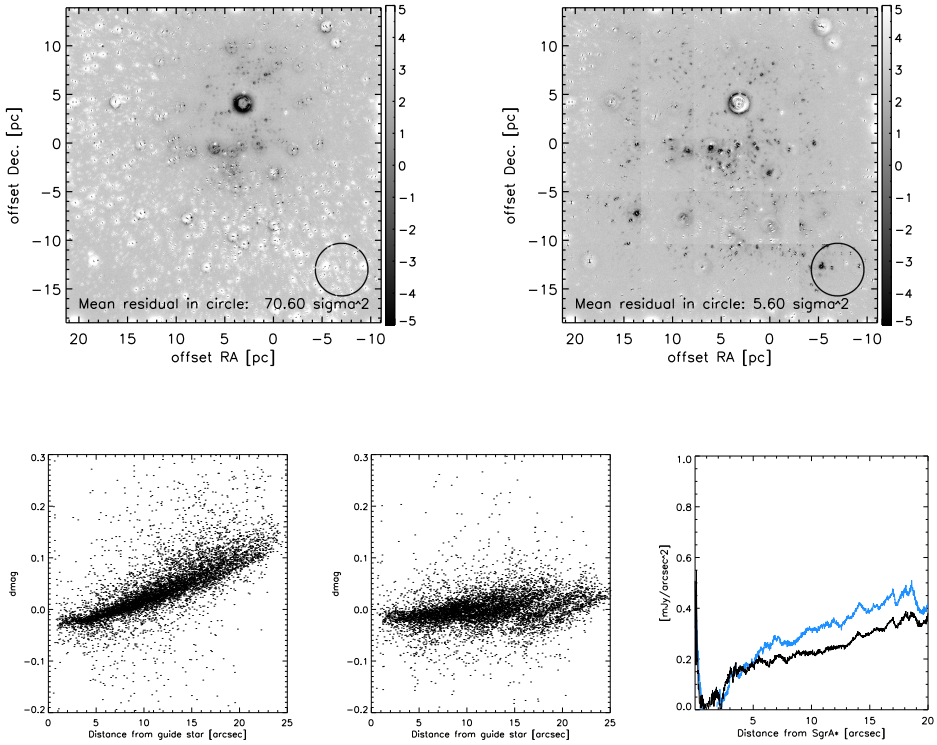

Figure D.1: PSF fitting test with a variable PSF and a constant background. Upper left: Point-source subtracted image after use of a single, constant PSF. The circle in the lower right shows a region in which we measured the sum of the squared residual, which is $70.6\,\sigma^2$ for this region. Upper right: Like upper left, but after using a variable PSF. The sum of the squared residual in the circle is $5.6\,\sigma^2$. The grey scales are expressed in terms of σ deviations from the noise image. Bottom left: Differences between the measured magnitudes of stars and their input magnitudes when a single, constant PSF is used. Bottom centre: Differences between the measured magnitudes of stars and their input magnitudes when a variable PSF is used. Bottom right: Plot of background, after point-source subtraction, as a function of distance from Sgr A*. The background is the median in rings around Sgr A*. The blue data are for the case of a single PSF and the black data for the case of a variable PSF.

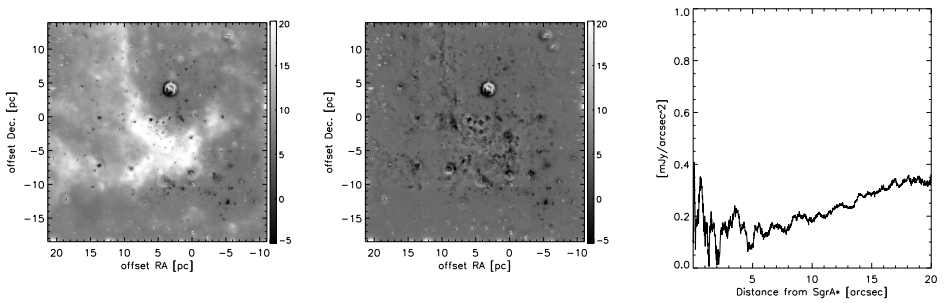

Figure D.2: PSF fitting test with a variable PSF and a complex, diffuse background. Left: Point-source subtracted image after use of a variable PSF. Middle: Residual image, after subtracting the input distribution of diffuse emission. Right: Background as function of distance from Sgr A* as measured in the residual image. The grey scales are expressed in terms of σ deviations from the noise image.

D.0.3 Variable PSF plus gas and power-law cusp

Finally, we added a power-law cusp from faint, diffuse stellar emission to the simulated image, proceeding as described in the previous sections. The cusp was simulated as a pure power-law with a 2D exponent of $\Gamma = -0.2$, a scale radius of $R_0 = 12.5''$, and a flux density of 10 mJy arcsec^2 at R_0. In Fig. D.3 we show the simulated image after fitting and subtracting the point-sources and the residual after, additionally, subtracting the gas emission. Finally, we show the plot of residual light density as a function of distance from Sgr A* with the input cusp model over-plotted. The recovered power-law cusp is almost identical to the input model, with minor deviations only near the edge of the field and near Sgr A*.

D.0.4 Variable PSF: Real data

Finally, we will take a closer look at the performance of our methodology with real data. For this purpose we use the $H-$band image used in this work. The point-source-subtracted images for a constant PSF (panel a)) and use of a variable PSF (panel b)) are shown in Fig. D.4. Significant sys-

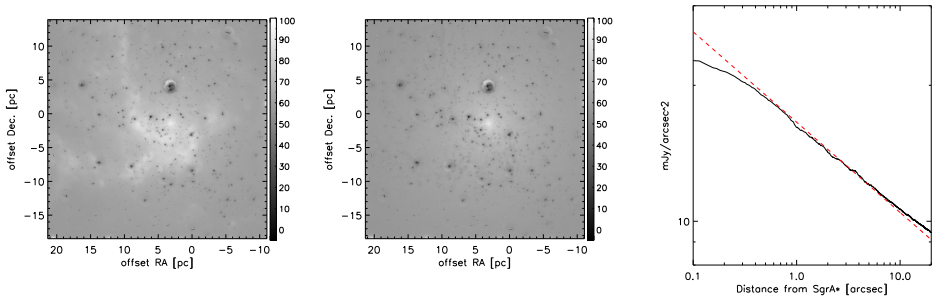

Figure D.3: PSF fitting test with a variable PSF, complex, extended emission from gas/dust, and diffuse emission from a population of unresolved faint stars. Left: Point-source subtracted image after use of a variable PSF. The grey scale is expressed in terms of σ deviations from the noise image. Middle: Residual image, after subtracting the input distribution of diffuse emission. Right: Background as function of distance from Sgr A* as measured in the residual image. The dashed red line is the power-law cusp used as input. The grey scales are expressed in terms of σ deviations from the noise image. We note that the scales are different from the ones used in in Fig. D.2

tematic residuals related to point-sources can be seen in case of the constant PSF. Moreover, those residuals vary strongly with position in the field. We point also out that the real data show a different residual pattern than the simulated data. In particular, the residuals look less symmetric than in case of the simulated data. We believe that this can probably be explained by time-variable AO performance because the final mosaic image is the result of observations of four different pointings. Variable AO perfomance is a frequent feature of AO instruments and is mostly related to changes in the atmospheric seeing. We did, however, not further investigate this effect here because it would go far beyond the purpose of this paper.

The point-source-subtracted image after using a variable PSF shows smaller residuals that are more homogeneous across the field. The total squared residuals are significantly lower than in case of a constant PSF. We note that the residuals here do still include diffuse emission from gas and unresolved stars.

Panel c) of Fig. D.4 shows the full extent of the PSF halo. It can be seen that it extends out to almost 2″ from the the centre of the PSF. Panels c) and d) show zooms onto the cores of locally estimated PSFs. It can be seen that the PSF core near the image edge, at roughly 15″ from the guide star, is elongated compared to the PSF core near the image centre.

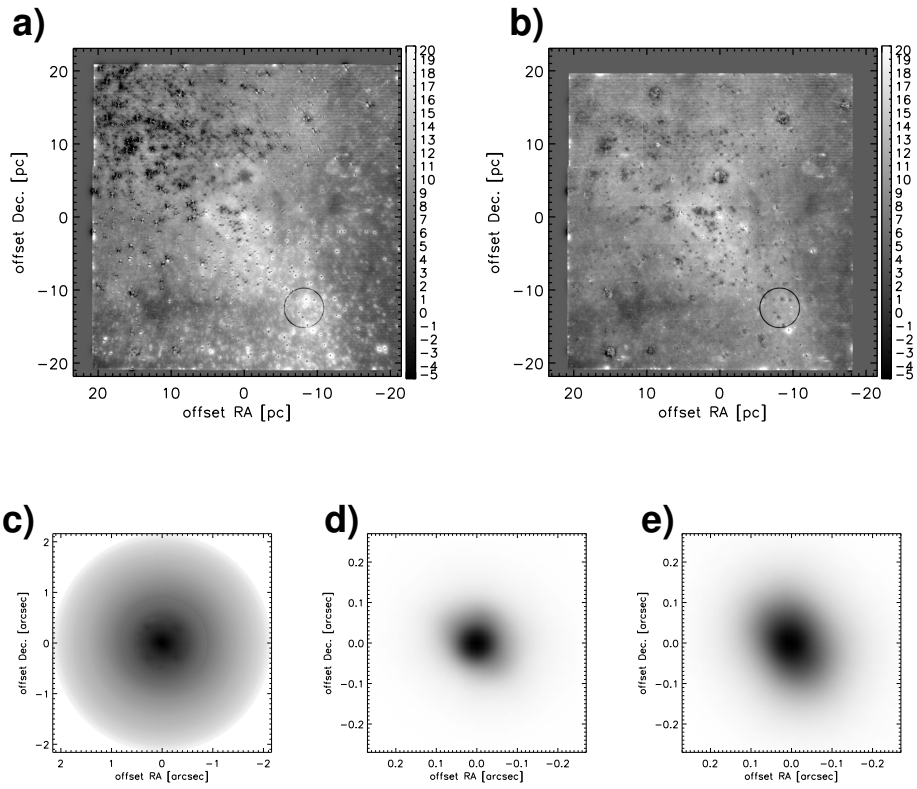

Figure D.4: PSF fitting test with a variable PSF on the H-band image used in this work. a) Point-source-subtracted image after use of a single, constant PSF. The circle in the lower right shows a region in which we measured the sum of the squared residual, which is $131\,\sigma^2$. b) Point-source-subtracted image after use of a variable PSF. The circle in the lower right shows a region in which we measured the sum of the squared residual, which is $41\,\sigma^2$. c) Full extent of the PSF. d) Zoom onto core of PSF near image centre. e) Zoom onto core of PSF near the lower right corner. All grey scale are logarithmic.

The conclusion of this appendix is that our variable PSF fitting with *StarFinder* with subsequent point-source-subtraction is well suited to recover the complex diffuse emission from gas/dust and, after removal of the latter, to measure the diffuse distribution from a faint, unresolved stellar population at the GC.

D.1 Systematic errors of the 2D fit of the SB profile

In this section we examine several potential sources of systematic errors in the power law plus scaled gas emission fits to the SFP profiles of the K_s wide field image. The results are readily applicable to the images in other filters.

D.1.1 Sky subtraction

Our experiments with the data suggest that the strongest systematic effect can arise from an unknown additive offset of the diffuse emission. Although the images were sky-subtracted – the sky background in the corresponding filters was measured on a dark cloud at a few arcminutes offset – there is some uncertainty related to this procedure: There was only one sky measurement done for the approximately one hour-long observations. Hence, the sky background may have varied. Also, we are interested in the SB profile of the nuclear star cluster, but there may be diffuse flux contributions from other structures, such as the nuclear stellar disc (see *Launhardt et al.*, 2002). Fortunately, there are several dark clouds contained in the field-of-view (FOV). Those clouds belong most probably to dense gas and dust in the so-called circumnuclear ring (CNR) in front of the nuclear star cluster (see, e.g. *Ekers et al.*, 1983; *Lo and Claussen*, 1983; *Christopher et al.*, 2005) and can thus serve to estimate the flux offset. We measured the median flux density at six positions within these dark clouds (see blue

circles in Fig. 4.13) and thus obtained an estimate for the mean and standard deviation of the constant diffuse flux offset in the K_s wide field image: 0.3 ± 0.1 mJy arcsec^{-2} (corresponding to roughly 5 mJy arcsec^{-2} if corrected for 3 mag of extinction). The surface flux density measurement was then repeated after subtracting this mean offset. The extinction correction was performed after the subtraction of this potential background bias. The resulting SB profile and best fit model is shown in panel a) of Fig. D.4, with the best-fit parameters listed in row 3 of Tab. D.1. It can be seen that uncertainty about an additive offset from the sky or from diffuse foreground radiation can have a significant (order 20%) effect on the measured value of Γ – and, by consequence, also on β.

Since in this work we analyse observations with different filters and instrument setups and taken under different conditions, we expect that we can accurately estimate the contribution from the variability of the atmospheric emission from the standard deviation of the results for the different filters (at least for Γ). As concerns the possible contribution of a diffuse component from Galactic structures in the foreground of the NSC, in particular the nuclear disc, its effect will always be a positive offset. That means that, if we subtract such an offset, Γ would increase.

D.1.2 Extinction correction

The strong differential extinction in the central parsecs of the Milky Way is well known and we correct for it in our measurements. If we assume simply a constant extinction and do not correct for its variation, then the reduced χ^2 becomes higher and the gas-subtracted SFP profile can be fit less well with a power-law. The normalisation of the SB changes by $< 10\%$ and Γ becomes steeper (see panel b) in Fig. D.5 and row 2 in Tab. D.1). The latter is to be expected because extinction is lower near Sgr A* (see, e.g. extinction maps presented in *Schödel et al.*, 2007, 2010).

In any case, this is an extreme test that overestimates the uncertainties probably significantly because, after all, interstellar extinction and its

variation towards the GC have been investigated well and can be robustly estimated (e.g. *Schödel et al.*, 2007; *Buchholz et al.*, 2009; *Schödel et al.*, 2010; *Nishiyama and Schödel*, 2013; *Hosek et al.*, 2015; *Fritz et al.*, 2016). We therefore repeated our analysis twice, once with the extinction map smoothed by a Gaussian of 2″ FWHM and once with the extinction map smoothed by a median filter in a box of of 4″ width. In these cases the final results agree, within the uncertainties, with our best estimate. We conclude that the correction for variable interstellar extinction is not a significant source of systematic error in this work.

D.1.3 Completeness effects

When studying stellar number densities, as in Paper I, assessing and correcting incompleteness due to sensitivity and, in particular, crowding can have significant effects on the results. In our study of the diffuse light density, bias related to completeness could occur as well. The contribution of the occasional bright star on the mean surface brightness at a given R will be negligible due to our use of the ROBUST_MEAN procedure, that rejects outliers and produces values very similar to the median. However, in small, crowded areas, such as the central arcseconds near Sgr A*, subtraction of faint stars may be significantly less complete so that, on average brighter stars remain in the image than in less crowded areas, which may create a systematic effect.

To examine this effect, we studied the SFP profile in images, in which stars down to different magnitude levels were subtracted: $K_s = 16$, $K_s = 18$, and all detectable stars. The $3\,\sigma$ detection limit for stars in the K_S wide field image is about $K_S \approx 19$ (albeit at low completeness). The resulting profiles and best fits are shown in panel c) of Fig. D.5. The corresponding best-fit parameters are listed in rows 5 and 6 of Tab. D.1. Apart from an overall $\sim 10 - 20\%$ shift between the measured SBs, the profiles look very similar. The best fit parameters - apart from the SB normalisation, Σ_0, - show only a small range of bias. In particular, no significant change of the

best-fit parameters occurs whether we subtract all detectable stars or only stars down to $K_s = 18$. We conclude that completeness effects are not any significant source of systematic error in this work.

D.1.4 Masking

As shown in Fig. 4.13, we mask several regions, that is, we exclude them from the analysis. These regions are extended dark clouds, residuals near the brightest star (IRS 7), objects with strong excess from line-emission or hot dust (e.g. IRS 1W, IRS 21, or IRS 13), or negative residuals around the densely clustered bright stars near Sgr A*. As panel d) in Fig. D.5 and row 4 in Tab. D.1 show, suppression of masking makes the fit noisier, but does not alter the best-fit parameters significantly. We conclude that the choice of masking applied in this work is not any significant source of systematic error.

D.1.5 Binning

We examined two different ways of binning the data. First, we binned the data in a way that each bin contained the same number of pixels. This will mean that the bins become smaller at larger R. A small ($\sim$15%) increase of Γ is observed (see panel e) in Fig. D.5 and row 7 in Tab. D.1). However, we have chosen an extreme case of binning (1×10^4 pixels or about 100 arcsec^2 per bin), which eliminates all data pints at $R < 0.1$ pc. For a less extreme binning of 10 arcsec^2 per bin, the differences in the best-fit parameters are much smaller, with $\Gamma = 0.25$.

We also tested logarithmic binning, which results in increasingly larger bins for larger R. As shown in panel f) in Fig. D.5 and row 8 in Tab. D.1, this produces no significant deviation in the best-fit parameters.

We conclude that binning is probably not any significant source of systematic errors in this analysis, but may contribute an uncertainty on the order of $\sim$5% to the value of Γ.

Table D.1: Best-fit parameters for Ks wide-field image, under different circumstances that may affect systematics. We note that all the formal uncertainties of the best-fit parameters are $\leq 1\%$, with the exception of row 8, which has significantly larger formal uncertainties due to the large reduced χ^2. The χ^2 listed here are smaller than the ones listed in Tab. 4.2 because the fitting range is different here ($R \leq 0.5\,\mathrm{pc}$ compared to $R \leq 1\,\mathrm{pc}$ in the main body of the paper; see discussion on the change of the projected power-law in sections D.1.6 and 4.6). Therefore they are not listed in this table, which serves to explore systematic uncertainties, which dominate the error budget.

	Σ_0 ($\mathrm{mJy\,arcsec^{-2}}$)	Γ	Σ_0	χ^2_{red}
1	14.3	0.32	0.057	0.3
2	22.6	0.33	0.045	1.0
3	15.7	0.31	0.057	0.5
4	20.5	0.24	0.062	0.3
5	26.8	0.25	0.058	0.1
6	21.7	0.23	0.057	0.4
7	20.7	0.27	0.062	0.5
8	21.4	0.28	0.054	2.5

Notes.

1) Final product as used in the results of this paper: Masking and extinction correction applied. 2) No correction of differential extinction, assumption of $A_{Ks} = 3.0$ constant. 3) Masking and extinction applied. Subtraction of potential sky offset of $0.3\,\mathrm{mJy\,arcsec^{-2}}$. 4) No masking applied. 5) Stars only subtracted if they are brighter than $K_s = 16$. 6) Stars only subtracted if they are brighter than $K_s = 18$. 7) Like 1), but using bins with constant number of pixels (1×10^4) per bin. 8) Like 1), but using bins of equal logarithmic width.

D.1.6 Fitting range

Finally, we study the role of the range in R used to fit the power-law from the stellar diffuse emission. When we only include data at $R \leq 0.4, 0.6, 0.8, 1.0, 1.2, 1.5\,\mathrm{pc}$, we obtain $\Gamma = 0.22, 0.21, 0.23, 0.24, 0.27, 0.31$, and $\Sigma_0 = 21.3, 21.7, 21.3, 20.9, 20.4, 20.3\,\mathrm{mJy\,arcsec^{-2}}$. As we can see, there is a systematic effect with the power-law becoming steeper at larger R. If we fit only data at $R \geq 0.5\,\mathrm{pc}$, then we obtain $\Gamma = 0.40$ and $\Sigma_0 = 22.2\,\mathrm{mJy\,arcsec^{-2}}$. We show the corresponding fit in Fig. D.6. On the other hand, if we fix the outer edge of the fitting range to $R = 1.0\,\mathrm{pc}$ and then use only data at $R \geq 0.2, 0.4, 0.6\,\mathrm{pc}$, we obtain $\Gamma = 0.30, 0.33, 0.35$, and $\Sigma_0 = 21.5, 21.7, 22.0\,\mathrm{mJy\,arcsec^{-2}}$.

We conclude that the data from the K_s wide field image show evidence for a steepening of the power-law with increasing R. When we analyse the SB profiles for the different observations in this work, we will always fit the power-law in the range $0\,\mathrm{pc} \leq R \leq 1\,\mathrm{pc}$. From our analysis here we estimate that the corresponding best-fit values of Γ may have an associated systematic uncertainty on the order of 0.05. The fitting range has only a minor contribution to the uncertainty of Σ_0, on the order of 3%.

D.1.7 Conclusion on systematic uncertainties

From the study of the different potential sources of systematic errors in this section we identify three effects with possibly significant contribution: 1) An unknown additive sky offset, 2) the fitting range, and 3) binning. Effect 1) will, however, be absorbed by our using of several independent data sets. It will mainly be important in the sense of any contribution of a non-nuclear stellar population to the diffuse light and then always act to increase the estimated Γ. Effect 2) may contribute with a systematic error of 0.05, compared to at most 0.02 from 3), and will therefore dominate the budget of systematic errors. We will adopt 0.05 as our systematic uncertainty for Γ.

As concerns the normalisation of the diffuse flux density, Σ_0 we cannot compensate potential atmospheric effects through the use of different filters. We therefore consider that a 25% systematic uncertainty may be a good estimate of the systematic uncertainty for this parameter (see above). The effects of binning and of fitting range can be neglected for this parameter.

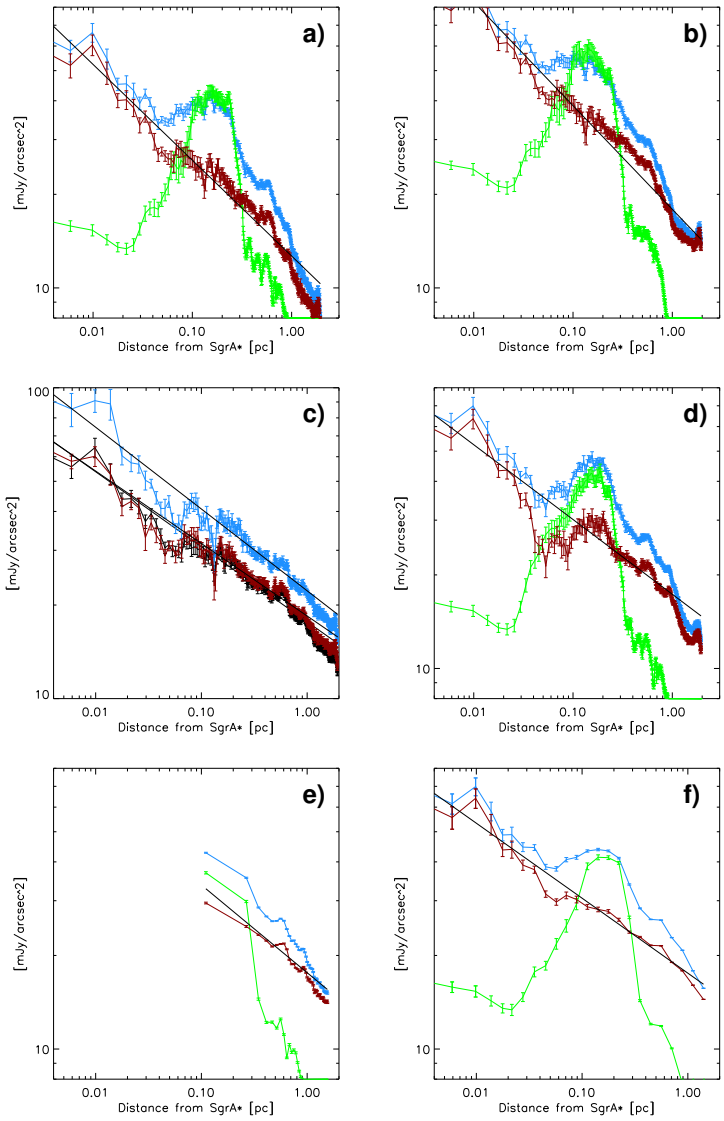

Figure D.5: Fits of the SB profile from the K_s wide field image to test potential sources of systematic errors. a) Subtraction of a potential sky offset. b) Assumption of constant extinction across the field. c) Subtraction of point sources down to $K_s = 16$ (blue), $K_s = 18$ (red), and all detectable point sources (back). d) No masking of dark clouds, or of systematic positive or negative residuals. e) Binning with a constant number of pixels (1×10^4) per bin. f) Logarithmic binning, leading to a higher weight of the inner bins.

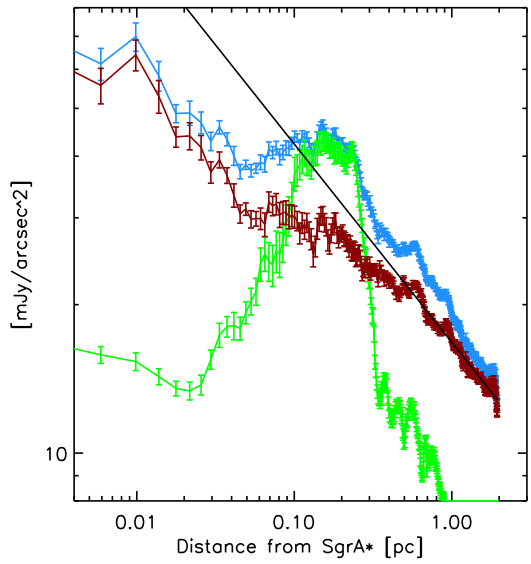

Figure D.6: Mean diffuse SB profiles in the K_S wide-field image before (blue) and after (red) subtraction of the scaled Paα emission (green). the straight black line is a simple power-law fit to the data at $R \geq 0.5\,\mathrm{pc}$.

D. PHOTOMETRIC ACCURACY AND RECOVERY OF DIFFUSE LIGHT WITH STARFINDER

Appendix E

Accurate uncertainty estimation in crowded fields: adaptive optics and speckle data

Optimal error estimation is key to achieve accurate photometry and astrometry. Stellar fluxes and positions in high angular resolution images are typically measured with PSF fitting routines, such as *StarFinder*. However, the formal uncertainties computed by these software packages tend to seriously underestimate the relevant uncertainties. In this appendix, we present a new approach to deal with this problem using a resampling method to obtain robust and reliable uncertainties without loss of sensitivity. We have published the results in the proceedings of the fifth AO4ELT Conference (*Gallego-Cano et al.*, 2017).

E.1 Introduction

In order to obtain the photometry and astrometry of crowded stellar fields, we can use different PSF fitting routines. In the present work, we use

StarFinder (*Diolaiti et al.*, 2000) to analyse two different data sets: adaptive optics (AO) and speckle data. Although the program gives a reliable detection of the point sources and determination of their position and flux, their formal uncertainties are underestimated. Therefore we want to look into other methods to obtain realistic uncertainties.

The Galactic center (GC) is a good example to study crowded fields. Obtaining sensitive, high-angular resolution photometry and astrometry is mandatory to study it. We are interested specially in the inner region around the super massive black hole, Sgr A*. This region is the most crowded region in the GC, therefore it is imperative to push the angular resolution to the limit and to estimate realistic uncertainties to obtain accurate photometry and astrometry.

There are many different methods for error estimation. Here, we study the bootstrapping (*Andrae*, 2010; , 1979) resampling method. The bootstrapping method uses "N" measurements (in our case "N" frames in one epoch) in order to create different data sets (in our case, different images). Moreover, the bootstrap samples are produced with replacement, which means that the same data point, can occur multiple times in our bootstrap sample. The main advantage is that the bootstrap method assumes that the measured data sample itself contains the information about its error distribution.

We compare three methods for uncertainty estimation. In the first method we apply the SF code to a deep image with the full data set and use the formal uncertainties from the program. In the second method we separate the data into three independent sets with 1/3 of the frames each, create three images and analyse them with SF, obtaining the uncertainties from the error of the mean of each star. Method three consists of producing 100 deep images via bootstrapping, with the uncertainties derived from the distribution of the *StarFinder* measurements on each of them. We compare the different methods and study their advantages and disadvantages. With the purpose of building a generic procedure to deal with different data sets,

we apply the three methods to AO and speckle data, respectively. This appendix aims at addressing a process to get robust and reliable uncertainties.

E.2 Observations and data reduction

On the one hand, we use K_s-band data from 08-09-2012 obtained with the S27 camera (0.027″ pixel scale) on NACO/VLT. Table 2.1 shows the details of the observations. The total integration time of each observation amounts to 480 seconds (N×NDIT×DIT). We want to analyse the most crowded region around Sgr A*. For this purpose, we consider the inner part with a field of view of 10″ × 10″ centered on the black hole (See Fig. E.1, on the left). We have 1920 frames for the epoch.

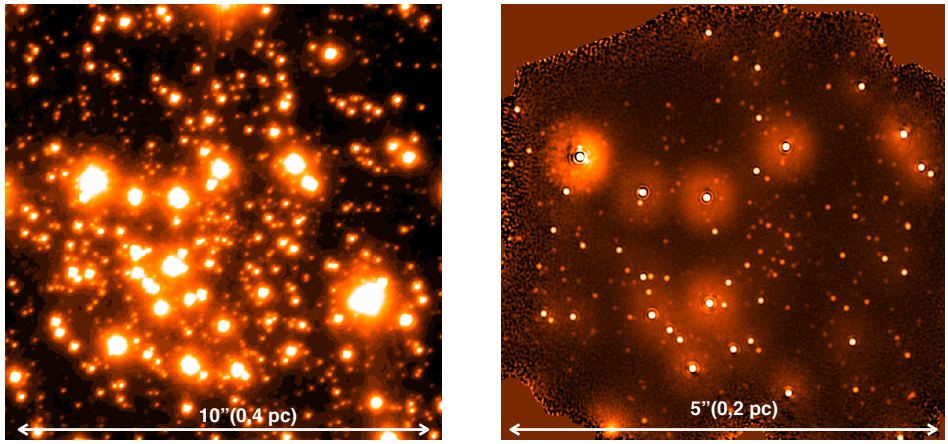

Figure E.1: Imaging data used in the analysis. Left: AO SSA image from 9th August 2008 obtained with NACO/VLT. The field-of-view is 10″ × 10″ centered on Sgr A*. Right: Speckle holography image from 23th May 2002 obtained with NIRC/Keck. The field-of-view is 5″ × 5″ centered on Sgr A*.

The details of the observations and data reduction are explained in Section 2.1.1. The main difference is that here we create a large number of bootstrap samples to which we then apply the simple shift-and-add (SSA) procedure to obtain final images, as we see in section 3.

On the other hand, we use K-band data from 04-23-2002 obtained with NIRC ($0.02''$ pixel scale and $\lambda_{\rm central} = 2.2$ μm) on the W. M. Keck I telescope (See Section 2.3 for more details). Table 2.6 shows the details of the observations.

E.3 Astrometry and photometry

In this section we explain the different methods that we tested to obtain the astrometry and photometry of the detected stars as well as the associated astrometric and photometric uncertainties. Fig. E.2 shows an outline of the procedure that we followed after the basic reduction for each method.

E.3.1 AO data

In **Method 1**, firstly a simple SSA procedure was applied to obtain the final deep image considering all the frames in the epoch. After that, we used the SF program to detect and subtract detected point sources from the image. We are interested in studying the resulting uncertainties of real stars and we want to avoid the possible contamination of spurious sources, hence we used the following conservative values for the *StarFinder* parameters: *min_correlation*= 0.80 and *deblend*= 0. The detection threshold was chosen as 3σ and we applied two iteration of SF algorithm. The photometry was calibrated with the stars IRS 16C,IRS 16NW, and IRS 33N (apparent magnitudes $K_s = 9.93, 10.14, 11.20$ see (*Schödel et al.*, 2010)). In Fig. E.3 we show the photometric and astrometric uncertainties obtained along with the KLF. We detected 1618 stars and the detection limit, that we define as the value of the magnitude where the cumulative number of all detected stars reached 90%, is 19.97. The median value of the photometric uncertainty for brighter stars ($K_s < 14$) is 0.002.

In **Method 2**, we divided the full data in 3 separate data sets with 1/3 of frames each. A simple SSA procedure was applied to each subset to obtain three final images. After that, we used the *StarFinder* program

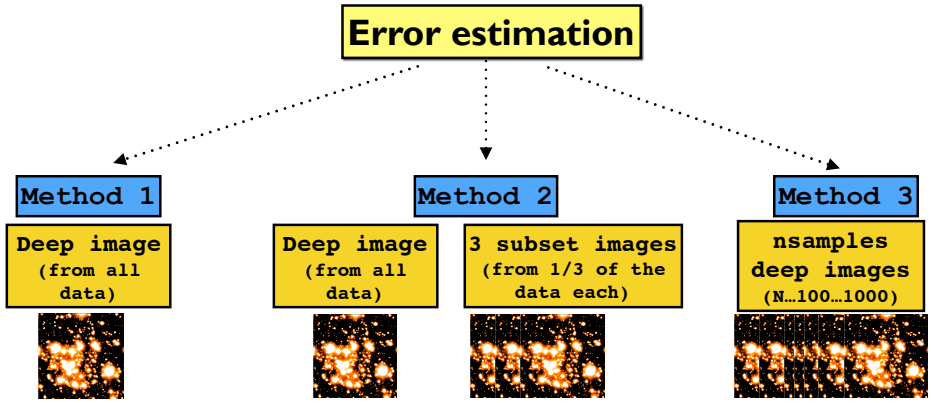

Figure E.2: Scheme of the different methods that we used to obtain the photometric and astrometric uncertainties. For AO, in method 1 we obtained a co-added image with the full data set, run *StarFinder* on the image and used the formal uncertainties from *StarFinder*. In method 2 we created three separate data sets with 1/3 of the frames each, created co-added images and analysed them with *StarFinder*. Finally we obtained realistic uncertainties from independent data obtained from the error of the mean of each star. In method 3 we created 100 bootstrap samples and corresponding co-added images, run SF on each bootstrapped images and computed the uncertainties from standard deviation of measurements of each star. For speckle data the procedure is the same, but we created co-added images not from samples of individual frames, but from samples of holographically reduced batches of speckle frames.

to detect and subtract detected point sources from the three images. We used the same values for the *StarFinder* parameters than for Method 1. We compared detected stars in the three subset and considered the common stars. We calibrated the images similar to Method 1, but in this case we corrected the offset in the positions and zero points that we could have due to small differences between their estimated PSFs. Finally, we computed uncertainties from the error of the mean of the position and flux of each star. In Fig. E.4 we show the photometric and astrometric uncertainties obtained from *Starfinder* and the KLF. We detected 1032 common stars and

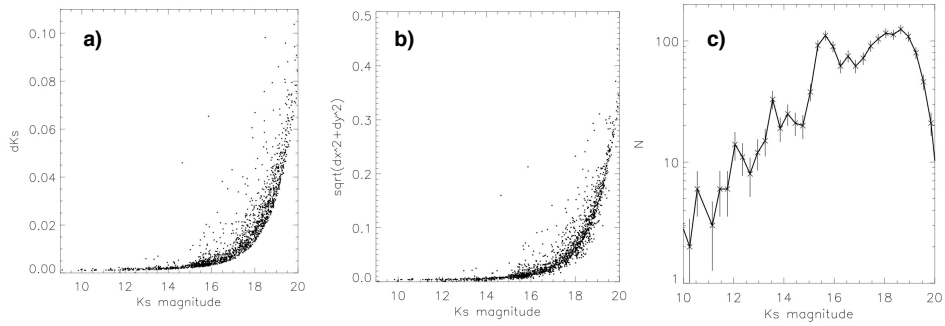

Figure E.3: Results obtained applying method 1 to AO data. a) Photometric uncertainties versus K_s magnitude from *Starfinder* program. b) Astrometric uncertainties versus K_s magnitude from *Starfinder* program. We represent $sqrt(dx^2 + dy^2)$ versus K_s, where dx and dy are the errors in the x-position and y-position, respectively, of each star. c) KLF for the deep image.

the detection limit is 18. The median value of the photometric uncertainty for brighter stars with $K_s < 14$ is 0.005.

In **Method 3**, we created 100 SSA images using the bootstrapping with replacement method. The number of frames considered in each bootstrap image is equal to the total number of frames. After that, we used the SF program to detect and subtract detected point sources from 100 bootstrap images. We used the same values for the SF parameters than for the previous methods. We defined the *detection frequency* parameter as the percentage of bootstrap deep images where each star is detected and we obtained a final list with all the stars detected in all the images and their associated detection frequency value. We selected *detection frequency*=50%, which means that we considered stars detected in 50% or more of the bootstrap images. We calibrated the images similar to method 2, correcting the offset in the positions and zero points that we could have between all the images, too. Finally, we computed uncertainties from the standard deviation of the position and flux of each star. In Fig. E.5 we show the photometric and astrometric uncertainties obtained with this method and the KLF. We

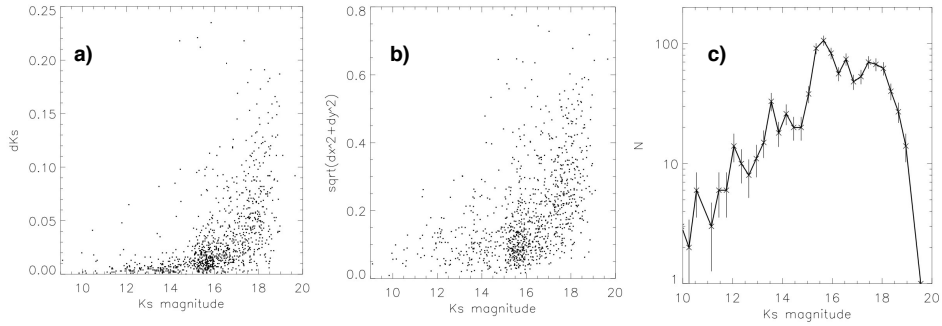

Figure E.4: Results obtained applying method 2 to AO data. a) Photometric uncertainties versus K_s magnitude from the errors of the mean of each star detected in all images. b) Astrometric uncertainties versus K_s magnitude c) KLF for the stars common to all images.

detected 1514 stars and the detection limit is 19. The median value of the photometric uncertainty for brighter stars with $K_s < 14$ is 0.002.

E.3.2 Speckle data

The procedure that we followed is the same than for AO data. The only difference is that in this case we first run holography on independent subsamples of the speckle frames and we combined the resulting holographic images, as we see in Section 2.

In this case, due to the small field of NIRC, we study the central 5″ around Sgr A*. In **Method 1** we used the following values for the SF parameters: *min_correlation*= 0.80 and *deblend*= 1. The other SF parameters are the same than for the AO data. The photometry was calibrated with the stars IRS 16C, IRS 16NW, and IRS 16CC (apparent magnitudes K= 9.83, 10.03, 10.36 see (*Blum et al.*, 1996)). In Fig. E.6 we show the photometric and astrometric uncertainties obtained and the K-luminosity function (KLF). We detected 741 stars and the detection limit is 18. The median value of the photometric uncertainty for brighter stars (K< 14) is 0.005.

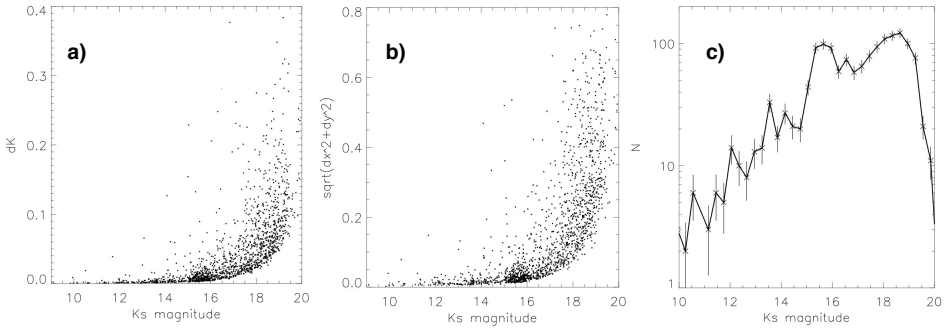

Figure E.5: Results obtained applying method 3 to AO data for *detection frequency*=50%. a) Photometric uncertainties versus K_s magnitude from the standard deviation of the measurements of each star. b) Astrometric uncertainties versus K_s magnitude. c) KLF for the final list.

After the holographic procedure, we obtained 76 holo images. The procedure for **Method 2** is the same than for AO data. We used the same values for the *StarFinder* parameters than for Method 1. Finally, we computed uncertainties from the error of the mean of the position and flux of each star. In Fig. E.7 we show the photometric and astrometric uncertainties obtained from *Starfinder* and the KLF. We detected 200 common stars and the detection limit is 16. The median value of the photometric uncertainty for brighter stars with K$<$ 14 is 0.06.

In this case, in **Method 3** we carry out a bootstrapping resampling method similar to AO. The only difference is that now we bootstrap holographically pre-reduced images and not bootstrap individual frames, as in the AO case, with the aim of speed up the process. We use the same values for the *StarFinder* parameters that for Method 1 and 2. We select *detection frequency*=50%. In Fig. E.8 we show the photometric and astrometric uncertainties obtained with this method and the KLF. We detect 457 stars and the detection limit is 17.05. The median value of the photometric uncertainty for brighter stars with $K_s < 14$ is 0.06.

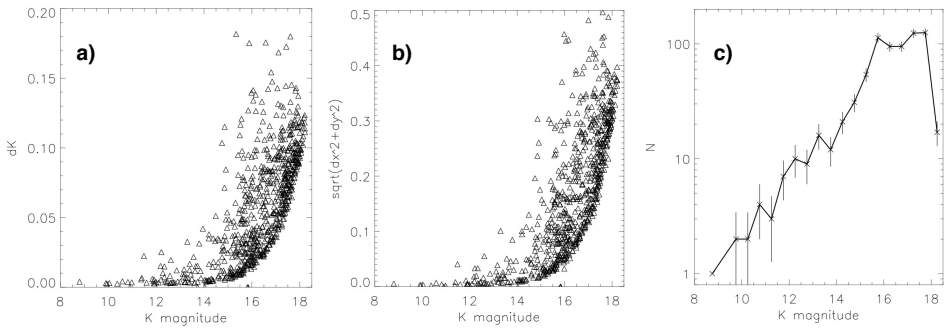

Figure E.6: Results obtained applying method 1 to speckle data. a) Photometric uncertainties versus K magnitude from *Starfinder* program. b) Astrometric uncertainties versus K magnitude from *Starfinder* program. c) KLF for the deep image.

E.4 Comparison between the three methods

In this section, we compare the results obtained by the three methods. Fig. E.9 and Fig. E.10 show the comparison between the different methods for AO data and speckle data, respectively. If we compare the uncertainties obtained by method 2 with the uncertainties obtained by method 1, we can see that *StarFinder* under-estimates the uncertainties (see *a*) in Fig. E.9 and Fig. E.10). If we compare the results obtained by the Method 2 and Method 3, we can see that we obtain similar uncertainties (see *b*) in Fig. E.9 and Fig. E.10). Therefore, we can get statistically similar uncertainties by both Methods 2 and 3.

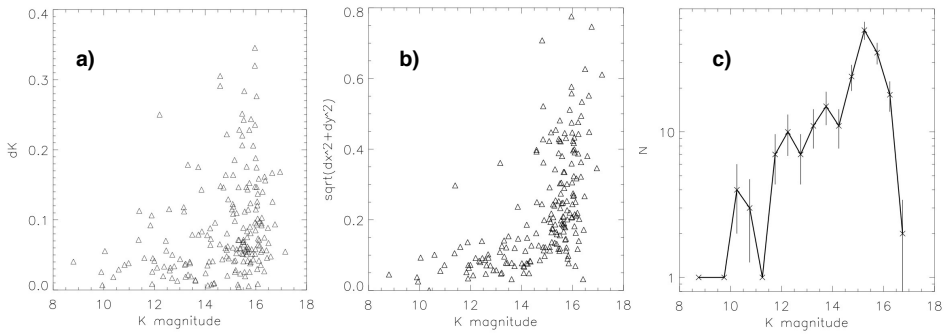

Figure E.7: Results obtained applying Method 2 to speckle data. a) Photometric uncertainties versus K magnitude from the errors of the mean of each star detected in all images. b) Astrometric uncertainties versus K magnitude. c) KLF for the common stars to all images.

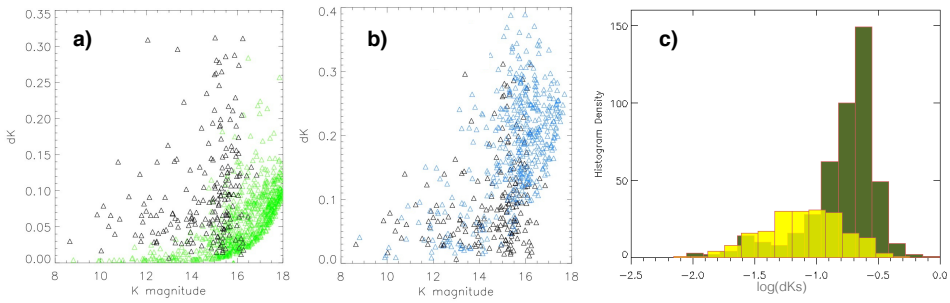

Figure E.10: Final comparison between the three methods for speckle. a) Comparison between the photometric uncertainties obtained by Method 1 (green) and Method 2 (black). b) Comparison between the photometric uncertainties obtained by Method 2 (black) and Method 3 (blue).c) Distributions of errors obtained by Method 2 (yellow) and Method 3 (green).

The Fig. E.11) compare KLFs obtained by Method 2 and 3, respectively. We can see that although both methods give reliable uncertainties, we can go almost **one magnitude deeper** by applying the bootstrapping procedure than by applying Method 2.

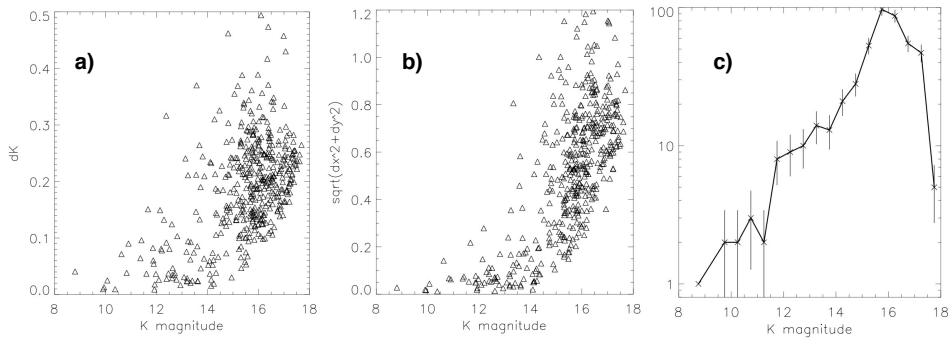

Figure E.8: Results obtained applying Method 3 to speckle data for *detection frequency*=50%. a) Photometric uncertainties versus K magnitude from the standard deviation of the measurements of each star. b) Astrometric uncertainties versus K magnitude. c) KLF for the final list.

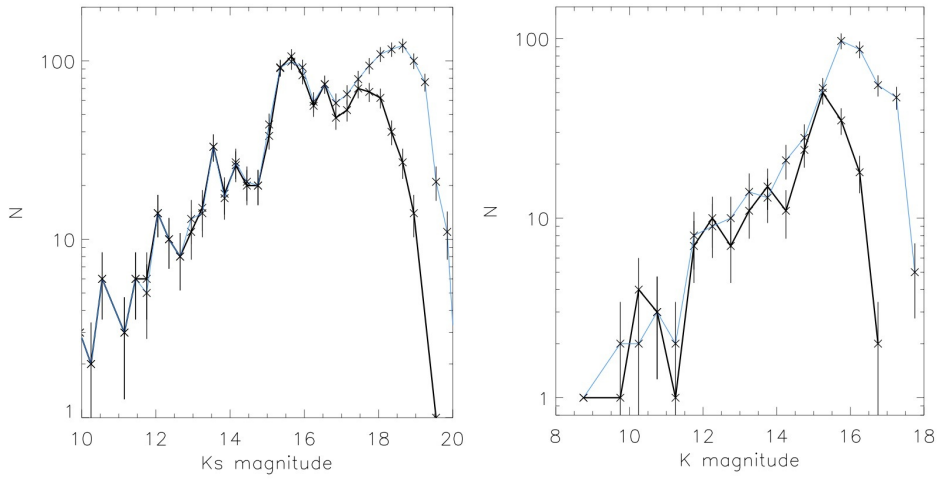

Figure E.11: Comparison between KLFs obtained by Method 2 and 3 for AO data (on the left) and for speckle data (on the right). Both give robust uncertainty estimates, but Method 3 is more sensitive.

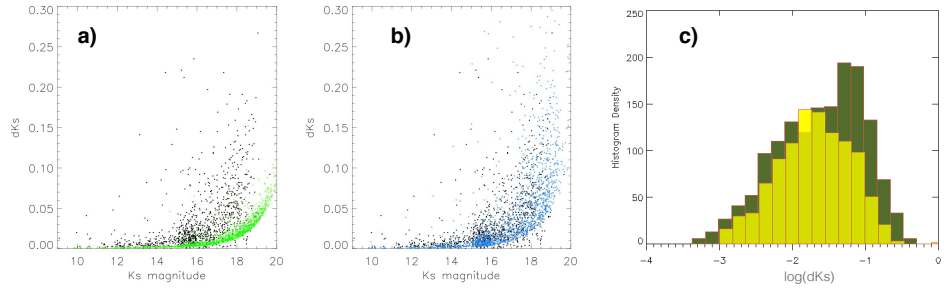

Figure E.9: Final comparison between the three methods for AO. a) Comparison between the photometric uncertainties obtained by Method 1 (green) and Method 2 (black). b) Comparison between the photometric uncertainties obtained by Method 2 (black) and Method 3 (blue).c) Distributions of errors obtained by Method 2 (yellow) and Method 3 (green).

E.5 Conclusions

In this appendix, we show three methods to obtain uncertainties. We see that *StarFinder* under-estimates the uncertainties. We obtain robust uncertainty estimates by separating the data into disjunct subsets, but at the cost of loss of sensitivity. We show a new method that uses bootstrapping resampling approach. This method allows us to obtain robust estimates of the uncertainty and is more sensitive than Method 2.

References

Abbott, B.P., Abbott, R., Abbott, T.D., Abernathy, M.R., Acernese, F., Ackley, K., Adams, C., Adams, T., Addesso, P., Adhikari, R.X. & et al. (2016). Observation of Gravitational Waves from a Binary Black Hole Merger. *Physical Review Letters*, **116**, 061102. 12

Alexander, T. (2005). Stellar processes near the massive black hole in the Galactic center [review article]. , **419**, 65–142. 8, 65, 84, 97, 123

Alexander, T. (2011). Key Questions about Galactic Center Dynamics. In M.R. Morris, Q.D. Wang & F. Yuan, eds., *The Galactic Center: a Window to the Nuclear Environment of Disk Galaxies*, vol. 439 of *Astronomical Society of the Pacific Conference Series*, 129. 6, 84, 110

Alexander, T. (2017). Stellar Dynamics and Stellar Phenomena Near a Massive Black Hole. , **55**, 17–57. 59, 67

Amaro-Seoane, P. (2012). Stellar dynamics and extreme-mass ratio inspirals. *ArXiv e-prints*. 124

Amaro-Seoane, P. (2018). Relativistic dynamics and extreme mass ratio inspirals. *Living Reviews in Relativity*, **21**, 4. 67, 124

Amaro-Seoane, P. & Chen, X. (2014). The Fragmenting Past of the Disk at the Galactic Center: The Culprit for the Missing Red Giants. , **781**, L18. 66, 124

Amaro-Seoane, P., Gair, J.R., Freitag, M., Miller, M.C., Mandel, I., Cutler, C.J. & Babak, S. (2007). TOPICAL REVIEW: Intermediate and extreme mass-ratio inspiralsastrophysics, science applications and detection using LISA. *Classical and Quantum Gravity*, **24**, 113. 63, 67, 124

Andrae, R. (2010). Error estimation in astronomy: A guide. *ArXiv e-prints*. 178

Aparicio, A. & Gallart, C. (2004). IAC-STAR: A Code for Synthetic Color-Magnitude Diagram Computation. , **128**, 1465–1477. 102

Athanassoula, E., Morin, S., Wozniak, H., Puy, D., Pierce, M.J., Lombard, J. & Bosma, A. (1990). The shape of bars in early-type barred galaxies. , **245**, 130–139. 38

Baganoff, F.K., Maeda, Y., Morris, M., Bautz, M.W., Brandt, W.N., Cui, W., Doty, J.P., Feigelson, E.D., Garmire, G.P., Pravdo, S.H., Ricker, G.R. & Townsley, L.K. (2003). Chandra X-Ray Spectroscopic Imaging of Sagittarius A* and the Central Parsec of the Galaxy. , **591**, 891–915. 126

Bahcall, J.N. & Wolf, R.A. (1976). Star distribution around a massive black hole in a globular cluster. , **209**, 214–232. 64

Bahcall, J.N. & Wolf, R.A. (1977). The star distribution around a massive black hole in a globular cluster. II Unequal star masses. , **216**, 883–907. 117, 210

Balick, B. & Brown, R.L. (1974). Intense subarcsecond structure in the galactic center. , **194**, 265–270. 6

Bartko, H., Martins, F., Trippe, S., Fritz, T.K., Genzel, R., Ott, T., Eisenhauer, F., Gillessen, S., Paumard, T., Alexander, T., Dodds-Eden, K., Gerhard, O., Levin, Y., Mascetti, L., Nayakshin, S., Perets, H.B., Perrin, G., Pfuhl, O., Reid, M.J., Rouan, D., Zilka, M. & Sternberg, A. (2010). An Extremely Top-Heavy Initial Mass Function in the Galactic Center Stellar Disks. , **708**, 834–840. 5, 10, 43, 66, 71, 89, 98, 100, 101, 102, 103, 149, 152, 208, 220

Baumgardt, H., Amaro-Seoane, P. & Schödel, R. (2018). The distribution of stars around the Milky Way's central black hole. III. Comparison with simulations. , **609**, A28. vii, xii, 117, 118, 119, 120, 121, 122, 210, 211

Becklin, E.E. & Neugebauer, G. (1968). Infrared Observations of the Galactic Center. , **151**, 145–+. 28

Bessell, M.S. (1990). UBVRI passbands. , **102**, 1181–1199. 102

Binney, J. & Tremaine, S. (1987). *Galactic dynamics*. 2, 64

Bland-Hawthorn, J. & Gerhard, O. (2016). The Galaxy in Context: Structural, Kinematic, and Integrated Properties. , **54**, 529–596. 3

Blum, R.D., Sellgren, K. & Depoy, D.L. (1996). JHKL Photometry and the K-Band Luminosity Function at the Galactic Center. , **470**, 864–+. 54, 183

Blum, R.D., Ramírez, S.V., Sellgren, K. & Olsen, K. (2003). Really Cool Stars and the Star Formation History at the Galactic Center. , **597**, 323–346. 98, 100

REFERENCES

Boehle, A., Ghez, A.M., Schödel, R., Meyer, L., Yelda, S., Albers, S., Martinez, G.D., Becklin, E.E., Do, T., Lu, J.R., Matthews, K., Morris, M.R., Sitarski, B. & Witzel, G. (2016). An Improved Distance and Mass Estimate for Sgr A* from a Multistar Orbit Analysis. , **830**, 17. 7, 24, 65

Böker, T., Laine, S., van der Marel, R.P., Sarzi, M., Rix, H., Ho, L.C. & Shields, J.C. (2002). A Hubble Space Telescope Census of Nuclear Star Clusters in Late-Type Spiral Galaxies. I. Observations and Image Analysis. , **123**, 1389–1410. 27

Böker, T., Sarzi, M., McLaughlin, D.E., van der Marel, R.P., Rix, H.W., Ho, L.C. & Shields, J.C. (2004). A Hubble Space Telescope Census of Nuclear Star Clusters in Late-Type Spiral Galaxies. II. Cluster Sizes and Structural Parameter Correlations. , **127**, 105–118. 27

Bolton, J.G., Stanley, G.J. & Slee, O.B. (1949). Positions of Three Discrete Sources of Galactic Radio-Frequency Radiation. , **164**, 101–102. 2

Bressan, A., Marigo, P., Girardi, L., Salasnich, B., Dal Cero, C., Rubele, S. & Nanni, A. (2012). PARSEC: stellar tracks and isochrones with the PAdova and TRieste Stellar Evolution Code. , **427**, 127–145. 98, 101

Buchholz, R.M., Schödel, R. & Eckart, A. (2009). Composition of the galactic center star cluster. Population analysis from adaptive optics narrow band spectral energy distributions. , **499**, 483–501. 43, 66, 89, 96, 137, 169

Capaccioli, M. (1987). Distribution of light - Outer regions. In P.T. de Zeeuw & S.D. Tremaine, eds., *Structure and Dynamics of Elliptical Galaxies*, vol. 127 of *IAU Symposium*, 47–60. 39

Carson, D.J., Barth, A.J., Seth, A.C., den Brok, M., Cappellari, M., Greene, J.E., Ho, L.C. & Neumayer, N. (2015). The Structure of Nuclear Star Clusters in Nearby Late-type Spiral Galaxies from Hubble Space Telescope Wide Field Camera 3 Imaging. , **149**, 170. 57, 58, 59

Chabrier, G. (2001). The Galactic Disk Mass Budget. I. Stellar Mass Function and Density. , **554**, 1274–1281. 98, 102

Chatzopoulos, S., Fritz, T.K., Gerhard, O., Gillessen, S., Wegg, C., Genzel, R. & Pfuhl, O. (2015a). The old nuclear star cluster in the Milky Way: dynamics, mass, statistical parallax, and black hole mass. , **447**, 948–968. 4, 28, 65

Chatzopoulos, S., Gerhard, O., Fritz, T.K., Wegg, C., Gillessen, S., Pfuhl, O. & Eisenhauer, F. (2015b). Dust within the nuclear star cluster in the Milky Way. , **453**, 939–950. 73, 74, 75, 205

Chen, Y., Girardi, L., Bressan, A., Marigo, P., Barbieri, M. & Kong, X. (2014). Improving PARSEC models for very low mass stars. , **444**, 2525–2543. 98, 101

Chen, Y., Bressan, A., Girardi, L., Marigo, P., Kong, X. & Lanza, A. (2015). PARSEC evolutionary tracks of massive stars up to 350 M at metallicities $0.0001 \leq Z \leq 0.04$., **452**, 1068 – −1080. 98, 101

Chen, Z., Gallego-Cano, E., Do, T., Witzel, G., Ghez, A.M., Schoedel, R., Sitarski, B., Lu, J., Becklin, E., Dehghanfar, A., Gautam, A., Hees, A., Jia, S., Mangian, J., Matthews, K. & Morris, M.R. (in preparation). Long-term near-infrared variability of the supermassive black hole at the Galactic center. vii, xii, 11, 12, 23, 24, 25, 128, 129, 130, 131, 132, 200, 211

Christopher, M.H., Scoville, N.Z., Stolovy, S.R. & Yun, M.S. (2005). HCN and HCO+ Observations of the Galactic Circumnuclear Disk. , **622**, 346–365. 167

Clarkson, W.I., Ghez, A.M., Morris, M.R., Lu, J.R., Stolte, A., McCrady, N., Do, T. & Yelda, S. (2012). Proper Motions of the Arches Cluster with Keck Laser Guide Star Adaptive Optics: The First Kinematic Mass Measurement of the Arches. , **751**, 132. 3

Côté, P., Piatek, S., Ferrarese, L., Jordán, A., Merritt, D., Peng, E.W., Haşegan, M., Blakeslee, J.P., Mei, S., West, M.J., Milosavljević, M. & Tonry, J.L. (2006). The ACS Virgo Cluster Survey. VIII. The Nuclei of Early-Type Galaxies. , **165**, 57–94. 27

Dale, J.E., Wünsch, R., Whitworth, A. & Palouš, J. (2009). The fragmentation of expanding shells - I. Limitations of the thin-shell approximation. , **398**, 1537–1548. 66

Dehghanfar, A., Do, T., Witzel, G., Ghez, A.M., Sitarski, B., Lu, J., Becklin, E., Gautam, A., Hees, A., Jia, S., Mangian, J., Matthews, K. & Morris, M.R. (in preparation). 130

Diolaiti, E., Bendinelli, O., Bonaccini, D., Close, L., Currie, D. & Parmeggiani, G. (2000). Analysis of isoplanatic high resolution stellar fields by the StarFinder code. , **147**, 335–346. 68, 129, 178

Do, T., Ghez, A.M., Morris, M.R., Lu, J.R., Matthews, K., Yelda, S. & Larkin, J. (2009). High Angular Resolution Integral-Field Spectroscopy of the Galaxy's Nuclear Cluster: A Missing Stellar Cusp? , **703**, 1323–1337. 10, 66, 71, 89, 97, 114

Do, T., Lu, J.R., Ghez, A.M., Morris, M.R., Yelda, S., Martinez, G.D., Wright, S.A. & Matthews, K. (2013). Stellar Populations in the Central 0.5pc of the Galaxy. I. A New Method for Constructing Luminosity Functions and Surface-density Profiles. , **764**, 154. 5, 31, 43, 84, 100, 102, 149, 220

Do, T., Wright, S.A., Barth, A.J., Barton, E.J., Simard, L., Larkin, J.E., Moore, A.M., Wang, L. & Ellerbroek, B. (2014). Prospects for Measuring Supermassive Black Hole Masses with Future Extremely Large Telescopes. , **147**, 93. 135

Do, T., Kerzendorf, W., Winsor, N., Øststad, M., Morris, M.R., Lu, J.R. & Ghez, A.M. (2015). Discovery of Low-metallicity Stars in the Central Parsec of the Milky Way. , **809**, 143. 10

Dong, H., Wang, Q.D., Cotera, A., Stolovy, S., Morris, M.R., Mauerhan, J., Mills, E.A., Schneider, G., Calzetti, D. & Lang, C. (2011). Hubble Space Telescope Paschen α survey of the Galactic Centre: data reduction and products. , **417**, 114–135. 18, 31, 33, 35, 36, 81, 201, 202

Dong, H., Wang, Q.D. & Morris, M.R. (2012). A multi-wavelength study of evolved massive stars in the Galactic Centre. , **425**, 884–906. 81

Dwek, E., Arendt, R.G., Hauser, M.G., Kelsall, T., Lisse, C.M., Moseley, S.H., Silverberg, R.F., Sodroski, T.J. & Weiland, J.L. (1995). Morphology, near-infrared luminosity, and mass of the Galactic bulge from COBE DIRBE observations. , **445**, 716–730. 37, 38

Eckart, A., Genzel, R., Ott, T. & Schödel, R. (2002). Stellar orbits near Sagittarius A*. , **331**, 917–934. 7

Eckart, A., Moultaka, J., Viehmann, T., Straubmeier, C. & Mouawad, N. (2004). Young Stars at the Center of the Milky Way? , **602**, 760–769. 83

Efron, B. (1979). *Bootstrap methods: Another look at the jackknife*, vol. 7 of *1-26*. The Annals of Statistics. 178

Eisenhauer, F., Genzel, R., Alexander, T., Abuter, R., Paumard, T., Ott, T., Gilbert, A., Gillessen, S., Horrobin, M., Trippe, S., Bonnet, H., Dumas, C., Hubin, N., Kaufer, A., Kissler-Patig, M., Monnet, G., Ströbele, S., Szeifert, T., Eckart, A., Schödel, R. & Zucker, S. (2005). SINFONI in the Galactic Center: Young Stars and Infrared Flares in the Central Light-Month. , **628**, 246–259. 6, 7, 110

Ekers, R.D., van Gorkom, J.H., Schwarz, U.J. & Goss, W.M. (1983). The radio structure of SGR A. , **122**, 143–150. 167

Fath, E.A. (1909). The spectra of some spiral nebulae and globular star clusters. *Lick Observatory Bulletin*, **5**, 71–77. 1

Fazio, G.G., Hora, J.L., Allen, L.E., Ashby, M.L.N., Barmby, P., Deutsch, L.K., Huang, J.S., Kleiner, S., Marengo, M., Megeath, S.T., Melnick, G.J., Pahre, M.A., Patten, B.M., Polizotti, J., Smith, H.A., Taylor, R.S., Wang, Z., Willner, S.P., Hoffmann, W.F., Pipher, J.L., Forrest, W.J., McMurty, C.W., McCreight, C.R., McKelvey, M.E., McMurray, R.E., Koch, D.G., Moseley, S.H., Arendt, R.G., Mentzell, J.E., Marx, C.T., Losch, P., Mayman, P., Eichhorn, W., Krebs, D., Jhabvala, M., Gezari, D.Y., Fixsen, D.J., Flores, J., Shakoorzadeh, K., Jungo, R., Hakun, C., Workman, L., Karpati, G., Kichak, R., Whitley, R., Mann, S., Tollestrup, E.V., Eisenhardt, P., Stern, D., Gorjian, V., Bhattacharya, B., Carey, S., Nelson, B.O., Glaccum, W.J., Lacy, M., Lowrance, P.J., Laine, S., Reach, W.T., Stauffer, J.A., Surace, J.A., Wilson, G., Wright, E.L., Hoffman, A., Domingo, G. & Cohen, M. (2004). The Infrared Array Camera (IRAC) for the Spitzer Space Telescope. , **154**, 10–17. 22

Feldmeier, A., Neumayer, N., Seth, A., Schödel, R., Lützgendorf, N., de Zeeuw, P.T., Kissler-Patig, M., Nishiyama, S. & Walcher, C.J. (2014). Large scale kinematics and dynamical modelling of the Milky Way nuclear star cluster. , **570**, A2. 4, 28, 52, 59, 60, 65, 106

Feldmeier-Krause, A., Neumayer, N., Schödel, R., Seth, A., Hilker, M., de Zeeuw, P.T., Kuntschner, H., Walcher, C.J., Lützgendorf, N. & Kissler-Patig, M. (2015). KMOS view of the Galactic centre. I. Young stars are centrally concentrated. , **584**, A2. 5, 10, 100, 149

Feldmeier-Krause, A., Zhu, L., Neumayer, N., van de Ven, G., de Zeeuw, P.T. & Schödel, R. (2017). Triaxial orbit-based modelling of the Milky Way Nuclear Star Cluster. , **466**, 4040–4052. 4, 28, 65

Ferrarese, L. & Ford, H. (2005). Supermassive Black Holes in Galactic Nuclei: Past, Present and Future Research. , **116**, 523–624. 2

Ferrarese, L. & Merritt, D. (2000). A Fundamental Relation between Supermassive Black Holes and Their Host Galaxies. , **539**, L9–L12. 2, 65

Ferrarese, L., Côté, P., Dalla Bontà, E., Peng, E.W., Merritt, D., Jordán, A., Blakeslee, J.P., Haşegan, M., Mei, S., Piatek, S., Tonry, J.L. & West, M.J. (2006). A Fundamental Relation between Compact Stellar Nuclei, Supermassive Black Holes, and Their Host Galaxies. , **644**, L21–L24. 2

Figer, D.F., McLean, I.S. & Morris, M. (1999). Massive Stars in the Quintuplet Cluster. , **514**, 202–220. 3

Figer, D.F., Najarro, F., Gilmore, D., Morris, M., Kim, S.S., Serabyn, E., McLean, I.S., Gilbert, A.M., Graham, J.R., Larkin, J.E., Levenson, N.A. & Teplitz, H.I. (2002). Massive Stars in the Arches Cluster. , **581**, 258–275. 3

Freitag, M., Amaro-Seoane, P. & Kalogera, V. (2006). Stellar Remnants in Galactic Nuclei: Mass Segregation. , **649**, 91–117. 64

Freudenreich, H.T. (1998). A COBE Model of the Galactic Bar and Disk. , **492**, 495–510. 37, 38

Fritz, T.K., Gillessen, S., Dodds-Eden, K., Martins, F., Bartko, H., Genzel, R., Paumard, T., Ott, T., Pfuhl, O., Trippe, S., Eisenhauer, F. & Gratadour, D. (2010). GC-IRS13EA Puzzling Association of Three Early-type Stars. , **721**, 395–411. 83

REFERENCES

Fritz, T.K., Gillessen, S., Dodds-Eden, K., Lutz, D., Genzel, R., Raab, W., Ott, T., Pfuhl, O., Eisenhauer, F. & Yusef-Zadeh, F. (2011). Line Derived Infrared Extinction toward the Galactic Center. , **737**, 73–+. 9, 35, 139

Fritz, T.K., Chatzopoulos, S., Gerhard, O., Gillessen, S., Genzel, R., Pfuhl, O., Tacchella, S., Eisenhauer, F. & Ott, T. (2014). The nuclear cluster of the Milky Way: total mass and luminosity. In L.O. Sjouwerman, C.C. Lang & J. Ott, eds., *IAU Symposium*, vol. 303 of *IAU Symposium*, 248–251. 28

Fritz, T.K., Chatzopoulos, S., Gerhard, O., Gillessen, S., Genzel, R., Pfuhl, O., Tacchella, S., Eisenhauer, F. & Ott, T. (2016). The Nuclear Cluster of the Milky Way: Total Mass and Luminosity. , **821**, 44. 4, 28, 29, 49, 50, 51, 52, 53, 86, 106, 107, 108, 111, 112, 114, 115, 116, 169, 209, 210

Gallego-Cano, E., Schödel, R., Gallego-Calvente, A.T. & Ghez, A.M. (2017). Accurate uncertainty estimation in crowded fields: adaptive optics and speckle data. 177

Gallego-Cano, E., Schödel, R., Dong, H., Nogueras-Lara, F., Gallego-Calvente, A.T., Amaro-Seoane, P. & Baumgardt, H. (2018). The distribution of stars around the Milky Way's central black hole. I. Deep star counts. , **609**, A26. 12, 17, 33, 43, 68, 110, 111, 151, 153, 209

Gallego-Cano, E., Schödel, R., Nogueras-Lara, F., Dong, H., Shahzamanian, B., Fritz, T.K., Gallego-Calvente, A.T. & Neumayer, N. (Accepted). New constraints on the structure of the nuclear stellar cluster of the Milky Way from star counts and MIR imaging. 12, 30

Gautam, A.K., Do, T., Ghez, A.M., Morris, M.R., Martinez, G.D., Hosek, M.W., Jr., Lu, J.R., Sakai, S., Witzel, G., Jia, S., Becklin, E.E. & Matthews, K. (2019). An Adaptive Optics Survey of Stellar Variability at the Galactic Center. , **871**, 103. 129, 130, 133

Gebhardt, K., Bender, R., Bower, G., Dressler, A., Faber, S.M., Filippenko, A.V., Green, R., Grillmair, C., Ho, L.C., Kormendy, J., Lauer, T.R., Magorrian, J., Pinkney, J., Richstone, D. & Tremaine, S. (2000). A Relationship between Nuclear Black Hole Mass and Galaxy Velocity Dispersion. , **539**, L13–L16. 2

Genzel, R., Pichon, C., Eckart, A., Gerhard, O.E. & Ott, T. (2000). Stellar dynamics in the Galactic Centre: proper motions and anisotropy. , **317**, 348–374. 7

Genzel, R., Schödel, R., Ott, T., Eckart, A., Alexander, T., Lacombe, F., Rouan, D. & Aschenbach, B. (2003a). Near-infrared flares from accreting gas around the supermassive black hole at the Galactic Centre. , **425**, 934–937. 128

Genzel, R., Schödel, R., Ott, T., Eisenhauer, F., Hofmann, R., Lehnert, M., Eckart, A., Alexander, T., Sternberg, A., Lenzen, R., Clénet, Y., Lacombe, F., Rouan, D., Renzini, A. & Tacconi-Garman, L.E. (2003b). The Stellar Cusp around the Supermassive Black Hole in the Galactic Center. , **594**, 812–832. 5, 65, 77, 97

Genzel, R., Eisenhauer, F. & Gillessen, S. (2010). The Galactic Center massive black hole and nuclear star cluster. *Reviews of Modern Physics*, **82**, 3121–3195. 6, 10, 20, 40, 59, 80, 81, 83, 110, 126, 127, 211

Georgiev, I.Y. & Böker, T. (2014). Nuclear star clusters in 228 spiral galaxies in the HST/WFPC2 archive: catalogue and comparison to other stellar systems. , **441**, 3570–3590. 2, 27, 57, 59

Georgiev, I.Y., Böker, T., Leigh, N., Lützgendorf, N. & Neumayer, N. (2016). Masses and scaling relations for nuclear star clusters, and their co-existence with central black holes. , **457**, 2122–2138. 2

Ghez, A.M., Klein, B.L., Morris, M. & Becklin, E.E. (1998). High Proper-Motion Stars in the Vicinity of Sagittarius A*: Evidence for a Supermassive Black Hole at the Center of Our Galaxy. , **509**, 678–686. 24, 26

Ghez, A.M., Morris, M., Becklin, E.E., Tanner, A. & Kremenek, T. (2000). The accelerations of stars orbiting the Milky Way's central black hole. , **407**, 349–351. 24, 26

Ghez, A.M., Duchêne, G., Matthews, K., Hornstein, S.D., Tanner, A., Larkin, J., Morris, M., Becklin, E.E., Salim, S., Kremenek, T., Thompson, D., Soifer, B.T., Neugebauer, G. & McLean, I. (2003). The First Measurement of Spectral Lines in a Short-Period Star Bound to the Galaxy's Central Black Hole: A Paradox of Youth. , **586**, L127–L131. 5, 7, 128

Ghez, A.M., Wright, S.A., Matthews, K., Thompson, D., Le Mignant, D., Tanner, A., Hornstein, S.D., Morris, M., Becklin, E.E. & Soifer, B.T. (2004). Variable Infrared Emission from the Supermassive Black Hole at the Center of the Milky Way. , **601**, L159–L162. 26

Ghez, A.M., Salim, S., Hornstein, S.D., Tanner, A., Lu, J.R., Morris, M., Becklin, E.E. & Duchêne, G. (2005). Stellar Orbits around the Galactic Center Black Hole. , **620**, 744–757. 7, 24

Ghez, A.M., Salim, S., Weinberg, N.N., Lu, J.R., Do, T., Dunn, J.K., Matthews, K., Morris, M.R., Yelda, S., Becklin, E.E., Kremenek, T., Milosavljevic, M. & Naiman, J. (2008). Measuring Distance and Properties of the Milky Way's Central Supermassive Black Hole with Stellar Orbits. , **689**, 1044–1062. 3

Gillessen, S., Eisenhauer, F., Trippe, S., Alexander, T., Genzel, R., Martins, F. & Ott, T. (2009). Monitoring Stellar Orbits Around the Massive Black Hole in the Galactic Center. , **692**, 1075–1109. 3

Gillessen, S., Plewa, P.M., Eisenhauer, F., Sari, R., Waisberg, I., Habibi, M., Pfuhl, O., George, E., Dexter, J., von Fellenberg, S., Ott, T. & Genzel, R. (2017). An Update on Monitoring Stellar Orbits in the Galactic Center. , **837**, 30. 7, 65

Graham, A.W. (2001). An Investigation into the Prominence of Spiral Galaxy Bulges. , **121**, 820–840. 39

Graham, A.W. & Spitler, L.R. (2009). Quantifying the coexistence of massive black holes and dense nuclear star clusters. , **397**, 1003–+. 28

Gravity Collaboration, Abuter, R., Amorim, A., Anugu, N., Bauböck, M., Benisty, M., Berger, J.P., Blind, N., Bonnet, H., Brandner, W., Buron, A., Collin, C., Chapron, F., Clénet, Y., Coudé Du Foresto, V., de Zeeuw, P.T., Deen, C., Delplancke-Ströbele, F., Dembet, R., Dexter, J., Duvert, G., Eckart, A., Eisenhauer, F., Finger, G., Förster Schreiber, N.M., Fédou, P., Garcia, P., Garcia Lopez, R., Gao, F., Gendron, E., Genzel, R., Gillessen, S., Gordo, P., Habibi, M., Haubois, X., Haug, M., Haussmann, F., Henning, T., Hippler, S., Horrobin, M., Hubert, Z., Hubin, N., Jimenez Rosales, A., Jochum, L., Jocou, K., Kaufer, A., Kellner, S., Kendrew, S., Kervella, P., Kok, Y., Kulas, M., Lacour, S., Lapeyrère, V., Lazareff, B., Le Bouquin, J.B., Léna, P., Lippa, M., Lenzen, R., Mérand, A., Müler, E., Neumann, U., Ott, T., Palanca, L., Paumard, T., Pasquini, L., Perraut, K., Perrin, G., Pfuhl, O., Plewa, P.M., Rabien, S., Ramírez, A., Ramos, J., Rau, C., Rodríguez-Coira, G., Rohloff, R.R., Rousset, G., Sanchez-Bermudez, J., Scheithauer, S., Schöller, M., Schuler, N., Spyromilio, J., Straub, O., Straubmeier, C., Sturm, E., Tacconi, L.J., Tristram, K.R.W., Vincent, F., von Fellenberg, S., Wank, I., Waisberg, I., Widmann, F., Wieprecht, E., Wiest, M., Wiezorrek, E., Woillez, J., Yazici, S., Ziegler, D. & Zins, G. (2018a). Detection of the gravitational redshift in the orbit of the star S2 near the Galactic centre massive black hole. , **615**, L15. 3, 7, 40, 65, 135

Gravity Collaboration, Abuter, R., Amorim, A., Bauböck, M., Berger, J.P., Bonnet, H., Brandner, W., Clénet, Y., Coudé Du Foresto, V., de Zeeuw, P.T., Deen, C., Dexter, J., Duvert, G., Eckart, A., Eisenhauer, F., Förster Schreiber, N.M., Garcia, P., Gao, F., Gendron, E., Genzel, R., Gillessen, S., Guajardo, P., Habibi, M., Haubois, X., Henning, T., Hippler, S., Horrobin, M., Huber, A., Jiménez-Rosales, A., Jocou, L., Kervella, P., Lacour, S., Lapeyrère, V., Lazareff, B., Le Bouquin, J.B., Léna, P., Lippa, M., Ott, T., Panduro, J., Paumard, T., Perraut, K., Perrin, G., Pfuhl, O., Plewa, P.M., Rabien, S., Rodríguez-Coira, G., Rousset, G., Sternberg, A., Straub, O., Straubmeier, C., Sturm, E., Tacconi, L.J., Vincent, F., von Fellenberg, S., Waisberg, I., Widmann, F., Wieprecht, E., Wiezorrek, E., Woillez, J. & Yazici, S. (2018b). Detection of orbital motions near the last stable circular orbit of the massive black hole SgrA*. , **618**, L10. 128

Gültekin, K., Richstone, D.O., Gebhardt, K., Lauer, T.R., Tremaine, S., Aller, M.C., Bender, R., Dressler, A., Faber, S.M., Filippenko, A.V., Green, R., Ho, L.C., Kormendy, J., Magorrian, J., Pinkney, J. & Siopis, C. (2009). The M-σ and M-L Relations in Galactic Bulges, and Determinations of Their Intrinsic Scatter. , **698**, 198–221. 2

Habibi, M., Gillessen, S., Martins, F., Eisenhauer, F., Plewa, P.M., Pfuhl, O., George, E., Dexter, J., Waisberg, I., Ott, T., von Fellenberg, S., Bauböck, M., Jimenez-Rosales, A. & Genzel, R. (2017). Twelve Years of Spectroscopic Monitoring in the Galactic Center: The Closest Look at S-stars near the Black Hole. , **847**, 120. 5

Häring, N. & Rix, H.W. (2004). On the Black Hole Mass-Bulge Mass Relation. , **604**, L89–L92. 2

Hopman, C. & Alexander, T. (2005). The Orbital Statistics of Stellar Inspiral and Relaxation near a Massive Black Hole: Characterizing Gravitational Wave Sources. , **629**, 362–372. 67

Hopman, C. & Alexander, T. (2006). The Effect of Mass Segregation on Gravitational Wave Sources near Massive Black Holes. , **645**, L133–L136. 64

Hornstein, S.D., Ghez, A.M., Tanner, A., Morris, M., Becklin, E.E. & Wizinowich, P. (2002). Limits on the Short-Term Variability of Sagittarius A* in the Near-Infrared. , **577**, L9–L13. 129

Hosek, M.W., Jr., Lu, J.R., Anderson, J., Ghez, A.M., Morris, M.R. & Clarkson, W.I. (2015). The Arches Cluster: Extended Structure and Tidal Radius. , **813**, 27. 169

Jansky, K.G. (1933). Radio Waves from Outside the Solar System. , **132**, 66. 6

Jia, S., Lu, J.R., Sakai, S., Gautam, A.K., Do, T., Hosek, M.W., Jr., Service, M., Ghez, A.M., Gallego-Cano, E., Schödel, R., Hees, A., Morris, M.R., Becklin, E. & Matthews, K. (2019). The Galactic Center: Improved Relative Astrometry for Velocities, Accelerations, and Orbits near the Supermassive Black Hole. , **873**, 9. 26, 129, 200

Kieffer, T.F. & Bogdanović, T. (2016). Can Star-Disk Collisions Explain the Missing Red Giants Problem in the Galactic Center? , **823**, 155. 124

Knuth, K.H. (2006). Optimal Data-Based Binning for Histograms. *ArXiv Physics e-prints*. 86, 147

Kroupa, P. (2001). On the variation of the initial mass function. , **322**, 231–246. 102, 118

Kroupa, P. & Weidner, C. (2003). Galactic-Field Initial Mass Functions of Massive Stars. , **598**, 1076–1078. 102

REFERENCES

Kunneriath, D., Eckart, A., Vogel, S.N., Teuben, P., Mužić, K., Schödel, R., García-Marín, M., Moultaka, J., Staguhn, J., Straubmeier, C., Zensus, J.A., Valencia-S., M. & Karas, V. (2012). The Galactic centre mini-spiral in the mm-regime. , **538**, A127. 4

Lau, R.M., Herter, T.L., Morris, M.R., Becklin, E.E. & Adams, J.D. (2013). SOFIA/FORCAST Imaging of the Circumnuclear Ring at the Galactic Center. , **775**, 37. 83

Lauer, T.R., Ajhar, E.A., Byun, Y.I., Dressler, A., Faber, S.M., Grillmair, C., Kormendy, J., Richstone, D. & Tremaine, S. (1995). The Centers of Early-Type Galaxies with HST.I.An Observational Survey. , **110**, 2622. 107

Launhardt, R., Zylka, R. & Mezger, P.G. (2002). The nuclear bulge of the Galaxy. III. Large-scale physical characteristics of stars and interstellar matter. , **384**, 112–139. 3, 28, 37, 38, 40, 48, 106, 167

Lenzen, R., Hartung, M., Brandner, W., Finger, G., Hubin, N.N., Lacombe, F., Lagrange, A., Lehnert, M.D., Moorwood, A.F.M. & Mouillet, D. (2003). NAOS-CONICA first on sky results in a variety of observing modes. In M. Iye & A. F. M. Moorwood, ed., *Society of Photo-Optical Instrumentation Engineers (SPIE) Conference Series*, vol. 4841 of *Society of Photo-Optical Instrumentation Engineers (SPIE) Conference Series*, 944–952. 17

Lightman, A.P. & Shapiro, S.L. (1977). The distribution and consumption rate of stars around a massive, collapsed object. , **211**, 244–262. 64

Lo, K.Y. & Claussen, M.J. (1983). High-resolution observations of ionized gas in central 3 parsecs of the Galaxy - Possible evidence for infall. , **306**, 647–651. 167

Lu, J.R., Ghez, A.M., Hornstein, S.D., Morris, M. & Becklin, E.E. (2005). IRS 16 SW: A New Comoving Group of Young Stars in the Central Parsec of the Milky Way. , **625**, L51–L54. 5, 24, 26, 77

Lu, J.R., Ghez, A.M., Hornstein, S.D., Morris, M.R., Becklin, E.E. & Matthews, K. (2009). A Disk of Young Stars at the Galactic Center as Determined by Individual Stellar Orbits. , **690**, 1463–1487. 5, 77

Lu, J.R., Do, T., Ghez, A.M., Morris, M.R., Yelda, S. & Matthews, K. (2013). Stellar Populations in the Central 0.5 pc of the Galaxy. II. The Initial Mass Function. , **764**, 155. 98, 100, 101, 102, 103, 149, 152, 208, 220

Lynden-Bell, D. & Rees, M.J. (1971). On quasars, dust and the galactic centre. , **152**, 461. 6

Maíz Apellániz, J. (2006). A Recalibration of Optical Photometry: Tycho-2, Strömgren, and Johnson Systems. , **131**, 1184–1199. 102

Markwardt, C.B. (2009). Non-linear Least-squares Fitting in IDL with MPFIT. In D.A. Bohlender, D. Durand & P. Dowler, eds., *Astronomical Data Analysis Software and Systems XVIII*, vol. 411 of *Astronomical Society of the Pacific Conference Series*, 251. 108

Martins, F., Hillier, D.J., Paumard, T., Eisenhauer, F., Ott, T. & Genzel, R. (2008). The most massive stars in the Arches cluster. , **478**, 219–233. 3

McConnell, N.J. & Ma, C.P. (2013). Revisiting the Scaling Relations of Black Hole Masses and Host Galaxy Properties. , **764**, 184. 2

Merritt, D. (2010). The Distribution of Stars and Stellar Remnants at the Galactic Center. , **718**, 739–761. 66

Merritt, D. & Szell, A. (2006). Dynamical Cusp Regeneration. , **648**, 890–899. 66

Meyer, L., Ghez, A.M., Schödel, R., Yelda, S., Boehle, A., Lu, J.R., Do, T., Morris, M.R., Becklin, E.E. & Matthews, K. (2012). The Shortest-KnownPeriod Star Orbiting Our Galaxys Supermassive Black Hole. *Science*, **338**, 84–. 20, 24, 40

Molinari, S., Bally, J., Noriega-Crespo, A., Compiègne, M., Bernard, J.P., Paradis, D., Martin, P., Testi, L., Barlow, M., Moore, T., Plume, R., Swinyard, B., Zavagno, A., Calzoletti, L., Di Giorgio, A.M., Elia, D., Faustini, F., Natoli, P., Pestalozzi, M., Pezzuto, S., Piacentini, F., Polenta, G., Polychroni, D., Schisano, E., Traficante, A., Veneziani, M., Battersby, C., Burton, M., Carey, S., Fukui, Y., Li, J.Z., Lord, S.D., Morgan, L., Motte, F., Schuller, F., Stringfellow, G.S., Tan, J.C., Thompson, M.A., Ward-Thompson, D., White, G. & Umana, G. (2011). A 100 pc Elliptical and Twisted Ring of Cold and Dense Molecular Clouds Revealed by Herschel Around the Galactic Center. , **735**, L33. 42

Morris, M. & Serabyn, E. (1996). The Galactic Center Environment. , **34**, 645–702. 3

Mužić, K., Eckart, A., Schödel, R., Meyer, L. & Zensus, A. (2007). First proper motions of thin dust filaments at the Galactic center. , **469**, 993–1002. 83

Narayan, R., Yi, I. & Mahadevan, R. (1995). Explaining the spectrum of Sagittarius A* with a model of an accreting black hole. , **374**, 623–625. 126

Neumayer, N. (2017). Nuclear Star Clusters. In C. Charbonnel & A. Nota, eds., *Formation, Evolution, and Survival of Massive Star Clusters*, vol. 316 of *IAU Symposium*, 84–90. 2

Neumayer, N. & Walcher, C.J. (2012). Are Nuclear Star Clusters the Precursors of Massive Black Holes? *Advances in Astronomy*, **2012**. 2, 28

Nishiyama, S. & Schödel, R. (2013). Young, massive star candidates detected throughout the nuclear star cluster of the Milky Way. , **549**, A57. 169

Nishiyama, S., Nagata, T., Tamura, M., Kandori, R., Hatano, H., Sato, S. & Sugitani, K. (2008). The Interstellar Extinction Law toward the Galactic Center. II. V, J, H, and $K_s Bands.$, **680**, 1174 – –1179. 9, 35

Nishiyama, S., Tamura, M., Hatano, H., Kato, D., Tanabé, T., Sugitani, K. & Nagata, T. (2009). Interstellar Extinction Law Toward the Galactic Center III: J, H, K_S Bands in the 2MASS and the MKO Systems, and 3.6, 4.5, 5.8, 8.0 μm in the Spitzer/IRAC System. , **696**, 1407–1417. 79

Nishiyama, S., Yasui, K., Nagata, T., Yoshikawa, T., Uchiyama, H., Schödel, R., Hatano, H., Sato, S., Sugitani, K., Suenaga, T., Kwon, J. & Tamura, M. (2013). Magnetically Confined Interstellar Hot Plasma in the Nuclear Bulge of Our Galaxy. , **769**, L28. 37, 38, 39, 40, 41, 202, 219

Nishiyama, S., Schödel, R., Yoshikawa, T., Nagata, T., Minowa, Y. & Tamura, M. (2016). Spectroscopically identified intermediate age stars at 0.5-3 pc distance from Sagittarius A*. , **588**, A49. 100

Nogueras-Lara, F., Gallego-Calvente, A.T., Dong, H., Gallego-Cano, E., Girard, J.H.V., Hilker, M., de Zeeuw, P.T., Feldmeier-Krause, A., Nishiyama, S., Najarro, F., Neumayer, N. & Schödel, R. (2018a). GALACTICNUCLEUS: A high angular resolution JHK_s imaging survey of the Galactic centre. I. Methodology, performance, and near-infrared extinction towards the Galactic centre. , **610**, A83. 9, 20, 35, 78, 140

Nogueras-Lara, F., Schödel, R., Dong, H., Najarro, F., Gallego-Calvente, A.T., Hilker, M., Gallego-Cano, E., Nishiyama, S., Neumayer, N., Feldmeier-Krause, A., Girard, J.H.V., Cassisi, S. & Pietrinferni, A. (2018b). Star formation history and metallicity in the Galactic inner bulge revealed by the red giant branch bump. , **620**, A83. 140

Nogueras-Lara, F., Gallego-Calvente, A.T., Dong, H., Gallego-Cano, E., Girard, J.H.V., Hilker, M., de Zeeuw, P.T., Feldmeier-Krause, A., Nishiyama, S., Najarro, F., Neumayer, N. & Schödel, R. (in preparation). 21, 56

Paumard, T., Genzel, R., Martins, F., Nayakshin, S., Beloborodov, A.M., Levin, Y., Trippe, S., Eisenhauer, F., Ott, T., Gillessen, S., Abuter, R., Cuadra, J., Alexander, T. & Sternberg, A. (2006). The Two Young Star Disks in the Central Parsec of the Galaxy: Properties, Dynamics, and Formation. , **643**, 1011–1035. 5, 77, 102

Peebles, P.J.E. (1972). Star Distribution Near a Collapsed Object. , **178**, 371–376. 2

Petr, M.G., Coude Du Foresto, V., Beckwith, S.V.W., Richichi, A. & McCaughrean, M.J. (1998). Binary Stars in the Orion Trapezium Cluster Core. , **500**, 825–+. 24

Pfuhl, O., Fritz, T.K., Zilka, M., Maness, H., Eisenhauer, F., Genzel, R., Gillessen, S., Ott, T., Dodds-Eden, K. & Sternberg, A. (2011). The Star Formation History of the Milky Way's Nuclear Star Cluster. , **741**, 108. 28, 54, 97, 98, 99, 100, 118, 208, 210

Pfuhl, O., Gillessen, S., Eisenhauer, F., Genzel, R., Plewa, P.M., Ott, T., Ballone, A., Schartmann, M., Burkert, A., Fritz, T.K., Sari, R., Steinberg, E. & Madigan, A.M. (2015). The Galactic Center Cloud G2 and its Gas Streamer. , **798**, 111. 132

Philipp, S., Zylka, R., Mezger, P.G., Duschl, W.J., Herbst, T. & Tuffs, R.J. (1999). The nuclear bulge. I. K band observations of the central 30 PC. , **348**, 768–782. 54

Plewa, P.M. (2018). Random forest classification of stars in the Galactic Centre. , **476**, 3974–3980. 137

Primot, J., Rousset, G. & Fontanella, J.C. (1990). Deconvolution from wave-front sensing - A new technique for compensating turbulence-degraded images. *Journal of the Optical Society of America A*, **7**, 1598–1608. 24

Rafelski, M., Ghez, A.M., Hornstein, S.D., Lu, J.R. & Morris, M. (2007). Photometric Stellar Variability in the Galactic Center. , **659**, 1241–1256. 24, 26

Rousset, G., Lacombe, F., Puget, P., Hubin, N.N., Gendron, E., Fusco, T., Arsenault, R., Charton, J., Feautrier, P., Gigan, P., Kern, P.Y., Lagrange, A., Madec, P., Mouillet, D., Rabaud, D., Rabou, P., Stadler, E. & Zins, G. (2003). NAOS, the first AO system of the VLT: on-sky performance. In P. L. Wizinowich & D. Bonaccini, ed., *Society of Photo-Optical Instrumentation Engineers (SPIE) Conference Series*, vol. 4839 of *Society of Photo-Optical Instrumentation Engineers (SPIE) Conference Series*, 140–149. 17

Sanchez-Bermudez, J., Schödel, R., Alberdi, A., Muzić, K., Hummel, C.A. & Pott, J.U. (2014). Properties of bow-shock sources at the Galactic center. , **567**, A21. 83

Schmidt, M. (1963). 3C 273 : A Star-Like Object with Large Red-Shift. , **197**, 1040. 2

Schödel, R. (2010). Accurate photometry with adaptive optics in the presence of anisoplanatic effects with a sparsely sampled PSF. The Galactic center as an example of a challenging target for accurate AO photometry. , **509**, A260000+. 69, 70, 79

REFERENCES

Schödel, R., Ott, T., Genzel, R., Hofmann, R., Lehnert, M., Eckart, A., Mouawad, N., Alexander, T., Reid, M.J., Lenzen, R., Hartung, M., Lacombe, F., Rouan, D., Gendron, E., Rousset, G., Lagrange, A.M., Brandner, W., Ageorges, N., Lidman, C., Moorwood, A.F.M., Spyromilio, J., Hubin, N. & Menten, K.M. (2002). A star in a 15.2-year orbit around the supermassive black hole at the centre of the Milky Way. , **419**, 694–696. 7

Schödel, R., Ott, T., Genzel, R., Eckart, A., Mouawad, N. & Alexander, T. (2003). Stellar Dynamics in the Central Arcsecond of Our Galaxy. , **596**, 1015–1034. 7

Schödel, R., Eckart, A., Alexander, T., Merritt, D., Genzel, R., Sternberg, A., Meyer, L., Kul, F., Moultaka, J., Ott, T. & Straubmeier, C. (2007). The structure of the nuclear stellar cluster of the Milky Way. , **469**, 125–146. 66, 72, 84, 85, 89, 97, 100, 105, 106, 168, 169

Schödel, R., Merritt, D. & Eckart, A. (2009). The nuclear star cluster of the Milky Way: proper motions and mass. , **502**, 91–111. 20, 77

Schödel, R., Najarro, F., Muzic, K. & Eckart, A. (2010). Peering through the veil: near-infrared photometry and extinction for the Galactic nuclear star cluster. Accurate near infrared H, Ks, and L' photometry and the near-infrared extinction-law toward the central parsec of the Galaxy. , **511**, A18+. 9, 69, 71, 73, 75, 79, 168, 169, 180

Schödel, R., Morris, M.R., Muzic, K., Alberdi, A., Meyer, L., Eckart, A. & Gezari, D.Y. (2011). The mean infrared emission of Sagittarius A*. , **532**, A83+. 83

Schödel, R., Yelda, S., Ghez, A., Girard, J.H., Labadie, L., Rebolo, R., Pérez-Garrido, A. & Morris, M.R. (2013). Holographic imaging of crowded fields: high angular resolution imaging with excellent quality at very low cost. , **429**, 1367–1375. 20, 24, 70

Schödel, R., Feldmeier, A., Kunneriath, D., Stolovy, S., Neumayer, N., Amaro-Seoane, P. & Nishiyama, S. (2014a). Surface brightness profile of the Milky Way's nuclear star cluster. , **566**, A47. 4, 23, 28, 29, 30, 37, 40, 42, 48, 49, 50, 51, 65, 86, 106, 107, 108, 109, 112, 113, 115, 116, 117, 201, 209, 210

Schödel, R., Feldmeier, A., Neumayer, N., Meyer, L. & Yelda, S. (2014b). The nuclear cluster of the Milky Way: our primary testbed for the interaction of a dense star cluster with a massive black hole. *Classical and Quantum Gravity*, **31**, 244007. 4, 28, 57, 65

Schödel, R., Gallego-Cano, E., Dong, H., Nogueras-Lara, F., Gallego-Calvente, A.T., Amaro-Seoane, P. & Baumgardt, H. (2018). The distribution of stars around the Milky Way's central black hole. II. Diffuse light from sub-giants and dwarfs. , **609**, A27. 12, 17, 43, 68, 159

Serabyn, E., Carlstrom, J., Lay, O., Lis, D.C., Hunter, T.R., Lacy, J.H. & Hills, R.E. (1997). High-Frequency Measurements of the Spectrum of Sagittarius A*. , **490**, L77–L81. 126

Seth, A.C., Dalcanton, J.J., Hodge, P.W. & Debattista, V.P. (2006). Clues to Nuclear Star Cluster Formation from Edge-on Spirals. , **132**, 2539–2555. 57, 58, 205

Shahzamanian, B., Eckart, A., Valencia-S., M., Witzel, G., Zamaninasab, M., Sabha, N., García-Marín, M., Karas, V., Karssen, G.D., Borkar, A., Dovčiak, M., Kunneriath, D., Bursa, M., Buchholz, R., Moultaka, J. & Straubmeier, C. (2015). Polarized light from Sagittarius A* in the near-infrared K_s-band. , **576**, A20. 127, 132

Stanek, K.Z., Udalski, A., Szymański, M., Kałużny, J., Kubiak, Z.M., Mateo, M. & Krzemiński, W. (1997). Modeling the Galactic Bar Using Red Clump Giants. , **477**, 163–175. 37

Stolovy, S., Ramirez, S., Arendt, R.G., Cotera, A., Yusef-Zadeh, F., Law, C., Gezari, D., Sellgren, K., Karr, J., Moseley, H. & Smith, H.A. (2006). A mid-infrared survey of the inner 2 x 1.5 degrees of the Galaxy with Spitzer/IRAC. *Journal of Physics Conference Series*, **54**, 176–182. 40

Stolte, A., Ghez, A.M., Morris, M., Lu, J.R., Brandner, W. & Matthews, K. (2008). The Proper Motion of the Arches Cluster with Keck Laser-Guide Star Adaptive Optics. , **675**, 1278–1292. 3

Støstad, M., Do, T., Murray, N., Lu, J.R., Yelda, S. & Ghez, A. (2015). Mapping the Outer Edge of the Young Stellar Cluster in the Galactic Center. , **808**, 106. 10

Tang, J., Bressan, A., Rosenfield, P., Slemer, A., Marigo, P., Girardi, L. & Bianchi, L. (2014). New PARSEC evolutionary tracks of massive stars at low metallicity: testing canonical stellar evolution in nearby star-forming dwarf galaxies. , **445**, 4287–4305. 98, 101

Trippe, S., Gillessen, S., Gerhard, O.E., Bartko, H., Fritz, T.K., Maness, H.L., Eisenhauer, F., Martins, F., Ott, T., Dodds-Eden, K. & Genzel, R. (2008). Kinematics of the old stellar population at the Galactic centre. , **492**, 419–439. 20, 77

van der Hucht, K.A. (2006). New Galactic Wolf-Rayet stars, and candidates. An annex to The VIIth Catalogue of Galactic Wolf-Rayet Stars. , **458**, 453–459. 3

Walcher, C.J., van der Marel, R.P., McLaughlin, D., Rix, H., Böker, T., Häring, N., Ho, L.C., Sarzi, M. & Shields, J.C. (2005). Masses of Star Clusters in the Nuclei of Bulgeless Spiral Galaxies. , **618**, 237–246. 27

Wang, Q.D., Dong, H., Cotera, A., Stolovy, S., Morris, M., Lang, C.C., Muno, M.P., Schneider, G. & Calzetti, D. (2010). HST/NICMOS Paschen-α Survey of the Galactic Centre: Overview. , **402**, 895–902. 81, 83

Witzel, G., Eckart, A., Bremer, M., Zamaninasab, M., Shahzamanian, B., Valencia-S., M., Schödel, R., Karas, V., Lenzen, R., Marchili, N., Sabha, N., Garcia-Marin, M., Buchholz, R.M., Kunneriath, D. & Straubmeier, C. (2012). Source-intrinsic Near-infrared Properties of Sgr A*: Total Intensity Measurements. , **203**, 18. 86, 147

Witzel, G., Ghez, A.M., Morris, M.R., Sitarski, B.N., Boehle, A., Naoz, S., Campbell, R., Becklin, E.E., Canalizo, G., Chappell, S., Do, T., Lu, J.R., Matthews, K., Meyer, L., Stockton, A., Wizinowich, P. & Yelda, S. (2014). Detection of Galactic Center Source G2 at 3.8 μm during Periapse Passage. , **796**, L8. 132

Witzel, G., Sitarski, B.N., Ghez, A.M., Morris, M.R., Hees, A., Do, T., Lu, J.R., Naoz, S., Boehle, A., Martinez, G., Chappell, S., Schödel, R., Meyer, L., Yelda, S., Becklin, E.E. & Matthews, K. (2017). The Post-periapsis Evolution of Galactic Center Source G1: The Second Case of a Resolved Tidal Interaction with a Supermassive Black Hole. , **847**, 80. 131, 133, 134

Witzel, G., Martinez, G., Hora, J., Willner, S.P., Morris, M.R., Gammie, C., Becklin, E.E., Ashby, M.L.N., Baganoff, F., Carey, S., Do, T., Fazio, G.G., Ghez, A., Glaccum, W.J., Haggard, D., Herrero-Illana, R., Ingalls, J., Narayan, R. & Smith, H.A. (2018). Variability Timescale and Spectral Index of Sgr A* in the Near Infrared: Approximate Bayesian Computation Analysis of the Variability of the Closest Supermassive Black Hole. , **863**, 15. 126, 127, 130, 131, 132

Wyller, A.A. (1970). Observational Aspects of Black Holes in Globular Clusters. , **160**, 443. 2

Yu, Q. & Tremaine, S. (2002). Observational constraints on growth of massive black holes. , **335**, 965–976. 2

Yuan, F., Quataert, E. & Narayan, R. (2003). Nonthermal Electrons in Radiatively Inefficient Accretion Flow Models of Sagittarius A*. , **598**, 301–312. 126

Yusef-Zadeh, F., Bushouse, H. & Wardle, M. (2012). Hubble Space Telescope Observations of the Stellar Distribution near Sgr A*. , **744**, 24. 43, 67

Yusef-Zadeh, F., Bushouse, H., Schödel, R., Wardle, M., Cotton, W., Roberts, D.A., Nogueras-Lara, F. & Gallego-Cano, E. (2015). Compact Radio Sources within 30' of Sgr A*: Proper Motions,Stellar Winds, and the Accretion Rate onto Sgr A*. , **809**, 10. 6, 199

List of Figures

LIST OF FIGURES

List of Tables

Acknowledgements

I would like to conclude this dissertation by expressing my gratitude to all the people who helped me, both in and outside of science. This dissertation would not have been possible without their help, advice and support.

First and foremost, I would like to thank my supervisor Dr. Rainer Schödel for trusting me and opening a door to the Galactic center for me. I was able to become an astrophysicist and finish this thesis thanks to his patience, support and continuous guidance, encouragement, enthusiasm, good ideas, help with English ... [many more things] ... at all times. Also, I would like to thank him for the good times that we enjoyed together having "tapas".

Thanks to my PhD thesis committee members: Dr. Koraljka Muzic, Dr. Nadine Neumayer, Dr. María Inmaculada Domínguez Aguilera, Dr. Antxon Alberdi Odriozola, Dr. Emilio J. Alfaro Navarro, Dr. Simon Verley, and Dr. Elisa de Castro Rubio.

I would like to acknowledge the University of Granada for allowing me to get a Ph.D. in the Physics and Space Science program. I would like to thank the coordinator of my PhD program Ángel V. Delgado for all his bureaucratic support and kindness since the beginnings of this thesis. Thanks to my tutor Carlos Abia for his help along these years. Thanks to Simon and Inma for giving me very good advices.

Thanks to Universidad Complutense of Madrid (UCM) for my first year of thesis, specially to Jesús Gallego and Elisa de Castro for all their support.

I would like to give special thanks to all the members of the Galactic Center Group at University of California (UCLA). Thanks to Wendy and Juleen for their kind help and patience with all my paperwork. Thanks to Gunther and Anna Boehle for their great support when I arrived and throughout my stay. Thanks to my officemates Greg and Aurelien for making the time there more enjoyable and confortable. Thanks to Bernie, Arezu and Ana Ciurlo for their great help. Thanks to all of them for the good time that we spent together. Thanks to Mark, Tuan, and Eric for their help and kindness. Special thanks to Andrea Ghez for giving the opportunity to share that time with the Galactic Center group in Los Angeles and in Hawaii, for her enthusiasm, sympathy, kindness, motivation, encouragement, strength. Thanks to all of them for sharing with me their love for the Galactic center.

Thanks to ESO for giving the opportunity to observe with the VLT telescopes in Chile. I enjoyed very much to be on Paranal under its amazing skies. Thanks to its highly qualified staff that helped me to solve any observational problem.

Also thanks to the other scientists who supported and encouraged me: Wolfgang E Kerzendorf, Andreas Eckart, Farhad Yusef Zadeh, Daryl Haggard, Chris Jacobs for giving the opportunity to visit JPL/NASA and give a talk, Tobias Fritz and Shogo Nishiyama for their great help, Nadine Neumayer for her help, for being so nice with me and for organising my visit to MPIA, Kora and Nick Stone for their words of encouragement.

Thanks to Keck observatory for allowing me to observe with such large telescopes and enjoy the wonderful Hawaiian nights, especially to Randy Campbell for his great help.

Thanks to all my colleagues at the Instituto de Astrofísica de Andalucía in Granada for making me feel at home. Thanks to Cristina, Susana, Concepción, Rosa, Alonso, and Eva for all the support in the bureaucracy along these years. Special thanks to Francisco Tapia for his professionalism and kindness and for finding always a solution to any problem. Thanks to Mirjana, Enrique Pérez, Mayra, Ancor, Antonio Delgado, Angela, and Emilio Alfaro, for their advices and words of encouragement. Thanks to Emilio and Silbia for their kindness and for giving me the opportunity to give many talks. Thank all the members of the Centro de Cálculo for all these years of great help. Thanks to César for his support, specially for helping me to find mistakes in crazy scripts. Thanks to all the officemates over the years: Fran, Carolina, Sandra, Alejandro, Ny, Sergio, specially Laura and Antonio for their help and for being so nice with me. Special thanks to Antonio Fuentes and Salva for their support, empathy, and kindness and for sharing with me the last hard year, much more enjoyable and funny thanks to them. Thanks to Sol, Javi, and María Passas for all the great help in the mysterious bureaucratic final procedures and with the thesis itself. Thanks also to all the members of the Comisión de Mujeres, specially Pepa and Isabel for their constant struggle for women's rights, both of them a great example to me. Thanks to M. Ángeles, our great kindly librarian, for her help over these years and for sharing with us her love for books. Special thanks to Antxon for being such a good director as well as a great scientist, and a kind and friendly person.

I would like to thank my colleagues from the Galactic Center group for all the support. Thanks to Alicia for helping me a lot with my first fight with the programming. Thanks to Hui for all his help and for his fast answers over the years. Thanks to Paco for making me laugh when we were observing during the long nights in Chile, as well as for making all the trips together very enjoyable and fun. Special thanks to Teresa for her great support over these years, always being willing to help, for sharing with me the good times of "operación mango", and for helping me with the corrections of the thesis. The greatest thanks to Banafsheh for supporting me so much in last year, for sharing with me her great knowledge in the "flaring" breakfasts in a modest and fun way, for giving me words of encouragement, for helping me with the corrections of the thesis... Thanks also to Mahmoud for his very good advice and encouragement.

Thanks to CAHA people to open another window to the Cosmos in Granada for me that gave me the last push to finish the thesis.

Many thanks to my yoga class colleagues who helped me to relax in difficult times. Thanks to Carmen, my teacher, who teaches me how to take care of myself and to be in contact with the earth and with the present moment.

Thanks to all my musicians friends for supporting and encouraging me and helping me to relax and enjoy very much, essential in the last times: Jesús Hernández, Carlos, my colleagues of Dopolavoro Zaidin Quintuplet Sebas, Lucas, Alejandro, Diego, y Román, Jessi, and Dani. Thanks also to Dani and "el Inglés" for helping me with the english.

Thanks to my comrades and very good friends for all their support: Andrew, Pepe, Alfonso, Chema, Alba, Andrea, Muru, Eli, Lucia, and Fran. Special thanks to María and Álvaro who were

with me in the worst moments of this last “epoch”, for all the support and fun times, always making me laugh even in moments of panic.

My special thanks to my friends since old times: Inma, J, Guti, Belén and Ángel, Ana, Rocío, Marta, Zapata, Canijo, Lola, and Alex, for being such good and caring friends.

Thanks to the beautiful skies of Extremadura that brought me closer to the Universe and aroused my passion for the Cosmos, and the wonderful city of Granada for hosting me.

Last but not least, the greatest thanks of all goes to my family for their support throughout my life. To my parents Aurelio and Ana, for all their unconditional support, and their great help in the last years taking care of Siro so that I could travel, specially my mother who always took care of me. To Aloña, my brother Aurelio, my sister Ana, and my wonderful nephews Juan and Ibai. Thanks to Ana and Estela for supporting me over the years. Thanks to my cousins Chiki and Asun. Special thanks to my life partners María and Theo for taking care of Siro so many times, helping me at all times, encouraging me, supporting me... Thanks to my sister Merce, I cannot find the words to express my gratitude for all her support and encouragement throughout my life. Thanks to the support and love of my children: thanks to Ana for her essential help and thanks to Siro, who always found a way to make me laugh in times of stress and panic. Thanks to them for making me a better person.

The research leading to these results has received funding from the European Research Council under the European Union's Seventh Framework Programme (FP7/2007-2013) / ERC grant agreement n° [614922]. This work is based on observations made with ESO Telescopes at the La Silla Paranal Observatory under programmes IDs 183.B-0100 and 089.B-0162. We thank T. Fritz for detailed and valuable comments. This work has made use of the IAC-STAR Synthetic CMD computation code. IAC-STAR is suported and maintained by the computer division of the Instituto de Astrofísica de Canarias.

Declaration

I herewith declare that I have produced this thesis without the prohibited assistance of third parties and without making use of aids other than those specified; notions taken over directly or indirectly from other sources have been identified as such. This thesis has not previously been presented in identical or similar form to any other Spanish or foreign examination board.

The thesis work was conducted from 2014 to 2019 under the supervision of Dr. Rainer Schödel.

Granada, April 1, 2019